ORNL/TM-10033

ornl

OAK RIDGE NATIONAL LABORATORY

MARTIN MARIETTA

Metals and Ceramics Division Materials Sciences Program Annual Progress Report for Period Ending December 31, 1985

OPERATED BY
MARTIN MARIETTA ENERGY SYSTEMS, INC.
FOR THE UNITED STATES
DEPARTMENT OF ENERGY

Printed in the United States of America. Available from
National Technical Information Service
U.S. Department of Commerce
5285 Port Royal Road, Springfield, Virginia 22161
NTIS price codes—Printed Copy: A15 Microfiche A01

ORNL/TM-10033
Distribution
Category UC-25

METALS AND CERAMICS DIVISION

METALS AND CERAMICS DIVISION MATERIALS SCIENCES PROGRAM ANNUAL PROGRESS REPORT FOR PERIOD ENDING DECEMBER 31, 1985

Compiled by
J. O. Stiegler, Manager, Materials Sciences Program

Date Published: June 1986

Prepared by the
OAK RIDGE NATIONAL LABORATORY
Oak Ridge, Tennessee 37831
operated by
MARTIN MARIETTA ENERGY SYSTEMS, INC.
for the
U.S. DEPARTMENT OF ENERGY
under Contract No. DE-AC05-84OR21400

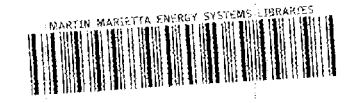

Reports previously issued in this series are as follows:

ORNL-5089	Period Ending June 30, 1975
ORNL-5182	Period Ending June 30, 1976
ORNL-5311	Period Ending June 30, 1977
ORNL-5437	Period Ending June 30, 1978
ORNL-5589	Period Ending June 30, 1979
ORNL-5672	Period Ending June 30, 1980
ORNL/TM-7970	Period Ending June 30, 1981
ORNL/TM-8627	Period Ending December 31, 1983
ORNL/TM-9357	Period Ending June 30, 1984

CONTENTS

INTRODUCTION

This report summarizes the activities of the Materials Sciences Program in the Oak Ridge National Laboratory (ORNL) Metals and Ceramics Division for the period July 1, 1984, to December 31, 1985. These activities constitute about one-fourth of the research and development conducted by the Division.

The emphasis of the program can be described as the scientific design of materials. The efforts are directed toward three classes of materials: high-temperature metallic alloys based on intermetallic compounds, structural ceramics, and radiation-resistant alloys. The first two materials are central to the theme of the High Temperature Materials Laboratory, and the third supports the Laboratory's mission in fission and fusion reactor technology. We combine the use of unique structural characterization facilities, the activities of the Theory Group, and accurate property determination to establish structure-property relationships.

An important aspect of the program is the interaction with universities, industry, and other laboratories. Two collaborative research centers established to aid these interactions are SHaRE and ORNL-ORAU Synchrotron X-Ray Group. These make our strong structural characterization capabilities available to researchers outside ORNL. Their activities are summarized in Chap. 1, "Structural Characterization," and Chap. 6, "Collaborative Research Centers." Other interactions with the scientific community are summarized in the Appendixes.

1. STRUCTURAL CHARACTERIZATION

1.1 MICROSCOPY AND MICROANALYSIS - J. Bentley

The microscopy and microanalysis task provides the core effort for modern structural characterization of materials for the Basic Energy Sciences (BES) Materials Sciences Program and indeed for the Metals and Ceramics Division. The task involves both analytical electron microscopy (AEM) and atom probe field ion microscopy (APFIM). The atom probe work is described in Sect. 1.2, although in practice many of the research topics involve both AEM and APFIM (e.g., segregation studies, Sect. 1.1.2), and many APFIM studies are greatly enhanced by complementary AEM results (e.g., G-phase identification, Sect. 1.1.1.5).

Three types of research are undertaken by the task: instrumentation acquisition, installation, and optimization; technique and method development and evaluation by application to basic materials science research; and application of state-of-the-art AEM to a range of materials, often in collaboration with other tasks.

The measurement of segregation (by both AEM and APFIM) remains a focus of the task, with the underlying goal of quantitatively relating the amount and spatial distribution of the segregant to grain boundary structure or type of secondary defect. There is also still much work that does not involve segregation directly - mostly phase transformations - but still makes use of state-of-the-art AEM. With the acquisition of the 300-kV Philips EM430T, a major portion of the in situ deformation and thick-section microscopy has switched to that instrument. The high-voltage electron microscope (HVEM) is used in a variety of collaborative work through the Shared Research Equipment (SHaRE) program and also finds application in several other programs, including the Ceramic Technology for Advanced Heat Engines Project and Energy Conversion and Utilization Technology Program and as an irradiation facility under several tasks.

Strong collaborative efforts with the tasks on structural ceramics, high-temperature alloy design, ion-implanted ceramics, radiation effects, and the fundamentals of welding and joining continue. The research efforts again included extensive collaborative work through the SHaRE program.

1.1.1 Analytical Electron Microscopy — J. Bentley

Several major items of equipment were put into operation during this reporting period. A Philips EM430T AEM (300-kV accelerating voltage) with an EDAX 9100/70 multichannel analyzer-computer system for energy dispersive X-ray spectroscopy (EDS) and electron energy loss spectroscopy (EELS) data acquisition and analysis and a Gatan 607 EELS spectrometer were delivered in September 1984. A voltage scanning unit for EELS and a Gatan double-tilt beryllium liquid-nitrogen-cooled specimen holder were added later. We plan to add scanning transmission electron microscopy (STEM) capabilities, a C400 computer control system, and a TV imaging system in the near future. In February 1985 a JEM 2000FX AEM (200-kV accelerating voltage) was installed under an agreement with the Japanese fusion materials development program. The instrument is largely dedicated to examination of radioactive specimens and is equipped with a complete scanning system including STEM, secondary electron and backscattered electron detectors, EELS, and a Tracor 5500 EDS system. Considerable effort was devoted to preparation of laboratories for these AEMs. A Gatan model 645 precision ion-milling system was delivered in September 1985 and is expected to play an important role in specimen preparation of "difficult" samples.

Evaluation and optimization of operating procedures for the new instrumentation figured strongly in the AEM efforts. Research on axial electron channeling X-ray microanalysis for site-occupancy determination of ternary additions to Ni_3Al and identification of G-phase precipitates in an aged cast stainless steel were among other projects not related to instrumentation.

1.1.1.1 Comparison of Performance of an Analytical Electron Microscope at 300 and 100 kV (ref. 1) – J. Bentley, E. A. Kenik, P. Angelini, A. T. Fisher, P. S. Sklad, G. L. Lehman,[2] and J. A. Horton, Jr.

Preliminary results on the performance of an analytical electron microscope (AEM) operating at 300 kV have been obtained and compared with the performance at 100 kV. The electron microscope used was a Philips EM430T operated with a LaB_6 cathode and equipped with EDAX 9100/70 EDS and Gatan 607 EELS systems.

For transmission electron microscopy (TEM) imaging, improved specimen penetration is expected as the accelerating voltage V_0 increases. The effect is due chiefly to the decrease in effective scattering cross sections with increased energy, but chromatic aberration is also important. Figure 1.1.1 shows a slip band in a wedge-shaped foil of Ni–20 at. % Mo. Specimen penetration is increased by nearly 3 times at 300 kV. Improved

ORNL-PHOTO 8129-84

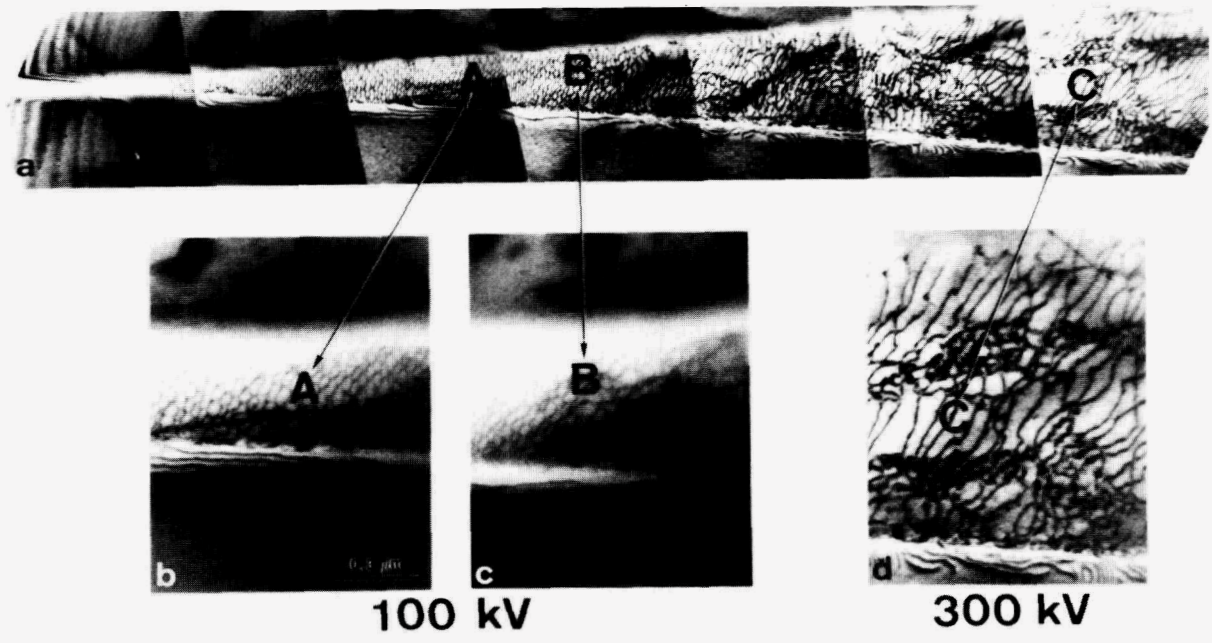

Fig. 1.1.1. Slip band in Ni–20 at. % Mo. (*a*) Low-magnification image at 300 kV. (*b*) 100 kV, 100-s exposure. (*c*) 100 kV, 100-s exposure, fully focused beam, thickness 0.6 μm. (*d*) 300 kV, 100-s exposure, thickness 1.5 μm; note high contrast and sharpness compared with (*b*) and (*c*).

resolution is also expected for increased accelerating voltage. The interpretable point-to-point resolution R should be 0.23 nm; it is limited by spherical aberration at Scherzer defocus and given by $R = 0.6\lambda^{3/4}C_S^{1/4}$, where λ is the electron wavelength and C_S is the spherical aberration coefficient.

The use of convergent beam electron diffraction (CBED) for lattice parameter, crystal symmetry (point and space group), and foil thickness determination is well established. The instrumental requirements have been preserved on the present instrument with little difference between 100- and 300-kV operation.

Although cross sections for inner shell ionizations in the 1- to 20-keV range decrease as V_0 is increased from 100 to 300 kV, the characteristic X-ray yield is expected to increase as a result of an increase in gun brightness (proportional to V_0), which more than offsets the decrease in cross sections. This behavior has been confirmed for a number of specimens. Also, since the bremsstrahlung becomes more forward peaked as V_0 increases, improved peak-to-background (P/B) ratios should result. Again, this behavior has been confirmed, but only after corrections for the hole count were made. Relativistically corrected cross sections must be used for standardless quantitative analysis at 300 kV. Such software modifications are under way.

The benefits for EELS microanalysis of operation at higher accelerating voltages should include improved P/B for constant thickness or an extended range of usable specimen thickness. Ionization cross sections should decrease, multiple scattering should be reduced, and collection efficiency should be increased. These benefits were confirmed by detailed measurements made on specimens of B_4C, BN, and SiC with particular care taken in the choice of optimum collection (and illumination) angles.

Displacement damage effects were observed at 300 kV in low-atomic-number materials. In aluminum at ambient temperature, faulted dislocation loops were observed to nucleate, grow, unfault, and then either glide from the foil or form a dislocation network. Also, during high resolution tests, the crystallinity of graphitized carbon was destroyed.

In spite of some instrumental problems, which remain to be overcome, the preliminary results on the overall performance of an AEM operating at

300 kV compared with 100 kV have confirmed the expected improvements. Such an instrument may indeed possess optimum performance with respect to cost, installation requirements, ease of operation, and specimen damage.

1.1.1.2 Microanalysis by Electron Energy Loss Spectroscopy at 100 to 300 kV (ref. 3) – P. Angelini and J. Bentley

Some features of the anticipated improvements in microanalysis by EELS at increased accelerating voltage have been studied with the use of a Philips EM430T equipped with EDAX 9100/70 and Gatan 607 EELS systems. Our main interest in operation at higher accelerating voltage is in the expected increase in the usable specimen thickness. With increased accelerating voltage, multiple scattering should be reduced, collection efficiency should be increased, and decreases in ionization cross sections should be more than offset by increases in gun brightness.

Detailed measurements have been made on a range of specimens, with emphasis on BN and SiC and with particular care being taken in the choice of optimum collection and illumination angles. As expected, for thin specimens little difference in peak-to-background (P/B) ratios was observed between 100 and 300 kV (see Fig. 1.1.2). Also, a significant increase (>2 times) in the usable specimen thickness at higher accelerating voltage was confirmed. The precise dependence of P/B on specimen thickness and accelerating voltage was found to be a function of ionization edge and material composition. For example, in boron nitride the nitrogen P/B decreases slowly with increasing thickness, since the background is mainly due to the tails of the boron edge, whereas the boron P/B decreases rapidly with increasing thickness. The carbon P/B for specimens of silicon carbide was similarly almost constant with increasing thickness since the background is mainly from the Si L edge. The rest of the SiC data was more complex. Values for the absolute partial ionization cross sections were determined for SiC. Measured values ranged between 0.9 and 3 times the calculated cross sections.

During this work it became apparent that the EELS instrumentation was not of optimal design, especially for 300-kV operation. There is a severe hole count, which causes difficulties in the measurement of thickness from

ORNL-PHOTO 8138-84

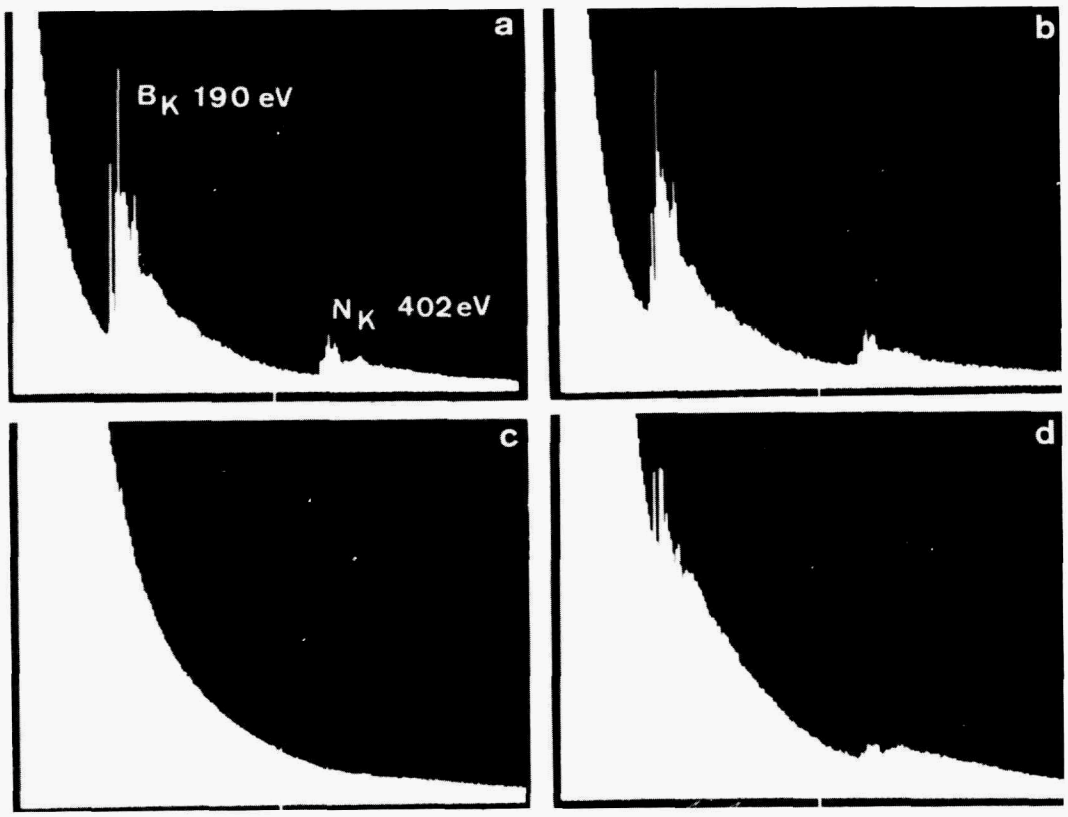

Fig. 1.1.2. Electron energy loss spectra of BN for two thicknesses, t, expressed as a fraction of the plasmon mean-free path length at 300 kV, λ_p. (*a*) 100 kV, $t/\lambda p$ about 0.1. (*b*) 300 kV, t/λ_p about 0.1. (*c*) 100 kV, t/λ_p about 0.7. (*d*) 300 kV, t/λ_p about 0.7.

the low loss spectrum and results in poorer P/B ratios than expected. Surprisingly, the edges most affected are at *large* losses at 100- and 300-kV operation.

1.1.1.3 Evaluation of a Precision Ion Milling System[4] – A. T. Fisher, J. Bentley, P. Angelini, P. S. Sklad, and E. A. Kenik

The operating characteristics, optimal procedures, and limitations of the Gatan Model 645 precision ion milling system are being evaluated. The device is a scanning ion beam instrument with which selected areas of a sample can be imaged using either secondary electron or secondary ion signals and selectively ion milled in a small region within the imaged area. The 1- to 10-keV ion beam (oxygen, hydrogen, nitrogen, or noble gases) can be focused to a 2-μm spot. Specimens are thinned without

removing them from the transmission electron microscope (TEM) specimen holder. The system (see Fig. 1.1.3) consists of an ion column, imaging system, eucentric goniometer stage, and vacuum system.

YP1372

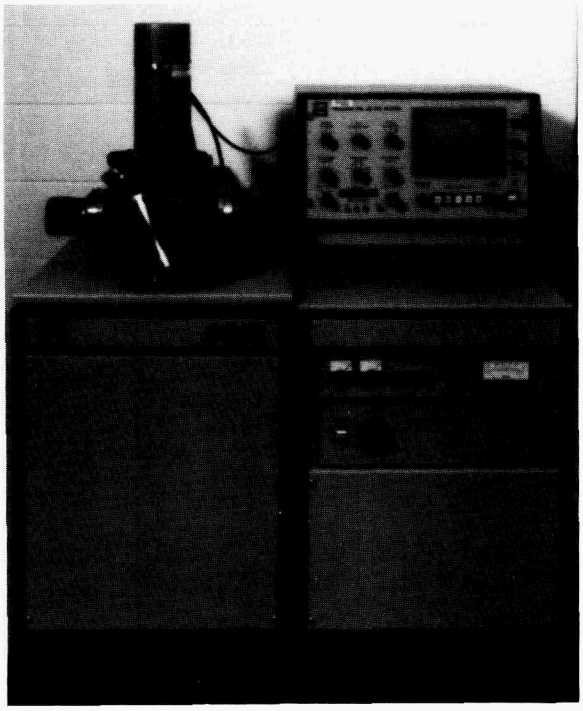

Fig. 1.1.3. Gatan Model 645 precision ion milling system.

The system is expected to greatly enhance the specimen preparation process. The localized thinning should prove beneficial for TEM characterization of cross-sectional specimens of ion-implanted ceramics (and metals), oxidized alloys, and rapidly solidified splats. The instrument should also be extremely useful in obtaining electron energy loss spectroscopy, high resolution X-ray microanalysis, and lattice imaging data on regions that would otherwise be too thick. Metallic alloy and semiconducting ceramic specimens have been successfully milled. Insulating ceramics have posed more of a problem because of secondary electron suppression due to buildup of charge. The loss of a secondary electron image of reasonable quality precludes the accurate location of the ion beam for localized milling. We are exploring the possibility of installing an electron flood gun to overcome this problem. An example of an area of SiC before and after localized milling is shown in Fig. 1.1.4.

ORNL-PHOTO 0564-86

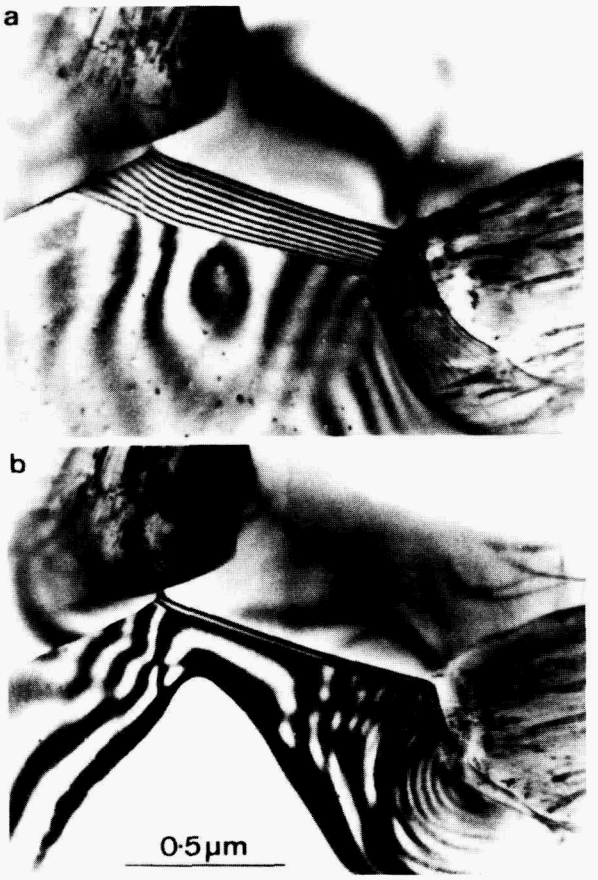

Fig. 1.1.4. Same area of SiC (*a*) before and (*b*) after localized milling from one side of the specimen. Identical diffracting conditions.

1.1.1.4 Preparation of Backthinned Ceramic Specimens[5] – A. T. Fisher and P. Angelini

Analytical electron microscopy (AEM) of the near surface microstructure of ion-implanted ceramics can provide much information about those materials. Backthinning of specimens results in relatively large thin areas for analysis of precipitates, voids, dislocations, depth profiles of implanted species, and other features. One of the most critical stages in the backthinning process is the ion milling procedure. Material sputtered during ion milling can redeposit on the back surface, thereby contaminating the specimen with impurities such as Fe, Cr, Ni, Mo, and Si. These impurities may originate from the specimen, specimen platform and clamping plates, vacuum system, and other components and may compromise many of the compositional and microstructural analyses. A method has been developed to protect the implanted surface by coating it with NaCl before backthinning.

Specimens approximately 100 μm thick are placed in a vacuum evaporator, and the center region (2.5 mm diam) is coated with approximately 1 μm of NaCl by a physical vapor deposition process. After the disk is clamped on a copper ion-milling specimen holder with the salted side in contact with the holder, the surface opposite the salted side is ion milled with argon (6 kV, 1 mA) to perforation in typically 12 h. The specimen is then immersed in water to remove the contamination as the salt dissolves. This procedure is shown schematically in Fig. 1.1.5. A TEM micrograph of single-crystal Al_2O_3 ion implanted with 150-keV Cr^+ ions to a dose of 4×10^{20} ions/m^2 and backthinned by using the method described is shown in Fig. 1.1.6(*a*). Note that some contamination is present, which may be due to incomplete removal during the salt dissolution stage. The energy-dispersive X-ray spectrum presented in Fig. 1.1.6(*b*) shows only Al (Al_2O_3 matrix), Ar (ion-milling gas), and Cr (ion-implantation species), suggesting nearly complete removal of both the NaCl coating and the contaminants.

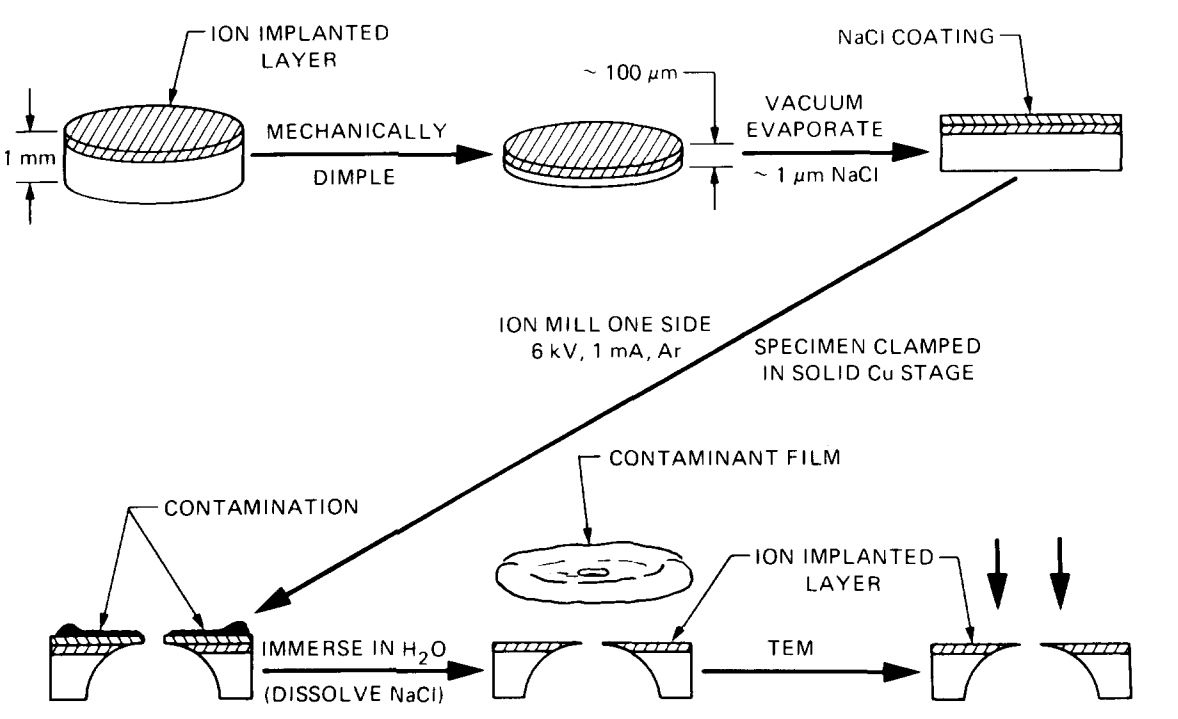

Fig. 1.1.5. Schematic diagram illustrating procedure for preparing backthinned ceramic specimens.

ORNL-PHOTO 4488-85

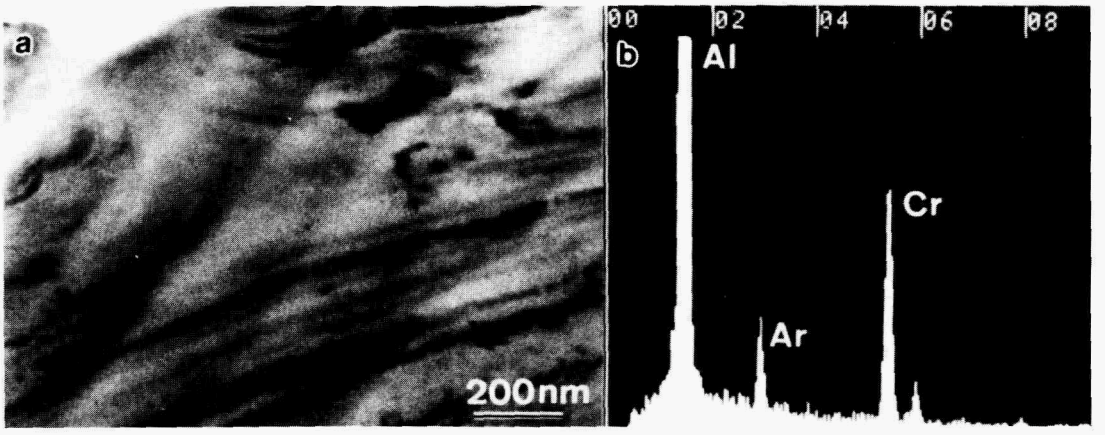

Fig. 1.1.6. (*a*) Bright-field micrograph of clean area of an Al_2O_3 specimen ion-implanted with chromium and backthinned by using the procedure shown in Fig. 1.1.5. (*b*) X-ray EDS spectrum of clean area (aluminum peak counts = 16 times full scale).

The technique does not always completely eliminate contamination but limits it so that the resulting microstructures can be effectively analyzed by AEM.

1.1.1.5 Identification of G-Phase in Aged Cast CF8-Type Stainless Steel[6] – J. Bentley, M. K. Miller, S. S. Brenner,[7] and J. A. Spitznagel[8]

Our earlier atom probe work[9] on phase transformations in the ferrite (~19 vol % of the duplex structure) in cast and aged CF8-type stainless steel used for primary coolant pipes in pressurized light-water nuclear reactors has been extended to include more detailed AEM studies. The present work deals with the identification of G-phase (prototype compound $Ni_{16}Ti_6Si_7$) observed in the ferrite of aged materials.

A dark-field image of the precipitates in the ferrite is shown in Fig. 1.1.7(*a*). All precipitates have the same orientation relationship with the matrix. The composition of the precipitates was obtained by X-ray microanalysis of carbon extraction replicas supported on beryllium grids. Single particles and clusters of precipitates [Fig. 1.1.7(*b*)] were analyzed. A typical X-ray spectrum is shown in Fig. 1.1.7(*c*), and quantative results are given in Table 1.1.1. The precipitate compositions

ORNL-PHOTO 0565-86

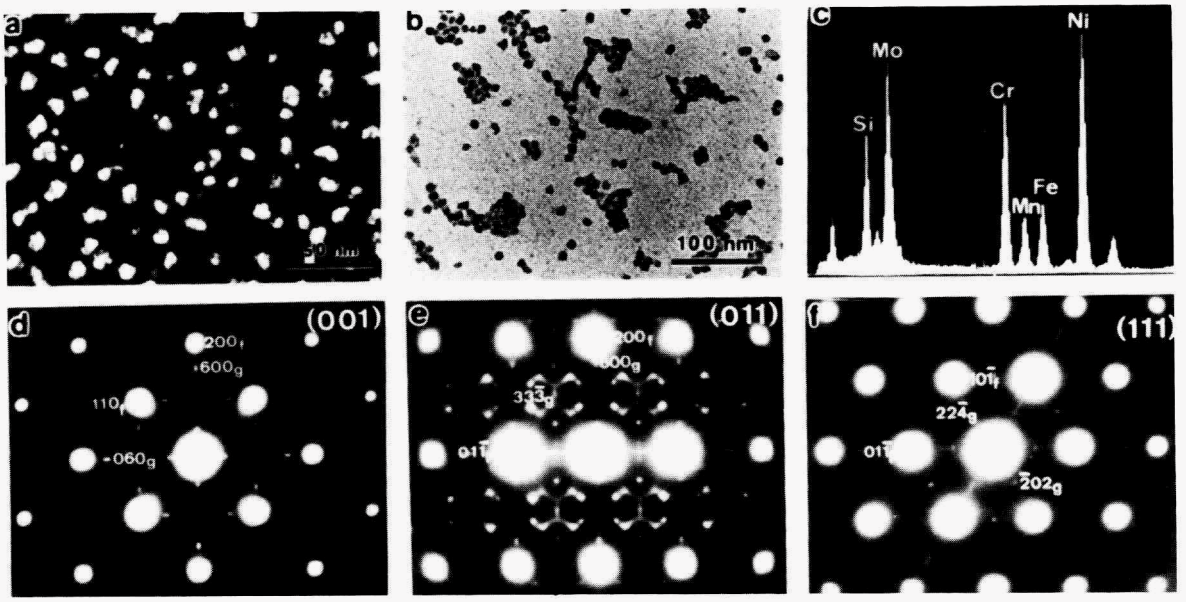

Fig. 1.1.7. (*a*) Dark-field image (precipitate reflection) showing G-phase particles in ferrite. (*b*) G-phase particles on carbon extraction replica. (*c*) Energy-dispersive X-ray spectrum. (*d*) [001], (*e*) [011], and (*f*) [111] diffraction patterns.

Table 1.1.1. Composition of G-phase precipitates (at. % ± standard deviation)

Element	Si	Cr	Fe + Mn	Ni	Mo	C
APFIM	27.7 ± 3.4	12.0 ± 2.5	20.6 ± 3.1	24.0 ± 3.2	13.0 ± 2.5	1.0 ± 0.7
AEM	20.9 ± 2.0	17.8 ± 2.1	10.5 ± 1.5	31.1 ± 2.2	19.9 ± 1.1	Not determined

determined by the atom probe and X-ray microanalysis differ significantly. The reasons are not clear. Leaching effects or retained surface films could affect the extracted particles. However, the particles are clearly alloy silicides.

Diffraction patterns [Fig. 1.1.7(*d–f*)] were obtained from the silicide precipitate plus the ferrite matrix. The patterns are consistent with cube-on-cube oriented fcc precipitates with a lattice parameter of 1.09 nm. The lattice parameter of the precipitates is 3.8 times that of the ferrite, and this mismatch results in splitting of the reflections by

double diffraction. Systematic tilting experiments away from zone axes confirmed the double diffraction effects and characteristic relative intensities such as weak 400 and 220 and strong 333 reflections. The exact location of some reflections, the diffuse scattering evident in Fig. 1.1.7(*e*), and the streaking of precipitate reflections are not fully understood. Internal faulting may account for the streaking and also explain the mottled appearance of the precipitates in dark-field images [see Fig. 1.1.7(*a*)]. Moiré fringes are another possibility. Nevertheless, on the basis of the elemental analysis, the diffraction information, and the behavior of similar steels, we are confident in the identification of the precipitates as G-phase.

1.1.1.6 Axial Electron Channeling Microanalysis of Ll_2 Alloys[10] – J. Bentley

Lattice site location of ternary and quaternary additions to A_3B-type ordered alloys with the Ll_2 structure is of interest for alloy development. Application of standard planar channeling ALCHEM1 techniques is complicated by the fact that no lattice planes contain only B atoms. Since certain zone axes (including <001> and <111>) contain columns of A atoms well separated from columns of B atoms, the ALCHEM1 method has been extended to use zone axis channeling conditions. Spectra are recorded from two orientations – an appropriate channeling zone axis and a "random" nonchanneling condition. The observed changes in X-ray count rates for constant thickness and probe current can exceed a factor of 2. Changes in characteristic X-ray intensity ratios of more than 50% have also been observed (see Fig. 1.1.8). Experiments were performed with Philips EM400T/FEG and EM430T analytical electron microscopes equipped with EDAX 9100/70 EDS systems. The effects of beam divergence, zone axis, specimen thickness, accelerating voltage, and diffraction conditions (deviation from exact zone axis orientation) were determined. The degree of localization of ionization and the presence of coherent bremsstrahlung peaks, as well as standard peak overlap, fluorescence, and absorption effects, were taken into account.

ORNL-PHOTO 0566-86

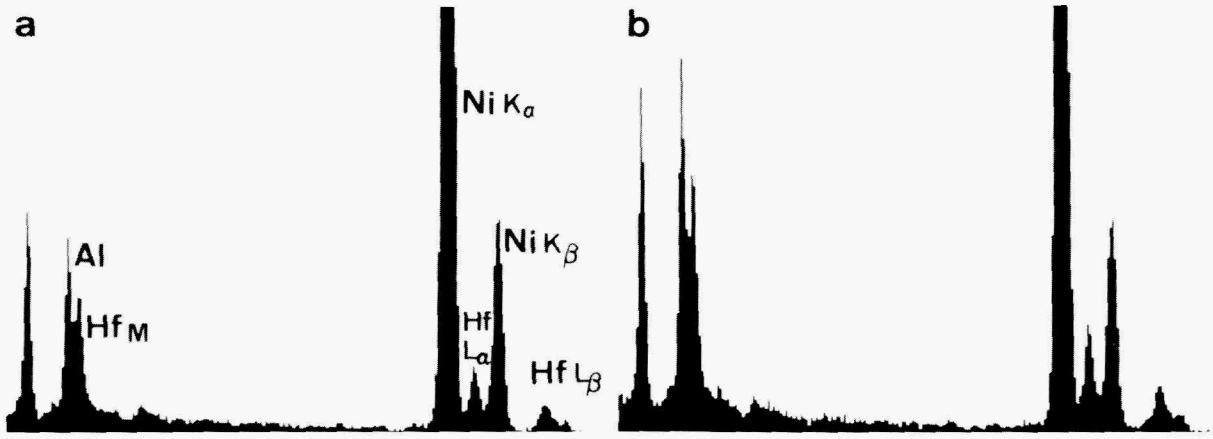

Fig. 1.1.8. Energy-dispersive X-ray spectra of $Ni_{76}Al_{21}Hf_3$. (*a*) <111> zone axis. (*b*) Random nonchanneling orientation.

Initial experiments have been with ternary additions of Fe, Co, or Hf to Ni_3Al. The percentage of the ternary addition on the Al sites was 34% Fe, 10% Co, and 84% Hf as determined from <111> axial channeling experiments. These results confirm the predictions of the extent of solubility lobes on ternary phase diagrams which indicate that Co substitutes for Ni, Hf substitutes for Al, and Fe substitutes for Ni and Al. Results from <100> axial channeling give indeterminate site occupations. Further work on these and other Ll_2 alloys is under way to explain the <100> behavior.

1.1.1.7 A Review of the Application of Analytical Electron Microscopy to Ion-Implanted Materials[11] – J. Bentley

Analytical electron microscopy of implanted materials, particularly of cross-sectioned specimens, allows direct observation and quantification of the microstructure (crystallinity, dislocations, precipitates, cavities) and direct measurement of concentration profiles at less than 10 nm resolution. Depth distributions of defects and composition are obtained without recourse to energy-depth conversions (required for ion backscattering) or sputtering rates (required for Auger electron spectroscopy and secondary ion mass spectroscopy). The work reviewed covers metals, ceramics, and semiconductors implanted over a wide temperature range (77 to ~1000 K) for studies of radiation damage response or surface modification. The observed depth distribution of damage structure and composition is

often different from that predicted by computer codes. Most of the differences can be explained if one accounts for electronic stopping powers that include "Z-oscillations," stresses generated by swelling, or point defect migration (diffusional spreading) and atom knock-on effects.

1.1.1.8 Diffraction Studies of Internal Interfaces[12] – J. M. Vitek and M. Rühle[13]

The diffraction effects normal to a planar internal interface are being evaluated. Diffraction profiles have been calculated for both grain boundaries and interphase interfaces with a lattice distortion in the vicinity of the interface. The calculations have included interference effects between the distorted zone and the perfect neighboring crystals.

For the case of grain boundaries, a twist grain boundary was considered, with an exponential lattice expansion at the interface. Profiles were calculated as a function of the maximum strain at the interface as well as the extent of the strain normal to the boundary. For the case of interphase interfaces, three different structural models were considered. The lattice spacing between the two bordering phases was allowed to remain constant, to vary linearly, and to vary exponentially. Diffraction profiles were evaluated as a function of the lattice mismatch between the two phases as well as the width of the intermediate zone. Finally, the effect of no distortion but simply facetting at an interface was also determined. Under most conditions examined, it was found that no simple relationship exists between the width of the diffraction effects calculated and the width of the distorted zone at the interface responsible for those effects. The calculated profiles were also compared with experimental results in the literature on diffraction effects at gold and nickel-oxide grain boundaries as well as on Mo/Mo_2C interfaces. Additional studies presently under way are examining the effect of segregation on the diffraction profiles.

1.1.2 Application of Analytical Electron Microscopy to Segregation – E. A. Kenik

A variety of materials science problems involve the segregation or depletion of solute atoms to defects in crystals. This includes equilibrium segregation of surface-active elements (as in grain boundary

segregation and embrittlement), diffusion gradients resulting from precipitate growth or dissolution, and radiation-induced segregation. The high spatial resolution of X-ray microanalysis available in the current generation of analytical electron microscopes allows the measurement of such profiles to approach the 1-nm level. The spatial resolution of the technique is determined by the incident probe size and by beam broadening in the specimen. The measured profile (composition) is determined by the convolution of the actual profile with the excited volume. Measurements are relatively straightforward when the excited volume is small with respect to the spatial extent of the profile. When it is not, the actual profile must be deconvoluted from the measured profile, which requires knowledge of the excited volume. To this end, Monte Carlo simulation of electron beam-specimen interactions are employed. The current computer code is based on that of D. C. Joy of AT&T Bell Laboratories, and it includes the effects of fast secondary electrons by a "double" Monte Carlo technique.

1.1.2.1 Equilibrium Grain Boundary Segregation[10,14] – E. A. Kenik

Segregation of solute atoms to grain boundaries can result in degradation of mechanical properties of alloys and a tendency toward intergranular failure. The presence of about 0.4 at. % antimony in a 16 at. % Cr, 14 at. % Ni stainless steel results in a threefold decrease in the elongation to fracture and a threefold increase in the density of intergranular cracks formed during high-temperature creep deformation. While antimony segregation to boundaries was the suspected culprit, Auger spectroscopy could not be applied as the material could not be fractured intergranularly in situ. The degree of segregation was measured by X-ray microanalysis in an AEM as a function of temperature and of boundary character. Table 1.1.2 gives the apparent compositions (averaged over the excited volume) of the matrix and several boundaries for different aging temperatures. At 827°C, a twofold increase of antimony is observed at high-angle boundaries, along with a slight decrease in chromium and iron. At 500°C, a threefold increase in antimony is accompanied by an approximately 40% increase in nickel and an approximately 33% decrease in chromium. In addition, little or no segregation was observed at coherent twin boundaries, while incoherent twin boundaries exhibit intermediate segregation.

Table 1.1.2. Apparent compositions measured by energy-dispersive X-ray spectroscopy

	Average composition ± standard deviation (at. %)					
	5 days, 827°C		99 days, 500°C			
	Matrix	Grain boundary	Matrix	Grain boundary	Twin	
					Coherent	Incoherent
Sb	0.34 ± 0.03	0.67 ± 0.03	0.40 ± 0.02	1.26 ± 0.03	0.37 ± 0.03	0.78 ± 0.02
Cr	17.40 ± 0.12	17.81 ± 0.17	18.02 ± 0.21	12.07 ± 1.06	17.40 ± 0.18	16.88 ± 0.21
Fe	68.32 ± 0.12	67.40 ± 0.25	67.64 ± 0.36	67.61 ± 0.10	68.88 ± 0.10	67.04 ± 0.45
Ni	13.94 ± 0.14	14.12 ± 0.19	13.94 ± 0.18	19.06 ± 0.96	13.35 ± 0.15	15.30 ± 0.22

Figure 1.1.9 gives the atomic ratios Ni/Fe and Cr/Fe as a function of distance from a high-angle grain boundary in the 500°C, 99-day aged material. The high Ni/Fe points and low Cr/Fe points are located adjacent to the boundary and deviate by more than 4σ (standard deviation) from the average matrix composition. When the experimental broadening of the actual profile by probe size (~1.5 nm), the analog scan (~1.7 nm), the projected width of the slightly tilted boundary (~1.2 nm), and specimen drift are taken into account, the measured width of the segregant profile (3.5–5 nm) indicates that the segregant layer was very thin (<1 nm).

1.1.2.2 Radiation-Induced Segregation in Stainless Steel[10] – E. A. Kenik

An earlier study of radiation-induced segregation in ion-irradiated stainless steel had shown segregation of silicon and nickel to the vicinity of faulted dislocation loops. However, as a result of the limited resolution (probe size) available at that time, the apparent segregation appeared roughly spherical in symmetry. Higher-resolution mapping of the segregation at the faulted dislocation loops has been performed. Figure 1.1.10 illustrates the radiation-induced segregation near a faulted loop formed by ion irradiation at 675°C to 1 dpa. Figure 1.1.10(*a*) shows the loop tilted away from the edge-on orientation (where the measurements were made) to illustrate several features. The loop is faulted and

ORNL-PHOTO 4951-85

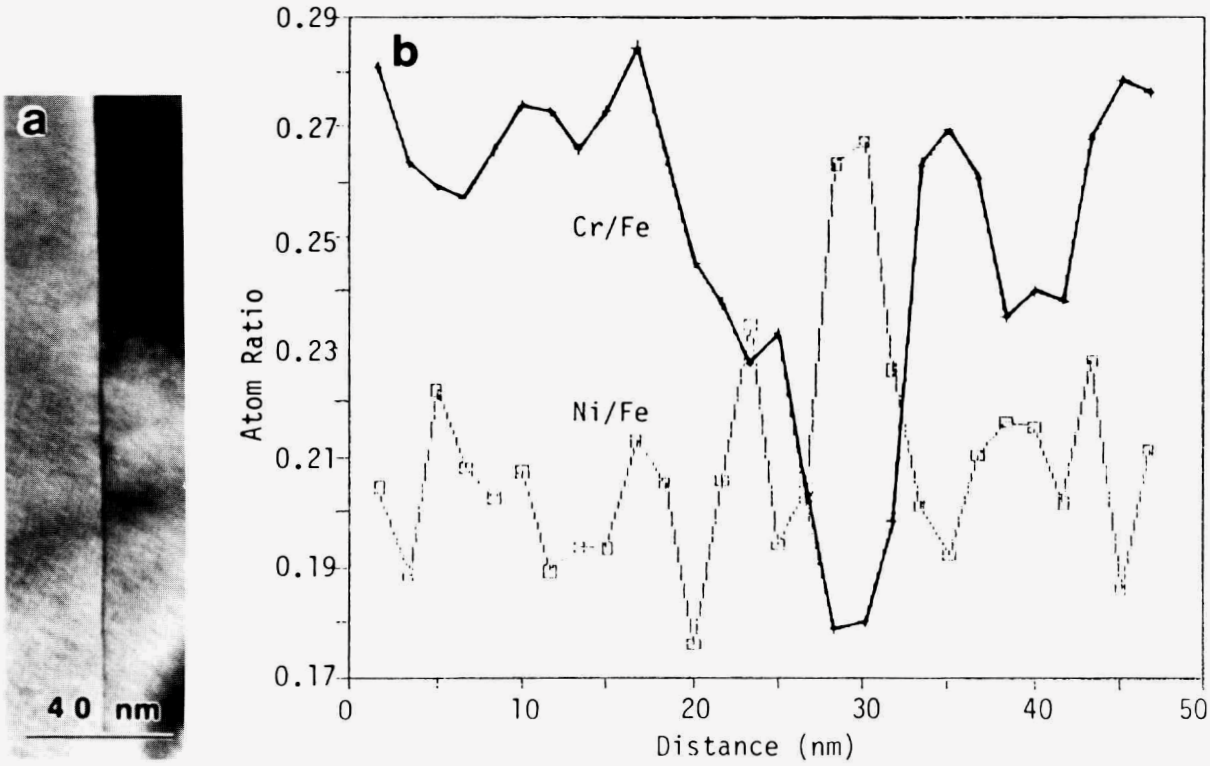

Fig. 1.1.9. (*a*) High-angle grain boundary in antimony-doped stainless steel aged 99 days at 500°C. (*b*) Nickel-to-iron and chromium-to-iron atomic ratios as a function of distance for line scans across the boundary. Probe diameter about 1.5 nm. High nickel and low chromium points straddle the position of the boundary.

extends through the foil thickness; the dislocation segments remain at the upper and lower edges of the fault. Silicon and nickel are undersized solutes and segregate at the fault plane, while oversized solutes chromium and iron (as well as manganese and molybdenum) are depleted at the fault plane. Similar measurements made in the vicinity of nearly face-on faulted loops indicate that the maximum segregation of nickel and silicon (or maximum depletion of chromium, iron, molybdenum, and manganese) occurs at the partial dislocation. The matrix outside the right cylinder defined by the dislocation loop shows little deviation from the bulk composition.

Measurements made of radiation-induced segregation at high-angle boundaries confirm the observations made at dislocations and faults; undersized solutes segregate toward point defect sinks, whereas oversized

ORNL-PHOTO 9439-85

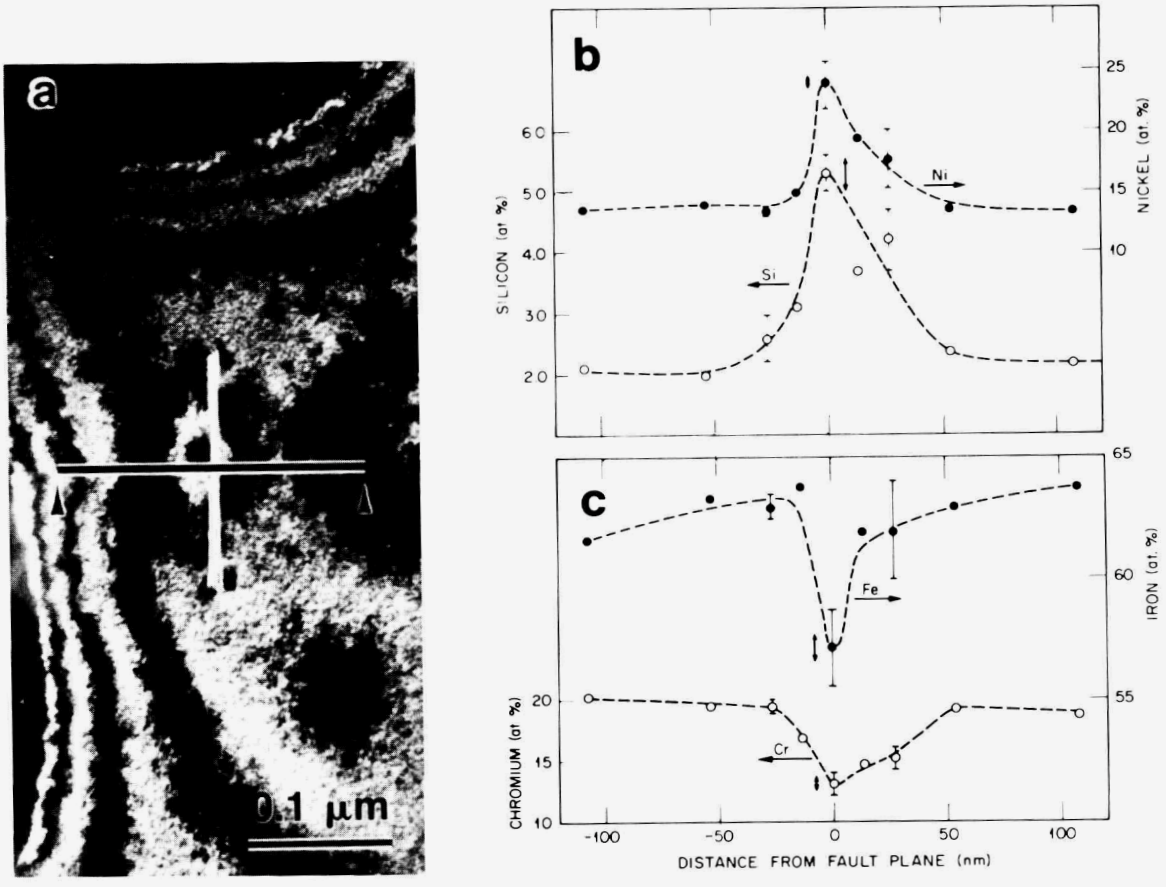

Fig. 1.1.10. (*a*) Weak-beam dark-field image of near-edge-on faulted dislocation loop in LS1A ion-irradiated to 1 dpa at 675°C. Arrowed line indicates position of line scan. (*b*) Silicon and nickel segregation to fault in (*a*). (*c*) Iron and chromium depletion at fault in (*a*). Error bars indicate standard deviation of multiple analyses. Arrowed bars near maxima and minima indicate errors based on counting statistics.

solutes segregate away from point defect sinks. In addition, the segregation profiles near grain boundaries exhibit local maxima or minima between 25 and 60 nm from the boundary, indicating the distances at which the diffusive processes involved in radiation-induced segregation transport the different elements. Iron, being the slowest diffusing species in stainless steel, exhibits the narrowest diffusion profile and closest extrema point; whereas chromium, the fastest diffusing species, exhibits the widest profile and most distant extrema point.

1.1.3 Collaborative Applications

Collaborative research with other tasks is promoted by assigning members of the Electron Microscopy Group to the respective tasks. In addition to the electron microscopy aspects emphasized in this section, other aspects of such work are found in Sects. 2.2, 2.3, 3, 4, and 5.1.

1.1.3.1 HVEM Amorphization and Disordering of Materials[4] – E. A. Kenik, J. M. Williams,[15] and M. Nastasi[16]

With the recent addition of a double-tilt cooling holder (liquid nitrogen or liquid helium cooled) for the HVEM, two projects have dealt with radiation-induced disorder and amorphization. The first program, in collaboration with J. M. Williams, attempted to amorphize silicon during low-temperature electron irradiation. No transformation occurred, even for doses up to 10 dpa, indicating that, apparently, the amorphization of silicon during ion bombardment is a consequence of cascade damage, not simply of high displacement rates. The second program, in collaboration with M. Nastasi and J. M. Williams, investigated the disordering and amorphization of several aluminum-nickel intermetallic compounds under low-temperature irradiation. Al_3Ni was amorphized by 1-MeV electron irradiation to about 0.4 dpa at 100 K, whereas no transformation occurred for similar doses at room temperature. Al_3Ni_2 disordered to a defected body-centered CsCl structure for irradiation at 100 K and room temperature. These results are being compared with results from neon and xenon ion irradiations in order to understand the radiation-induced amorphization and disordering in these alloys.

1.1.3.2 Microstructural Development during Post-Implantation Annealing of Al_2O_3 Implanted with Fe (ref. 17) – P. S. Sklad, C. J. McHargue, C. W. White,[15] and G. C. Farlow[18]

One critical aspect of the investigation of surface modification of ceramic materials is the stability of the implanted microstructure during post-implantation annealing. One example of particular interest is α-Al_2O_3 implanted with 160-keV ^{56}Fe ions to a dose of 4×10^{16} ions/cm^2. After implantation the microstructure was typical of many implanted ceramics, i.e., a tangled array of dislocations extending from the surface to a depth of about 170 nm. The implanted iron concentration profile, as

measured by X-ray energy-dispersive spectroscopy (EDS), is characterized by a well defined peak at about 60 nm and a maximum iron-to-aluminum atom ratio of 9.5%. No precipitates were observed.

In order to investigate the response of Al_2O_3 implanted with iron to the annealing environment, selected specimens were annealed at 1500°C for 1 h in either nominally pure flowing oxygen or in a flowing mixture of 96% argon and 4% hydrogen (Sect. 5.1.4). Whereas Rutherford backscattering (RBS) and ion channeling measurements indicated a relaxation of damage regardless of annealing environment, those techniques were not able to indicate the nature of the redistribution. Analytical electron microscopy techniques were used to provide a basis for interpreting the RBS results.

Examinations of a cross-sectioned oxidized specimen revealed the presence of a distribution of precipitates 15 to 50 nm in diameter, Fig. 1.1.11(*a*). In addition, two populations of faceted cavities were observed, one lying near the implanted surface and one associated with the precipitates. Identification of the precipitates was carried out with convergent-beam electron diffraction (CBED) on individual precipitates in a backthinned specimen, Fig. 1.1.11(*b*). Figure 1.1.11(*c*,*d*) shows CBED patterns from a precipitate and from the Al_2O_3 matrix immediately adjacent

ORNL-PHOTO 0390-86

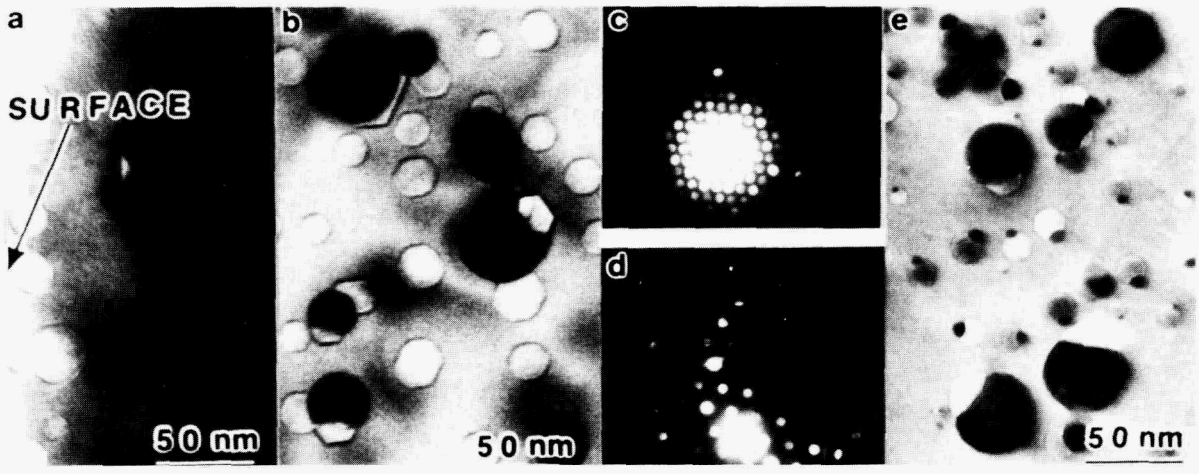

Fig. 1.1.11. Precipitates and cavities in (*a*) cross-sectioned and (*b*) backthinned specimens of iron-implanted Al_2O_3 annealed in oxygen. (*c*) CBED pattern of precipitate in (*b*). (*d*) CBED pattern of matrix in (*b*). (*e*) Precipitates and cavities in backthinned iron-implanted Al_2O_3 annealed in a mixture of argon and hydrogen.

to it. The precipitate pattern is a [011] cubic zone axis. The measured interplanar spacings are similar to those of diamond cubic Fe_3O_4. However, compositions of the form $Fe(Fe_xAl_{1-x})_2O_4$ cannot be ruled out. The phase diagram for the Fe-Al-O system suggests that Fe_3O_4 or the mixed spinel are equally likely given the oxygen partial pressure and the temperature of the annealing conditions.

Examination of the specimen annealed in a reducing atmosphere also reveals precipitates and cavities, Fig. 1.1.11(*e*). The only apparent difference in the appearance of this specimen when compared with the oxidized specimen is the one-to-one association of precipitates with each of the cavities [cf. Fig. 1.1.11(*b*) with 1.1.11(*e*)]. However, CBED analysis shows that the precipitates present after the reducing anneal are body centered cubic iron.

1.1.3.3 Analytical Electron Microscopy of the Recrystallization Behavior of Ion Beam Modified α-Al_2O_3 (ref. 4) – P. S. Sklad, C. J. McHargue, C. W. White,[15] and G. C. Farlow[18]

As part of an ongoing program to investigate the effects of surface modification on ceramic materials, specimens of α-Al_2O_3 have been implanted with a variety of ion species to study the effect of size, solubility, and chemical activity. In addition the effects of post-implantation annealing have also been evaluated. In one phase of this work it has been found that a stoichiometric implant (two parts aluminum, three parts oxygen with ion energies adjusted to give an overlap of the profiles) at liquid nitrogen temperatures can be used to produce an impurity-free, 150-nm-thick amorphous surface layer on a single-crystal α-Al_2O_3 substrate (see also Sect. 5.1.2). Analytical electron microscopy techniques, in particular CBED, have been used to investigate the recrystallization behavior of this amorphous material.

As expected, the recrystallization behavior varied as a function of both annealing temperature and annealing time. Annealing at relatively low temperatures, e.g., 800°C, and short times, e.g., 1 to 4 h, resulted in the transformation of the amorphous material to cubic γ phase, characterized by a columnar structure with the columns extending from the former crystalline-amorphous interface to the surface. Figure 1.1.12 shows a TEM

ORNL-PHOTO 0392-86

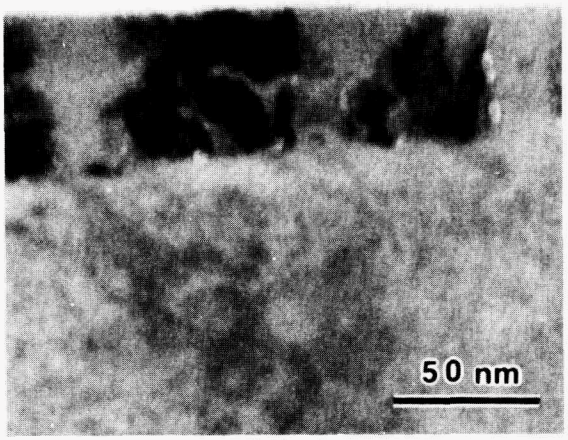

Fig. 1.1.12. Bright-field micrograph of α-Al_2O_3 implanted with ^{27}Al (90 keV, $2 \times 10^{16}/cm^2$) and ^{16}O (55 keV, $3 \times 10^{16}/cm^2$) at 77 K and annealed 1.5 h at 800°C. Specimen prepared in cross section.

image from a specimen annealed for 1.5 h at 800°C and prepared in cross section. A number of cavities can be seen along the boundaries between the columns. The bright-field micrograph shown in Fig. 1.1.13 illustrates the appearance of the "columns" of γ phase seen in a backthinned specimen that had been annealed for 1.5 h at 800°C. The diffraction pattern shown in the inset confirms that (111) is parallel to (0001).

ORNL-PHOTO 7818-85R

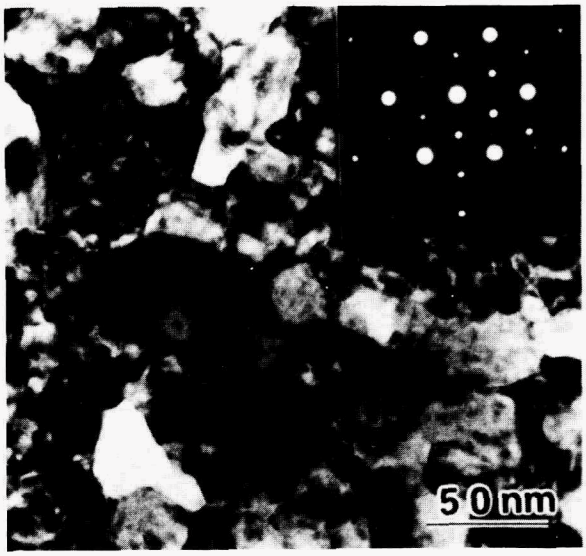

Fig. 1.1.13. Bright-field micrograph of specimen implanted stoichiometrically at 77 K and annealed 1.5 h at 800°C. Specimen prepared by backthinning. Inset indicates that $(111)_\gamma$ is parallel to $(0001)_\alpha$.

Annealing at intermediate temperatures, e.g., 960°C for 1.5 h, resulted in a dual phase microstructure comprising an epitaxial layer of α phase, extending approximately 85 nm from the original amorphous-crystalline interface toward the surface, and a layer of γ phase. An example of such a microstructure is shown in Fig. 1.1.14(*a*). The convergent-beam diffraction patterns shown in Fig. 1.1.14(*b*,*c*,*d*) correspond to the γ layer, the epitaxial α layer, and the α substrate, respectively. The transformation of the γ to α takes place at a well defined interface. Similar dual-phase microstructures have been observed in specimens annealed at different temperatures and times. The temperature dependence of the velocity of the γ-α interface as it moves toward the surface has been measured, and an activation energy of about 3.6 eV has been determined for the γ-α transformation.

ORNL-PHOTO 9301-85

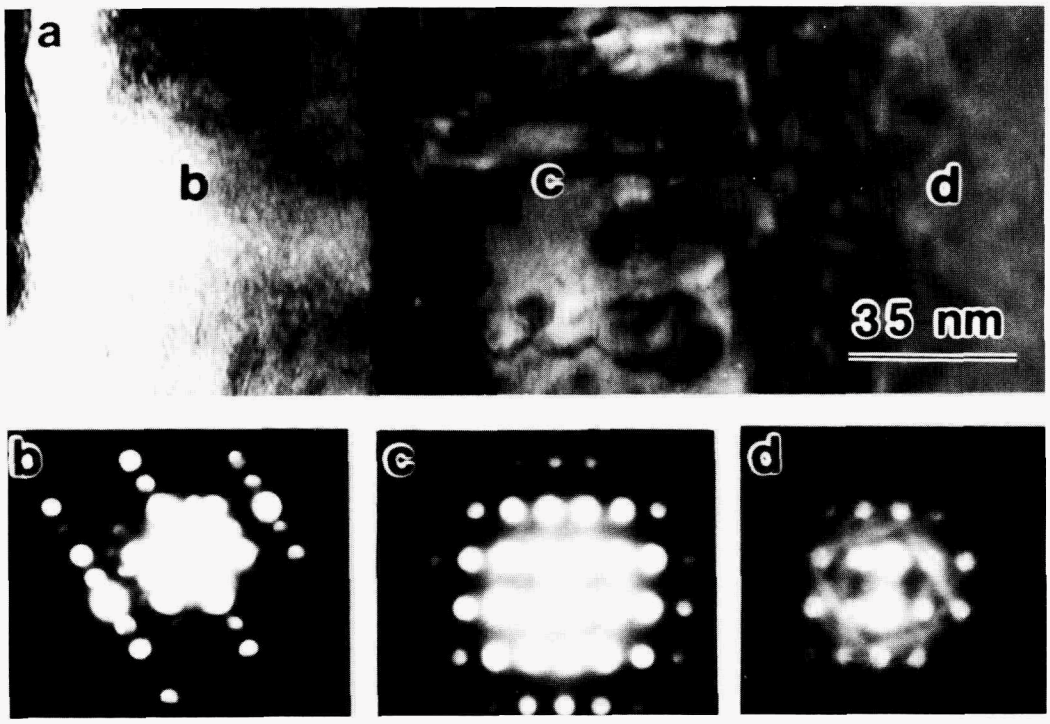

Fig. 1.1.14. (*a*) Bright-field micrograph of specimen implanted stoichiometrically at 77 K and annealed for 1.5 h at 960°C. Specimen prepared in cross section. (*b*) CBED pattern from γ phase. (*c*) CBED pattern from epitaxial α phase. (*d*) CBED pattern from substrate.

Both electron microscopy and RBS techniques have confirmed that the microstructure produced by annealing at 1190°C is composed of only epitaxial α phase. While the RBS results indicate that this layer is nearly perfect, TEM reveals the presence of a population of faceted cavities throughout the implanted layer as well as a band of dislocation loops at the location of the original amorphous-crystalline interface (approximately 150 nm from the surface). The micrograph in Fig. 1.1.15 from a backthinned specimen annealed 15 min at 1190°C shows the distribution of these extended defects.

Investigations are continuing to determine the mechanisms involved in the recrystallization process and to further characterize the kinetics of the reaction.

ORNL-PHOTO 7817-85

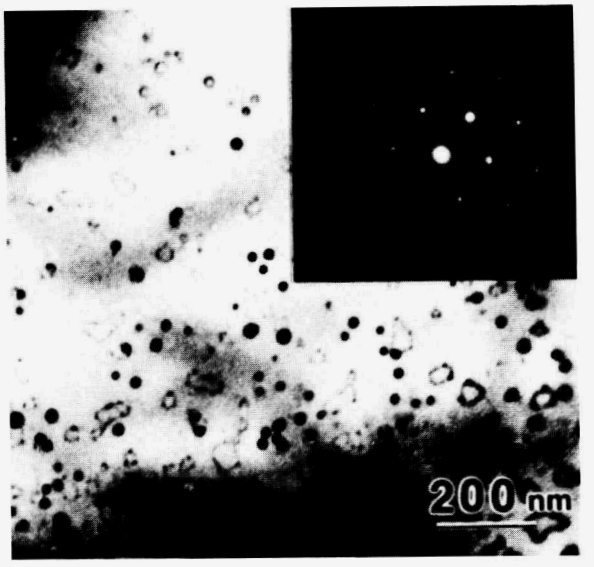

Fig. 1.1.15. Bright-field micrograph of specimen implanted stoichiometrically at 77 K and annealed 15 min at 1190°C. Specimen prepared by backthinning.

1.1.4 Collaborative SHaRE Program Research

In addition to the research described in this section, several other collaborative SHaRE program research projects involving electron microscopy were active. They include the studies with J. J. Wert and students of Vanderbilt University on the role of structure in the wear process, with R. J. Arsenault and a student of the University of Maryland on HVEM examination of SiC-Al alloy composites, with K. R. Lawless of the

University of Virginia on HVEM in situ oxidation studies of nickel aluminides, and with D. Northwood and a student of the University of Windsor, Ontario, on HVEM examination of $Zr(Fe_xCr_{1-x})_2$ hydrogen storage materials.

1.1.4.1 Grain Boundary, Glassy-Phase Identification and Possible Artifacts[10,19] – Y. Kouh Simpson,[16] C. B. Carter,[16] P. Sklad, P. Angelini, and J. Bentley

The presence of an amorphous phase at grain boundaries in ceramic materials can significantly affect the properties of the materials. Such grain boundary films can be identified by the dark-field, diffuse-scattering technique, the Fresnel fringe method, high-resolution TEM, and analytical electron microscopy (AEM).

Experimentally it is observed that, during TEM specimen preparation of polycrystalline aluminas and other materials, grooving of grain boundaries, locally enhanced Si contamination, and structural damage of the surface can occur. Grain boundary grooving is often difficult to detect, since the dimensions of such grooving can be extremely small. Moreover, the grooving characteristics of a grain boundary are intimately related to the character of the grain boundary, the orientation of the grain boundary with respect to the specimen surface, and grain boundary configuration. The present work shows that with the use of the above techniques specimen artifacts can cause the clean grain boundaries in commercial alumina specimens to appear to contain glassy phases. The ambiguity in interpreting the results from each of the techniques was carefully investigated.

A schematic diagram of a grooved grain boundary is shown in Fig. 1.1.16(*a*). A grain boundary with clearly visible periodicities in the image of the tilted boundary showed a misleading Fresnel-fringe contrast when the boundary was viewed edge-on. A 10° tilt boundary with a dislocation spacing of 7.5 nm produced a bright line in the dark-field, diffuse-scattering image viewed edge-on. Other boundaries that appeared as single bright lines in the edge-on condition appeared as two distinct bright lines when the same boundaries were tilted. This is explained by the diagram shown in Fig. 1.1.16(*b*). Asymmetric grooving of boundaries was also observed [Fig. 1.1.16(*c*)].

High spatial resolution silicon and calcium profiles across grain boundaries were also measured. Such apparent segregation of silicon and

ORNL-DWG 86-7610

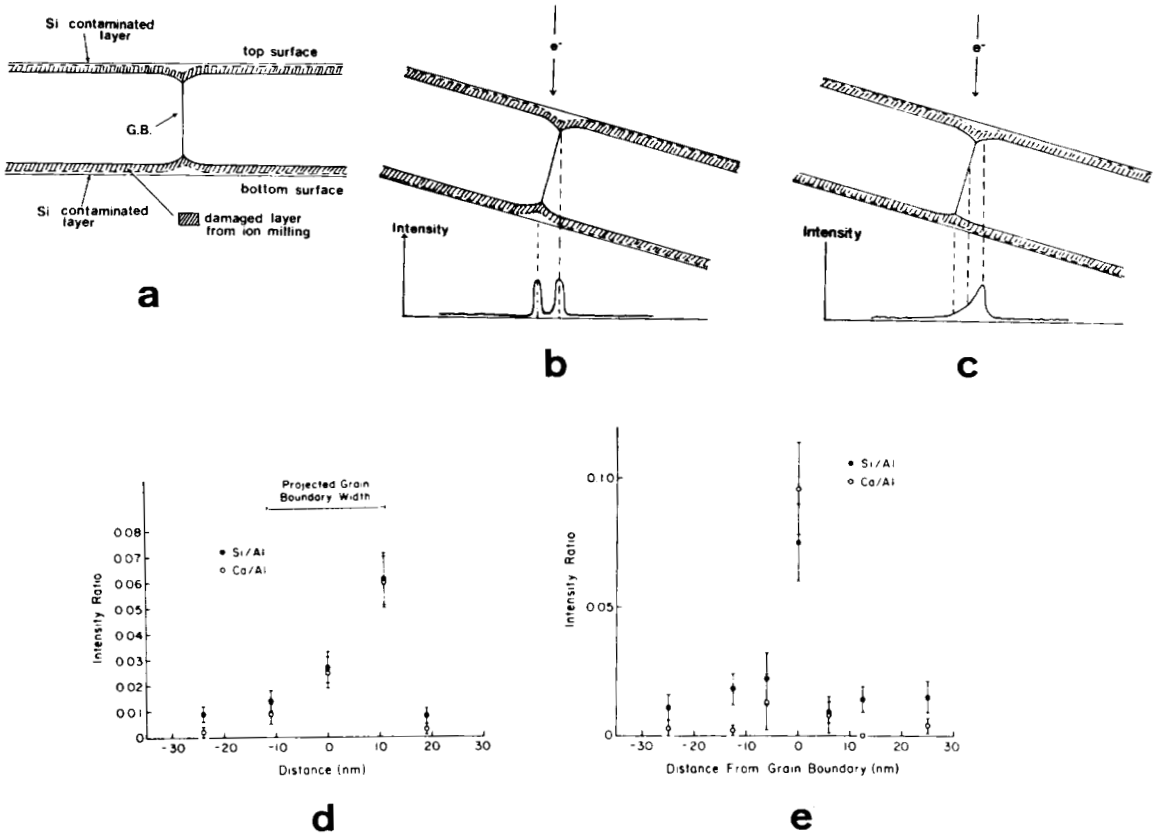

Fig. 1.1.16. Schematic diagrams of grooved grain boundaries (*a*) edge-on, (*b*) tilted, (*c*) tilted asymmetric grooving. X-ray intensity ratios Si/Al and Ca/Al versus distance across an asymmetrically grooved grain boundary (*d*) tilted, (*e*) the same boundary edge-on.

calcium at grain boundaries in alumina has been reported by other researchers. Figure 1.1.16(*d*,*e*) shows profiles for an edge-on boundary and for the same boundary analyzed in a tilted geometry giving further evidence of asymmetric grain boundary grooving.

The results of this work indicate that, whenever possible, high-resolution lattice imaging or diffraction contrast of grain boundary dislocations must be used in conjunction with other techniques.

1.1.4.2 Twinned Colloidal Gold Particles[20] — A. G. Dhere,[21] R. J. DeAngelis,[21] P. J. Reucroft,[21] and J. Bentley

Colloidal gold particles were prepared in aqueous solution by reducing gold chloride with phosphorus (P-reduced), or sodium citrate.

Specimens for X-ray diffraction were prepared by mixing the gold solution with silica (approximately 15% Au) and pressing the mix into a specimen holder. Specimens were prepared for TEM by transferring the suspended material onto a beryllium grid with a carbon substrate on a formvar film. X-ray diffraction studies were carried out on a Rigaku D-MAX 2A X-ray diffractometer unit interfaced to a PDP-11/23 computer for line broadening analysis. The TEM studies were carried out on a Philips EM400T/FEG AEM operated at 100 keV. Microdiffraction patterns obtained in STEM mode from regions about 1 nm in size were video-recorded from the conventional viewing screen.

Colloidal gold particles from the P-reduced solution were equiaxed in shape and fairly uniform in size, ranging from 15 to 35 nm. Multiple twin contrast was visible in most of the particles. Each twinned particle contained two to four twin planes confirmed by STEM probe diffraction scans across the particles.

Specimens prepared by reducing gold chloride with sodium citrate contained colloidal gold particles of varying sizes, ranging from 15 to over 100 nm. The particles tended to coalesce, resulting in larger, nonuniform-shaped particles. Multiple twin contrast was present in most particles. Typically there were three twin planes in the smallest particles and up to ten in larger particles. Twinning was also evident from the changes in the microdiffraction patterns.

X-ray diffraction analysis of the (111) and (200) peaks from the citrate-reduced colloidal gold indicated a twin fault probability (the average area of twin fault to the total area of {111} plane in a particle) of 0.01, which (assuming 50-nm spherical particles) corresponds to an average of four radial twin planes per particle. The X-ray result compares very well with the actual TEM observations.

Colloidal gold particles are usually in the form of twinned polytetrahedra. The multiple twinning of the colloidal gold is similar to the twin structure observed in vapor-deposited gold particles.

1.1.4.3 Nickel Oxide Morphology in Nickel-Silica Catalysts[22] –

A. G. Dhere,[21] P. J. Reucroft,[21] R. J. DeAngelis,[21] and J. Bentley

Supported metal catalysts of nickel on a suitable ceramic support are widely used in hydrogenation processes because of their high dispersion.

However, large rafts of nickel in reduced Ni/SiO_2 catalyst have been observed. A study is being conducted to determine the origin of these structures in the catalyst preparation stage. Quantitative X-ray diffraction analysis has shown that more nickel is bound in the form of nickel silicate than in nickel oxide, thereby confirming the coexistence of nickel oxide and nickel silicate. No previous direct observations of these structures have been reported.

An 11.9% Ni/SiO_2 catalyst was prepared by nitrate impregnation. The catalyst was dried at 100°C in an oven and calcined in air at 500°C for 1 h. The reduction was carried out in flowing hydrogen at 500°C for 3 h. Transmission electron microscopy observations were made with the use of a Philips EM400T analytical electron microscope equipped with a field emission gun.

An interesting structure was observed in nickel oxide particles from the calcined 11.9% Ni/SiO_2 catalyst. The contrast variation in through-focus-series indicates the presence of faceted voids or cavities. The origin of these structures and their influence on the development of the nickel metal particles, formed during reduction, remain unknown. Certainly, there is a wide variation in the size of the final nickel particles. No observations were made that would indicate the presence of a nickel silicate interlayer.

Knowledge of the structure and transformation of the nickel-containing phase at each stage of the processing and treatment of the catalyst should allow improvements in the dispersion of nickel on silica, which should, in turn, lead to improvements in the efficiency of the catalyst.

1.1.4.4 Morphological Development of Nickel Particles in Supported Metal Catalysts[10] – A. G. Dhere,[21] R. J. DeAngelis,[21] P. J. Reucroft,[21] J. Bentley, G. E. Ice, and A. Habenschuss

The morphology of nickel-containing phases in a 12% Ni/SiO_2 catalyst prepared by liquid impregnation of nickel nitrate from an aqueous solution into silica was studied at each stage of the treatment of the catalyst by X-ray diffraction and TEM. The ORNL beam line of the National Synchrotron Light Source at Brookhaven National Laboratory and a conventional diffractometer were used for the X-ray diffraction studies.

After impregnation and oven drying, the catalyst contains nickel in the form of its nitrate as a film on the surface of the silica. The catalyst was calcined in air at 500 and 800°C. Particle size distributions were obtained by TEM and single profile analysis of NiO (111) X-ray diffraction (synchrotron) data. Good agreement was obtained. The synchrotron radiation scan of the catalyst calcined at 800°C indicates a weak and broad nickel silicate 310 diffraction peak. Moire fringes in TEM images are also consistent with the presence of nickel silicate between the NiO and silica support. Faceted surface pits were observed on large rafts of NiO. Catalysts were reduced in situ at 500°C for 3 h in hydrogen in the high-temperature camera of a Picker diffractometer. Nickel particle size distributions indicate a dependence on the NiO particle size and morphology in the calcined catalyst.

1.1.4.5 Kinetics and Mechanisms of Creep in Hot Isostatically Pressed Niobium Carbide[23] – R. D. Nixon,[24] R. F. Davis,[24] and J. Bentley

Constant compressive stress creep experiments in the temperature and stress range of 1730 to 2100 K and 16 to 70 MPa on $NbC_{0.74}$ formed by hot isostatic pressing have revealed stress exponents of 2.0 under stress levels of 16 to 54 MPa at all temperatures investigated and 3.2 under stress levels of 54 to 70 MPa at 1830 K. The activation energy of steady state creep is approximately 230 kJ/mole.

Transmission electron microscopy of the uncrept and annealed material reveals grown-in low-angle dislocation subboundaries. At 1730 K and under 34 to 54 MPa, these subboundaries are broken into tangles or single junctions. At 1930 K and under 34 to 54 MPa, subboundaries form but are not as well defined as in the annealed $NbC_{0.74}$. At 1830 K and under 54 to 70 MPa, the subboundaries evolve into knitted simple tilt boundaries, indicating more glide activity at higher stresses. At 2100 K and under 16 to 48 MPa, the subboundaries are polygonized knitted tilt boundaries which are curved, indicating subboundary movement.

The experimental and TEM results indicate that at low temperature and low stress, grain boundary sliding is the primary contributor to creep since glide activity is limited. Under higher stresses at low temperature, strain occurs by dislocation glide and recovery by dislocations

being absorbed on grain boundaries. At high temperature and low stresses, strain occurs by glide and subboundary movement with recovery by dislocation annihilation.

1.1.4.6 The Nature of Grain Boundaries in Silicon Carbide[4] – J. Bentley, C. H. Carter, Jr.,[24] and R. F. Davis[24]

As part of our continuing study of creep mechanisms and kinetics in various forms of silicon carbide, grain boundaries were examined by TEM to determine the presence or absence of amorphous grain boundary films. Such films can completely dominate creep deformation at high temperatures. As discussed in Sect. 1.1.4.1, many artifacts can give misleading indications of the presence of thin amorphous grain boundary films. The detection of a film thicker than, say, about 5 nm is straightforward. Such films should be clearly visible by diffraction contrast, and CBED patterns can be obtained that show the complete absence of Bragg maxima. However, for films of thickness less than 1 nm, only the techniques of high-resolution imaging (diffraction contrast on tilted boundaries, or phase contrast lattice imaging of edge-on boundaries) are dependable. This is because grooving at grain boundaries and subsequent accumulation of amorphous contamination films occurs during specimen preparation. Such effects can lead to bright lines in dark-field diffuse-scattering images, to enhanced Fresnel fringes in through-focus phase contrast images, and to the detection of impurities by AEM. Such methods, when used alone, are therefore suspect. For general high-angle grain boundaries the application of lattice imaging is restricted by specimen geometry. It is necessary to fulfill low-order two-beam diffracting conditions in each grain, with the added constraint of having the boundary edge-on. Two out of three conditions can be met routinely in a double-tilt stage. All three conditions can hardly ever be achieved. The examination of (tilted) boundaries by diffraction contrast, particularly weak-beam dark-field imaging, is generally applicable. The criterion for the absence of thin amorphous films is the presence of grain boundary dislocations. Of course it is necessary to distinguish ledge contrast from dislocation character by tilting experiments. Such experiments have been performed on sintered

α-SiC crept at 414 MPa and 1747°C for randomly selected low- and high-angle grain boundaries. Grain boundary dislocation contrast was observed, indicating the absence of thin amorphous films.

1.1.4.7 Some Characteristics of $Al_{12}Mo$ in Aluminum Annealed after Implantation with Molybdenum[25] – L. D. Stephenson,[26] J. Bentley, R. B. Benson, Jr.,[24] G. K. Hubler,[27] and P. A. Parrish[28]

The characteristics of $Al_{12}Mo$ formed in aluminum annealed after implantation with selected maximum molybdenum concentrations were examined by AEM techniques. The $Al_{12}Mo$ was isolated as the only precipitate in the microstructure for maximum as-implanted molybdenum concentrations up to 11.4 at. %. The morphology of the $Al_{12}Mo$ can be selected by choosing the maximum as-implanted molybdenum level up to 11.4 at. %. A predominantly lamellar $Al_{12}Mo$ precipitate structure formed when aluminum was annealed at 550°C after implantation with maximum molybdenum concentrations in the range of 3.3 to 4.4 at. %. The orientation of the body centered cubic (bcc) $Al_{12}Mo$ precipitate with respect to the face centered cubic (fcc) matrix can be expressed as $(\bar{1}23)_p \| (002)_m$ and $[301]_p \| [310]_m$. An explanation of the experimentally observed orientation relationship was developed on the basis of the characteristic relationships between the bcc $Al_{12}Mo$ precipitate and the fcc matrix. A continuous film of $Al_{12}Mo$ formed in the surface modified region upon annealing aluminum implanted with maximum molybdenum concentrations in the approximate range of 8 to 11.4 at. %. The structure of the $Al_{12}Mo$ film was found to depend on the annealing temperature. A granular film formed after annealing at 550°C, whereas a mottled film formed after annealing at 400°C. Sequential annealing experiments revealed that the mottled film structure transforms to a granular film, which indicates that the mottled film is a metastable structure.

1.1.4.8 Microstructures of Niobium-Germanium Alloys Solidified under Supercooled Conditions[4] – E. A. Kenik, R. J. Bayuzick,[29] and N. D. Evans[29]

Niobium alloys containing 18 to 27 at. % germanium were solidified under large degrees of undercooling in the NASA 100-m drop-tube at Huntsville, Alabama. Analytical electron microscopy was employed to study

the phases present and their compositions. The major phase present was the A15 Nb_3Ge_{1-X} phase; however, other phases (Nb, Nb_5Ge_3) were present, depending on the initial composition. Though large degrees of undercooling (300°C) were achieved prior to solidification, the solubility limit of germanium in the A15 phase was not extended, even with splat-cooling. This is probably the result of recalescence, which reheats the drop to near the melting temperature as the heat of fusion is released during solidification. An amorphous phase containing 18 to 20 at. % germanium was observed in the 26 at. % germanium splat-cooled material.

1.1.4.9 Phase Transformations in Mechanically Alloyed Niobium-Germanium Powders[4] - E. A. Kenik, R. Bayuzick,[29] and C. Koch[24]

Mechanical alloying of elemental niobium and germanium powders in a high-energy ball mill initially produces intermetallic compounds and finally produces material that, on the basis of X-ray diffraction, appears amorphous. Analytical electron microscopy was performed on samples of a 75 at. % Nb-25 at. % Ge powder blend that had been mechanically alloyed for 5, 7, and 13 h. In the 5- and 7-h milled material, the major phase present is the A15 Nb_3Ge phase. In selected area diffraction patterns of these materials, interspersed among the sharp rings associated with the A15 crystalline phase, are several diffuse rings that could arise from an amorphous phase. In the material mechanically alloyed for 13 h, the diffuse rings are pronounced and the associated phase is a significant, if not major, component of the powder. Figure 1.1.17 gives typical microdiffraction patterns from this material made with an approximately 10-nm-diam probe. Figure 1.1.17(*a*) shows ring patterns very similar to those for classical amorphous materials, such as vitreous carbon or silica glass. Figure 1.1.17(*b*) shows an identical ring pattern superimposed on the spot pattern from a small crystalline region contained in the probe. X-ray microanalysis indicates that the only significant impurity ($Z > 11$) is iron, picked up during mechanical alloying, whereas EELS indicates the presence of a small amount of oxygen. Bulk chemical analysis of the powders indicates oxygen contents typically less than 5 at. % O.

ORNL-PHOTO 1242-86

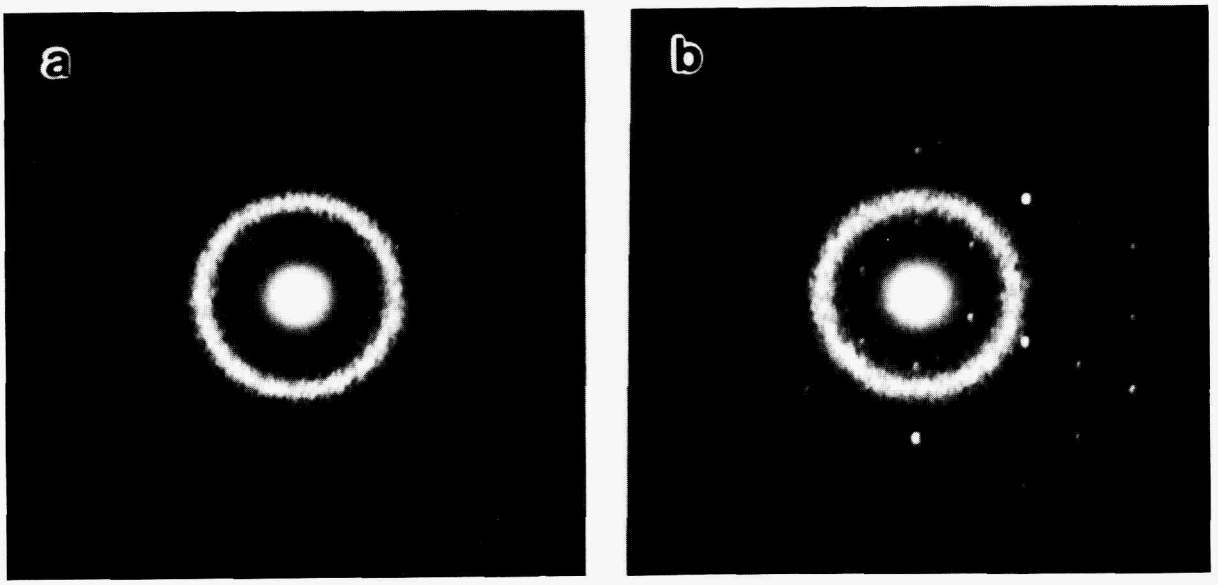

Fig. 1.1.17. Convergent-beam electron diffraction patterns from niobium-germanium powder mechanically alloyed for 13 h. Probe diameter about 10 nm. (*a*) Continuous ring pattern from amorphous phase. (*b*) Continuous ring pattern from amorphous phase and spot pattern from small crystallite.

1.1.4.10 Electron Radiation Damage in TaC_{1-x} (ref. 4) – E. A. Kenik, R. Stoller, and C. Allison[30]

Electron irradiations of TaC have been performed at 100 to 300 kV at room temperature and below. At such incident energies, the electrons cannot displace the tantalum atoms; however, fine defect clusters are observed, indicating that carbon atoms are being displaced and presumably diffusing to form the observed clusters. On the basis of the density of defects observed after different energy irradiations, the threshold voltage is about 150 kV, which represents a threshold energy for carbon displacements in TaC of about 32 eV.

1.1.4.11 The Structure of Consolidated Rapidly Solidified Powders of Ni_3Al (ref. 31) – I. Baker,[32] J. A. Horton, and E. M. Schulson[32]

Rapidly solidified powders of stoichiometric Ni_3Al and Ni_3Al containing boron and titanium have each been consolidated by two distinct

routes, viz., hot extrusion or hot compaction. The resulting microstructures have been examined by optical microscopy, scanning electron microscopy, and transmission electron microscopy.

The consolidated material did not retain the nonequilibrium structure of the rapidly solidified powders. The addition of titanium and boron produced material with a larger final grain size and a decreased incidence of twinning, and, in the extruded material, it led to cracking. Although all processing was performed in inert atmospheres, oxides were present in all consolidated products.

1.1.4.12 TEM of Rapidly Solidified Powders of Ni_3Al (ref. 33) – I. Baker,[32] J. A. Horton, and E. M. Schulson[32]

Rapidly solidified powders (<100 μm diam) of stoichiometric Ni_3Al and $Ni_3Al(B,Ti)$ prepared by Pratt & Whitney's RSR process were examined at ORNL with the Philips EM400T/FEG. Specimens for TEM were prepared by embedding the powder in epoxy in a 3-mm metal ring, mechanically thinning, and then ion milling.[34] The powders consisted of martensitic dendrites in a Ll_2 matrix that contained numerous dislocations. The stoichiometric Ni_3Al powder also contained martensitic lamellae between the dendrites. The martensite plates were internally twinned and enriched in aluminum, and they probably were formed by the transformation of β-NiAl. Figure 1.1.18 is an example of the structure in stoichiometric Ni_3Al. X-ray microanalysis line scans across these lamellae showed the degree of aluminum enrichment.

1.1.4.13 Grain Boundary Accommodation of Slip in Ni_3Al Containing Boron[35] – E. M. Schulson,[32] T. P. Weihs,[32] I. Baker,[32] H. J. Frost,[32] and J. A. Horton

Experiments at Dartmouth College on Ni_3Al over a wide range of grain sizes have shown that boron additions reduce the effectiveness with which grain boundaries strengthen the alloy. While many think that somehow boron increases atomic bond strength across a grain boundary and so prevents intergranular failure and thereby ductilizes Ni_3Al, these experiments suggest the opposite. Boron additions may actually make the grain boundaries more accommodating to slip and thereby increase the ductility of Ni_3Al.

ORNL-PHOTO 1243-86

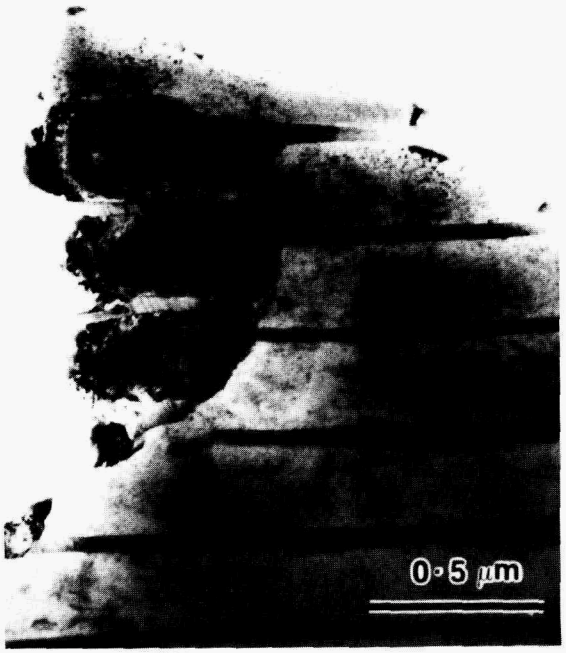

Fig. 1.1.18. Transmission electron micrograph of stoichiometric, rapidly solidified Ni_3Al powder.

In situ tensile experiments were conducted in a Philips EM430T transmission electron microscope at ORNL in order to provide supporting evidence that dislocations were accommodated at grain boundaries. In material containing boron a realignment of slip dislocations upon entering grain boundaries was observed. The deformation stage provides a minimum unloaded crosshead speed of 40 nm per second with a motor-driven mechanism or a much lower speed with a piezoelectric drive element. Recently, in situ tensile experiments were conducted on Ni_3Al with a grain size of approximately 10 μm and no boron additions. This material has little ductility. It was expected that slip dislocations from the first crack to initiate would intersect a grain boundary, and then subsequent crack propagation would be intergranular. Instead, in sections thinner than 1 μm (less than one grain thick), the crack propagation was entirely transgranular and was very similar to that of the boron-containing material.

1.1.4.14 Dislocation Analysis in Ni_4Mo (ref. 4) – H. Kao,[36] C. R. Brooks,[36] and J. A. Horton

The alloy Ni–20 at. % Mo has an fcc disordered structure above 868°C but forms a superlattice below this temperature. The formation of an ordered structure imparts considerable strengthening to the alloy, but with an accompanying embrittlement. The strength is quite sensitive to the fine structure, which can be varied by different thermal treatments. An analysis of the dislocation structure was performed in material in the ordered condition with large domains and with small amounts of prior deformation. This analysis showed a structure consisting both of overlapping stacking faults along a distinct slip trace, with superlattice dislocations present in groups of five, and more complicated interwoven arrays of single dislocations. In situ deformation experiments at 300 kV in the Philips EM430T showed that a twinning type deformation mechanism was the first to operate, whereas glide of single dislocations occurred later. Pairs of dislocations were observed to separate, leaving a stacking fault in between. Subsequent deformation resulted in similar separations of pairs of dislocations on adjacent planes, yielding an overlapping stacking fault configuration also present in the bulk deformed material.

1.1.4.15 TEM Studies of Phase Transformations in Ni_4Mo–Cr Alloys[4] – K. Vasudevan,[36] E. E. Stansbury,[36] and J. A. Horton

Alloying elements such as iron and chromium play an important role in governing the physical metallurgy and corrosion properties of the commercial Ni_4Mo-based alloys Hastelloy B and Hastelloy B-2. This investigation was carried out to examine the changes in structure and properties of Ni_4Mo alloys containing varying amounts of chromium. The identity, compositions, evolution, and formation mechanisms of various second phases that appear in these alloys were established by TEM and AEM observations in the Philips EM-300 at UT-K and Philips EM400 and JEM-100CX microscopes at ORNL.

The results indicate that the chromium partially substitutes for the molybdenum, so that the Ni_4Mo alloy behaves as though it were richer

in molybdenum, which, in turn, leads to the formation of second phases such as Ni_3Mo and Ni_2Mo. The Ni_3Mo forms by two mechanisms: (1) direct transformations from bands of DO_{22} parallel to {111} fcc planes (see Fig. 1.1.19) and (2) the conventional sequence at grain boundaries observed in the binary Ni_3Mo alloy. Minor second phases at the grain boundaries were established as η-carbides by CBED.

ORNL-PHOTO 1244-86

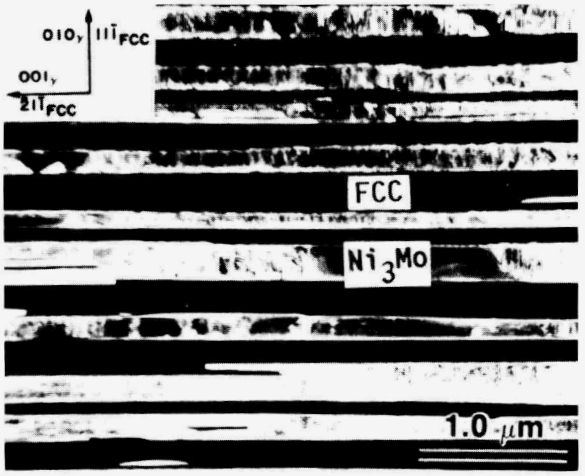

Fig. 1.1.19. Micrograph of Ni_4Mo + 2.08 wt % Cr aged at 800°C for 96 h, illustrating the direct transformation from DO_{22} to Ni_3Mo.

1.1.5 References

1. Adapted from a paper presented at the Materials Research Society Meeting, Nov. 27–29, 1984, Boston, and published in Materials Research Society Symposia Proceedings, vol. 41, pp. 363–68, *Advanced Photon and Particle Techniques for the Characterization of Defects in Solids*, ed. J. B. Roberto, R. W. Carpenter, and M. C. Wittels.

2. Formerly at Oak Ridge Associated Universities. Now at JEOL USA Inc., Peabody, Mass.

3. Adapted from a paper presented at EMAG-'85, Sept. 2–5, 1985, Newcastle-upon-Tyne, England.

4. Work in progress.

5. Adapted from a paper presented at the 43d Annual Meeting of the Electron Microscopy Society of America, Aug. 5–9, 1985, Louisville (pp. 182–83 in the proceedings, ed. G. W. Bailey, San Francisco Press, San Francisco, 1985).

6. Adapted from a paper presented at the 43d Annual Meeting of the Electron Microscopy Society of America, Aug. 5–9, 1985, Louisville (pp. 328–29 in the proceedings, ed. G. W. Bailey, San Francisco Press, San Francisco, 1985).

7. Department of Metallurgical and Materials Engineering, University of Pittsburgh.

8. Westinghouse R&D Center, Pittsburgh.

9. *Metals and Ceramics Division Materials Science Program Annual Progress Report for Period Ending June 30, 1984*, ORNL/TM-9357, November 1984, p. 26.

10. Adapted from a paper presented at the Materials Research Society Meeting, Dec. 2–7, 1985, Boston; to be published in Materials Research Society Symposia Proceedings, vol. 62, *Materials Problem Solving with the Transmission Electron Microscope*, ed. L. W. Hobbs, K. H. Westmacott, and D. B. Williams.

11. Abstract of a paper presented at the Metallurgical Society Fall Meeting, Oct. 14–16, 1985, Toronto; *J. Met.* **37**, insert p. 8 (1985).

12. Abstracted from papers submitted to *Acta Metall.*

13. Max-Planck Institut für Metallforschung, Stuttgart, West Germany.

14. Adapted from a paper presented at the 43d Annual Meeting of the Electron Microscopy Society of America, Aug. 5–9, 1985, Louisville (pp. 252–53 in the proceedings, ed. G. W. Bailey, San Francisco Press, San Francisco, 1985).

15. Solid State Division.

16. Cornell University, Ithaca, N.Y.

17. Adapted from a paper presented at the 43d Annual Meeting of the Electron Microscopy Society of America, Aug. 5–9, 1985, Louisville (pp. 276–79 in the proceedings, ed. G. W. Bailey, San Francisco Press, San Francisco, 1985); from a paper presented at the Materials Research

Society Meeting, Dec. 2–7, 1985, Boston, to be published in Materials Research Society Symposia Proceedings, vol. 62, *Materials Problem Solving with the Transmission Electron Microscope*, ed. L. W. Hobbs, K. H. Westmacott, and D. B. Williams; and *Nucl. Instr. Methods* **7/8**, 541–46 (1985).

18. Wright State University, Dayton, Ohio.

19. Adapted from a paper to be published in *J. Micros*.

20. Adapted from a paper presented at the Arizona State University Centennial Symposium on High-Resolution Electron Microscopy, Jan. 7–11, 1985, and accepted for publication in *Ultramicroscopy*.

21. Department of Metallurgical Engineering and Material Science, University of Kentucky, Lexington.

22. Adapted from a paper presented at the 43d Annual Meeting of the Electron Microscopy Society of America, Aug. 5–9, 1985, Louisville (pp. 378–79 in the proceedings, ed. G. W. Bailey, San Francisco Press, San Francisco, 1985).

23. Abstract of a paper presented at the Materials Research Society Meeting, Dec. 2–7, 1985, Boston; to be published in Materials Research Society Symposia Proceedings, vol. 60, *Defect Properties and Processing of High-Technology Nonmetallic Materials*, ed. Y. Chen, W. D. Kingery, and R. J. Stokes.

24. Department of Materials Engineering, North Carolina State University, Raleigh.

25. Abstract of a paper presented at the Materials Research Society Meeting, Dec. 2–7, 1985, Boston; to be published in Materials Research Society Symposia Proceedings, vol. 51, *Beam-Solid Interactions and Phase Transformations*, ed. H. Kurz, G. L. Olson, and J. M. Poate.

26. U.S. Army Construction Engineering Research Laboratory, Champaign, Ill.

27. Naval Research Laboratory, Washington, D.C.

28. Defense Advanced Research Project Agency, Arlington, Va.

29. Department of Mechanical Engineering and Materials Science, Vanderbilt University, Nashville, Tenn.

30. Department of Physics, Oklahoma State University, Stillwater.

31. Abstract of paper accepted by *J. Mater. Sci.*

32. Thayer School of Engineering, Dartmouth College, Hanover, N.H.

33. Abstracted from a paper submitted to *Metallography*.

34. Technique developed by C. K. H. DuBose.

35. Adapted from *Scr. Metall.* **19**, 1497 (1985), and from a paper to be published in *Acta Metall.*

36. Department of Materials Science and Engineering, University of Tennessee, Knoxville.

1.2 ATOM PROBE – M. K. Miller

The atom probe is a microanalytical tool for studies in materials science at the atomic level. Research with this instrument will include (1) applying microstructural and microchemical analysis to a wide range of materials and (2) developing new methods of analysis. Initial research will concentrate on segregation to internal boundaries, early stages of phase transformations, and radiation-induced segregation.

The main vacuum system for the atom probe was delivered from Vacuum Generators in November 1985. In December, this system was integrated with the microcomputer-controlled timing and control systems designed at Oak Ridge National Laboratory (ORNL).

The field-ion microscope, field-emission microscope, and energy-compensated time-of-flight atom probe sections of the instrument are operational. However, some modifications are planned before the specifications are fully realized. The imaging atom probe single-atom CEMA detector has been delivered and will be installed shortly. We also plan to add a laser for pulsed laser atom probe operation in the near future.

Research with this instrument will interface closely with the electron microscope facilities. The instrument will also be available for a limited amount of collaborative research with external users through the Shared Research Equipment (SHaRE) Program.

1.2.1 The ORNL Atom Probe[1] – M. K. Miller

The ORNL atom probe was designed to be an easily used microanalytical tool for studies in materials science by both specialists and inexperienced operators. The atom probe combines several instruments into one,

namely, a field-ion microscope (FIM), a field emission microscope, an energy-compensated time-of-flight atom probe, an imaging atom probe, and a pulsed laser atom probe.

The instrument is a combination of a customized version of the vacuum system of the commercial VG FIM-100 atom probe combined with ORNL-designed electronic and computing systems. A schematic diagram of the main features of the instrument is shown in Fig. 1.2.1. The FIM section features a dual-polarity 30-kV supply for field ionization and emission. The distance from the FIM channel plate to the specimen may be adjusted to provide a variable effective probe aperture for changing the area of analysis. The specimen temperature may be varied from 20 K to 300 K by using a closed-cycle helium-gas cryogenerator. The energy-compensated mass spectrometer for chemical analysis consists of a 163° Poschenrieder type analyzer with a flight path of 2.26 m, and a double channel-plate single-atom detector. The microcomputer-controlled eight-channel CAMAC-based digital timing system has a time resolution of 1 ns over the entire flight time.

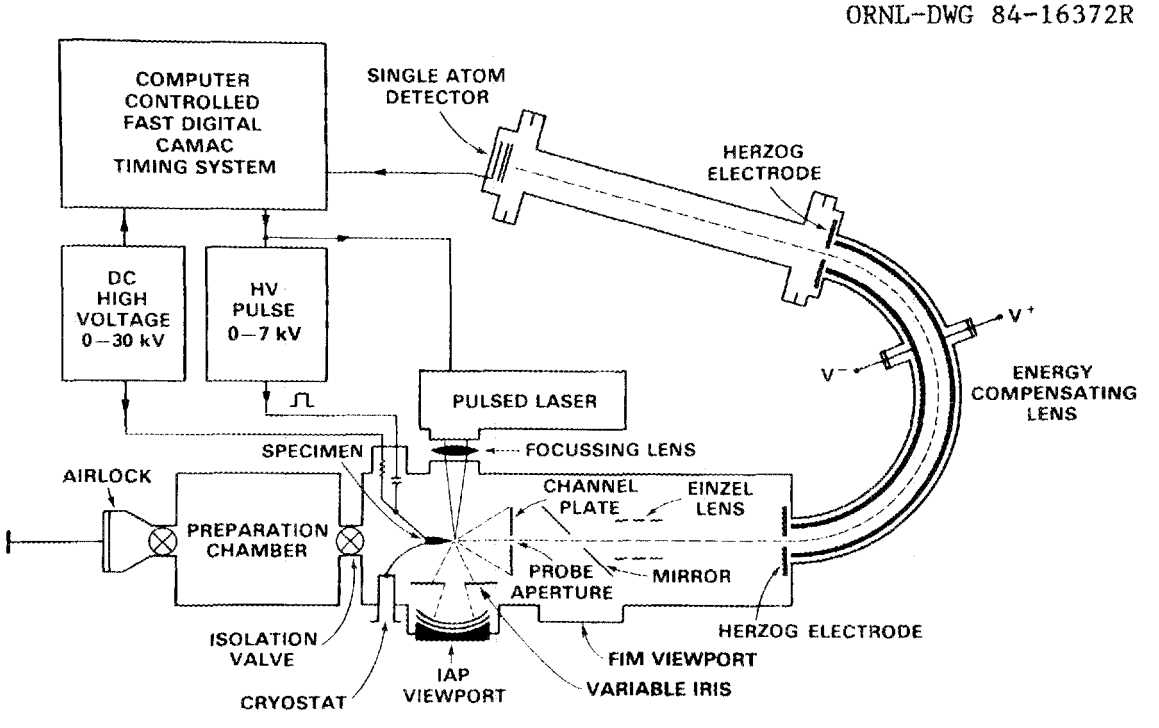

Fig. 1.2.1. Schematic diagram of the ORNL atom probe.

The imaging atom probe section features a curved CEMA single-atom detector with a radius of curvature of 146.0 mm. A continuously variable iris is positioned between the detector and the specimen to restrict the field of view to allow mass analysis of a selected region of the image. Mass spectra are accumulated on a Tektronix 7912AD waveform digitizer. The time delay for producing gated elemental maps is generated dynamically by computer-controlled CAMAC modules with a time resolution of 1 ns.

The instrument is also equipped with a real-time video digitizing system to assist in morphological interpretation and quantification of microstructural features.

1.2.2 Atom Probe Software[1] – M. K. Miller

A software package for on-line control of the atom probe field-ion microscope has been developed. The programs were written to provide the maximum information to the operator, and they have the flexibility to view the experimental data in the most appropriate mode for the type of analysis being undertaken. The data may be displayed in real time, either as raw mass or as times-of-flight, ion-by-ion element identification, mass or time spectra, multi-element composition profiles, ladder diagrams, cumulative plots, and composition. The data may also be statistically analyzed immediately with autocorrelations, cross correlations, Fourier analysis, and frequency distributions or compared with previously stored data. A built-in data base containing isotope abundances and normal charge states of all elements is available for element identification.

The package also contains programs for simulating field-ion micrographs and imaging atom probe elemental maps. A program for digitizing field-ion micrographs from standard video signals is also available. An image analysis program is under development to enable a three-dimensional reconstruction and quantification of the morphology of a microstructure.

1.2.3 An Atom Probe Study of Boron in Ni_3Al[1] – M. K. Miller and J. A. Horton

The atom probe field-ion microscope is being used in conjunction with other techniques to study the role of boron and other substitutional

elements in the ductilization of Ni_3Al. The atom probe is able to measure the concentration of any element that is present in unembrittled boundaries including grain boundaries and anti-phase boundaries (APBs).

Rapid solidification has been shown to improve the ductility of these materials and also to refine the grain size. This smaller grain size also improves the frequency of observing a boundary in the limited field of view of a field-ion specimen. Specimens of Ni_3Al doped with boron were rapidly solidified directly into wire form by a melt extraction procedure. The microstructure of these specimens was characterized by transmission electron microscopy and was found to have a structure similar to that of previously studied rapidly solidified material. A transmission electron micrograph of a field-ion specimen of this material is shown in Fig. 1.2.2. The grain size was found to be approximately 4 μm. A field-ion micrograph of a specimen containing a high-angle grain boundary and a APB intersecting a 220 plane is shown in Fig. 1.2.3. Further studies are in progress to characterize the boron distribution at boundaries.

ORNL-PHOTO 4194-85

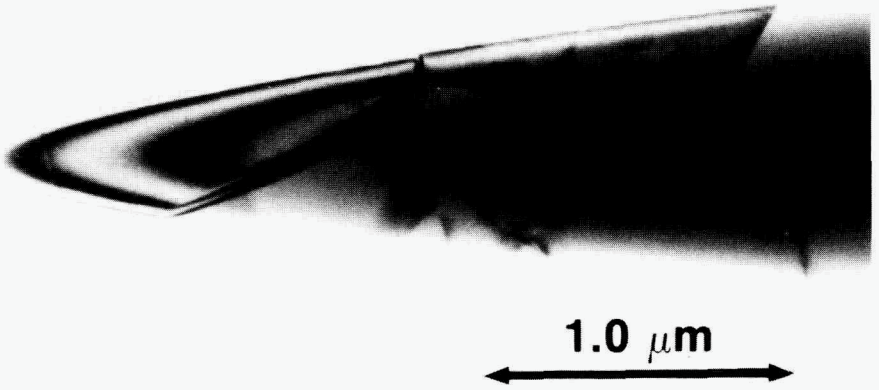

Fig. 1.2.2. Transmission electron micrograph of a field-ion specimen of rapidly solidified Ni_3Al containing grain boundaries and anti-phase boundaries.

ORNL-PHOTO 1151-86

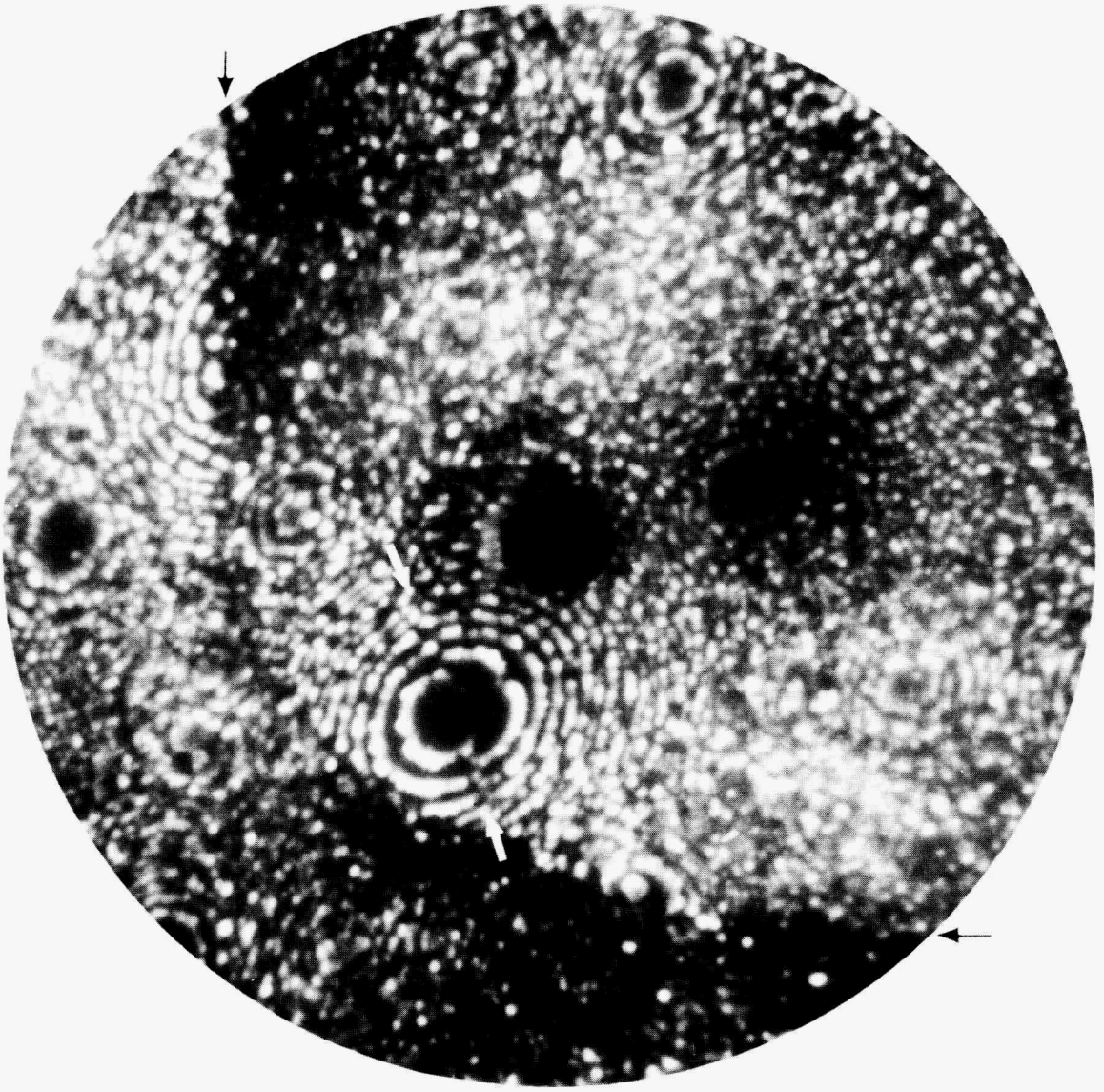

Fig. 1.2.3. Field-ion micrograph of a rapidly solidified Ni_3Al specimen containing a high-angle grain boundary and an anti-phase boundary.

1.2.4 A Comparison of Characteristic Distance Measurements by Atom Probe Field-Ion Microscopy, Transmission Electron Microscopy, and Small-Angle Neutron Scattering[1] – M. K. Miller, L. L. Horton, and S. Spooner[2]

Characteristic distance measurements may be used to characterize the nature and kinetics of phase transformation and coarsening in an alloy. A

comparison was made between measurements obtained from field-ion and transmission electron micrographs, atom probe composition profiles, and small-angle neutron scattering data.

The material used for this comparison was a commercial Fe–28.6% Cr–10.6% Co alloy that had been spinodally decomposed and aged at 525°C within a low-temperature miscibility gap. This treatment produces a very fine scaled isotropic two-phase microstructure comprising an iron-rich α and a chromium-enriched α phase as shown in Fig. 1.2.4.

ORNL-PHOTO 4050-85

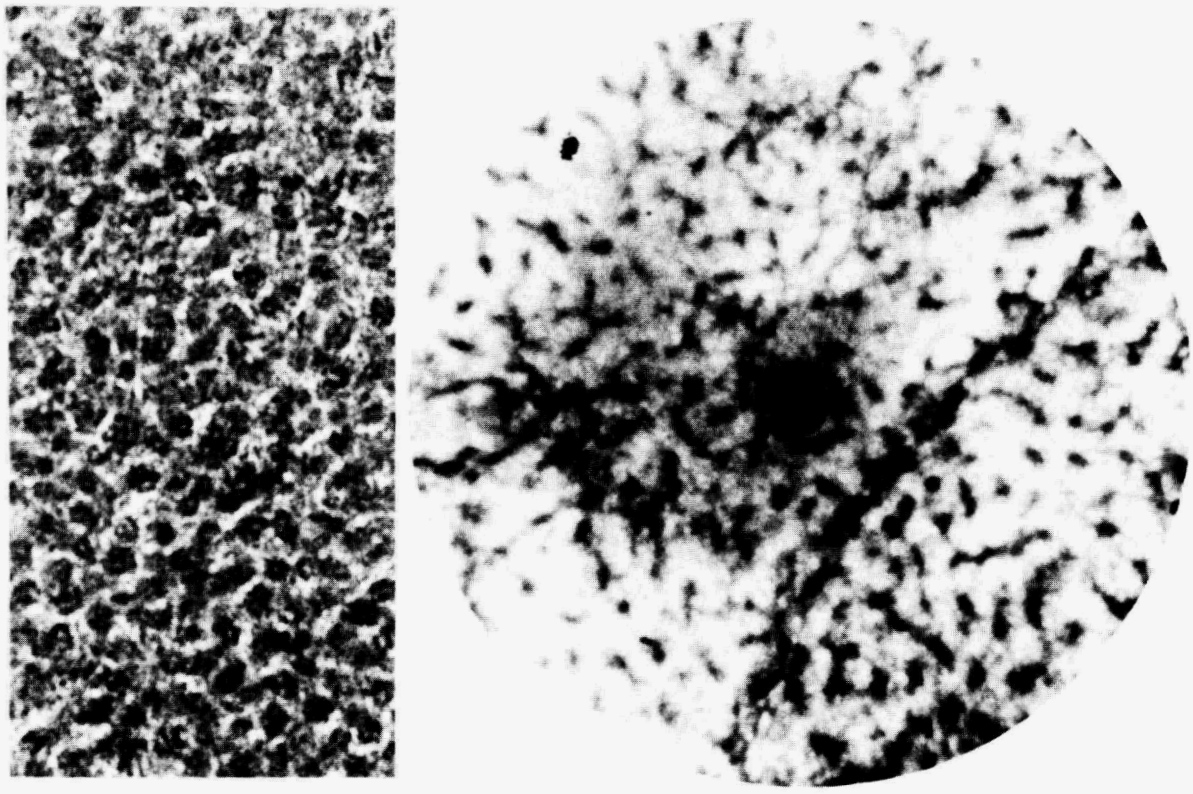

Fig. 1.2.4. Field-ion and transmission electron micrographs of the microstructure of a spinodally-decomposed Fe-Cr-Co alloy. The isotropic nature of the resulting two-phase microstructure is evident.

The results from the three techniques are summarized in Tables 1.2.1 and 1.2.2. The results are in general agreement although there are significant differences in the manner in which the phase transformation and

Table 1.2.1. Comparison of characteristic distance measurements (nm)

Aging time at 525°C (h)	FIM[a,c] (Λ)	TEM[b,c] (Λ)	Atom probe			Small-angle neutron scattering[c]		
			Composition profile[c]		Auto-correlation[c] $[(k_2 - k_1)d]$	$(2\pi/K^*)$	(l_c)	(R_G)
			(λ)	(τ)				
2	5.3		4.9	2.6	4.6	4.4	5.7	1.6
8	6.4	5.8	6.2	3.0	6.1	5.0	6.6	1.8
24	7.9	7.4	7.7	2.9	8.3	5.8	7.5	2.1
72	9.5	10.2	9.2	3.4	11.0	7.8	9.7	2.7
192	12.6	11.0	12.8	4.4	14.0	10.1	13.5	3.6
485	15.3	14.6	17.1	4.2	18.0	12.1	16.3	4.1

[a]Field-ion micrographs.

[b]Transmission electron micrographs.

[c]λ and Λ are the mean liner intercept between the α' phase, τ is the linear thickness of the α' phase, k_1 and k_2 are the first and second maxima in the autocorrelation of the composition profile, d is the interplanar distance of the reference plane, K^* is the scattering vector, l_c is the linear correlation length, and R_G is the Guinier radius.

Table 1.2.2. Comparison of time exponents of the log-log plot of the characteristic distance versus aging time

Time exponent[†]	FIM (Λ)	TEM (Λ)	Atom probe			Small-angle neutron scattering		
			Profile		Autocor-relation $[(k_2 - k_1)d]$	$(2\pi/K^*)$	(l_c)	(R_G)
			(λ)	(τ)				
a_0	0.20	0.22	0.22	0.10	0.25	0.19	0.20	0.18
fit R^2	0.993	0.990	0.977	0.872	0.998	0.966	0.959	0.964
a_1	0.16	0.22	0.18	0.05	0.24	0.10	0.12	0.11
fit R^2	0.995	1.0	0.999	0.608	0.996	0.990	0.999	0.986
a_2	0.23	0.22	0.27	0.14	0.26	0.25	0.26	0.23
fit R^2	0.995	0.979	0.989	0.849	0.999	0.995	0.992	0.985

[†]R^2 is the coefficient of determination; a_0, a_1, and a_2 are the time exponents of the overall curve, the first and second portions of the log-log plot; other symbols and abbreviations are the same as in Table 1.2.1.

the evolving microstructure affect the measurements. The comparison also provided an insight into the significance and relative influence of some of the parameters that may be extracted from the data. These parameters include the composition and volume fraction of the two phases, the morphology, and the presence of other phases in the microstructure. The results highlight the advantages of using a variety of techniques to fully characterize the scale and nature of a microstructure.

1.2.5 Atom Probe Studies of Phase Transformations Within Miscibility Gaps – M. K. Miller, P. P. Camus,[3] M. G. Burke,[3] and S. Spooner[2]

The atom probe is being used to study phase transformations that occur within low-temperature miscibility gaps in Fe-Cr, Fe-Cr-Co, and Fe-Be systems. The transformations are being characterized in terms of their kinetics, the morphology of the microstructure, and the composition and volume fraction of the two phases that are produced.

Research on the Fe-Cr and Fe-Cr-Co alloys has indicated that the time and temperature of treatments above the miscibility gap have a strong effect on the scale of the resulting microstructure that is produced after aging within the miscibility gap and on its coarsening kinetics. Further systematic experiments are planned to fully characterize these effects as a function of alloy composition.

1.2.6 Measurement of Characteristic Wavelengths in Modulated Microstructures by Field-Ion Microscopy[4] – M. K. Miller and M. G. Burke[3]

A procedure to determine the characteristic wavelength of a modulated microstructure from field-ion micrographs has been developed. The procedure accounts for the effects of the orientation of the modulations in the specimen and the projection of the curved field-ion specimen surface. Measurements from the field-ion micrograph are correlated with computer-simulated micrographs generated with the same orientation. The results exhibit excellent agreement with measurements determined from the spacing of sidebands in electron diffraction patterns of similarly aged material as shown in Table 1.2.3.

Table 1.2.3. Comparison of mean wavelengths from field-ion micrographs and from the spacing of sidebands in electron diffraction patterns of an Fe-25 at. % Be alloy aged at 350°C

Aging time (h)	Field-ion micrograph (nm)	Sideband spacing (nm)
2	4.3 ± 0.8	4.3 ± 0.7
8	6.6 ± 1.4	6.0 ± 0.8
32	9.3 ± 1.6	10.1 ± 1.0

1.2.7 References

1. Adapted from papers submitted to *J. Phys.* (Orsay, France) and presented at the 32d International Field Emission Symposium, Wheeling, Pa., July 1985.

2. Solid State Division.

3. University of Pittsburgh.

4. Adapted from *J. Micros.* **139**, 41-47 (1985).

1.3 X-RAY DIFFRACTION RESEARCH - C. J. Sparks, Jr.

The achievement of operational status for our synchrotron radiation beamline facility at the National Synchrotron Light Source has brought an important research capability to the X-Ray Research Group, the Division, and the Oak Ridge National Laboratory (ORNL). Our new concept in X-ray optics and its development permits both monochromatization and focusing of the synchrotron radiation to produce a flux at the sample from 5 to 30 times greater than obtained with previous mirror optics in the energy range from 10 to 40 keV. The precision bending device was built to tolerances of 1 μm with the combined efforts of the engineering staffs and shops at ORNL and at the Y-12 plant. The Instrumentation and Control Division provided electronic and computer interfacing that places the energy tuning and focusing under control of a computer. These optics require that the atomic planes of a curved crystal match those of a flat crystal to tolerances of 0.1 arc second to achieve the highest

throughput of radiation. Ribs attached to the curved crystal prevent anticlastic bending from destroying the match between the two crystals.

These optics are mounted in the cylindrical tank seen in the foreground in Fig. 1.3.1, which shows the ORNL beamline at the National Synchrotron Light Source. The complexity of modern experimental apparatus can also be seen from this figure. Though funded by the Basic Energy Sciences and used by groups in the Chemistry, Solid State Physics, and Metals and Ceramics Divisions, the facility will also support our applied programs, making available a unique capability for characterizing materials. More information about our beamline as a user's facility is given in Sect. 6, Collaborative Research Centers. We expect to report in the near future on the science generated by this facility.

A 6-GeV storage ring, a major new facility planned for the next decade, offers great advantages over our present synchrotron sources. The long straight sections will provide for undulators that will increase the brilliance by 10^3 over present storage rings in the 8- to 40-keV energy region. In fact, with these magnetic devices especially suited for extracting the radiation, the brilliance in units of photons or particles s^{-1} mm^{-2} $mrad^{-2}$ will exceed 10^{19} and will be equivalent to that for the most advanced electron probes having field-emission electron guns.[1] It is not possible to focus X rays to such small probe diameters as achieved with electron sources; however, the detectable mass fractions will be 10^{-3} to 10^{-5} smaller than those obtained with electrons. We are presently involved in using pinhole collimators to produce micron-diameter beams for diffraction from small areas. We will say more about this in our next report.

Preliminary experiments at our synchrotron beamline have included studies of thin metallic films of nickel and Ni_3Fe on Al_2O_3 substrates. We were able to discern diffraction effects associated with the metal-air interface and the metal-ceramic interface. Analysis of this data requires a new formulation of the diffraction theory to include surfaces and interfaces. The brilliance of our synchrotron beamline will open new avenues for materials characterization. Large changes in diffuse X-ray scattering were measured for disordered single crystals of Ni_3Fe as the

YP-1171

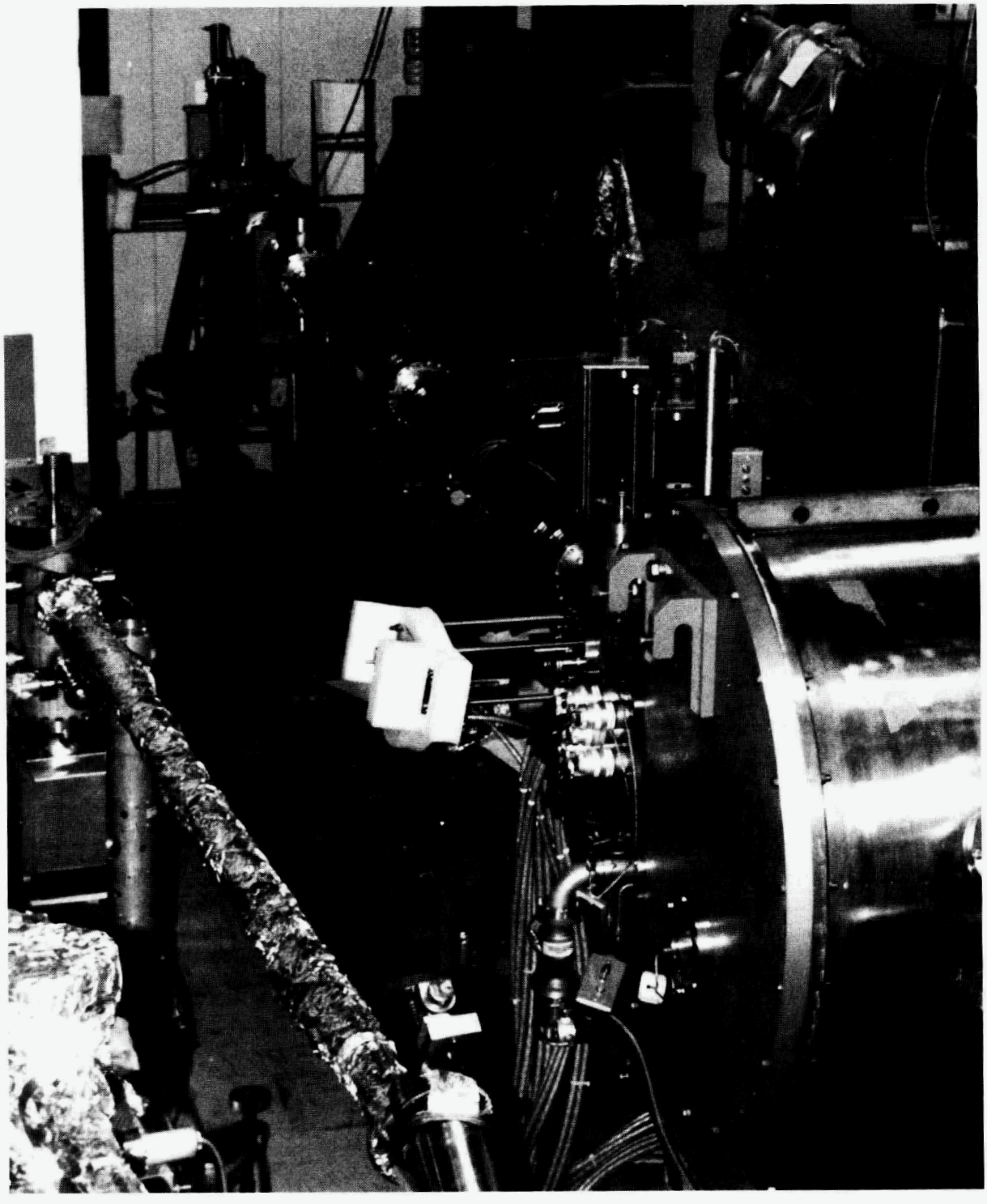

Fig. 1.3.1. The ORNL beamline installed at the National Synchrotron Light Source became operational during July 1985 as the performance of the storage ring improved.

energy of the incident X-radiation was changed to below and above the energy of the iron K absorption edge. These intensity changes permit highlighting specific atoms so that their distribution functions can be recovered and their chemical environments deduced. This is the beginning of a major program to unravel the local atomic arrangements and interatomic distances of binary and ternary iron based alloys.

Structural studies of the minor second phase in steels have continued. A review paper on the crystal structure of stable and metastable iron-containing carbides was published. From this work new perspectives emerge suggesting possible relationships among the structures. The structural chemistry of boron and the higher borides was also reviewed. Stabilization effects produced by impurity elements on the boron polyhedral units and their packing in three-dimensional space lattices are emphasized. The pentagonal pyramid framework of the boron combines naturally into icosahedra and clusters of face-sharing and partial icosahedra. These icosahedra suggest similarities between boride crystal chemistry and the developing subject of quasicrystalline structures.

Extension of our studies on the $(Cr_{23-x}Fe_x)C_6$ tau carbide structure has demonstrated that iron atoms prefer to substitute for chromium atoms at sites that are least bonded to carbon atoms. As these sites are filled, iron begins to occupy the chromium sites most closely bonded to carbon. The tau solid solution then becomes thermodynamically unstable relative to other phases. This research on the substitution of elements on various coordination sites has produced new insights to the crystal chemistry of alloy phases.

We have continued our studies of X-ray-induced resonant and threshold phenomena near absorption edges. An understanding of the X-ray interaction processes near absorption edges is important to our developing use of anomalous dispersion to interpret X-ray diffraction data. Near-edge resonant X-ray spectroscopies can have important attributes such as a sensitivity to the unfilled density of states around a particular atomic species and the ability to resolve structure normally convoluted with the initial hole lifetime width. Measurements of hard-X-ray-induced electron interactions near threshold show the theoretically predicted difference

between the dependence of shakeup and shakeoff probabilities for the first time. To avoid solid state effects, these measurements were made on gases. Absolute cross sections requires a calculation of the solid angle subtended by the detector to every scattering point in the gas sample. Methods for calculating changes in solid angle as a function of the angle of scattering have been derived.[2]

An X-ray diffraction service laboratory supplies chemical phase identification, among other services, in support of both basic and applied materials research. This work is more than routine and often results in journal articles on a variety of materials characterization subjects.

1.3.1 X-Ray Scattering

1.3.1.1 Atom Distributions in Tau Carbide Phases: Fe and Cr Distributions in $Cr_{23-x}Fe_x)C^6$ With $x = 0$, 0.7_4, 1.7_0, 4.1_3, and 7.3_6 (ref. 3) — H. L. Yakel

Mo Kα Bragg diffraction data collected from single crystals of tau carbides were used in least-squares refinements of structural models that (for $x \neq 0$) included *a priori* distribution parameters for iron on three of the four metal-atom sites of the known $M_{23}C_6$ tau carbide structure. Conventional data for the crystal with $x = 0.7_4$ were supplemented by synchrotron-radiation (SR) diffraction data collected at energies near Cr K and Fe K absorption edges. Results show that distribution parameters whose differences from chemical-average values have statistical and physical significance can be derived from extensive, precise conventional diffraction data. They demonstrate that iron atoms preferentially substitute for chromium at sites not bonded to carbon atoms; when 30 to 35% of the sites that are bonded to carbon are occupied by iron, the tau solid solution becomes thermodynamically unstable relative to other phases. Calculations with the SR data sets collected near the Cr K-edge energy suggest a $(\sin\theta)/\lambda$ dependence of the real part of the dispersion correction to the atomic scattering factor for chromium as well as significant departures from the theoretical free-atom calculations for these corrections at $(\sin\theta)/\lambda = 0$. A review of iron-containing carbides outlines these areas where research is needed.[4]

1.3.1.2 Recent Developments in the Structural Crystallography of Boron and the Higher Borides[5] – H. L. Yakel

The present status of knowledge about the structural crystallography of elemental boron and the higher borides may be summarized by the following four statements. (1) The basic structural unit of the boron framework in most of these phases is a B_7 group in which a central boron atom is equidistant from six others that lie at the vertices of a pentagonal pyramid. (2) This unit combines naturally into icosahedra and clusters of face-sharing icosahedra or partial icosahedra. (3) While these individual combinations may be close-packed entities, they cannot be repeated so as to form a continuous close-packed structure in a crystalline solid whose lattice is propagated by *only* three noncoplanar translations; the structure of a solid containing such combinations will necessarily have many interstices of varying size and atomic environment. (4) The actual combination(s) observed in the crystal structure of a given phase can be sensitively dependent on the physical conditions under which the phase forms as well as on the presence or absence of minor concentrations of electron-donating "impurity" elements that may occupy interstitial sites or may substitute for boron atoms in the electron-deficient icosahedral framework.

This paper reviews structural studies of boron and boron-rich borides over the last decade using as a framework the classification scheme proposed by Matkovich and Economy. Chemical bonding in boron polyhedral units and the packing of these units in normal 3D space lattices are described with emphasis on stabilization effects that may be produced by "impurity" elements. Potentially useful areas for structural work with several new scattering and spectroscopic techniques are suggested. The paper concludes with a discussion of possible connections between boride crystal chemistry and the developing subject of quasicrystalline structures.

1.3.2 X-Ray Physics

1.3.2.1 Experimental X-Ray Scattering Cross Sections for Hydrogen and Rare Atomic Gases[6] – G. E. Ice

The absolute measurement of X-ray scattering from rare gases provides unambiguous test of *ab initio* wave functions and theoretical X-ray scattering cross sections. When solid state effects are not present, wave functions can be calculated very accurately; there is no bonding between the gas atoms. Though absolute measurements of X-ray scattering from gases is not easily done, the measurements avoid the complications of extinction effects and the need to know the local and long-range structure of the sample.

1.3.2.2 Threshold Double Photoexcitation of Argon With Synchrotron Radiation[7] – G. B. Armen,[8] T. Åberg,[9] Kh Rezaul Karim,[8] J. C. Levin,[8] B. Crasemann,[8] G. S. Brown,[9] M. H. Chen,[10] and G. E. Ice

In atomic inner-shell photoionization, multiple excitation processes occur with significant probability. The resulting final states are approximately described by configurations formed by removal of a core electron and excitation of additional electrons to higher bound states (shakeup) or to the continuum (shakeoff). Such multiple excitation processes result in satellites in the photoelectron spectra and in the Auger and X-ray spectra from transitions through which the photoexcited states decay. The study of these multiple excitation processes is important because they epitomize the breakdown of the independent-particle model and can provide important clues for the understanding of electron correlation and of excitation dynamics. The energy dependence of the cross sections for double excitation is particularly informative near threshold; the observation of Auger satellites makes it possible to measure this dependence. Auger satellites were measured to determine the probability of M-shell excitation accompanying K-shell photoionization of argon, as a function of photo energy. The theoretically predicted difference between the dependence of shakeup and shakeoff probabilities on the photo energy near threshold is demonstrated for the first time. Results are critically compared with calculations.

1.3.2.3 Threshold Excitation of Short-Lived Atomic Inner-Shell Hole States With Synchrotron Radiation[11] - G. B. Armen,[8] T. Åberg,[9] J. C. Levin,[8] B. Crasemann,[8] M. H. Chen,[10] G E. Ice, and G. S. Brown[9]

In threshold excitation of short-lived, deep atomic inner-shell hole states, ionization and decay cannot be treated as distinct processes. Directly at threshold, photoionization and radiationless deexcitation occur in a single process, the resonant Raman effect. Above threshold, excitation and deexcitation are still linked by post-collision interaction (PCI), in which the Auger decay takes place under the influence of the Coulomb field of the receding photoelectron and some of the photoelectron's energy is transferred to the Auger electron. Measurements of the Auger spectrum excited near threshold can therefore probe the dynamics of inner-shell transitions and provide a stringent test of the semiclassical PCI theory which has been shown to be valid in the limit of long hole-state lifetimes. The first fully quantum-mechanical calculation of PCI becomes possible, based on resonant scattering theory, since the intermediate-state summations can be restricted to states associated with the initial inner-shell hole.

Here we report on an investigation of the Xe L_3-$M_4M_5(^1G_4)$ Auger spectrum, photoexcited in the vicinity of the L_3 edge measured as a function of photon energy. The nd spectator-electron satellite lines show resonant behavior. The diagram line exhibits the largest (≥1 eV) post-collision interaction shift yet observed. For comparison with the data, the first fully quantum-mechanical calculation of the post-collision interaction in deep inner-shell Auger decay is performed, based on a resonant-scattering approach that involves a complete summation over intermediate L_3 one-hole states.

1.3.3 X-Ray Service Laboratory

1.3.3.1 Preliminary Study of the Thermal-Expansion Coefficients of Long-Range-Ordered Aluminides[12] - T. Leventouri,[13] O. B. Cavin, and J. S. Faulkner

The technological interest in these aluminides has generated a need for a better understanding of the phase stability of iron-nickel-aluminum

alloys. It is widely accepted that the existence of magnetism has a profound effect on phase stability, although differing views about the mechanism responsible for this have been advanced in the literature of metallurgy and physics. A major effort is being made to develop a new understanding of magnetism in transition metals and their alloys at finite temperatures. It has recently been recognized that magnetoelasticity measurements provide useful clues to the nature of the magnetism in such materials. The spontaneous magnetoelastic coefficients are obtained from measurements of thermal expansion with no applied magnetic field.

We have measured the thermal-expansion coefficients $\alpha(T)$ of $Ni_{76}Al_{24}$, $Ni_{70}Fe_{10}Al_{20}$, and $Ni_{67.5}Fe_{15}Al_{17.5}$ between room temperature and 900 K by using X-ray diffraction. Particular emphasis is placed on the peak in $\alpha(T)$ that is found near the magnetic-ordering temperature for the alloys that contain iron.

1.3.3.2 Hydrothermal Growth of Single-Crystal Cu_2Se (Berzelianite)[14] – O. C. Kopp[15] and O. B. Cavin

The literature is replete with papers on the growth, properties, and characterization of sulfides, selenides, and tellurides because of their important semiconductor and photoelectric properties. Most crystals have been grown by processes such as vapor deposition, melt growth, from gels, solvent evaporation, liquid phase epitaxy, chemical vapor transport, sometimes catalyzed by an organic (or metalorganic) vapor. A few have been produced hydrothermally. Our single crystals of Cu_2Se were produced as a by-product reaction between H_2SeO_4 and the upper copper gasket of a hydrothermal pressure vessel during the production of α-quartz crystals. The growth took place in the presence of 0.5N RbOH solvent, at T = 440 ± 5°C, P = 1275 ± 35 MPa (18,500 ± 500 psi), and $f(O_2)$ about 10^{-25}.

1.3.3.3 Crystal Growth and Properties of Trinickel Boride, Ni_3B (ref. 16) – C. B. Finch, O. B. Cavin, and P. F. Becher

The orthorhombic compound Ni_3B (cementite structure) is of current research interest as an intergranular second phase in TiB_2-Ni compacts being fabricated for wear applications. It was first detected in 1950 by Andersson and Kiessling and was reported by Schöbel and Stadelmaier as a

congruently melting compound (1166°C) in the Ni-B system. Its existence was confirmed by Sobolev and Fedorov. However, none of these authors prepared the compound as large single crystals, and none reported properties for oriented material. In view of its importance as a binder in nickel-bonded TiB_2, we embarked on a program to grow and characterize single crystals of Ni_3B of known orientation and defined growth direction. Single crystals of Ni_3B were grown by the Czochralski method at 1080 to 1090°C with a pyrolytic BN crucible in a vacuum environment. Crystals up to 1.5 cm in diameter and 5 cm long were prepared at growth rates of 1 to 2 cm/h. Oriented sections were tested for hardness, Young's moduli, and fracture toughness. Chemical analyses confirmed the crystals to be ≥99.8 wt % Ni_3B, with 0.1 wt % C as the major impurity.

1.3.4 References

1. C. J. Sparks, Jr., "X-Ray Microprobe Characterization of Materials: The Case of Undulators on Advanced Storage Rings," in *Major Facilities for Materials Research and Related Disciplines*, National Academy Press, Washington, D.C., 1984.

2. F. Parente and G. E. Ice, "Predictions of Scattering from an Absorbing Gas Target," *Nucl. Instrum. Methods Phys. Res.* **B9**, 89–96 (1985).

3. H. L. Yakel, "Atom Distributions in Tau Carbide Phases: Fe and Cr Distributions in $(Cr_{23-x}Fe_x)C_6$ with $x = 0, 0.7_4, 1.7_0, 4.1_3$, and 7.3_6," to be submitted for publication in *Acta Cryst.*

4. H. L. Yakel, "Crystal Structures of Stable and Metastable Iron-Containing Carbides," *Int. Metall. Rev.* **30**(1), 17–40 (1985).

5. H. L. Yakel, "Recent Developments in the Structural Crystallography of Boron and the Higher Borides," to be published in the proceedings of the International Conference on the Physics and Chemistry of Boron and Boron Rich Borides held at the University of New Mexico, Albuquerque, July 29–31, 1985.

6. G. E. Ice, "Experimental X-Ray Scattering Cross Sections for H_2 and Rare Atomic Gases," presented to the New Directions in X-Ray Scattering Workshop, April 3–5, 1985, Asilomar, Calif.

7. G. B. Armen, T. Åberg, Kh Rezaul Karim, J. C. Levin, B. Crasemann, G. S. Brown, M. H. Chen, and G. E. Ice, "Threshold Double Photoexcitation of Argon with Synchrotron Radiation," *Phys. Rev. Let.* **54**(3), 182–85 (January 1985).

8. Department of Physics and Chemical Physics Institute, University of Oregon, Eugene.

9. Laboratory of Physics, Helsinki University of Technology, Helsinki.

10. Lawrence Livermore National Laboratory, Livermore, Calif.

11. G. B. Armen, T. Åberg, J. C. Levin, B. Crasemann, M. H. Chen, G. E. Ice, and G. S. Brown, "Threshold Excitation of Short-Lived Atomic Inner-Shell Hole States with Synchrotron Radiation," *Phys. Rev. Let.* **54**(11), 1142–45 (March 1985).

12. T. Leventouri, O. B. Cavin, and J. S. Faulkner, "Preliminary Study of the Thermal-Expansion Coefficients of Long-Range-Ordered Aluminides," *Phys. Rev. B* **31**(11), 7436–39 (June 1985).

13. On leave to Metals and Ceramics Division from Solid State Section, Department of Physics, University of Athens, Greece.

14. O. C. Kopp and O. B. Cavin, "Hydrothermal Growth of Single Crystal Cu_2Se (Berzelianite)," *J. Crys. Growth* **67**, 391–92 (1984).

15. University of Tennessee, Knoxville.

16. C. B. Finch, O. B. Cavin, and P. F. Becher, "Crystal Growth and Properties of Trinickel Boride, Ni_3B," *J. Crys. Growth* **67**, 556–58 (1984).

2. HIGH-TEMPERATURE ALLOY RESEARCH

2.1 THEORETICAL STUDIES OF METALS AND ALLOYS – W. H. Butler

Research in the Theory Group is directed at obtaining an understanding of the properties of materials based on the underlying laws of physics. Recent progress in the theory of many electron systems and in the techniques for dealing with disorder, coupled with advances in computers, have made it possible to calculate many properties of materials from first principles.

During the reporting period important progress has been made in several areas. We have performed very basic studies of the forces that bind atoms together with the aim of improving techniques for calculating those forces. We have improved our techniques for calculating the properties of random alloys and have developed the capability to calculate the lattice constants and total energies of alloy phases. We have implemented a new and apparently very accurate theory for transport in random alloys. We have developed two complementary techniques for calculating the tendency of alloys to develop short-range order. We have also made progress in our understanding of finite temperature magnetism and of liquid and amorphous metals.

Section 2.1.1 describes general progress in alloy theory during the reporting period. Section 2.1.2 describes work on the theory of ordering and clustering in alloys. Section 2.1.3 concerns progress in transport theory. Section 2.1.4 is devoted to applications of alloy theory to the understanding of finite temperature magnetism and of magnetism in alloys. Section 2.1.5 describes research on the bonding between atoms and calculations of the properties of clusters of atoms. Section 2.1.6 describes work on liquid and amorphous metals, and Sect. 2.1.7 describes work on transition-metal aluminides.

2.1.1 Theory of Random Alloys – G. M. Stocks, D. M. Nicholson,[1] J. S. Faulkner, and A. P. Maclin[2]

In the past we have developed techniques for calculating the properties of alloys from first principles. The theoretical techniques used are based on three fundamental ideas: density functional theory, multiple scattering theory, and the coherent potential approximation.

Density functional theory is a very general and powerful idea that makes it possible to treat a system consisting of many electrons by concentrating on the motion of a single electron moving in a self-consistent field created by the others. In principle, density functional theory can give the exact ground state energy and charge density of any system. In practice, it appears to correctly explain most of the physics and chemistry of solids.

Multiple scattering theory allows one to separate the problem of an electron interacting simultaneously with many potentials into two simpler problems, that of an electron scattering off of a single potential and that of a free electron propagating from one point to another in space. When applied to a periodic array of identical potentials, multiple scattering theory yields the Korringa-Kohn-Rostoker (KKR) method of band theory.

The coherent potential approximation (CPA) allows one to treat a random substitutional alloy by replacing the random potential of the alloy by a periodic, effective, or "coherent" potential. This "coherent" potential is chosen self-consistently by requiring that the additional scattering caused by replacing a "coherent" potential with a "real" one vanish on the average.

Several years ago a very fundamental and important step in alloy theory was made when the KKR-CPA was implemented by us and our collaborators. Previously, the CPA could only be applied to rather artificial tight-binding models of alloys. The wedding of multiple scattering techniques with the CPA allowed the CPA to be used to treat random substitutional alloys rather generally.

This year an additional important step has been taken. The CPA and density functional theories have been extended and made consistent and compatible. We have developed new expressions for calculating the

configurationally averaged total energy and pressure of random alloys. The new expressions satisfy all of the very general internal consistency requirements of standard density functional theory; e.g., the energy is a minimum for the self-consistent charge densities (in this case the species decomposed single-site charge densities), and the variation of the potential energy with respect to a single-site charge density gives the self-consistent effective potential that enters the Schrödinger equation. The new theory gives a clear physical picture of the meaning of the configurationally averaged total energy within the coherent-potential approximation, thereby solving a longstanding conceptual problem.

The new theory has been used to calculate the concentration variation of the equilibrium lattice parameter for fcc Cu_cZn_{1-c} alloys, and the results are shown in Fig. 2.1.1. The equilibrium was located by finding the lattice parameter for which the pressure is zero. For the α-phase alloys, theory is within 1.5% of experiment. We find a slight departure from Vegard's rule which, for Cu-rich alloys, implies an initial slope of 0.0054 a.u./at. %. We obtain 0.0042 a.u./at. %, in good agreement with the experimental value of 0.0045 a.u./at. %. We believe that the major part of the discrepancy in the absolute value of the lattice constant results from the neglect of high angular momentum components (ℓ = 3 and 4) in our KKR-CPA calculations. When we have included these we expect the residual error to be of the same order as that for calculations on pure metals, i.e., 0.5%.

A preliminary attempt to use the theory to calculate the concentration dependence of the heat of mixing yielded encouraging results, both in sign and magnitude. However, it is clear that the inclusion of the higher angular momentum components is required in order to obtain completely reliable results.

During this reporting period we have also made a number of significant technical improvements in the techniques that we use to solve the basic equations of the KKR-CPA theory. Indeed, without the significant reductions in computation effort that these improvements give, it would not have been possible to perform calculations of total energies with reasonable expenditures of computing time. In performing self-consistent calculations, extensive use is made of the complex energy plane. Many of

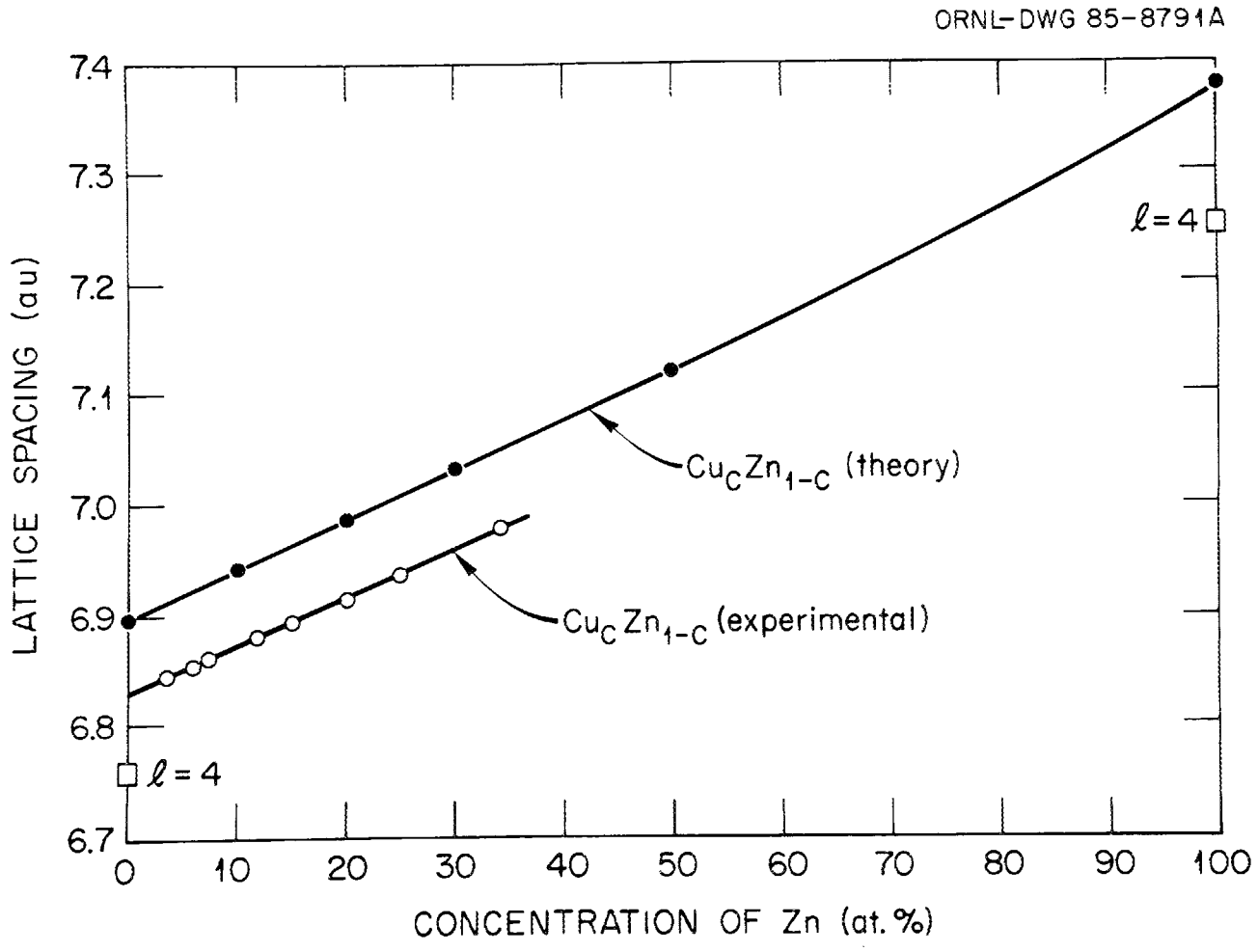

Fig. 2.1.1. Concentration variation of the lattice spacing of α-phase $Cu_C Zn_{1-C}$ alloys. Calculated KKR-CPA results – solid circles. Experimental room-temperature results – open circles.

the quantities required in these calculations involve integrals of densities of states, charge densities, etc. over the occupied states. Rather than performing such integrals along the real energy axis, we distort the contour of integration into the complex plane. The two major effects of this are a reduction of the effort required to solve the KKR-CPA equations at each of the energies considered, and a reduction in the total number of energies that are required in order to obtain accurate values for the necessary integrals. Although these methods were developed within the context of the KKR-CPA, they are applicable to all electronic structure calculations that are based on multiple scattering theory.

2.1.1.1 A First Principles Approach to the Band Theory of Random Metallic Alloys[3] - G. M. Stocks and H. Winter[4]

These notes to a course of five lectures explore the extent to which first-principles calculations of the electronic structure of random substitutional alloys can be performed. They include a brief description of density functional theory, an introduction to the KKR-CPA and the formulas necessary to calculate observables, a description of the self-consistent field (SCF) KKR-CPA and the results of applications to Ag_cPd_{1-c} alloys, application of the theory to the calculations of residual resistivities, and alloy Fermiology experiments using 2γ-angular correlation of annihilation radiation.

2.1.1.2 Electronic States in Disordered Solids. III. Applications to Materials Science[5] - J. S. Faulkner

The electronic states of many alloy systems have now been calculated by using a framework of theory that is based on the coherent-potential approximation. Some of the results of classic experiments on alloys are explained on the basis of these calculations.

2.1.1.3 A Fast Method for Calculating the Self-Consistent Electronic Structure of Random Alloys[6] - D. D. Johnson,[7] F. J. Pinski,[8] and G. M. Stocks

We describe a computationally efficient method for performing self-consistent field calculations of the electronic structure of random solid-solution alloys within the multiple-scattering coherent-potential approximation formalism (KKR-CPA). We utilize a cluster method for

solving the KKR-CPA equations and integrate along a contour in the complex energy plane to reconstruct the single-site electronic densities.

2.1.1.4 Use of Integration in the Complex Energy Plane in Multiple Scattering Green's Function Methods: An Optimal Contour[9] – G. M. Stocks and F. J. Pinski[8]

Multiple scattering Green's function band structure techniques such as the KKR method for ordered systems and the KKR-CPA method for disordered substitutional alloys are particularly suited to the use of integration in the complex energy plane when properties are required that involve an energy integration over occupied states. Such properties include charge densities required in self-consistent field calculations as well as many response functions. Here we describe the use of an optimal contour that allows the accurate calculation of such quantities using a small number of complex energies. This method involves a separation of the single and multiple scattering parts of the Green's function. The importance of this contour for finite temperature band structure calculations is stressed.

2.1.1.5 A Fast Method for Calculating the Self-Consistent Electronic Structure of Random Alloys. II. Optimal Use of the Complex Plane[10] – F. J. Pinski[8] and G. M. Stocks

In a previous paper, it was shown that calculations of electronic properties involving energy integrations over the occupied energy bands are greatly facilitated by moving the integration contour into the complex energy plane. In this paper, by separating the single-particle Green's function into a single-scatterer contribution and a multiple-scattering contribution, we show that an optimal contour can be found that yields a further substantial increase in computational efficiency. This method applies to all multiple-scattering-based electronic-structure calculations.

2.1.1.6 Self-Consistent Electronic Structure of α-Phase Hume-Rothery Electron Compound Alloys Cu_cZn_{1-c}, Cu_cGa_{1-c}, and Cu_cGe_{1-c} (ref. 11) – G. M. Stocks, M. Boring,[12] D. M. Nicholson,[1] F. J. Pinski,[8] D. D. Johnson,[7] J. S. Faulkner, and B. L. Gyorffy[7]

We have performed charge self-consistent electronic structure calculations for the α-phase Hume-Rothery electron compound alloys Cu_cZn_{1-c},

Cu_cGa_{1-c}, and Cu_cGe_{1-c} having electron to atom ratios 1:1, 1:2, and 1:3 for each alloy series. The calculations are based on the self-consistent-field Korringa-Kohn-Rostoker coherent-potential approximation (KKR-CPA). We show results for the densities of states and Fermi surface of these alloys; the behavior of these quantities is quite different from that predicted on the basis of the rigid band model. We also show results for the ground state properties of the Cu_cZn_{1-c} alloys that were obtained on the basis of a recent generalization of the density functional theory to random alloys. The theory provides a basis for understanding the concentration variation of the lattice parameter (Vegard's Law) for Cu_cZn_{1-c} alloys at the microscopic quantum mechanical level.

2.1.1.7 Density Functional Theory for Random Alloys: Total Energy Within the Coherent Potential Approximation[13] – D. D. Johnson,[7] D. M. Nicholson,[1] F. J. Pinski,[8] B. L. Gyorffy,[7] and G. M. Stocks

A density functional-based theory is developed for calculating the total energy and pressure of random substitutional alloys within the KKR-CPA. The theory is used to calculate the concentration variation of the equilibrium lattice spacing of α-phase Cu_cZn_{1-c} alloys. We find, in agreement with experiment, that the variation is almost linear and that it deviates from Vegard's rule.

2.1.1.8 Density Functional Theory and the Total Energy and Pressure of Random Alloys Within the Coherent Potential Approximation[14] – G. M. Stocks, D. M. Nicholson,[1] D. D. Johnson,[7] B. L. Gyorffy,[7] and F. J. Pinski[8]

We have derived expressions for calculating the total energy and pressure of random substitutional alloys that place the theory of the ground state properties of random alloys on the same sound basis as the theory of the ground state properties of pure metals and ordered alloys. The expressions are based on density functional theory; the first principles KKR-CPA method is used to treat the disorder. We present results for the concentration variation of the lattice parameter of α-phase Cu_cZn_{1-c} alloys that are in good agreement with experiment and show a departure from Vegard's rule. We also present results for the concentration variation of the heat of mixing and draw some conclusions about the consequences of this work for the theory of alloy phase stability.

2.1.1.9 The Electronic Structure, the X-Ray Photoelectron Spectra, and the Specific Heat Coefficients of Cu-Pd alloys[15] - H. Winter,[4] P. J. Durham,[16] W. M. Temmerman,[16] and G. M. Stocks

Copper and palladium form random alloys throughout the concentration range in which both diagonal and off-diagonal disorder is of importance. A realistic description of their electronic structure requires going beyond tight-binding models.

We present SCF-KKR-CPA calculations of the electronic density of states. We find strong hybridization of the palladium d-bands with the copper d-bands over the entire concentration range. We do not obtain a palladium virtual bound state for the copper-rich alloys and therefore contradict the interpretation generally placed on valence band X-ray photoelectron spectroscopy (XPS) spectra for copper-palladium. Nevertheless, our first-principles calculations of the XPS spectra are in excellent agreement with recent measurements, and we discuss why this is so. Furthermore, we compare our density of states at the Fermi energy with specific heat measurements.

2.1.1.10 Electron and Electron-Positron Momentum Distributions in Concentrated Random Alloys[17] - Z. Szotek,[16] B. L. Gyorffy,[7] G. M. Stocks, and W. M. Temmerman[16]

We present a formalism for calculating the two-photon momentum densities $\bar{\rho}^{2\gamma}(\vec{p})$ for substitutional random alloys within the KKR-CPA band-theory scheme and apply it to $Cu_{60}Ni_{40}$ and $Cu_{60}Pd_{40}$ random alloys. In particular we study $\bar{\rho}^{2\gamma}(\vec{p})$ along the directions ΓX, ΓK, and ΓL in $Cu_{60}Ni_{40}$ and along ΓX in $Cu_{60}Pd_{40}$ and compare it with the appropriate electron momentum distribution. We conclude that the extent to which the positron wave function influences the results of positron annihilation experiments is slight, and it can now be studied in quantitative detail.

2.1.1.11 Self-Consistent Electronic Structure of Disordered $Fe_{0.65}Ni_{0.35}$ (ref. 18) - D. D. Johnson,[7] F. J. Pinski,[8] and G. M. Stocks

We present the results of the first *ab initio* calculation of the electronic structure of a disordered alloy $Fe_{0.65}Ni_{0.35}$. The calculation

is based on the multiple-scattering coherent-potential approach (KKR-CPA) and is fully self-consistent and spin-polarized. Magnetic effects are included within local-spin-density functional theory using the exchange-correlation function of Vosko-Wilk-Nusair. The most striking feature of the calculation is that electrons of different spins experience different degrees of disorder. The minority spin electrons see a very large disorder, whereas the majority spin electrons see little disorder. Consequently, the minority spin density of states is smooth compared with the very structured majority spin density of states. This difference is due to a subtle balance between exchange splitting and charge neutrality.

2.1.1.12 Local Density Theory of Random Alloys[9] – D. M. Nicholson,[1] G. M. Stocks, D. D. Johnson,[7] F. J. Pinski,[8] and B. L. Gyorffy[7]

Within the coherent-potential approximation an internally consistent local density theory is proposed. This determines the prescription for generating the self-consistent charge density and the total energy. The preservation of the variational property of the total energy allows direct evaluation of the pressure from an appropriately modified virial theorem. Examples will be taken from the $Cu_{1-x}Zn_x$ and $Cu_{1-x}Pd_x$ systems.

2.1.1.13 Electronic Structure of $Ni_{1-x}Mo_x$ Alloys[9] – D. M. Nicholson[1] and G. M. Stocks

Nickel-molybdenum is an achetypical K-state alloy having a resistivity reduction of up to 15% upon cold working. The short-range order in the alloy is characterized by a peak in electron diffuse scattering at the $(1, \frac{1}{2}, 0)$ point. Coherent-potential approximation calculations reveal interesting features in the density of states and a Fermi surface nearly washed out by disorder. Calculated diffuse scattering intensities are compared with experiment. Resistivity will be evaluated assuming no short-range order and compared with experimental results for cold-worked samples.

2.1.1.14 Electronic Structure of Aluminum-Rich Al_cLi_{1-c} Alloys[9] – A. P. Maclin[2] and G. M. Stocks

At high temperatures aluminum-rich Al_cLi_{1-c} alloys can be produced in a disordered fcc phase for $c \leq 0.25$. At lower temperatures a metastable ordered precipitate forms that has the $L1_2$ crystal structure. Here we report the results of calculations of the ground state properties and

electronic structure of these alloys both in the ordered phase [using the atomic sphere approximation linear muffin-tin orbital (ASA-LMTO) method] and in the disordered phase (using the KKR-CPA method) that are based on the use of (local) density functional theory. We stress the changes in the electronic structure that accompany ordering and suggest how they might be observed experimentally by using modern band spectroscopy methods. For the disordered-alloys plots of the Bloch spectral function we show how the alloy Fermi surface evolves as a function of concentration.

2.1.1.15 The Electronic Density of States and the X-Ray Photoelectron Spectra of the Valence Band of Cu-Pd Alloys[19] - H. Winter,[4] P. J. Durham,[16] W. M. Temmerman,[16] and G. M. Stocks

We present SCF-KKR-CPA calculations of the electronic density of states of random Cu_cPd_{1-c} alloys. We find strong hybridization of the palladium d-bands with the copper d-bands over the entire concentration range. We do not obtain a palladium virtual-bound state for the copper-rich alloys and therefore contradict the interpretation generally placed on valence band X-ray photoelectron spectroscopy (XPS) spectra for copper-palladium. Nevertheless, our first-principles calculations of the XPS spectra are in excellent agreement with recent measurements, and we discuss why this is so. Furthermore we compare our density of states at the Fermi energy with specific heat measurements.

2.1.1.16 Non-Muffin-Tin Band Theories of the Multiple Scattering Type[20] - J. S. Faulkner

Numerical calculations on an empty-lattice model are used to illustrate the fact that the greatest improvement in the accuracy of the eigenvalues for a non-muffin-tin potential comes from the inclusion of the off-diagonal elements of the scattering matrices. The eigenvalues calculated with a recently proposed formulation are seen to be no better than those obtained with other schemes that ignore near-field corrections.

2.1.2 Ordering in Alloys - G. M. Stocks, W. H. Butler, and D. M. Nicholson[1]

At temperatures close to, but above, their ordering temperatures most alloy systems exhibit either clustering or short-range order. Previously, in collaboration with B. L. Gyorffy,[7] we have developed a concentration

functional approach to ordering that is based on the KKR-CPA. On the basis of this theory we were able to obtain an expression for the band structure contribution to the short-range-order (SRO) diffuse scattering in alloys from which we concluded that diffuse scattering maxima observed in electron and X-ray diffuse scattering experiments on copper-rich Cu_cPd_{1-c} alloys in the solid solution phase resulted from concentration waves, the wavelength of which is determined by a Fermi-surface spanning vector. This year we have used the theory to calculate actual SRO diffuse scattering maps for a number of alloys.

In Fig. 2.1.2 we show SRO diffuse scattering patterns for a $Cu_{75}Pd_{25}$ disordered alloy calculated on the basis of the concentration functional theory. Also shown in Fig. 2.1.2 is the measured diffraction pattern of Ohshima and Watanabe.[21] The calculated results exhibit all of the structure seen in the electron diffuse scattering experiment with the exception of the main Bragg maxima associated with the underlying fcc lattice, which is not included in our calculation. Our full diffuse scattering intensity calculations confirm our earlier explanation that the SRO is Fermi-surface driven. The calculated diffuse scattering pattern is calculated entirely from first principles. The required inputs were the atomic numbers of the constituents of the alloy and the crystal structure. The calculation was carried out at the experimentally observed lattice spacing.

Preliminary studies of SRO diffuse scattering from Ag_cPd_{1-c} predict that this alloy has SRO similar to that of Cu_cPd_{1-c}, but with a much lower ordering temperature. Our results offer specific predictions regarding the shape of the SRO diffuse scattering and its temperature dependence. These predictions are being checked by X-ray diffuse scattering using synchrotron radiation.

In collaboration with A. Gonis,[22] A. J. Freeman,[22] P.E.A. Turchi,[23] and D. deFontaine,[23] we are also developing two other approaches to studying ordering in alloys that are aimed at obtaining pair and multiple atom interaction potentials for alloys. Again both methods build on the KKR-CPA method for treating the homogenous disordered system. In the embedded cluster method (ECM) interaction potentials are calculated from the energies associated with specific local atomic configurations embedded

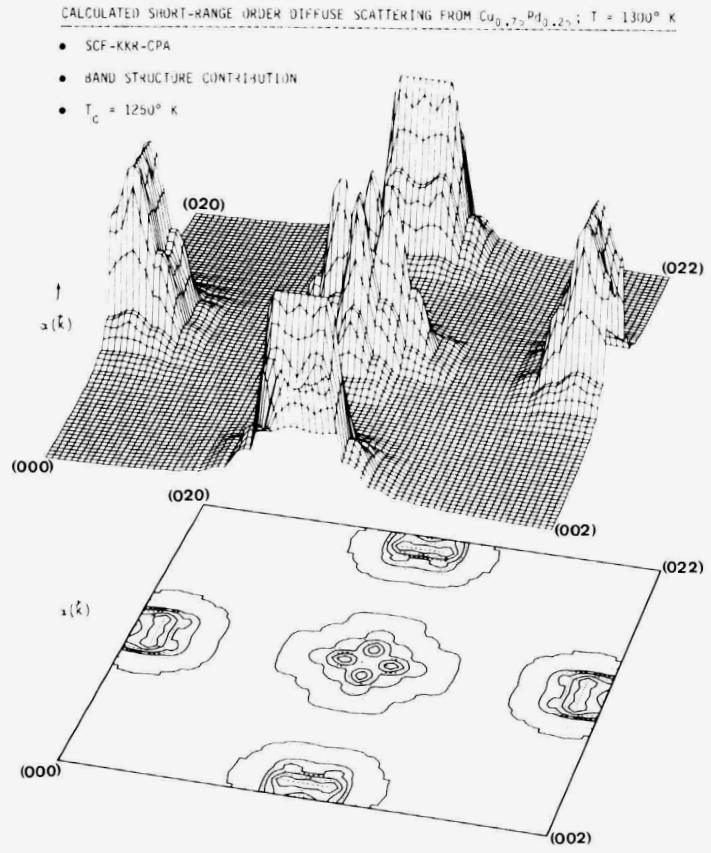

(*a*)

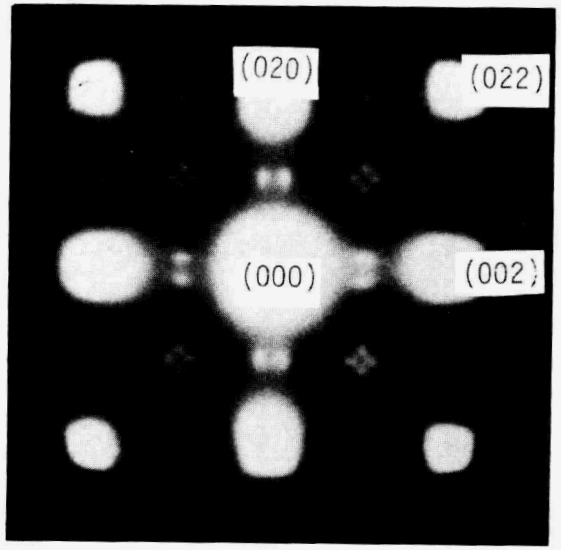

(*b*)

Fig. 2.1.2. Calculated and measured diffuse scattering for a $Cu_{0.75}Pd_{0.25}$ alloy. (*a*) Calculated short-range-order diffuse scattering contour (lower) and relief (upper) maps for T = 1300 K using the Gyorffy-Stocks concentration function theory. The part of reciprocal $(\vec{k})$-space for which the calculation was performed is defined by the $\vec{k}$-vectors specifying the corners of the plots. (*b*) Measured electron defraction patterns of Ohshima and Watanabe for $Cu_{0.75}Pd_{0.25}$ quenched from 1000 K. Diffuse scattering spots corresponding to those calculated and shown in (*a*) are seen between the bright Bragg maxima spots that correspond to the underlying fcc lattice (these Bragg peaks are not included in the calculation). The full electron diffuse scattering pattern shown in (*b*) can be obtained from the calculated pattern by repeating four times. The four-fold diffuse scattering pattern about the (011) superlattice point and the streaking close to (001) are seen clearly in both theory and experiment.

in an otherwise random alloy. This method is based on our earlier work on calculating the electronic structure of compact clusters.[24] In the generalized perturbation method (GPM), pair and multiple atom interchange potentials are calculated directly. Their calculation requires the results of a KKR-CPA calculation as well as the inter-site Green function for the effective CPA medium. Preliminary results for the Pd_cV_{1-c} alloy system for the first four nearest neighbor interchange potentials indicate that they are decreasing in magnitude with increasing distance. However, the distance at which they become negligibly small has not yet been determined.

The pairwise interchange potentials obtained by using the ECM and GPM methods will be used with the cluster variation method (CVM) for treating the statistical mechanics of alloy configurations to predict alloy phase diagrams.

2.1.2.1 First Principles Approach to the Calculation of Short-Range Order in Metallic Alloys[25] – G. M. Stocks, J. Wadsworth[7] and B. L. Gyorffy[7]

The modern first-principles theory of the electronic structure of random alloys is reviewed, and concepts that allow the depiction of band structures and Fermi surfaces of random alloys are introduced. A new parameter-free theory of the forces that drive ordering in metallic alloys is described. It is shown that observed concentration-dependent diffuse-scattering spots seen in X-ray and electron-scattering experiments in many alloy systems (e.g., Cu_cPd_{1-c}, Cu_cPt_{1-c}) result from concentration waves whose wavelength is determined by spanning vectors connecting parallel sheets of the alloy's Fermi surface.

2.1.2.2 First-Principles Theory of Fermi-Surface Driven Concentration Waves in Cu_cPd_{1-c} Alloys[26] – G. M. Stocks, J. Wadsworth,[7] and B. L. Gyorffy[7]

Recently a number of alloy systems have been identified that show characteristic concentration-dependent diffuse scattering resulting from short-range order in the nominally disordered state. Copper-palladium alloys quenched from the disordered phase show a four-fold pattern of diffuse intensity around the 110 and equivalent reciprocal lattice positions.

In these alloys the separation m between the diffuse maxima varies approximately linearly with concentration.

By adapting a density-functional approach (developed for treating the statistical mechanics of classical liquids) to a lattice gas model of alloy configurations, we have been able to develop a mean-field theory of ordering in alloys. The method is based on the KKR-CPA method for treating the underlying electronic structure. Within our theory, once a KKR-CPA calculation of the electronic structure has been performed, all of the quantities necessary for the evaluation of the diffuse intensity, $\alpha(\vec{k})$, are available. We display contour maps of $\alpha(\vec{k})$ for two Cu_cPd_{1-c} alloys having $c = 0.75$ and $c = 0.60$ calculated on the basis of our theory. The results are in good agreement with experimental electron diffraction patterns.

2.1.2.3 First-Principles Calculations of Short-Range-Order Diffuse Scattering: Fermi-Surface Driven Concentration Waves in Cu_cPd_{1-c} Alloys[27] – J. Wadsworth,[7] B. L. Gyorffy,[7] and G. M. Stocks

A brief review of the current standing of the first-principles Korringa-Kohn-Rostoker coherent-potential approximation (KKR-CPA) theory of the electronic structure of random substitutional alloys is given. A concentrational function theory of short-range ordering (SRO) is reviewed. Results for the SRO diffuse-scattering patterns for $Cu_{0.75}Pd_{0.25}$ and $Cu_{0.60}Pd_{0.40}$ alloys are presented. The positions of the diffuse maxima are in excellent agreement with experiment. It is shown that this position is determined by the length of a Fermi-surface spanning vector connecting well-defined flat, parallel sheets of the alloy's "Fermi surface."

2.1.2.4 Short-Range Order in Ag_cPd_{1-c} Alloys: A Prediction of Fermi-Surface Driven Concentration Waves[28] – D. M. Nicholson,[1] G. M. Stocks, J. Wadsworth,[7] and B. L. Gyorffy[7]

We have used the first-principles KKR-CPA-based theory of short-range order (SRO) diffuse scattering formulated by Gyorffy and Stocks to calculate SRO diffuse scattering maps for Ag_cPd_{1-c} alloys in the disordered phase. We predict the existence of Fermi surface driven concentration waves similar to those found in Cu_cPd_{1-c} alloys. We show how the diffuse

scattering evolves in concentration and temperature. For $Ag_{0.5}Pd_{0.5}$, the expected transition temperature is 575 K, which is suggestive that kinetics will allow the SRO to be observed experimentally by using modern anomalous scattering techniques based on synchrotron radiation.

2.1.2.5 Effective Interactions in Substitutionally Disordered Alloys: Tight Binding Approximation[28] – P. E. A. Turchi,[23] D. deFontaine,[23] G. M. Stocks, W. H. Butler, A. Gonis,[22] and A. J. Freeman[22]

We report the results of calculations of concentration-dependent effective pair interactions in substitutionally disordered alloys based on an average medium described in the coherent potential approximation. These calculations were carried out in the tight binding scheme using both the generalized perturbation method and the embedded cluster method. The interactions so obtained are used with the cluster variation method to calculate phase diagrams for model alloy systems. We discuss the effects of multiplet interactions and the need for more realistic Hamiltonians.

2.1.3 Transport in Metals and Alloys – W. H. Butler, J. C. Swihart,[29] G. M. Stocks, and D. M. Nicholson[1]

During the reporting period we have implemented a new theory for calculating the residual electrical resistivity of random alloys. The new theory was developed in the Metals and Ceramics Theory Group and is based on the Korringa-Kohn-Rostoker coherent-potential approximation (KKR-CPA). It is an advance over previous theories in that it can be applied even when the energy bands of the alloy are obliterated by disorder. It properly includes "vertex corrections," and it reduces to the semiclassical Boltzmann equation when the disorder is sufficiently weak that the energy bands are well defined.

Calculations of the electrical resistivity of copper-zinc alloys are shown in Fig. 2.1.3. The agreement between theory and experiment is excellent considering that the theory contains no adjustable parameters. We also obtain good agreement with the experimentally determined diffusion thermopower. Vertex corrections are very important in this system. Calculated resistivities of silver-palladium alloys and nickel-molybdenum alloys are also in good agreement with experiment.

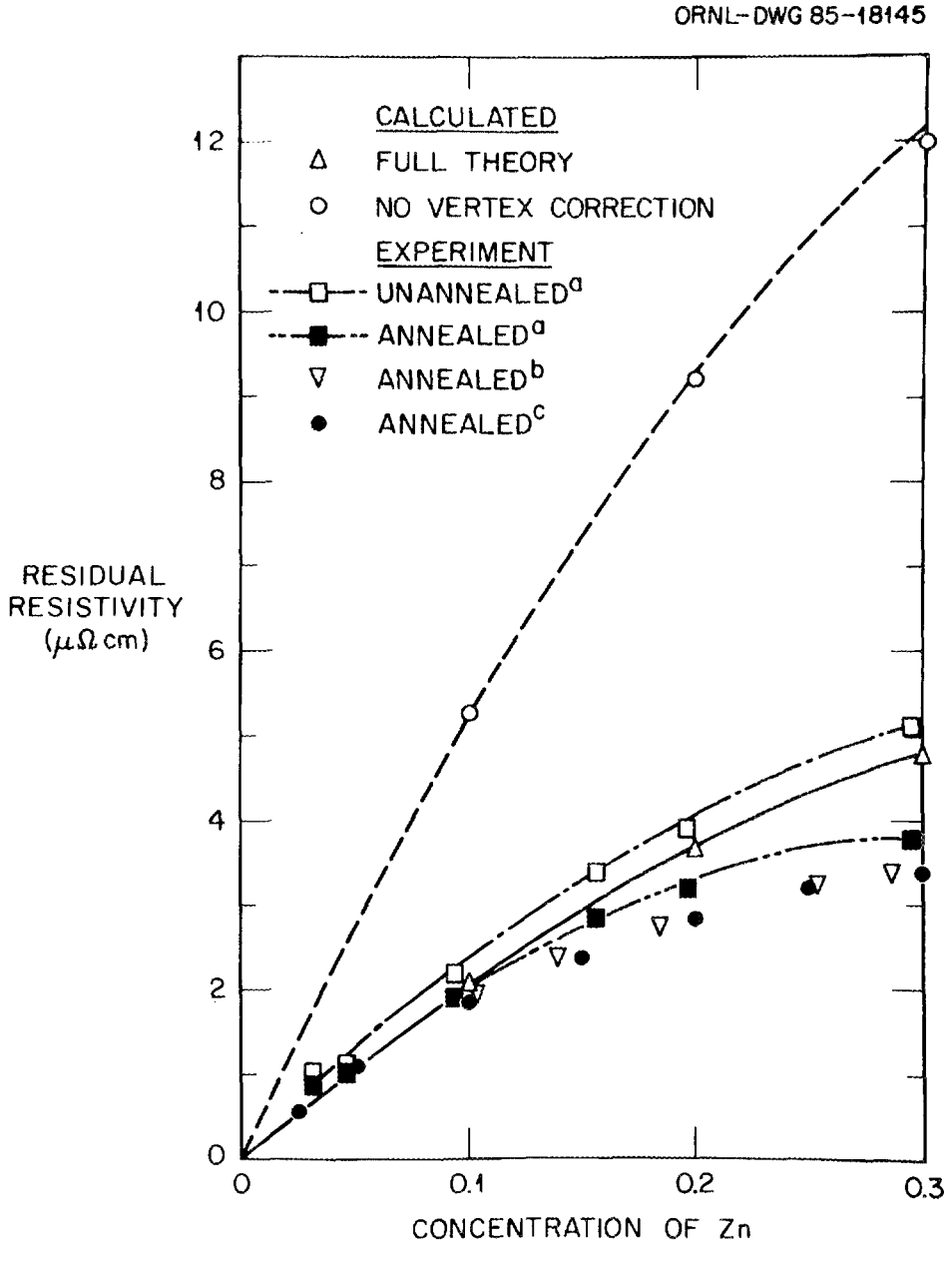

Fig. 2.1.3. Residual electrical resistivity for copper-zinc alloys as a function of concentration. The open triangles are our calculated results using the full theory. The solid line is the Nordheim relation $[Ac(1 - c)]$ with A chosen so the curve goes through the calculated result at $c = 0.1$. The open circles are our calculated resistivities with no vertex corrections. The dashed curve is the Nordheim relation going through the $c = 0.1$ result for no vertex correction. Experimental data are open squares with dash-single-dot curve (unannealed wires) and black squares with dash-double-dot curve (annealed wires). Other experimental data are open inverted triangles and black circles, both sets on annealed wires.

We are currently using the new theory to investigate a phenomenon called "resistivity saturation," which has evoked much discussion and conjecture during recent years. This phenomenon consists of the observation that the resistivity of a metal or metallic alloy seldom exceeds a value of approximately 200 micro-ohm centimeters no matter how much it is disordered. Preliminary results indicate that resistivity saturation is a natural consequence of the breakdown of the band picture in alloys.

During the reporting period we continued our calculations of the electron-phonon interaction in metals by using the rigid-muffin-tin approximation. Recently completed calculations for tantalum give extremely good agreement with the temperature-dependent electrical resistivity. We also collaborated with researchers at other institutions on studies of electromigration in metals and electron scattering rates in cadmium.

2.1.3.1 Theory of Electronic Transport in Random Alloys: Korringa-Kohn-Rostoker Coherent-Potential Approximation[30] - W. H. Butler

The KKR-CPA is a powerful and versatile tool for calculating the single-particle properties of disordered alloys. Here this technique is extended to transport properties. The formalism is based on the one-electron Kubo formula. It yields correct results in the limits of weak scattering or low concentration, i.e., the solution to the Boltzmann equation including vertex corrections. Transport coefficients can also be easily evaluated in the strong-scattering, high-concentration regime where the Boltzmann equation is not valid. The structure of the formalism is displayed by applying it to a one-dimensional muffin-tin model alloy.

2.1.3.2 Conductivity and Thermopower of Cu-Zn and Ag-Pd Random Alloys[31] - J. C. Swihart[29] and W. H. Butler

We have carried out the first calculations based on a rigorous one-electron theory[30] of the electrical conductivity and electron diffusion thermopower for both copper-rich zinc (α brass) and silver-palladium random alloys. We have included vertex corrections, and the results should be valid for strong as well as weak scattering. Our calculated copper-zinc residual resistivities as a function of concentration fall slightly

below experimental results for unannealed wires (which probably have additional dislocation scattering) and slightly above results for annealed wires (which probably have some short-range order). Vertex corrections are extremely important. Our agreement with experiment is excellent for the silver-rich end of the silver-palladium system. For the palladium-rich end, higher ℓ values will have to be included; we are in the process of doing that.

2.1.3.3 Saturation of Resistivity in Metallic Alloys[31] – W. H. Butler and J. C. Swihart[29]

We have calculated the electrical resistivity of several highly resistive alloy systems by using a theory of transport[30] based on the KKR-CPA. The results of these first-principles calculations, which use no adjustable parameters, are in good agreement with experiment. We have also investigated model alloy systems in which the potentials of the alloy constituents are adjusted so that the strength of the alloy scattering can be adjusted at will. The saturation of the resistivity of metals in the range 150 to 200 micro-ohm centimeters can be understood very simply in terms of the theory of ref. 30.

2.1.3.4 Resistivity of Alloys[32] – W. H. Butler

The problem of calculating the electrical resistivity of metals and alloys is briefly reviewed, and a new theory for the transport properties of random alloys is presented. The new theory is based on the KKR-CPA and allows the calculation of the transport coefficients of real alloys from first principles without the need for adjustable parameters. It reduces to the Boltzmann equation when the energy bands are well defined, but it is also applicable when the electronic mean free path is so short that the energy bands can no longer be defined.

2.1.3.5 Is It Possible to Calculate Thermal Conductivities of Metals and Alloys from First Principles?[33] – W. H. Butler

In a metal or alloy, heat is carried by electrons and phonons. Both carriers are scattered by electrons, phonons, and compositional disorder. Much progress has been made in recent years in calculating electron-phonon, phonon-electron, electron-disorder, and phonon-disorder

scattering. Progress can and probably will be made in our ability to calculate phonon-phonon scattering. The current state of the art in first-principles calculations of the transport properties of real metals and alloys is reviewed, and prospects for improvements are assessed.

2.1.3.6 Electron-Phonon Interaction Effects in Tantalum[34] –

A. Al-Lehaibi,[35] J. C. Swihart,[29] W. H. Butler, and F. J. Pinski[8]

The results of calculations of a number of electron-phonon interaction effects for tantalum are presented. The calculations are based on Korringa-Kohn-Rostoker energy bands, Born-von Kármán phonons, and the rigid-muffin-tin approximation for the electron-phonon interaction. The calculated Eliashberg spectral function α^2F is compared with the earlier tunneling data of Shen and the proximity tunneling data of Wolf et al. We find, as in the case of niobium, that the calculated and tunneling transverse-phonon peaks agree well but the tunneling longitudinal-phonon peak is suppressed compared with our calculated result. We find a value for the electron-phonon coupling parameter $\lambda = 0.88$. We present calculated phonon linewidths along various symmetry directions. The transport spectral function, $\alpha^2_{tr}F$, is determined, and from this the temperature dependence of the electrical resistivity due to phonon scattering is calculated in the lowest-order variational approximation. The point-contact spectral function of Kulik, $G(\omega)$, is determined and compared with $\alpha^2F(\omega)$.

2.1.3.7 Suggested Mechanism for Temperature Dependence of Orbitally Averaged Fermi-Surface Scattering Rates in Cd[36] –

W. E. Lawrence,[37] W. Chen,[29] and J. C. Swihart[29]

Electron-phonon scattering leads naturally to cubic and exponential $\exp(-\theta/T)$ temperature dependences of quasiparticle scattering rates at low temperatures. We describe a mechanism by which a quadratic dependence can arise in orbital averages without necessarily appearing in point rates anywhere on the orbit. The estimated magnitude agrees with recent radio frequency size effect data in cadmium. We predict that cubic or exponential behavior should be recovered at temperatures below about 1 K.

2.1.3.8 Calculations of the Driving Force of Electromigration in hcp Metals: Zn, Cd, Mg[38] – L. Lou,[29] W. L. Schaich,[29] and J. C. Swihart[29]

By using a pseudopotential, weak scattering formalism we calculate the driving force for electromigration by the vacancy mechanism in the hcp metals zinc, cadmium, and magnesium. The general formula is evaluated in a succession of approximate models to illustrate the influence of different physical effects. The final results are compared both with the experimental data and with a previous evaluation for zinc. Our form factors, which have been fit to low-temperature data and then scaled to account for volume changes near the melting point, yield an effective valence for the wind force of about twice the experimental value and only in qualitative agreement with the observed anisotropy. Possible resolutions are discussed.

2.1.3.9 Electrical Resistivity and Thermopower of Copper-Zinc Alloys[39] – J. C. Swihart,[29] W. H. Butler, and G. M. Stocks

Results of numerical calculations of the electrical resistivity and thermopower of copper-rich random alloys with zinc are presented. Our theoretical model, reported earlier by Butler, uses a charge self-consistent KKR-CPA. The calculations are valid for strong as well as weak scattering, and, for the first time, vertex corrections are included. Excellent agreement is obtained with experiment for the resistivity. Our calculations also agree with experiment for the electron-diffusion contribution to thermopower from solute scattering.

2.1.4 Theory of Magnetism in Metals and Alloys – G. M. Stocks and D. M. Nicholson[1]

In collaboration with B. L. Gyorffy,[7] J. B. Staunton,[40] F. J. Pinski,[8] and D. D. Johnson[7] we are studying the finite temperature magnetic state of the 3d-transition metal magnets within the framework of the first-principles disordered local moment (DLM) theory that we have developed previously. In this theory local moments are associated with each site in the metal. At T = 0 K, in the ferromagnetic state, the moments are aligned. As the temperature increases their orientations are

increasingly randomized by thermal fluctuations. In the paramagnetic state there is no longer a macroscopic moment, but there may still be disordered local moments associated with each site.

The DLM state is treated by using a spin-polarized local density functional KKR-CPA theory. On the basis of these calculations we are able to make specific predictions about the electronic stucture that can be checked experimentally, to calculate such quantities as the Curie temperature and the magnetic susceptibility, and to study the nature of the magnetic correlations that exist at finite temperature. The theory has yielded finite local moments above T_C for iron, nickel, and cobalt. For iron it also gave a good value for the T_C and a Curie-Wiess susceptibility

This year we have used the DLM theory to study the magnetic correlations in fcc iron in the paramagnetic state and to study the paramagnetic state of chromium. For paramagnetic fcc iron we find that as the lattice parameter is reduced there is a transition from a high moment state in which the magnetic correlations are ferromagnetic to a low moment state in which the correlations are antiferromagnetic.

For chromium we have not been able to find a stable DLM state for any lattice spacing within a range from 97.5 to 107.5% of the experimental lattice spacing. It thus appears that the nature of the spin correlations in paramagnetic chromium and the origins of the "local" moment formation in the paramagnetic state are qualitatively different from those of the late 3d-magnets. This may not be altogether suprising because the ground state of chromium is antiferromagnetic while the late 3d-magnets are ferromagnetically aligned.

In collaboration with F. J. Pinski[8] and D. D. Johnson[7] we have further developed the spin-polarized KKR-CPA method for treating metallic alloys that are ferromagnetic. We have extended the theory for calculating the configurationally averaged total energy and pressure to the spin-polarized case and have implemented this theory in our computer codes. This code now allows us to treat the ground state properties of a number of metallurgically interesting alloy systems that have ferromagnetic ground states within a sound theoretical framework.

2.1.4.1 A First-Principles Theory of Ferromagnetic Phase Transitions in Metals[41] – B. L. Gyorffy,[7] A. J. Pindor,[42] J. Staunton,[40] G. M. Stocks, and H. Winter[4]

On the basis of a spin-polarized density functional description of the electrons, we develop a "mean-field" theory of magnetic phase transitions in metals. The one-electron-like finite-temperature Schrödinger equation is solved, formally, for random orientations of local moments, and the corresponding grand potential is used in a statistical mechanics of the spin configurations. This latter, in the mean-field approximation, requires the knowledge of the electronic grand potential averaged over various ensembles of such "spin" configurations. These averages are carried out with the help of the KKR-CPA method for dealing with electrons in random potential fields. Then, the whole procedure is made self-consistent on the average.

The theory determines the local moment, $\bar{\mu}$, the Curie temperature, T_C, and the susceptibility $\chi(q,T)$ in addition to the electronic structure at finite temperatures without adjustable parameters. We illustrate the method by explicit calculations for iron. The local moment is found to be 1.9 μ_B above T_C, and our preliminary estimate of T_C is 1250 K.

2.1.4.2 Ferromagnetism in Metals at Finite Temperatures[43] – B. L. Gyorffy,[7] J. B. Staunton,[40] and G. M. Stocks

The conventional spin-polarized band theory is known to give a reasonable description of the magnetic ground states of metals. Here it is generalized to finite temperatures. The resulting theory is the first "first-principles" theory of the ferromagnetic phase transition in metals. It is a mean-field theory. For iron we find T_C = 1250 K and $\chi^{-1}(\vec{q} = 0)$ follows a Curie-Weiss law. We also report on our results for the wave-vector dependent susceptibility $\chi(\vec{q})$ which is a measure of magnetic short-range order above T_C.

2.1.4.3 The "Disordered Local Moment" Picture of Itinerant Magnetism at Finite Temperatures[44] – J. Staunton,[40] B. L. Gyorffy[7], A. J. Pindor,[42] G. M. Stocks, and H. Winter[4]

With an emphasis on a realistic description of the underlying electronic structure, we discuss the disordered local moment (DLM) picture of metallic magnetism. Its formation, based on first-principles

foundations of the spin density functional approach, is briefly derived. Within the context of this theory, we place our previous, self-consistent calculations of local moments in the paramagnetic state for several transition metals and describe some details of the electronic structure which may ultimately be compared with modern experimental measurements. Finally the theory and physical picture for the wave-vector-dependent, static spin susceptibility, $\chi(q,T)$ above the Curie temperature, T_C, is outlined, and the degree of short range magnetic order driven by the DLM electronic structure is estimated. We illustrate the theory by explicit calculations for iron and preliminary calculations for nickel. Curie-Weiss behavior is found for $\chi(0;T)$ of both metals, and Curie temperatures are 1260 K for iron and 225 K for nickel. While the calculations for $\chi(q;T)$ are broadly consistent with the initially imposed DLM state, their interpretation for nickel is rather different from that for iron. A comparison with quasi-elastic neutron scattering measurements is briefly made.

2.1.4.4 On the Theory of Ferromagnetism of Transition Metals at Finite Temperatures[45] – G. M. Stocks, B. L. Gyorffy,[7] J. Kollar,[46] A. J. Pindor,[42] J. Staunton,[40] and H. Winter[4]

The nature and origin of magnetic order in metals is one of the most elusive problems in solid state physics. Fifty years after the pioneering work of Bloch (1929), Mott (1935), Stoner (1936), and Slater (1936) it is still not as well understood as the apparently more esoteric phenomenon of superconductivity (Parks 1969). While this subject has never lacked devotees, at the moment we are witnessing a particularly active period due to the fact that recent progress seems to have brought the possibility of a fairly complete microscopic quantitative theory within sight. The purpose of these lectures is to sketch the outlines of the emerging picture and the prospects for doing realistic first-principles calculation for metallic magnets at finite temperatures.

2.1.4.5 Moment Formation and the Electronic Structure of Disordered fcc Alloys: Fe_cNi_{1-c} and $Mn_{25}Ni_{75}$ (ref. 47) – F. J. Pinski,[8] D. D. Johnson,[7] B. L. Gyorffy,[7] D. M. Nicholson,[1] and G. M. Stocks

By using the self-consistent spin-polarized KKR-CPA we have performed, for a range of volumes, calculations of the electronic structure of disordered fcc $Mn_{25}Ni_{75}$ and Fe_cNi_{1-c} alloys ($0.75 \leq c \leq 0.25$). For Fe_cNi_{1-c},

the average magnetic moment lies close to the straight section of the Slater-Pauling curve as long as the majority d-band is filled. For the iron-rich alloys, as the volume is decreased, the Fermi energy is pulled into the sharp leading edge of the majority d-band causing the moment to fall dramatically, similar to the scenario for fcc iron. For $Mn_{25}Ni_{75}$, the moment changes more gradually, due to it having a less peaked density of states. Some ramifications of these observations are discussed.

2.1.4.6 Ferromagnetism Versus Antiferromagnetism in fcc Iron[47] – D. D. Johnson,[7] B. L. Gyorffy,[7] F. J. Pinski,[8] J. Staunton,[40] and G. M. Stocks

Using the disordered local moment (DLM) picture of itinerant magnetism, we have calculated the temperature and volume dependence of the magnetic moment and spin-spin correlation for fcc iron in the paramagnetic state. These calculations are based on the parameter-free, first-principles approach of local spin density functional theory. The coherent potential approximation is used to treat the disorder associated with the random orientation of the local moment.

In the DLM state, as the lattice parameter is reduced, there is a transition from a high-moment state to a low-moment state with the correlation between the moments changing from ferromagnetic to antiferromagnetic, respectively.

2.1.4.7 Electronic Structure of Metallic Ferromagnets above the Curie Temperature[48] – J. Staunton,[40] B. L. Gyorffy,[7] A. J. Pindor,[42] G. M. Stocks, and H. Winter[4]

We describe the electronic structure of iron and nickel above their Curie temperature in their disordered local moment states as a function of wave vector $\vec{k}$ and energy ϵ. In particular, we calculate the Bloch spectral function, $\bar{A}_B(\vec{k},\epsilon)$, averaged over the orientational configurations of the local moments, at selected points in the brillouin zone to determine the shape and smearing of the Fermi surface. We find that bcc iron, with a local moment $1.9\mu_B$, can show an exchange splitting at some points while in other regions of the brillouin zone no such splitting occurs. For comparison we also studied fcc iron, which also supports a substantial local moment. We find that it has similar features, but the smearing of the bands is more pronounced. On the other hand the electronic structure

of nickel is quite different and shows no such local exchange splitting. Although nickel has a small local moment, $0.2\mu_B$, all the bands are virtual crystal-like and sharp. The resulting picture for the electronic structure of nickel is that of a smeared Stoner-Wohlfarth model.

2.1.5 Total Energy Studies of Atomic Clusters – G. S. Painter, F. W. Averill,[49] and F. W. Kutzler[50]

The physical and chemical properties of materials depend ultimately on the electronic interactions among the constituent atoms on a microscopic (atomistic) level. In this research program, electronic structure and total energy calculations are carried out for atomic clusters in order to establish a direct connection between the atomistic bonding properties and macroscopic phenomena. This effort divides into two stages.

1. The development of a theoretical base and computational techniques accurate enough to treat the systems of interest. The density functional formalism serves as the starting point, and our contributions to deriving refined exchange-correlation potentials for calculations in the local spin density approximation (LSDA) were recently reviewed[51] by J. Callaway and N. H. March. Theoretical techniques (the augmented Gaussian orbital approach) to implement the LSDA in its complete form were further extended to go beyond local functionals in collaboration with F. W. Kutzler.[50] This new scheme permits the study of nonlocal exchange-correlation functionals – a basic theory problem of intense interest among workers in density functional theory. Our cluster techniques require only the nuclear charge of each constituent atom of the cluster as input – the ground state geometry, total energy, and other electronic properties are determined in a wholly self-consistent spin-polarized treatment. This capability is crucial to the successful calculation of total energy surfaces.

In another development of major importance to this stage of our effort (and to the field in general), in collaboration with F. W. Averill,[49] we derived procedures to directly calculate the vector force field in atomic clusters (see Sects. 2.1.5.3–2.1.5.5). By directly differentiating the LSD total energy (with respect to nuclear coordinate), expressions were obtained for each individual orbital's contribution to

the total force on a nucleus. Summed over all occupied states, a total gradient force is determined equivalent to the negative derivative of the total-energy hypersurface at a prescribed point in the $3N$ (where N is the number of atoms) parameter space of nuclear coordinates. Knowledge of the force on each atom of the cluster is of great value in mapping out the $3N$ dimensional adiabatic energy surface. Since the forces directly provide the gradient of the energy surface in the space of nuclear positions, the number of independent total energy evaluations required is reduced by a factor of the order of $3N$. In addition to this computational advantage, the vector force field also provides a useful characterization of system behavior in readily understood terms. This additional capability in our theoretical effort offers great promise to advance our understanding of bonding at the microscopic level.

2. The second stage of our program involves calculations for systems of interest and relation of results to problems of interest. Activities in this stage were divided into two areas: (1) calculations for molecules and small metal clusters, which can be produced in laser vaporization molecular beam experiments, and (2) studies of atomic clusters chosen to simulate some region of a bulk material where localization effects can be expected to be important.

In the first study area (1 above), the Cr_2 dimer is a very difficult system to treat theoretically because the high spin ($3d^54s^1$) chromium atoms form a $^1\Sigma_g^+$ ground state dimer. Our study[52] of this dimer (Fig. 2.1.4) revealed an interesting bond mechanism characterized by a subtle balance of site-localized spin polarization stabilization and delocalized molecular bond (charge overlap) stabilization, which are competing effects varying with atom separation in the dimer. We also published results from the first LSDA calculation of the gradient force in a transition metal dimer[53] identifying a compensation effect between core polarization and valence hybridization in the total force. More recently, we have carried out force calculations for the entire first-row dimer series, identifying the relationship between orbital forces and relative stabilities of members of the series. We also established the concept of static and dynamic orbital forces in density functional theory and showed the relationship to corresponding forces in Hartree-Fock theory (see Sect. 2.1.5.5). We recently carried out the first complete

ORNL DWG 85-18448R

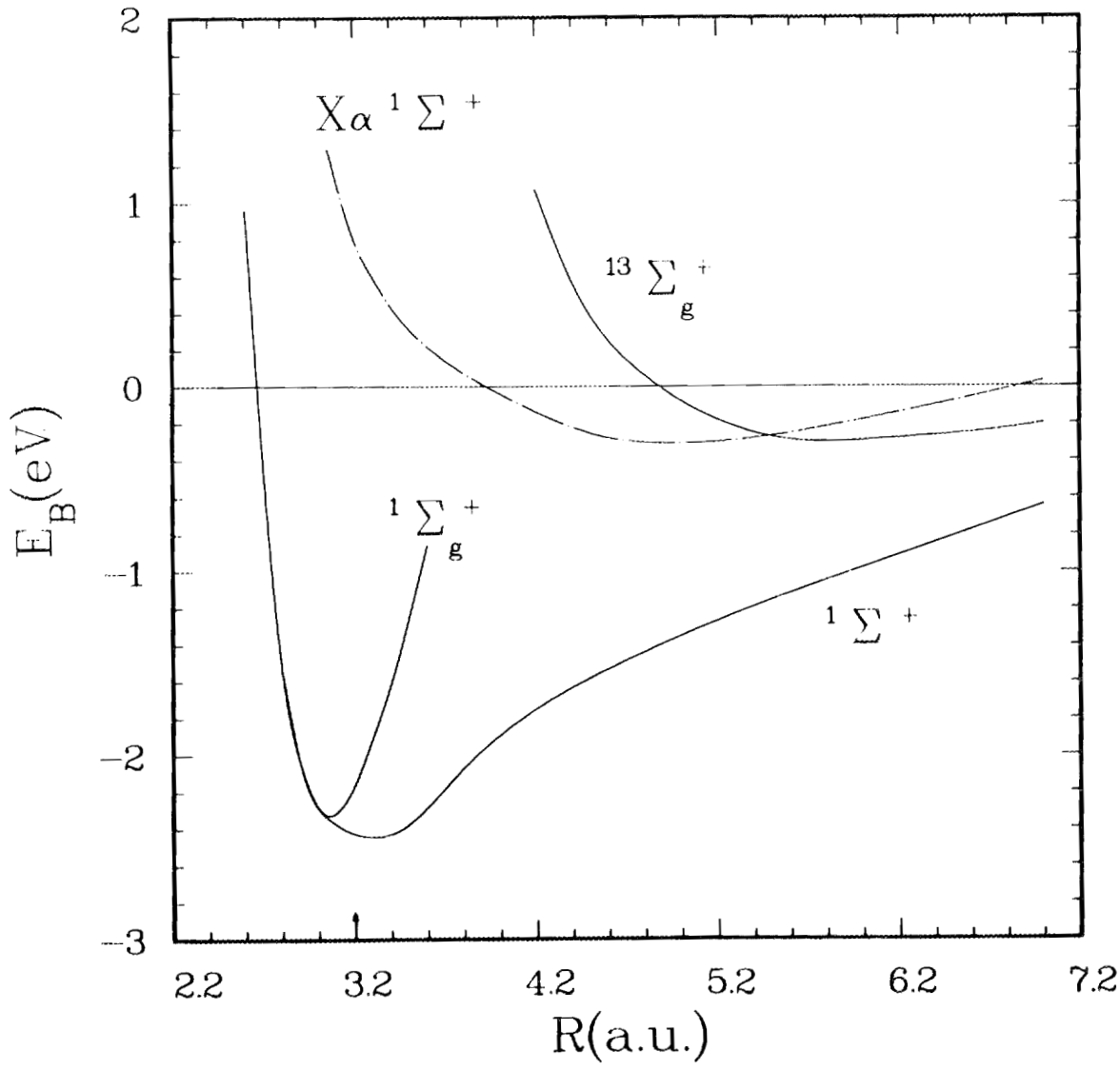

Fig. 2.1.4. Potential energy curves for various symmetry states of the Cr_2 dimer as functions of atom separation (bond length). The high spin molecular orbital state $^{13}\Sigma_g^+$ is associated with a weakly bound dimer of large bond length. An X_α exchange-correlation approximation yields a similar description for a symmetry-broken treatment ($X_\alpha\,^1\Sigma^+$ curve). The symmetry-broken description in a more refined treatment of the spin-polarization energy ($^1\Sigma^+$) agrees very well with experimentally determined equilibrium bond length and vibrational frequency, while a molecular orbital description ($^1\Sigma_g^+$) fails to give a proper dissociation path.

calculations which go beyond the local density approximation in the gradient scheme of Langreth and Mehl[54] for some first-row dimers (see Sect. 2.1.5.6). Results will be used to assess the importance of nonlocal corrections and to define further improvements to the basic theory. Calculations have been carried out within the LSDA for some small transition-metal clusters. Ionization potentials compare favorably with measurements made in metal cluster molecular beam experiments.

In the second area of activity (2 above), calculations were carried out for tetrahedral and octahedral alkali and transition-metal clusters representative of the hole sites in bcc and fcc metals. The calculated binding energies and equilibrium geometries show a close correspondence with bulk calculations (the near-neighbor bond length is contracted approximately 7% in the cluster). Studies have been started to explore the effects of light impurities and metalloids on the properties of the bare clusters. For hydrogen in nickel, the calculated lattice expansion (~3%) is consistent with experimental data. The calculation of the gradient force field serves to directly determine the impurity effect on cluster geometry (see Sect. 2.1.5.7). The accuracy of these calculations is sufficient to determine a binding energy per atom (in the case of Cu_6) of approximately 2 eV out of a calculated total energy greater than 267,000 eV! Similarly, the force is accurately calculated in a delicate balance of attractive and repulsive components each of approximate magnitude 3000 eV/bohr.

These activities form part of our program goal to understand the role of impurity bonding on the cohesive properties of metal atoms at defects and interfaces.

2.1.5.1 The Bonding Properties of Transition Metal Clusters Within the Local Spin Density Method[55] – G. S. Painter

There is growing recognition in the field of materials science of the important role of the chemistry of small concentrations of impurities in determining the macroscopic physical properties of metals and alloys. In this regime atomic cluster models are useful for electronic structure studies to understand the atomic-level microchemical interactions occurring at impurity sites. The local spin density approximation (LSDA) affords a reasonable theoretical basis for calculations on such complex

systems, balancing completeness of treatment against calculational tractability. More importantly, the LSDA provides a simple conceptual framework for understanding materials properties. The development of a variational technique for solving the density functional equations and evaluating the cluster force field is described. Applied to well-characterized diatomics, the high precision results permit critical assessment of the LSDA. Studies are reported on transition-metal clusters where the predictive capability of the LSDA provides understanding of their bonding properties.

2.1.5.2 Density Functional Description of Molecular Bonding Within the Local Spin Density Approximation[52] – G. S. Painter

The description of the ground state properties of solids has been greatly advanced through the density functional theory applied in the LSDA. The range of validity of the LSDA has been found to encompass even the small molecule regime. Representative results are reviewed for the first-row dimers, with particular focus on a detailed comparison of molecular bonding of the Be_2 molecule as described in many-electron and LSDA theories. The success of the LSDA in applications to inhomogeneous systems is discussed in terms of the known properties of the exchange-correlation hole. Bonding in the transition-metal dimer, Cr_2, as described in the LSDA is discussed and related to other studies.

2.1.5.3 Orbital Forces in the Density-Functional Formalism: Application to the Copper Dimer[53] – F. W. Averill[49] and G. S. Painter

The force field in an atomic cluster, given as the direct gradient of the total energy in the density-functional formalism, is expressed in terms of components corresponding to the solutions of the one-particle Schrödinger equation. The resulting relationship between eigenfunctions and orbital forces provides a useful framework for analysis of the bonding in the system. The expression for the orbital force is given as the sum of a traditional Hellmann-Feynman term and an orbital derivative term which cancels the first-order error due to basis-set incompleteness. The sum of orbital forces gives the total gradient force on the nuclei in the system to essentially the same accuracy as the total-energy surface

itself. Results are reported for an all-electron calculation of the orbital forces in the copper dimer. This first local-spin density calculation of the gradient force for a transition-metal dimer represents a challenging test because of the heavy core. By the introduction of a simple screening force, an orbital cohesive force is defined which provides an interesting and useful framework for quantifying the relative contribution of the molecular orbitals to the chemical bond. The effects of core polarization and valence hybridization and their compensating influence are demonstrated in the results.

2.1.5.4 The Total Energy Hypersurface and Force Field in Transition-Metal Clusters as Calculated in the Local Spin Density Approximation[56] – G. S. Painter and F. W. Averill[49]

Results from fully self-consistent spin-polarized all-electron total-energy calculations are reported for high-symmetry clusters of transition-metal atoms using the augmented Gaussian orbital technique. For nickel clusters, spin polarization effects only a slight stabilization (~0.03 eV/atom) accompanied by a very small dilation of the cluster compared with the paramagnetic case. The forces acting on the atoms in the cluster are determined by direct calculation of the gradient of the total energy hypersurface. Analysis of the force field in terms of one-electron orbital components provides a useful framework for discussion of bonding in metal clusters.

2.1.5.5 Orbital Forces and Chemical Bonding in Density Functional Theory: Application to First-Row Dimers[46] – F. W. Averill[49] and G. S. Painter

Chemical bonding in first-row homonuclear dimers is analyzed in terms of both a static orbital force, $(-\partial\epsilon_i/\partial X_p)\psi$, and a dynamic orbital force, $-\partial\epsilon_i/\partial X_p$. The static force is the i^{th} orbital's contribution to the total Hellmann-Feynman force, whereas the dynamic force describes the change in the total force due to ionization of the i^{th} molecular state. The nature of the chemical bond in first-row dimers is observed to change with occupation of the $3\sigma_g$ level. The formalism and results are shown to be comparable to earlier Hartree-Fock studies.

2.1.5.6 Ground State Properties in Nonlocal Density Functional Theory: Application to Atoms and Diatomic Molecules[46] - F. W. Kutzler[50] and G. S. Painter

We report calculations for atoms and first-row dimers using the augmented Gaussian orbital-linear variational technique in combination with recent exchange-correlation functionals which go beyond the local spin density approximation (LSDA). We discuss implementation of the gradient corrections of Langreth and Mehl in a study of N_2 where we find a significant improvement over the LSDA for the total energy curve as a function of bond length. This system also affords an interesting case for comparison with results from calculations including the self-interaction correction. Atomic ground state energies are in good agreement with the results of Langreth and Mehl.

2.1.5.7 Local Spin Density Calculations for Transition-Metal Clusters Containing Interstitial Atoms[46] - G. S. Painter and F. W. Averill[49]

Self-consistent spin-polarized total energy calculations for high symmetry transition-metal clusters containing interstitial impurities (hydrogen and helium) have been carried out with the augmented Gaussian orbital approach in the local spin density approximation. Results for the impurity binding energy, cluster ionization potential, and ground state structural change effected by the host-impurity interaction are discussed. For hydrogen in an fcc octahedral hole site in nickel, a binding energy of 2.3 eV and cluster volume expansion of 3.3% is calculated, and the ionization potential is increased by about 0.3 eV. Results are compared with available experimental data in order to define the local bonding contribution to the microchemistry of these impurities in bulk metals.

2.1.6 Theory of Liquid and Amorphous Metals - D. M. Nicholson[1]

Our work on liquid and amorphous metals complements the Theory Group's studies of random alloys and ordered crystalline metals, making it possible to calculate the electronic properties of all phases in the binary-phase diagram. The arrangement of atoms in structurally disordered metals is described by experimentally determined pair-distribution functions. Experimental uncertainty in these functions leads to the violation of certain statistical mechanical constraints. As a result, theoretical

models of the structure have generally been used as a basis for electronic calculations. We have developed a Monte Carlo method for introducing infinitesimal changes into experimental pair-distribution functions in such a way that they obey all theoretical constraints. These improved pair-distribution functions open the possibility of investigating the changes in electronic properties resulting from the experimentally observed changes in structure due to temperature or sample history. The abstracts below illustrate these techniques and their application within the effective-medium approximation to various transition-metal systems.

2.1.6.1 Electronic Structure Calculations in Liquid and Amorphous Metals[57] – A. Chowdhary,[58] D. M. Nicholson,[1] and L. M. Schwartz[59]

We review the theoretical methods employed to describe electronic states in structurally disordered metallic systems. Substantial progress has been made in this area by using techniques based on multiple scattering theory. We focus on the way in which X-ray and neutron scattering data enter the calculation of the average electronic spectrum. Applications to molten copper and to amorphous nickel-phosphorus alloys are discussed.

2.1.6.2 Electronic Structure of Liquid-Metal Alloys[60] – D. Nicholson[1] and A. Chowdhary[58]

Electronic structure calculations within the effective-medium approximation will be used as a basis for discussion of total electronic energies in liquid-metal alloys. Experience gained in investigating the total energies of crystalline metals makes similar studies of structurally disordered metals feasible. An improved understanding of the energetics of the liquid phase will be important in the theoretical construction of high-temperature-phase diagrams.

2.1.7 Theory of Transition-Metal Aluminides – G. M. Stocks, J. S. Faulkner, and A. P. Maclin[2]

In collaboration with W. M. Temmerman[16] and P. Sterne[16] we are studying the ground state properties and electronic stuctures of the ordered nickel and iron aluminides Ni_3Al and Fe_3Al. The aim of this work is to gain a better understanding of the physical mechanisms that govern the stability of these compounds.

We are using the atomic-sphere-approximation linear-muffin-tin-orbital method to study the electronic structure of Ni_3Al and Fe_3Al in both the $L1_2$ and DO_3 structures. Ni_3Al forms in the metallurgically favorable $L1_2$ structure, while Fe_3Al forms in the metallurgically unfavorable DO_3 structure. The results of these calculations will be used as a basis for the interpretation of the results of angle-resolved photoemission experiments that are being performed by A. DasGupta (under Office of Naval Research sponsorship) in collaboration with D. Zehner of the ORNL Solid State Division.

2.1.7.1 The Electronic Structure of Transition-Metal Aluminides[61] – G. M. Stocks, A. P. Maclin,[2] and W. M. Temmerman[16]

We have performed parameter-free first-principles calculations of the electronic structure of Ni_3Al and Fe_3Al in the $L1_2$ crystal structure as well as Fe_3AlC. We find Ni_3Al to be a weak itinerant ferromagnet in apparent agreement with observation, although the precise magnitude of the magnetic moment appears to be rather sensitive to the details of the calculational procedures. If we assume Fe_3Al to be ferromagnetically ordered, our results predict that this material would be strongly ferromagnetic if it could be stabilized in the $L1_2$ structure, each iron atom having a moment little different from that of pure iron in the bcc structure. The consequence of the addition of one carbon atom per unit cell is a decrease in the equilibrium lattice spacing and the destruction of the magnetism. In the light of these calculations we comment on the reported stabilization of Fe_3Al in a $L1_2$-like structure by the addition of carbon.

2.1.7.2 Band Structure Calculations of Aluminides[62] – A. P. Maclin,[2] G. M. Stocks, and W. M Temmerman[16]

Recently considerable attention has been focused on the aluminides because of their good mechanical properties at high temperatures. Results of band theory calculations using the linearized muffin-tin orbitals techniques on the $L1_2$ structure of Ni_3Al and Fe_3Al are presented, and comments are made on the stability of Fe_3Al with carbon added. The theoretical results are compared with available experimental data.

2.1.7.3 Preliminary Study of the Thermal-Expansion Coefficients of Long-Range-Ordered Aluminides[63] – T. Leventouri,[64] O. B. Cavin, and J. S. Faulkner

The thermal expansion coefficient $\alpha(T)$ of $Ni_{76}Al_{24}$, $Ni_{70}Fe_{10}Al_{20}$, and $Ni_{67.5}Fe_{15}Al_{17.5}$ are studied experimentally between room temperature and 900 K by using X-ray diffraction. Particular emphasis is placed on the peak in $\alpha(T)$ that is found near the magnetic-ordering temperature for the alloys that contain iron.

2.1.8 References

1. Department of Materials Science and Engineering, University of Tennessee, Knoxville.

2. NovaLink, Inc., Washington, D.C.

3. Abstract of paper in *The Electronic Structure of Complex Systems*, ed. P. Phariseau and W. M. Temmerman, Plenum Press Advanced Studies Institute, New York, 1984, pp. 463–579.

4. Institut für Technische Physik, Kernforschungszentrum Karlsruhe GmbH, Karlsruhe, Federal Republic of Germany.

5. Abstract of paper accepted by *Int. J. Quantum Chem.*, March 1985.

6. Abstract of *Phys. Rev. B* 30(10), 5508–15 (1984).

7. H. H. Wills Physics Laboratory, University of Bristol, United Kingdom.

8. Department of Physics, University of Cincinnati.

9. Abstract of paper presented at American Physical Society Meeting, Baltimore, Mar. 25–29, 1985.

10. Abstract of *Phys. Rev. B* 32(6), 4204–07 (1985).

11. Abstract of invited paper presented at the Symposium of Noble Metal Alloys, 114th TMS-AIME Annual Meeting, New York, Feb. 25–27, 1985.

12. Los Alamos National Laboratory, Los Alamos, N.M.

13. Abstract of paper submitted to *Phys. Rev. Lett.*

14. Abstract of paper submitted for presentation at American Physical Society Meeting, Las Vegas, Mar. 31 – Apr. 4, 1986.

15. Abstract of paper presented at Fifth General Conference of the Condensed Matter Division of the European Physical Society, Berlin, Mar. 18–22, 1985.

16. Department of Physics, Daresbury Laboratory, Science and Engineering Research Council, Daresbury, Warrington, United Kingdom.

17. Abstract of *J. Phys. F* **14**, 2571–99 (1984).

18. Abstract of *J. Appl. Phys.* **57**(1), 3018–20 (1985).

19. Abstract of paper accepted for publication in *Phys. Rev. B*.

20. Abstract of *Phys. Rev. B* **32**(2), 1339–42 (1985).

21. K. Ohshima and D. Watanabe, *Acta Crystallogr. A* **25**, 520 (1973).

22. Department of Physics, Northwestern University, Evanston, Ill.

23. Department of Materials Science and Mineral Engineering, University of California, Berkeley.

24. A. Gonis, G. M. Stocks, W. H. Butler, and H. Winter, *Phys. Rev. B* **29**, 555 (1984).

25. Abstract of paper presented at the Materials Research Society Meeting, Boston, Nov. 26–30, 1984.

26. Abstract of extended abstract published in *Proceedings of Symposium on Alloy Phase Stability*, ed. L. H. Bennett, B. C. Geissen, and T. B. Massalski, Materials Research Society, Nov. 1984, p. 15.

27. Abstract of paper in *High Temperature Alloys: Theory and Design*, ed. J. O. Stiegler, The Metallurgical Society of AIME, New York, 1984, pp. 183–98.

28. Abstract of paper submitted for presentation at American Physical Society Meeting, Las Vegas, Mar. 31 – Apr. 4, 1986.

29. Department of Physics, Indiana University, Bloomington.

30. Abstract of *Phys. Rev. B* **31**(6), 3260–77 (1985).

31. Abstract of paper submitted for presentation at American Physical Society Meeting, Las Vegas, Mar. 31 – Apr. 4, 1986.

32. Abstract of paper in *High Temperature Alloys: Theory and Design*, ed. J. O. Stiegler, The Metallurgical Society of AIME, New York, 1984, pp. 215–30.

33. Abstract of invited paper presented at the 19th International Thermal Conductivity Conference, Tennessee Technological University, Cookeville, Oct. 20–23, 1985.

34. Abstract submitted to *Phys. Rev.*

35. Deceased.

36. Abstract of article submitted to *J. Phys. F*.

37. Department of Physics, Dartmouth College.

38. Abstract of *Phys. Rev. B* **33**, 2170–78 (1986).

39. Abstract of article submitted to *Phys. Rev. Lett.*

40. Department of Physics, University of Warwick, Coventry, United Kingdom.

41. Abstract of *J. Phys. F* **15**, 1337–86 (1985).

42. Department of Physics, University of Toronto, Canada.

43. Abstract of paper in *High Temperature Alloys: Theory and Design*, ed. J. O. Stiegler, The Metallurgical Society of AIME, New York, 1984, pp. 231–47.

44. Abstract of *J. Magn. Magn. Mater.* **45**, 15–22 (1984).

45. Abstract of paper in *The Electronic Structure of Complex Systems*, ed. P. Phariseau and W. M. Temmerman, Plenum Press Advanced Studies Institute, New York, 1984, pp. 593–656.

46. Max-Planck Institute für Festkörperforschung, Stuttgart, Federal Republic of Germany.

47. Abstract of paper submitted for presentation at American Physical Society Meeting, Las Vegas, Mar. 31–Apr. 4, 1986.

48. Abstract of *J. Phys. F* **15**(6), 1387–1404 (1985).

49. Judson College, Elgin, Ill.

50. Department of Chemistry, Tennessee Technological University, Cookeville.

51. J. Callaway and N. H. March, "Density Functional Methods: Theory and Application," *Solid State Phys.* **38**, 135–221 (1985).

52. Abstract submitted to *J. Phys. Chem.*

53. F. W. Averill and G. S. Painter, *Phys. Rev. B* **32**(4), 2141–48 (1985).

54. D. C. Langreth and M. J. Mehl, *Phys. Rev. B* **28**, 1809 (1983).

55. Abstract of invited paper presented at Symposium on Applications of Local Density Functional Theory in Chemistry at Southeast-Southwest Regional Meeting of American Chemical Society, Memphis, Oct. 9–11, 1985.

56. Abstract of paper presented at American Physical Society Meeting, Baltimore, Mar. 25–29, 1985.

57. Abstract submitted to *J. Non-Cryst. Solids.*

58. Department of Physics, Brandeis University, Waltham, Mass.

59. Schlumberger-Doll Research Laboratory, Ridgefield, Conn.

60. Abstract of paper in *High Temperature Alloys: Theory and Design*, ed. J. O. Stiegler, The Metallurgical Society of AIME, New York, 1984, pp. 257–64.

61. Abstract of paper presented at the Materials Research Society Meeting, Boston, Nov. 26–30, 1984.

62. Abstract of paper in *High Temperature Alloys: Theory and Design*, ed. J. O. Stiegler, The Metallurgical Society of AIME, New York, 1984, pp. 257–64.

63. Abstract of *Phys. Rev. B* **31**(11), 7436–39 (1985).

64. Physics Laboratory, University of Athens, Greece.

2.2 ALLOYING BEHAVIOR AND DESIGN – C. T. Liu

The Alloying Behavior and Design Group originally had three Materials Sciences Tasks – (1) High-Temperature Alloy Design, (2) Deformation and Fracture of Metals and Alloys, and (3) Research on Metastable Materials. Tasks 2 and 3 have been merged with Task 1, but the three are treated separately in this report because they were separate during most of the report period.

The first task, High-Temperature Alloy Design, is concerned with understanding and designing new high-temperature structural materials based on ordered intermetallic alloys. Ordered intermetallics constitute a unique class of metallic materials that form long-range-ordered crystal structures below a critical temperature in the solid state. Many intermetallics possess attractive high-temperature properties; however, brittle fracture and poor fracture toughness restrict their use for structural applications. This task investigates the basic material phenomena and fundamental alloy variables that influence the design of ordered intermetallic alloys. The long-term goal is to develop a scientific basis for design of new-generation structural materials having superior high-temperature mechanical properties and oxidation/corrosion resistance.

The second task, Deformation and Fracture, investigates fundamental materials properties and processes that control the strength and ductility of structural components in energy technology systems. Establishment of quantitative relationship between microstructure, composition, and

mechanical behavior is emphasized. Multidisciplinary investigations combining mechanical testing, microstructural analysis, and theoretical modelling are carried out on simple model systems as well as complex commercial alloys. The technology impact of this research will include improvements in both the level and reproducibility of mechanical properties at elevated temperatures.

The third task, Metastable Materials, investigates the preparation and characterization of amorphous alloys and their crystallization into stable and metastable crystalline structures. The broad goals of this task are to understand the formation and stability of amorphous alloys with the aim of creating new materials, and to study the amorphous structure and selected properties. The use of the amorphous state as the basis for the creation of new metastable crystalline structures is included. Rapid solidification is also used as a tool for control of alloy homogeneity and microstructure in technologically interesting alloys, such as aluminides.

Because of recent increasing emphasis on high-temperature ordered intermetallic alloys, the two tasks on Deformation and Fracture and Metastable Materials were merged with the High-Temperature Alloy Design task beginning in FY 1986. This merger ensures a close coordination of research on ordered intermetallics and permits a more comprehensive approach to the key scientific questions concerning the design of these alloys.

2.2.1 High-Temperature Alloy Design – C. T. Liu

The nickel aluminide Ni_3Al has been chosen as a model material for study of physical metallurgy and mechanical behavior of ordered intermetallic alloys. Polycrystalline Ni_3Al alloys are inherently brittle because of poor grain-boundary cohesion. Ductility and cold fabricability of Ni_3Al containing less than 25% Al (hypostoichiometric compositions) can be dramatically improved by microalloying with a small quantity of boron. The improvement results from the unusual segregation behavior of boron in Ni_3Al, first revealed at Oak Ridge National Laboratory (ORNL), by using Auger electron spectroscopy. Boron has a strong tendency to segregate to grain boundaries but not at all to free surfaces. This segregation behavior leads to a decrease in grain-boundary energy and an increase in free-surface energy, resulting in a substantial increase in grain-boundary

cohesive energy in Ni_3Al. Our observation of boron segregation is the first direct confirmation of Rice's theory for the case of beneficial grain-boundary segregants. Positron annihilation studies reveal the formation of constitutional vacancies in Ni_3Al with ≥25 at. % Al. The clustering of boron around these vacancies is proposed to be the controlling factor that limits the long-range transport of boron to grain boundaries in stoichiometric and hyperstoichiometric alloys. The residual electrical resistivity, ρ, of Ni_3Al alloys with and without boron is currently studied at low temperatures, which may provide additional information about how boron interacts with constitutional vacancies in stoichiometric and hyperstoichiometric alloys.

The test environment does not affect yield stress but does strongly influence ductility and fracture behavior of boron-doped Ni_3Al tested at elevated temperatures, particularly in the range from 500 to 900°C. Our study reveals that the embrittlement is caused by a dynamic effect, simultaneously involving high localized stresses, elevated temperature, and gaseous oxygen. Identification of the mechanism responsible for the dynamic embrittlement leads to metallurgical solutions to the problem.

Microstructural features and deformation behavior of Ni_3Al alloys has been studied at room and elevated temperatures. The anti-phase boundary (APB) energy in Ni_3Al is anisotropic, with its lowest energy on {100} planes. This observation provides the first experimental support for the cross-slip model proposed to explain the increase in yield stress with temperature in Ni_3Al and other ordered intermetallic alloys. The creep behavior of Ni_3Al alloys has been studied as functions of applied stress and grain size. The diffusional creep based on the Nabarro-Herring model is the rate controlling step at stresses less than 10 MPa at 760°C, and dislocation creep based on a viscous glide model appears to be the rate controlling step at higher stresses. Grain-boundary sliding apparently plays an important role on both creep deformation and rupture processes. Creep rupture in Ni_3Al is associated with nucleation, growth, and coalescence of grain-boundary cavities. The kinetic factors governing these processes are sensitive to minor impurities that tend to segregate strongly to cavity surfaces.

Industrial interest in ductile aluminides is high. Several U.S. companies are currently involved in different stages of the development process aimed at alloy scale-up and commercialization. At present, Martin Marietta Energy Systems, Inc., is negotiating with several companies in order to obtain license agreements for the use of nickel aluminides as hot components in advanced heat engine systems.

2.2.1.1 Ductile Ordered Intermetallic Alloys[1] – C. T. Liu and J. O. Stiegler

Many ordered intermetallic alloys have attractive high-temperature properties; however, low ductility and brittle fracture limit their use for structural applications. The embrittlement in these alloys is mainly caused by an insufficient number of slip systems (bulk brittleness) and poor grain-boundary cohesion. Recent studies have shown that the ductility and fabricability of ordered intermetallics can be substantially improved by alloying processes and control of microstructural features through rapid solidification and thermomechanical treatments. These results demonstrate that the brittleness problem associated with ordered intermetallics can be overcome by using physical metallurgical principles. Application of these principles is illustrated by results on Ni_3Al and Ni_3V-Co_3V-Fe_3V. The potential for developing these alloys as a new class of high-temperature structural materials is discussed.

2.2.1.2 Effect of Boron on Grain Boundaries in Ni_3Al (ref. 2) – C. T. Liu, C. L. White, and J. A. Horton

The effects of boron additions (up to 0.4 wt % B) on grain-boundary chemistry and tensile properties of Ni_3Al containing 24 to 26 at. % Al were studied. Room-temperature ductility and fracture behavior of boron-doped Ni_3Al depend critically on deviation from alloy stoichiometry. As the aluminum content of boron-doped Ni_3Al is decreased below 25 at. %, the ductility increases dramatically and the fracture mode changes from intergranular to transgranular (Fig. 2.2.1). Auger studies indicate that the intensity of boron segregation to grain boundaries increases and the concentration of grain-boundary aluminum decreases significantly with decreasing bulk aluminum concentration. These results suggest that alloy stoichiometry strongly influences grain-boundary chemistry, which in turn

ORNL-DWG 85-18476R

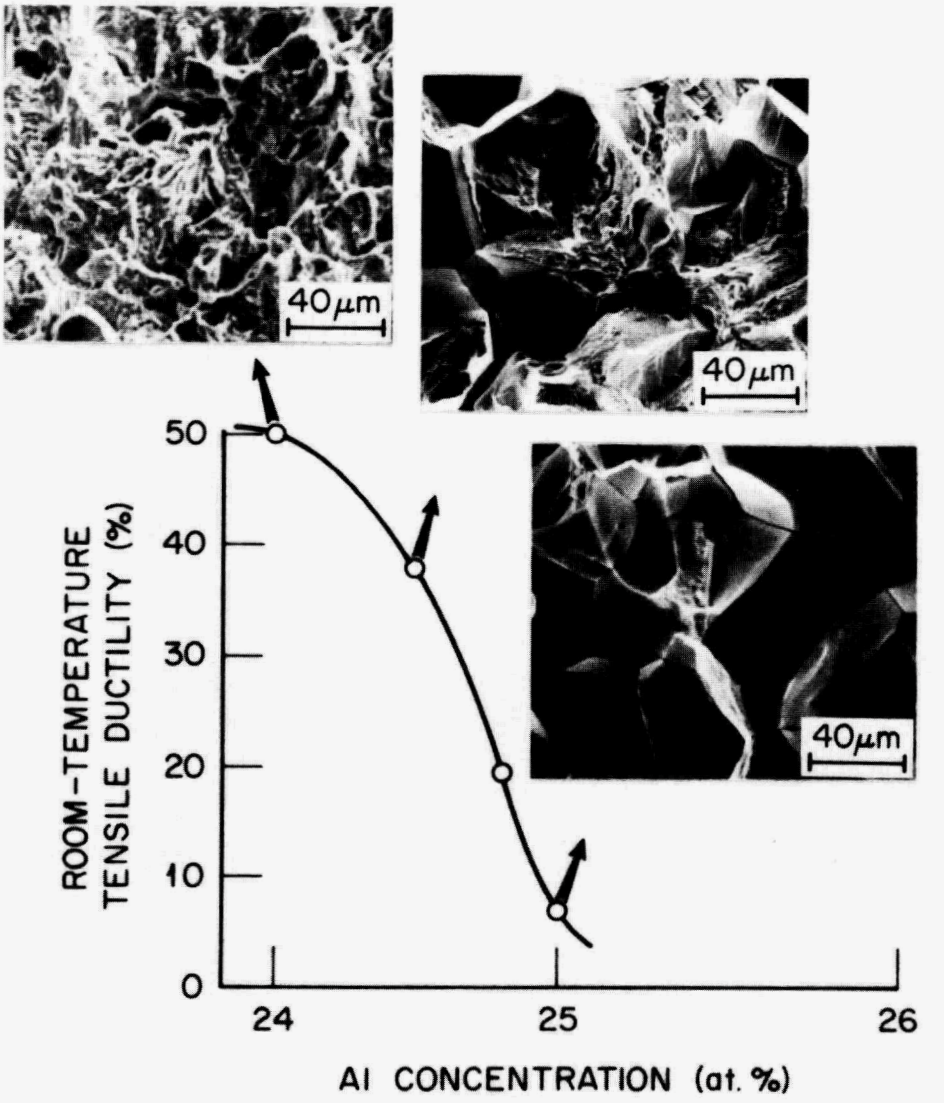

Fig. 2.2.1. Effect of aluminum concentration on room-temperature ductility and fracture behavior of Ni_3Al doped with 0.1 at. % B.

affects the grain-boundary cohesion. Boron exhibits an unusual segregation behavior in Ni_3Al, i.e., it has a strong tendency to segregate to the grain boundaries but not to cavity (free) surfaces. On the other hand, sulfur, an embrittling impurity, tends to segregate more strongly to free surfaces than to grain boundaries. The beneficial effect of boron is in agreement with existing theories of solute segregation effects on grain-boundary cohesion. The yield stress of boron-doped Ni_3Al decreases with

increasing grain size produced by long-term annealing at 1000°C. The yield stress obeys the Hall-Petch relation: $\sigma_y = \sigma_{o,y} + k_y d^{-1/2}$, where $\sigma_{o,y}$ = 163 MPa and k_y = 8.2 MPa $cm^{1/2}$. The tensile elongation was initially independent of grain size and showed only a moderate decrease from about 50 to 40% with grain diameters larger than 110 μm.

2.2.1.3 Surface and Grain Boundary Segregation in Relation to Intergranular Fracture: Boron and Sulfur in Ni_3Al (ref. 3) – C. L. White, R. A. Padgett, C. T. Liu, and S. M. Yalisov[4]

Comparisons of free-surface segregation and grain-boundary segregation in Ni–24% Al–0.2% B indicate that while boron (a beneficial segregant) segregates strongly to grain boundaries, it does not segregate strongly to free surfaces (Fig. 2.2.2). The opposite behavior was observed for sulfur, which is a well-known embrittler of Ni_3Al. These observations are interpreted in terms of a classical thermodynamic theory of segregant effects on grain boundary cohesion, developed by Rice. These results constitute the first well-documented example of agreement between Rice's theory and observed segregation behavior in a system where the solute in question enhances grain-boundary cohesion.

2.2.1.4 Recent Developments Concerning Segregation and Fracture at Grain Boundaries[5] – C. L. White

Certain trace impurities have long been known to segregate to and embrittle grain boundaries in polycrystalline metals and alloys. For a time, in fact, conventional wisdom held that all intergranular failure could be attributed to impurity segregation, and, conversely, all trace element segregation to grain boundaries was detrimental to their cohesion. In recent years, however, there have been several interesting experimental and theoretical developments that run counter to this conventional wisdom. Some of these developments, which may significantly advance our understanding of the mechanism by which trace element segregation affects grain boundary cohesion, are discussed in this paper.

Perhaps the most significant development concerns the strikingly beneficial effect of boron segregation on grain boundary cohesion in Ni_3Al. While other beneficial segregants have been identified during the past ten years, ductilization of Ni_3Al by boron additions has clearly received the

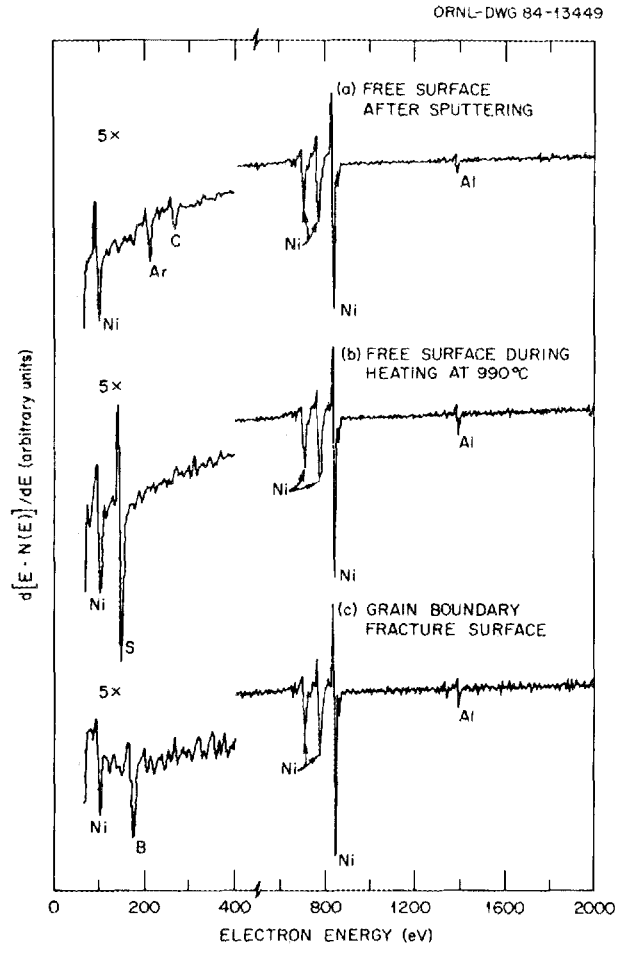

Fig. 2.2.2. Auger spectra from an external surface of Ni_3Al containing 24 at. % Al and 0.05 wt % B after sputter etching (*a*), then heating at about 990°C (*b*). Curve (*c*) shows an Auger spectrum from an intergranular portion of a fracture surface in this alloy.

most attention. This beneficial effect of grain boundary segregation is attributed to the unusual relationship between free-surface and grain-boundary segregation. Embrittling impurities are generally observed to segregate even more strongly to free surfaces than to grain boundaries, but boron segregates weakly if at all to free surfaces. This unusual segregation behavior is consistent with a thermodynamic treatment of grain boundary cohesion first suggested by Rice.

The relationship between grain boundary cohesive energy and the processes occurring at a crack tip are discussed. The valve-like control

of crack tip plasticity by cohesive strength, and the need for improved understanding of segregation-induced effects on grain boundary plasticity, are emphasized.

2.2.1.5 Boron Segregation at Grain Boundaries in Rapidly Solidified Ni_3Al (ref. 6) – C. C. Koch[7], C. L. White, R. A. Padgett, and C. T. Liu

The results of Auger electron spectroscopy (AES) and scanning electron microscopy measurements provide support for the rationalization of the ductile-to-brittle transition with solidification rate in Ni_3Al (24 at. % Al) + 0.5 at. % B presented previously. Although boron segregation to the grain boundaries cannot be completely suppressed by the cooling rates available in the arc-hammer apparatus, at sufficiently high cooling rates (i.e. for foil thicknesses less than about 45 μm) the segregation can apparently be reduced below the critical boron concentration required to strengthen the Ni_3Al grain boundaries. Previous AES results indicate that the boron concentration found on the ductile bulk 24 at. % Al alloy would be about 11% while that observed on the brittle, rapidly quenched 24 at. % Al alloy would be about 7%. Thus, the critical boron concentration for strengthening of the Ni_3Al grain boundaries must fall between these limits. While the stated concentration values cannot presently be confirmed via standards, these experiments do provide some guidance on the magnitude of the segregation required.

In summary, rapid solidification of Ni_3Al (24 at. % Al) + 0.5 at. % B in an arc-hammer apparatus has revealed a ductile-to-brittle transition with solidification rate that is attributable to the degree of boron segregation possible at a given solidification rate. Auger spectroscopy results on the rapidly solidified specimens along with previous work on bulk materials suggest that the critical concentration for strengthening the Ni-24 at. % Al grain boundaries is between 7 and 11 at. % B.

2.2.1.6 Study of Grain Boundary Segregation and Strength in Boron-Doped Ni_3Al Using Scanning AES and Hydrogen Charging[8] – A. Choudhury,[9] C. L. White, and C. Brooks[9]

Boron segregation to grain boundaries in Ni_3Al is known to strengthen the grain boundaries and to dramatically ductilize this intermetallic

compound. This unusual result of grain-boundary segregation is largely responsible for the current scientific and technological interest in intermetallic alloys based on this composition.

In the past, we have been frustrated in our attempts to study the detailed behavior of boron segregation in Ni_3Al. The most useful experimental techniques for studying grain-boundary segregation rely on exposing the grain boundaries via in-situ fracture in ultra-high-vacuum surface analysis facilities. Because of the potent ductilizing effect of boron segregation, only a small fraction of these in-situ fracture surfaces were intergranular, and consequently the resulting analyses sampled *only the weakest of the boron-strengthened boundaries*.

In this paper, we describe a procedure for studying segregation to *both strong and weak grain boundaries* in boron-doped polycrystalline Ni_3Al. The procedure involves scanning Auger electron spectroscopy (AES) analyses of boron segregation to grain boundaries exposed by fracturing nominally ductile specimens, both with and without electrolytic hydrogen-charging. Uncharged specimens fail predominantly by transgranular fracture, exposing only a few of the weakest grain boundaries in the polycrystalline aggregate. Hydrogen-charged specimens, however, exhibit large regions of nearly 100% intergranular failure, where both strong and weak grain boundaries are exposed for examination.

This procedure has permitted the *first* direct analyses of boron segregation to large fractions of the grain boundaries in ductile, boron-doped Ni_3Al that normally fails almost 100% transgranularly. Comparison of grain-boundary boron levels in charged and uncharged Ni_3Al indicates that those few weak boundaries exposed in uncharged specimens have significantly lower (about half) boron/nickel ratios than those exposed in hydrogen-charged specimens having the same boron content and thermal history. This indicates that those boundaries that are exposed in uncharged specimens are weaker and have lower boron levels that the average boundaries in the polycrystalline aggregate.

2.2.1.7 Positron Annihilation Study of Boron-Doped Ni_3Al (ref. 10) – A. DasGupta, L. C. Smedskjaer,[11] D. G. Legnini,[11] and R. W. Siegel[11]

Positron-lifetime and Coppler-broadening measurements were performed at room temperature on well-annealed polycrystalline $Ni_{75-x}Al_{25+x}$ alloys

(x = 1, 0, and +1) containing 0, 100, and 500 wt ppm boron. The large grain size (≈300–500 μm) in these alloys rendered the grain-boundary contribution negligible in the positron annihilation process. Systematic dependences of the positron lifetimes and the Doppler-broadening lineshape parameters were observed as a function of both the aluminum and boron contents of the alloys (Fig. 2.2.3). Positron trapping by defects was found in both the x = 0 and x = 1 alloys but was most pronounced in the nominally stoichiometric alloys containing boron. No positron trapping was evident in the x = −1 alloys with or without boron. A model is suggested for the relationship between these results and the problem of ductilizing polycrystalline Ni_3Al by boron doping.

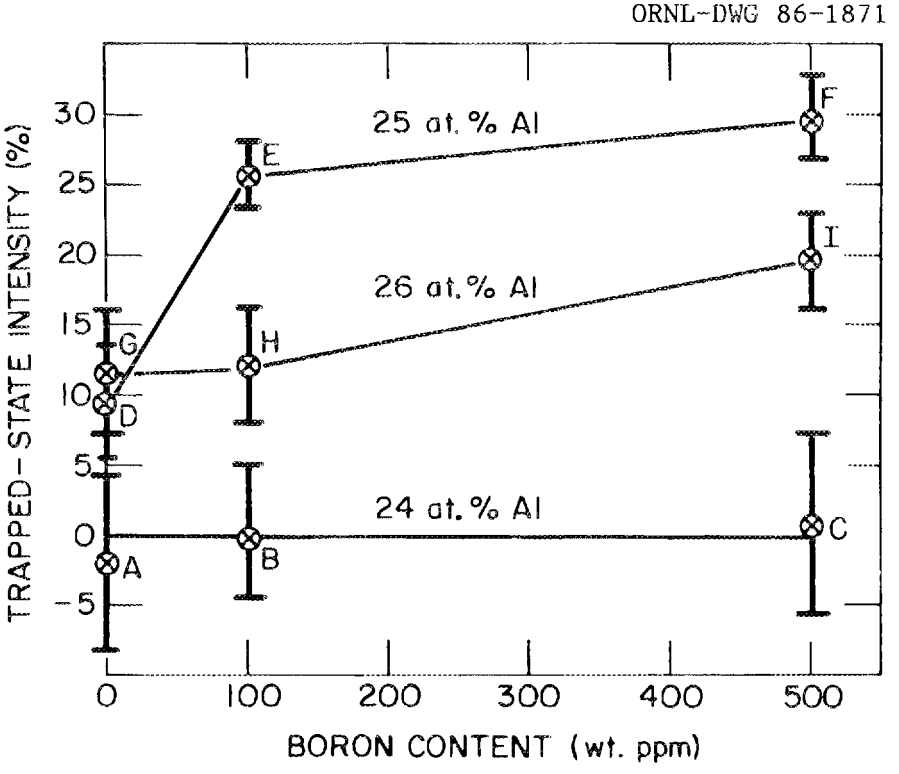

Fig. 2.2.3. The intensity of the trapped-state (180 ps) lifetime component as a function of the boron content in Ni_3Al alloys with different aluminum concentrations.

2.2.1.8 The Hardness of Ni_3Al Very Near Grain Boundaries[12] – W. C. Oliver and C. T. Liu

Small additions of boron in Ni_3Al drastically improve its ductility at room temperature. These improvements are clearly due to the boron segregating to the grain boundaries and modifying their behavior. An ultra-low-load, automated hardness testing system has been used to determine the hardness of small volumes of Ni_3Al near grain boundaries. The hardness testing system records the displacement of the indenter and the force on the indenter with a resolution of 0.16 nm and 1 μN, respectively. These measurements are made continuously during loading and unloading processes. The studies produce hardness versus depth versus position plots. Hardness increases of up to 20% were found in Ni–24% Al, Ni–24% Al doped with 0.1% B, and Ni–26% Al. No obvious differences associated with stoichiometry or boron additions were found. This means that there are not large differences in the stresses required for dislocation/boundary interactions associated with stoichiometry or boron additions.

2.2.1.9 Grain Boundary Accommodation of Slip in Ni_3Al Containing Boron – E. M. Schulson,[13] T. P. Weihs,[13] I. Baker,[13] H. J. Frost,[13] and J. A. Horton

Experiments at room temperature have established that the addition of 700 ppm by weight (0.35 at. %) of boron to stoichiometric Ni_3Al reduces the effectiveness with which grain boundaries strengthen the alloy. This effect leads to boron-induced weakening of the most finely grained aggregates ($d \leq 10$ μm). The effect of boron is explained in terms of an increase in the mobility of grain boundary dislocations (Fig. 2.2.4) and is related to boron-induced ductility.

2.2.1.10 Design of Ductile Polycrystalline Ni_3Al Alloys[14] – C. T. Liu and C. L. White

This paper provides a comprehensive review of current efforts on design of ductile polycrystalline Ni_3Al alloys. Microalloying has proven to be very effective in alleviating the grain-boundary embrittlement problem. The room-temperature ductility and fabricability of Ni_3Al (24 at. % Al) are dramatically improved by adding a few hundred parts per million of boron. The beneficial effect of boron is related to its

K775

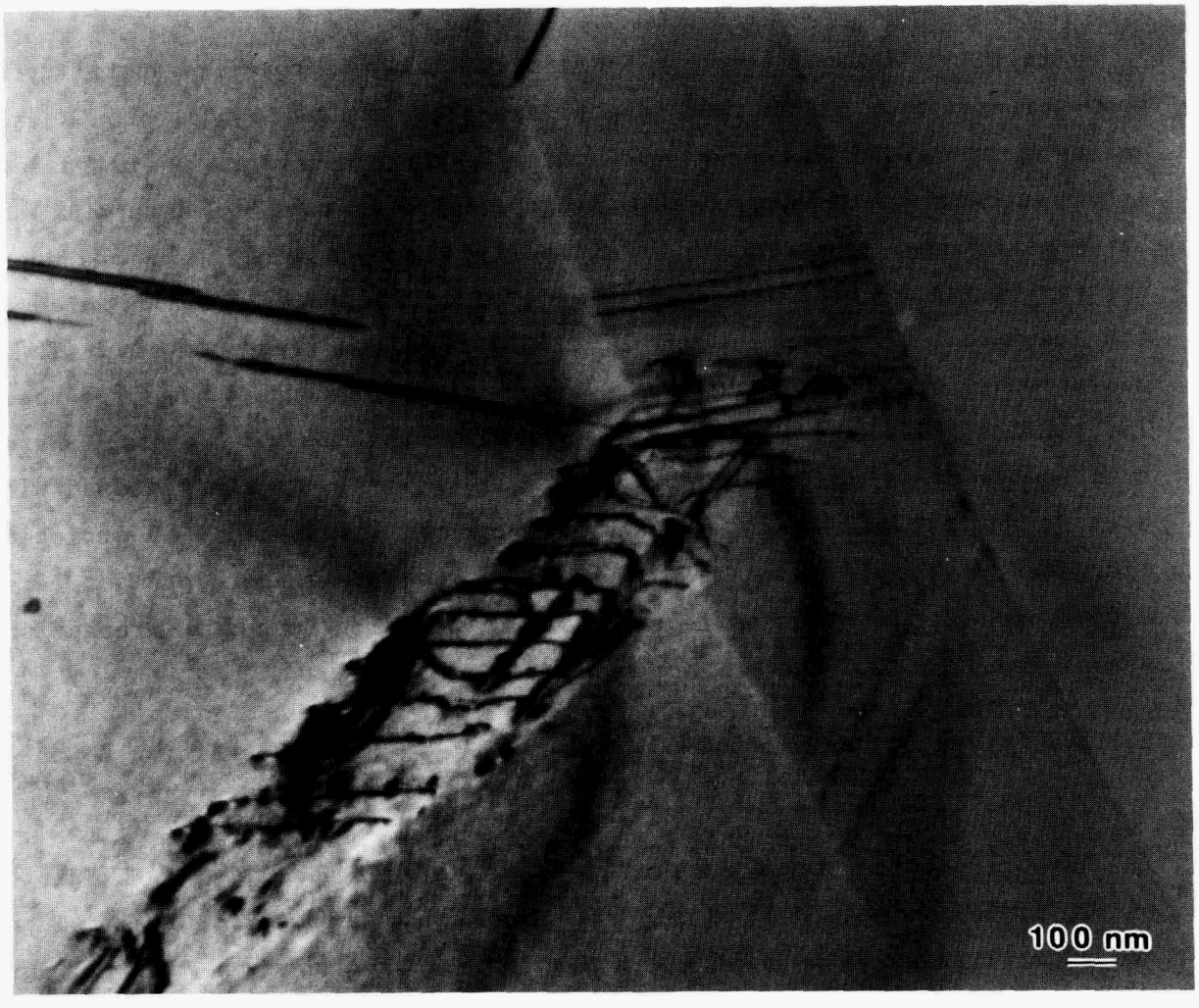

Fig. 2.2.4. Transmission electron micrograph of in-situ strained Ni_3Al showing an apparent realignment of slip dislocations upon entering a grain boundary.

unusual segregation behavior as predicted from the thermodynamic theory of grain-boundary cohesion developed by Rice. Alloy stoichiometry strongly influences grain-boundary chemistry, which, in turn, affects the boundary cohesion and overall ductility of Ni_3Al.

The solid-solution hardening of Ni_3Al depends on the substitutional behavior of alloying elements, atomic size misfit, and the degree of non-stoichiometry of the alloy. Hafnium additions are very effective in improving high-temperature properties of ternary Ni_3Al (Al + Hf = 24 at. %) doped with boron. Alloying with hafnium (up to 2%) substantially

increases the yield stress and raises the peak-strength temperature. In addition, hafnium substantially improves creep properties and oxidation resistance. The Ni_3Al aluminides truly represent a new series of heat-resistant materials that do not depend on chromium for oxidation resistance.

2.2.1.11 Anisotropic Antiphase Boundaries in Rapidly Solidified Ni_3Al (ref. 15) – J. A. Horton and C. T. Liu

Rapid solidification of Ni_3Al produces a network of curved antiphase boundaries (APBs). Annealing, which allows a structure closer to equilibrium to develop, results in the APBs preferentially aligned on {100} planes, thus indicating that the APB energy is less on {100} planes than on other planes. This provides the first direct experimental evidence of an APB energy anisotropy, which forms the basis of the Kear-Wilsdorf cross slip model used to explain the increase in yield stress with an increase in temperature.

2.2.1.12 Effect of Test Environment on Ductility and Fracture Behavior of Boron-Doped Ni_3Al at 600°C[16] – C. T. Liu, C. L. White, and E. H. Lee

The test environment strongly affects the ductility and fracture behavior of boron-doped Ni_3Al alloys tested at 600°C. A change in test environment from vacuum to oxidizing environments such as air causes a sharp drop in ductility from above 45% to less than 1%. This drop in ductility is accompanied by a change in fracture mode from transgranular to intergranular (Fig. 2.2.5). Scanning electron microscopy and optical metallography of air-tested specimens failed to reveal any evidence of oxide or other second-phase formation along grain boundaries. The fact that gage sections of air-tested specimens remain ductile at room temperature indicates that no permanent microstructural or compositional change sufficient to cause low-temperature brittleness occurs as a result of tensile tests in air at 600°C. These observations suggest that the effect of test environment reported here involves the *simultaneous* action of localized stress concentration, elevated temperature, and gaseous oxygen. Results from a more extensive study of environmental effects on boron-doped $Ni_3(Al,Hf)$ alloys further reveal that low-pressure oxygen

M-21385

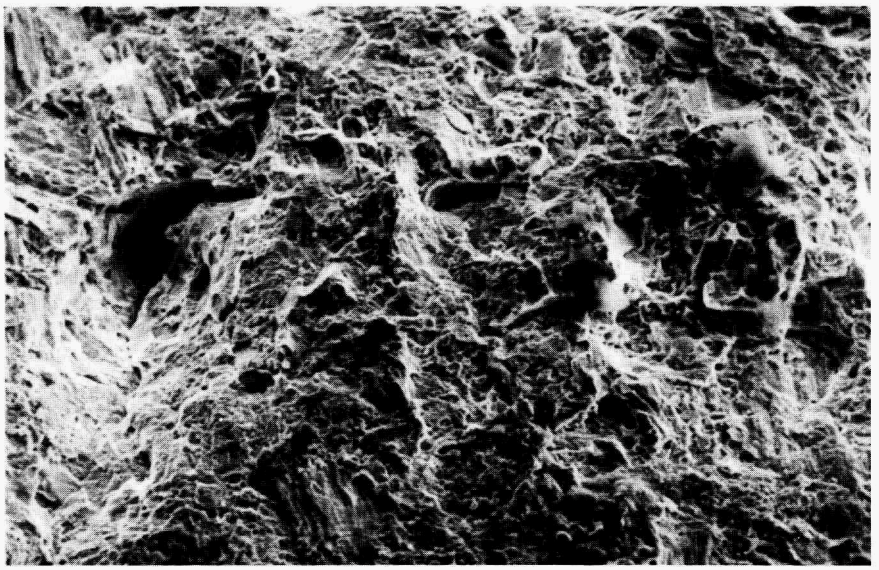

(*a*) 10 μm

M-21389

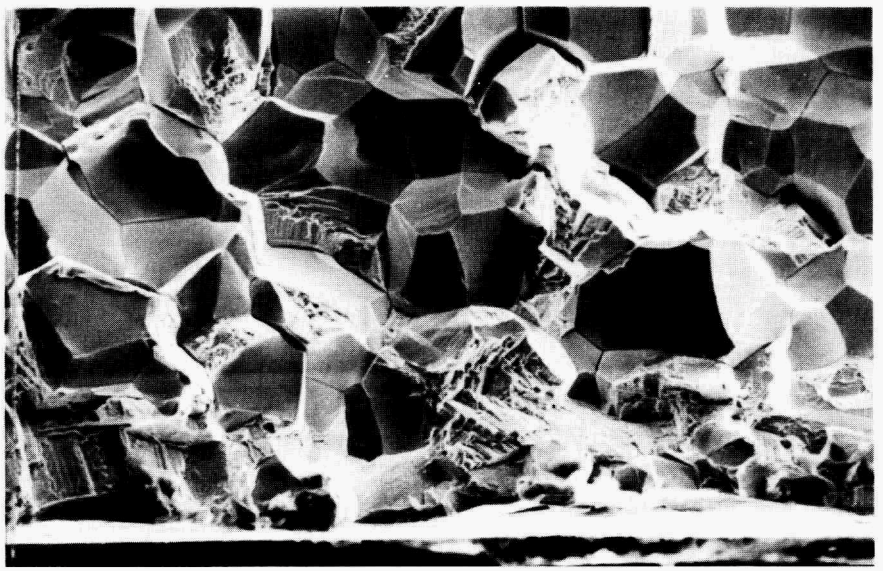

(*b*) 100 μm

Fig. 2.2.5. Scanning electron fractographs of Ni–24 at. % Al–0.2 at. % B tested in vacuum and air at 600°C. (*a*) Vacuum-tested specimen showing transgranular fracture. (*b*) Air-tested specimen showing predominantly intergranular fracture.

causes severe ductility loss at 600°C, and that the embrittling effects of oxidizing environments can be reduced by lowering the aluminum content and/or oxidizing the specimens before air-testing.

2.2.1.13 Isothermal Forging of a Nickel Aluminide – J. H. Schneibel, C. T. Liu, and W. D. Porter

In order to optimize the isothermal hot-forging characteristics of Ni_3Al-type intermetallic alloys, the influence of the initial microstructure, as well as the forging rate, needs to be studied. Compression experiments have been performed in vacuum with an alloy of the composition Ni-22.5Al-0.5Hf-0.1B (at. %) in the as-cast condition as well as in the homogenized condition. At 1000°C, the homogenized material fails in a brittle manner at strain rates above approximately 10^{-4} s^{-1} (Fig. 2.2.6). In the as-cast condition, however, ductilities are satisfactory at strain rates as high as 10^{-1} s^{-1}.

The high ductility of the as-cast material is attributed to its dendritic structure. Hafnium-enriched dendritic boundaries, with a spacing of typically 50 μm, act as sites for dynamic recrystallization and, after forging, are laced with newly formed grains with diameters in

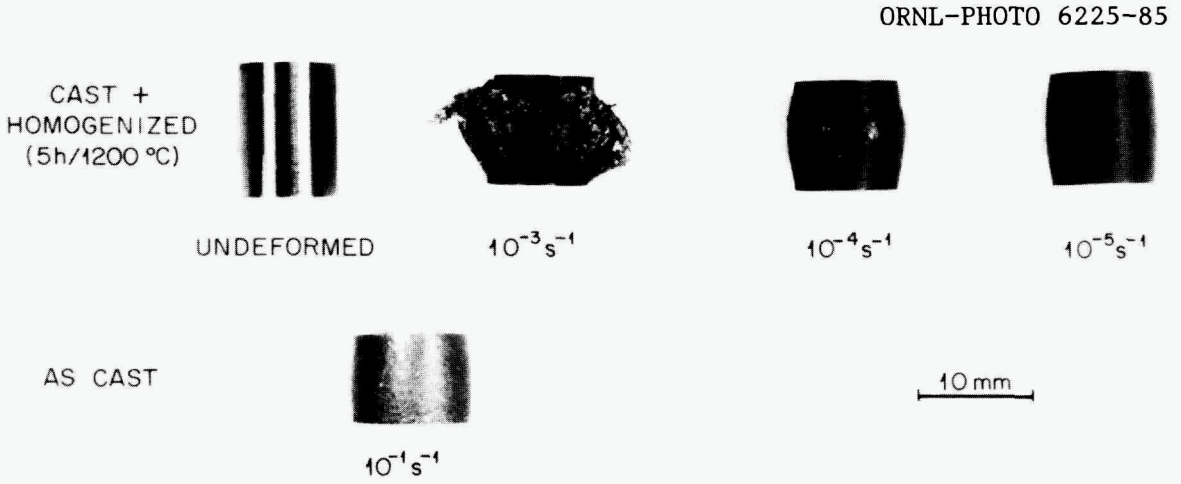

Fig. 2.2.6. Effect of homogenization treatment and strain rate on isothermal forging behavior of an Ni_3Al alloy.

the micron range. For identical strains and strain rates, the as-cast alloy contains a much higher volume fraction of recrystallized material than the homogenized alloy with its large grain size (which is typically 500 μm). It appears that this is an important factor in explaining the pronounced effect of heat treatment on the forging properties. Further work is being conducted in order to identify more accurately the mechanisms controlling the ductility. In particular, experiments are being conducted on hafnium-free alloys in order to verify the possible importance of hafnium enrichment in the as-cast dendritic structures.

2.2.1.14 Creep Behavior of a Polycrystalline Nickel Aluminide: Ni–23.5 at. % Al–0.5 at. % Hf–0.2 at. % B (ref. 17) – J. H. Schneibel, G. F. Petersen, and C. T. Liu

The creep behavior of a polycrystalline nickel aluminide with the composition Ni–23.5 at. % Al–0.5 at. % Hf–0.2 at. % B has been measured as a function of stress, temperature, and grain size. At high stresses, of the order of 100 MPa, the strain rate is nonlinear in the stress, with a stress exponent greater than two. Below approximately 10 MPa, at 1033 K, the steady-state strain rate is almost proportional to the stress, indicating that diffusional creep is rate controlling (Fig. 2.2.7).

Calculations of expected Nabarro-Herring and Coble creep rates did not answer whether diffusive mass transport through the grains, or along the grain boundaries, is rate controlling. The grain-size dependence of the strain rate indicates, however, predominance of volume diffusion control, i.e., Nabarro-Herring creep, for our experimental conditions.

2.2.1.15 Effect of Hafnium Additions on Creep Behavior of Nickel Aluminides[18] – C. T. Liu, C. L. White, and J. H. Schneibel

Creep properties of boron-doped nickel aluminides (based on Ni_3Al) containing up to 2 at. % Hf have been studied as functions of applied stress and grain size at 760°C in vacuum. Hafnium additions substantially extend the rupture life of nickel aluminides by lowering creep rate and by increasing rupture ductility. The aluminides exhibited an increase rather than a decrease in rupture ductility with decreasing applied stress. Metallographic examination reveals extensive cavities and cracks

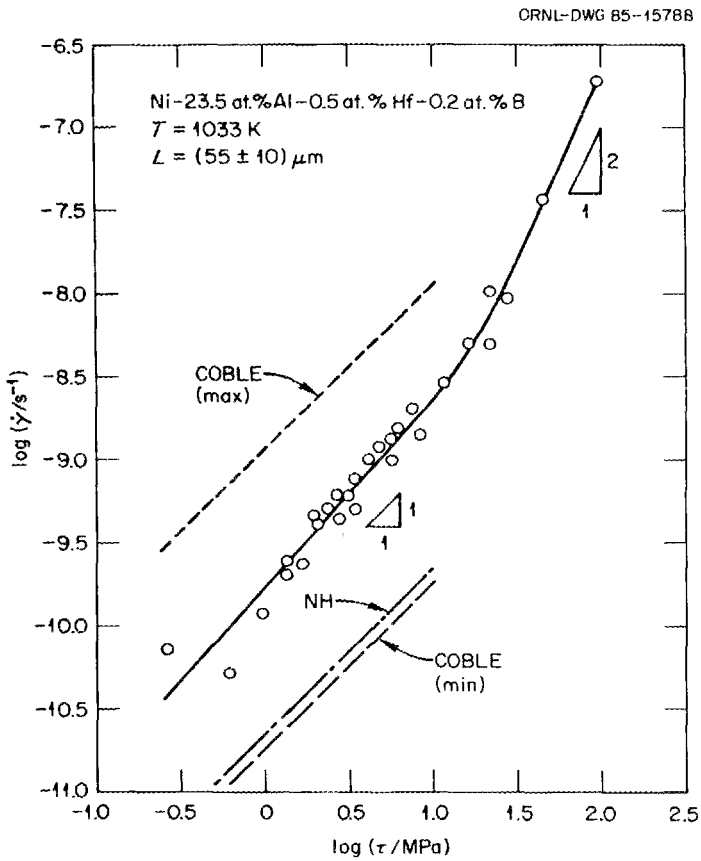

Fig. 2.2.7. Stress dependence of the creep rate of Ni–23.5 at. % Al–0.5 at. % Hf–0.2 at. % B. Theoretical predictions are shown as broken lines.

formed along grain boundaries. These results are discussed in terms of solid-solution hardening effects as well as the grain-boundary chemistry determined by Auger electron spectroscopy.

2.2.1.16 Phase Formation and Stability in the Pseudobinary Ni_3Al-Ni_3V Alloy System[19] – A. DasGupta, J. A. Horton, and C. T. Liu

In order to study the formation of phases and their thermal stability, differential scanning calorimetry (DSC), X-ray diffraction, and optical microscopy were performed simultaneously in the Ni_3Al-Ni_3V pseudobinary alloy system. For the alloy series represented by $Ni_3(Al_xV_{100-x})$,

a tetragonal DO_{22} phase was found to form for $x < 10$, and a cubic $L1_2$ phase for $x > 75$ at room temperature. For $10 < x < 75$, the DO_{22} and $L1_2$ phases were found to coexist. Contrary to some theoretical expectations, no complex ordered equilibrium phases formed in this alloy system at any intermediate composition between Ni_3Al and Ni_3V. Measurements of the order-disorder transition temperature, T_c, by DSC, and the associated details of the phase transformations and stability, are discussed.

2.2.1.17 Transport Properties of Polycrystalline Ni_3Al (ref. 20) — R. K. Williams, F. J. Weaver, and R. S. Graves

Recent advances in ductilizing the intermetallic compound Ni_3Al may lead to practical applications. These applications, which are based on the outstanding strength and oxidation resistance of the compound, also require physical property data. In this paper, the room-temperature electrical and thermal conductivities of annealed high-purity specimens containing 74 to 76 at. % Ni are presented and compared with theoretical predictions. Residual (4.2 K) electrical resistivity data are also employed in the analysis, and these results show a pronounced minimum at the stoichiometric composition. The data show that the thermal conductivity of this compound is quite sensitive to stoichiometry and, at room temperature, has a maximum value at about 74.8 at. % Ni. Calculated and experimentally derived phonon thermal conductivity values agree well, and they indicate that this carrier is responsible for about 25% of the room temperature thermal conductivity. The electronic Lorenz function is essentially equal to the Sommerfeld value.

2.2.1.18 Physical Properties of Ni_3Al Containing 24 and 25 Atomic Percent Aluminum[21] — R. K. Williams, R. S. Graves, F. J. Weaver, and D. L. McElroy

Thermal conductivity, electrical resistivity, Seebeck coefficient, and thermal expansion data were obtained on well-annealed Ni_3Al containing 24 and 25 at. % Al. The results span the temperature range 300 to 1000 K. The expansion coefficients did not vary with composition and increased with temperature, reaching values of about $17 \times 10^{-6}\ K^{-1}$ at 1000 K. The thermal conductivity and electrical resistivity changed rapidly with composition, and the thermal conductivity of 24 at. % Al is as much as 30%

lower than that for stoichiometric Ni_3Al. The electronic Lorenz function of Ni_3Al was obtained by subtracting the estimated phonon conductivity component and found to be within about 5% of the Sommerfeld prediction from 300 to 1000 K. The electrical resistivity results for stoichiometric Ni_3Al are influenced by the loss of ferromagnetic order at lower temperatures and are not adequately described by the Bloch-Grüneisen equation.

2.2.1.19 Effects of Iron and Boron Additions on the Physical Properties of Ni_3Al – R. K. Williams, R. S. Graves, and F. J. Weaver

Electrical resistivity and thermal conductivity data were obtained on nine single-phase alloys that contained 1 to 10 at. % Fe and 0, 0.25, and 0.5 at. % B. The resistivity data, which were obtained at 4.2, 78, and 300 K, show that both iron and boron produce strong electron scattering and thus would be expected to significantly reduce the electronic thermal conductivity. Two somewhat surprising results were obtained: (1) for iron additions the resistivity increments were not dependent on temperature, although the 1 and 3 at. % Fe alloys were only ferromagnetic at lower temperatures, and (2) the resistivity increase produced by boron was found to decrease as the nickel/aluminum concentration ratio increased. The latter effect, which may give some information about how boron behaves in the solid solutions, is currently being investigated further in binary Ni_3Al.

The thermal conductivity data for Ni_3Al containing 10 at. % Fe are much smaller than values for the binary, and are about equal to the values for austenitic stainless steels. Using the measured resistivity data with the Sommerfeld Lorenz number shows that iron additions effectively reduce the electronic part of the thermal conductivity. A theoretical calculation based on Callaway's formula shows that iron should not be very effective in reducing the phonon part of the thermal conductivity, and this is consistent with the experimental observations.

The thermal expansion behavior of an Ni–20% Al–10% Fe alloy was also studied. The dilatometric results were essentially identical to the values found for the binary compound and gave no evidence of an anomaly at the Curie temperature.

2.2.1.20 Thermal Conductivity of Metals and Alloys[22] – P. G. Klemens and R. K. Williams

The theory of the thermal conductivity of metals at high temperatures is reviewed and compared with experimental results for the metallic elements and three alloy systems. The phonon and electron components of the thermal conductivity are treated separately, and the electronic part is discussed in terms of its relationship to the electrical resistivity through the electronic Lorenz function. For elastic scattering in a completely degenerate electron gas, the Lorenz function should equal the Sommerfeld value,

$$L_0 = \frac{\pi^2}{3}\left(\frac{K_B}{e}\right)^2 ,$$

and the effects that can cause deviations from this value are described.

The phonon component is described in terms of the scattering processes that limit energy transport by lattice vibrations: phonon–phonon (self), phonon–electron, and phonon–point defect scattering. Because there is no common factor which determines all three scattering strengths, a wide variety of behavior is expected.

High-temperature data for the metallic elements were compared with theory, and for several elements the Sommerfeld Lorenz number was found to be only approximately (±20%) appropriate. Calculations of the phonon component seem to be generally correct to about a factor of ±2, and the formulas predict a wide variation of this component. Its relative importance also varies greatly because the interelement variation of the electronic component is also large.

Three alloy systems, Al, Ti, and Fe-Ni-Cr base, were considered. The Al-base alloys are electronic conductors, and L_0 is nearly correct at high temperatures. For the other two alloy systems, phonon conduction is probably much more important because the electronic component is not large. Except for alloys containing small amounts of Mo, point defect scattering is weak in the fcc Fe-Ni-Cr alloys. This is not the case for many Ti-base alloys, because Al should be a powerful scatterer of phonons. An unusual

contribution to the electronic specific heat coefficient makes it difficult to estimate the electron-phonon scattering in Fe-Ni-Cr γ phase alloys, but this process is probably important in both Fe-Ni-Cr and Ti-base alloys.

2.2.1.21 Constant Strain Rate Indentation Tests at Ultra-Low Loads – W. C. Oliver

Programming has been developed to dynamically control continuous indentation experiments for determining mechanical properties on a microscopic scale. The strength of a material is determined by three variables, the temperature, the strain rate of the test, and the microstructure of the material. When standard hardness tests are performed, the strain rate of the test is not closely controlled. The ultra-low-load microindentation testing system at ORNL allows the dynamics (strain rate) of such tests to be controlled. Software has been developed to do constant strain rate indentation tests. The characteristic strain rate of an indentation test is given by a constant times $\dot{d}/d$, where $\dot{d}$ is the indentation rate and d is the indentation depth. The form of this dependence makes it very difficult to control the strain rate at small displacement. By using the new programming, the $\dot{\epsilon}$ can be held constant from approximately 5 nm to the final depth of the indents.

2.2.1.22 Nucleation of Intergranular Creep Cavities[23] – M. H. Yoo and H. Trinkaus[24]

Intergranular cavity nucleation under creep-induced microscale stress concentrations is studied on the basis of a recently developed theory of nucleation under time-dependent supersaturation. The spacial and temporal evolution of the stress concentration resulting from grain boundary sliding or slip–grain boundary interaction is modelled by using a linear elasto-diffusion approach. The quasi-steady-state analysis shows that significant cavity nucleation is possible only under the condition that the characteristic time for the stress evolution is large compared with the incubation time for nucleation. This condition is satisfied when the spatial range of the stress concentration is large compared with the size of the critical cavity embryo. In this case, it also ensures that, once nucleated, stable clusters will remain stably growing permanently.

Integration of the quasi-steady-state nucleation rate over time gives the total cavity number density nucleated during a single stress pulse. If the kinetics of stress and cavity evolutions are controlled by the same diffusion process, they simply scale with each other. In this case, the cavity density yield per stress pulse is independent of the corresponding diffusivity. The average cavity nucleation rate associated with a stoichastic sequence of stress pulses will, however, depend on the diffusivity controlling the frequency of the stress pulses, which is expected to increase with strain rate.

Because cavity nucleation can occur only under stress levels far above typical applied stress values, it is controlled by the extreme tail of the probability distribution of the internal stresses. Integration of the quasi-steady-state nucleation over appropriate probability distributions shows that the average nucleation rate depends much less strongly upon the average of a microscopically fluctuating (macroscopically constant) stress than on a microscopically constant stress. This result provides a possible explanation of the so-far unexpected mild stress dependence of intergranular cavitation observed in some creep experiments. If the probability of high stress concentrations is proportional to the strain rate, the overall cavity nucleation rate will appear to be strain controlled although the individual nucleation event is actually stress controlled.

2.2.1.23 Slip-Interface Interaction at Elevated Temperatures[25] – M. H. Yoo

A dislocation model for the slip-interface interaction during high-temperature deformation is developed by use of the concept of continuously distributed dislocations. The fact that the $\ell^{-1/2}$ type stress singularity (ℓ is the distance from the head of a dislocation pile-up) in a general nonplanar static pile-up, including glide and climb of extrinsic grain boundary dislocations, is the same as that of a planar pile-up was established by a numerical calculation. The strength of stress concentration at the interface depends on both geometrical and kinetic variables. A dislocation pile-up caused by microstructural instability may offer the most favorable site for cavity nucleation. A discussion is given on the extension of this model to study the dynamics of microplastic flow near grain boundaries and/or intergranular fracture.

2.2.1.24 Interaction of Slip with Grain Boundary and Its Role in Cavity Nucleation[26] - M. H. Yoo and H. Trinkaus[24]

Localized stress evolution resulting from the interaction of slip with a grain boundary is characterized by a superposition of the "internal loading" of a subsystem by dynamic dislocation pile-up and the diffusional relaxation along the grain boundary. The probability of cavity nucleation per stress pulse is evaluated by using a quasi-steady-state extension of the classical nucleation theory. The nominal efficiency of a grain boundary as vacancy source and sink is related to the climb mobility of grain-boundary dislocations. The critical stress for cavity nucleation (a Hall-Petch type relationship) is derived, which is related to the effective slip length. Once nucleated, cavities are stable through the transient growth stage. The frequency of slip/grain-boundary interaction and continuous cavity nucleation during creep are discussed by comparing theoretical predictions with the available experimental data.

2.2.2 Deformation and Fracture of Metals and Alloys - M. H. Yoo

As part of the alloy design effort, the fundamental processes controlling the mechanical behavior of structural materials are investigated. By understanding basic deformation and fracture mechanisms, microstructural evolution, and the effects of alloying elements and impurities on deformation and fracture, we can develop a scientific basis for design of materials used in energy technology systems.

The current emphasis is focused on the physical mechanisms of intergranular creep fracture involving nucleation, growth, and interlinkage of grain-boundary cavities. A model austenitic stainless steel (Fe-15% Ni-15% Cr) as well as a commercial stainless steel (type 304) have been studied. Experimental and theoretical research on this model system is reported in this section. Increasing emphasis is placed on model alloys based on the intermetallic compound Ni_3Al. The research on the latter model system is reported in Sect. 2.2.1, High-Temperature Alloy Design.

2.2.2.1 Grain Boundary Sliding in Wires with Bamboo Structure[27] - J. H. Schneibel and G. F. Petersen

Grain boundary sliding during the torsional creep deformation of austenitic stainless steel wires (Fe-15 wt % Cr-15 wt % Ni) with bamboo

structures has been investigated. At 1100 K, the sliding rate $\dot{u}$ is approximately proportional to $\tau^{2.5}$ where τ is the applied shear stress. Although Reading and Smith's model [*Phil. Mag. A* **51**, 71 (1985)] of grain boundary sliding by lattice dislocations has shortcomings, it predicts the observed sliding rates quite well. At sufficiently small grain sizes and low stresses, the observed nonlinear grain boundary sliding may inhibit diffusional creep.

2.2.2.2 A Method to Determine Surface Free Energies from Cavity Radius Distribution[28] – L. Martinez[29] and J. H. Schneibel

The possibility of determining surface free energies by annealing cavitated polycrystals is investigated theoretically. During sintering at zero stress, the surface free energy γ, obtained from the evolution of a cavity radius distribution, was found to be sensitive to the sintering kinetics. However, if cavity radius distributions are studied after annealing at low tensile stresses, it is possible to obtain a value of γ that is independent of the kinetics of the underlying growth and sintering processes.

2.2.2.3 Comments on "A New Method for the Determination of the Precipitate-Matrix Interfacial Energy"[30] – L. Martinez[29] and J. H. Schneibel

The advantages of the determination of precipitate-matrix interfacial energies from critical radius measurements as compared with those calculated from precipitate coarsening rate data were discussed. The evolution of precipitate radius distributions, with and without size gradient, during a dissolution and growth process was modelled. In both cases techniques for time-independent critical radius determination were suggested.

2.2.2.4 Determination of Cavity Growth Rates from Cavity Size Distributions[31] – J. H. Schneibel and L. Martinez[29]

We describe a simple method to determine grain-boundary cavity growth kinetics from cavity size distributions developed during creep. The technique is applicable in the presence of continuous nucleation and may be used for studying cavity growth as well as sintering. The influence of an assumed internal stress distribution on its accuracy is discussed. Cavity

size distributions obtained by Yang and Weertman by small-angle neutron scattering (SANS) of crept copper are reanalyzed with the above method. The results agree with quasi-equilibrium diffusive growth kinetics. However, they indicate also that the cut-off error of the SANS technique can be serious.

2.2.2.5 SANS and TEM Studies of Carbide Precipitation and Creep Damage in Type 304 Stainless Steel[32] – M. H. Yoo, J. C. Ogle, J. H. Schneibel, and R. W. Swindeman

Small-angle neutron scattering (SANS) and transmission electron microscopy (TEM) studies were performed to characterize the carbide ($M_{23}C_6$) precipitation and creep damage induced in type 304 stainless steel in the primary creep stage. The size distribution of matrix carbides evaluated from SANS analyses was consistent with TEM data, and the expected accelerated kinetics of precipitation under applied stress was confirmed. Additional SANS measurements after the postcreep solution annealing were made in order to differentiate cavities from the carbides. Potential advantages and difficulties associated with characterization of creep-induced cavitation by the SANS techniques are discussed.

2.2.2.6 Studies of Heterogeneities of Micrometer Range with Double Crystal Diffractometer[33] – D. Schwahn[24] and M. H. Yoo

The resolution of the double crystal diffractometer (DKD) at KFA-Jülich is obtained at about 10^{-4} nm^{-1} by using channel-cut perfect silicon crystals. Procedures for the absolute intensity calibration and the slit-height deconvolution are demonstrated by an experiment utilizing latex spheres of the known size distribution. Applications of high-resolution small-angle neutron scattering using DKD in metal physics are discussed with a specific example of creep-induced cavities in austenitic stainless steel.

2.2.2.7 Role of Interfaces in Cavity Formation[34] – M. H. Yoo and H. Trinkaus[24]

A variety of two-phase microstructures in structural alloys for which the evidences for cavity formation during high-temperature deformation exist are reviewed. A decohesion mode similar to the process of ductile

fracture initiation is suggested in order to explain the reported dependency of cavity density on the grain boundary orientation with respect to the stress in austenitic stainless steel. The evolution of localized stress concentration resulting from the interaction between slip or interfacial sliding and interface is analyzed by using a linear elasto-diffusion approach. The strength of stress concentration depends on a geometrical factor and the mobilities of dislocations involved. On the basis of quasi-steady-state classical nucleation model, the probability of cavity nucleation at each potential site is examined in terms of the dislocation mobilities. Cavity nucleation in two-phase materials can be suppressed significantly if the mobility of interfacial dislocations is increased to a value comparable to that of grain boundary dislocations.

2.2.2.8 Study of Solute Segregation at Interfaces Using Auger Electron Spectroscopy[35] – C. L. White

Interfacial segregation, often confined to within a few atomic distances of the interface, can strongly influence the processing and properties of metals and ceramics. The thinness of such solute-enriched regions can cause them to be particularly suitable for study by using surface-sensitive microanalytical techniques such as Auger electron spectroscopy (AES). The application of AES to studies of interfacial segregation in metals and ceramics is briefly reviewed, and several examples are presented.

Auger electron spectroscopy is a powerful and versatile tool for the study of interfacial composition in cases where the interface can be obtained as an external free surface. Its usefulness derives from the fact that it probes only the top few atom layers on a surface, and that it is just these top few atom layers that are often greatly different in composition from the bulk material. Through the use of appropriate standards, the technique can be made quantitative; however, the effort required for careful quantitative analysis is usually substantial, and semiquantitative evaluation of AES results is often adequate.

Electron-excited AES can achieve spatial resolutions down to tens of nanometers, which is better than any of the other available surface sensitive techniques. It is also nominally nondestructive on most

specimens. If sensitivity to very small concentrations, or detection of hydrogen or helium, is important, then secondary ion mass spectroscopy may offer advantages over AES. If information regarding the chemical state of segregant and matrix species is important, then X-ray photoelectron spectroscopy would be preferred. If even the shallow analysis depth of AES is not adequate to resolve details of interfacial chemistry, the "top" atom layer sensitivity of ion scattering spectroscopy can be useful. While each of these techniques offers its own set of advantages and disadvantages, AES is probably the most widely applied and generally is the technique of choice if only a single one can be selected.

2.2.3 **Research on Metastable Materials** – D. M. Kroeger

As part of the alloy design effort, the preparation and properties of rapidly solidified and vapor-deposited alloys have been studied. The focus of our efforts is shifting from the study of metallic glasses to the utilization of these processes for producing novel microstructures and metastable states in crystalline alloys, primarily Ni_3Al. It has been found that boron-doped Ni_3Al specimens prepared by rapid solidification can have mechanical properties differing significantly from those of conventionally cast materials. These differences may be attributed to the small grain sizes of the rapidly solidified material (as small as 2–3 μm) and to altered distributions of boron, the segregation of which can be inhibited by rapid solidification processing. These materials are thus of interest in studies utilizing microanalytical techniques such as transmission electron microscopy, atom probe field ion microscopy, and Auger electron spectroscopy to correlate microstructure and dopant distribution with bulk properties, and in studies of the kinetics of boron segregation.

In our work on metallic glasses we have contributed to understanding of the structure-property relationship through careful studies of the compositional dependences of physical properties derived from measurements of the low-temperature specific heat and differential scanning calorimetry of the crystallization process. The absence of crystalline order in the glass limits the information that can be obtained from diffraction techniques, thus increasing the importance of inferences concerning structure

that can be drawn from property measurements. A detailed study of the crystallization process in ZrNi metallic glasses prepared both by rapid solidification and vapor deposition has been stimulated by an earlier study of the compositional dependences of parameters derived from low-temperature specific measurements on glasses in that alloy system. The detection of two distinct superconducting transitions in specific heat curves for amorphous specimens with compositions near the eutectic at 63.5 at. % Zr demonstrated that glasses in this composition range tend to phase separate. Estimates of the compositions of the individual phases were obtained by comparing their superconducting transition temperatures T_c with the measured compositional dependence of T_c. Our recent studies of the crystallization process in this system have demonstrated a correspondence in composition between these amorphous phases and the crystalline phases to which specimens in this composition range transform upon heating, thus tending to support the idea of a similarity in short-range structures of amorphous and crystalline phases.

2.2.3.1 A New Metastable Phase Near 60 at. % Zr From Amorphous Ni-Zr (ref. 36) - D. S. Easton, C. G. McKamey, D. M. Kroeger, and O. B. Cavin

Metallic glass alloys of Ni-Zr were prepared by vapor and liquid quenching. For glass compositions at and near 60 at. % Zr, crystallization proceeded by the sequence: amorphous → metastable crystalline phase → $NiZr_2$ + NiZr. The metastable phase exhibited a very distinctive X-ray diffraction pattern and was present in both liquid- and vapor-quenched samples. Long-term anneals of samples with the metastable structure produced the equilibrium phases $NiZr_2$ and NiZr. An observation of peaks and valleys in a plot of the compositional dependence of Q_p, the scattering vector corresponding to the first maximum in the X-ray diffraction pattern, suggests that the structure of the glass varies significantly with small compositional changes, in support of conclusions drawn previously from the dependences of quantities derived from low-temperature specific heat measurements.

2.2.3.2 Crystallization of Ni-Zr Metallic Glasses[37] – C. G. McKamey, D. M. Kroeger, D. S. Easton, and J. O. Scarbrough

The crystallization of Ni-Zr metallic glasses with compositions between 55 and 70 at. % Zr was investigated by using differential scanning calorimetry (DSC) and X-ray diffraction (XRD). The samples were prepared by liquid quenching in an arc-hammer device. Transformation temperatures, effective activation energies, and enthalpy changes were obtained as a function of composition. X-ray diffraction patterns were obtained as a function of thermal history for specimens heated in the differential scanning calorimeter. A high-temperature exothermic DSC peak and XRD patterns indicate the development of a metastable phase during crystallization of specimens with zirconium concentrations between 57 and 63.2 at. % Zr. It was found that the metastable phase, whose presence is strongest at 57 to 59 at. % Zr, and the process of phase separation around the eutectic composition (63.5 at. % Zr) play important roles in the crystallization process. For compositions between 57 and 66.7 at. % Zr, the first crystalline phase to appear upon heating is either the stable intermetallic Zr_2Ni or the metastable phase with composition 58 at. % Zr. These are the approximate compositions of the glassy phases found from superconducting transition temperatures in phase-separated samples. Thus, these results establish a correspondence in composition between amorphous and crystalline phases, and they tend to support the suggestion of a connection between the short-range structures of the glass phases and the crystalline phases that form from them.

2.2.4 References

1. Abstracted from *Science* **226**, 636–42 (1984).

2. Abstracted from *Acta Metall.* **33**, 213–29 (1985).

3. Abstracted from *Scr. Metall.* **18**, 1417–20 (1984).

4. Department of Materials Science and Engineering, University of Pennsylvania, Philadelphia.

5. Abstracted from an invited lecture at the 32d National Symposium of the American Vacuum Society, accepted for publication in *J. Vac. Sci.*

6. Abstracted from *Scr. Metall.* **19**, 963–66 (1985).

7. Materials Engineering Department, North Carolina State University, Raleigh.

8. Summary of a paper to be presented at the 1986 Annual AIME Meeting, New Orleans, La.

9. Department of Materials Science and Engineering, University of Tennessee, Knoxville.

10. Abstracted from *Materials Letters* **11**, 457–61 (1985).

11. Materials Science and Technology Division, Argonne National Laboratory, Argonne, Ill.

12. Abstracted from a paper presented at the 1985 AIME Fall Meeting, Toronto, Oct. 14–17, 1985.

13. Thayer School of Engineering, Dartmouth College, Hanover, N.H.

14. Abstract of a paper in symposium proceedings *High Temperature Ordered Intermetallic Alloys*, ed. C. C. Koch, C. T. Liu, and N. S. Stoloff, vol. 39, MRS publication, 1985, pp. 365–80.

15. Abstracted from *Acta Metall.* **33**, 2191–98 (1985).

16. Abstracted from *Scr. Metall.* **19**, 1247–50 (1985).

17. Abstracted from a paper to be published in *J. Mater. Res.*, 1986.

18. Abstract of a paper presented at the 1985 AIME Fall Meeting, Toronto, Oct. 14–17, 1985.

19. Abstracted from a paper in *High Temperature Alloys: Theory and Design*, ed. J. O. Stiegler, AIME publication, 1985, pp. 115–23.

20. Abstracted from a paper published in *Thermal Conductivity 18*, ed. T. Ashworth and R. Smith, Plenum Press, 1985, pp. 165–74.

21. Abstracted from a paper in symposium proceedings *High Temperature Ordered Intermetallic Alloys*, ed. C. C. Koch, C. T. Liu, and N. S. Stoloff, MRS publication, 1985, pp. 505–12.

22. Abstracted from an invited paper to be published in *Int. Met. Rev.*, 1986.

23. Abstract of paper presented at Second International Conference on Fundamentals of Fracture, Gatlinburg, Tenn., Nov. 4–7, 1985.

24. Institut für Festkörperforschung, Kernforschungsanlage Jülich, Jülich, Federal Republic of Germany.

25. Abstracted from paper in the proceedings of the Conference to Celebrate the Fiftieth Anniversary of the Concept of Dislocations in Crystals, *Dislocations and Properties of Real Materials*, The Royal Society of London, Dec. 11–12, 1984, pp. 241–43; an invited talk presented at the Gordon Research Conferences on Physical Metallurgy, *Role of Interfaces in Deformation and Strengthening*, Plymouth, N.H., Aug. 5–9, 1985.

26. Abstract of paper submitted to *Acta Metall.*, 1985.

27. Proceedings of the 4th Japan Institute of Metals International Symposium (JIMIS-4), *Grain Boundary Structure and Related Phenomena*, Nov. 25–29, 1985, Minakami Spa, Japan.

28. Abstract from *Philos. Mag. A* **51**, L29–L34 (1985).

29. Institute of Physics, University of Mexico, Mexico City.

30. Abstracted from *Scr. Metall.* **19**, 1015–18 (1985).

31. Abstract of paper to be submitted to *Philos. Mag.*

32. Abstract of paper in the proceedings of the 5th International Symposium on Metallurgy and Materials Science, *Microstructural Characterization of Materials by Non-Microscopic Techniques*, RISO National Laboratory, Roskilde, Denmark, Sept. 3–7, 1984, pp. 595–600.

33. Abstract of paper to be published in *Proc. in Physics*, Springer Verlag, Berlin, proceedings of Workshop on Atomic Transport and Defects in Metals by Neutron Scattering, KFA Jülich, Federal Republic of Germany, Oct. 2–4, 1985.

34. Abstract of an invited paper to be published in *Phase Boundary Effects on Deformation*, proceedings of a symposium at the 1985 Fall Meeting of TMS-AIME, Toronto, Oct. 13–17, 1985.

35. Abstracted from *Am. Ceram. Soc. Bull.* **64**, 1571–80 (1975), and from an invited lecture at the 36th Annual Pacific Coast Regional Meeting of the American Ceramic Society, Oct. 30, 1984.

36. Abstracted from a paper to be published in *J. Mater. Sci.*, 1986.

37. Abstracted from papers to be published in *J. Non-Cryst. Solids, J. Mater. Sci.*, and proceedings of the Materials Research Society Fall Meeting, Boston, December 1985.

2.3 FUNDAMENTALS OF WELDING AND JOINING – S. A. David and J. M. Vitek

The principal aim of the Materials Science Welding Program is to investigate the physical metallurgy of weldments during fabrication, in the as-welded condition, and during anticipated service. The program consists of three major parts relating to the study of (1) solidification behavior of weld metal, (2) phase stability of weldment microstructure, and (3) structure-property correlations.

The solidification behavior study is directed toward an understanding and modeling of the basic solidification characteristics of weld metal over a range of welding conditions.

The phenomenon of hot cracking in austenitic stainless steel welds is being investigated by using model Fe-Ni-Cr ternary alloys in single- and poly-crystalline forms. The effect of impurities is being examined by selectively doping the pure ternary alloys. In addition, weld microstructures solidified at high cooling rates have been investigated and their hot-cracking tendencies are being evaluated.

The phase stability study is directed toward understanding the stability of weld microstructures after aging in the range 400 to 850°C. This is essential in understanding the influence of thermal cycling during multipass welding, postweld heat treatment, and elevated temperature service.

The program is also aimed at correlating weld metal structure and properties and thereby aiding in the development of predictive modeling of weld metal structure and properties. The results of aging studies on type 308 and 308 CRE (controlled residual elements) stainless steels are being compared with microstructures of interrupted creep tests.

Through this program a cooperative research program was initiated with the American Welding Institute (AWI) and CBI Industries. An investigation was carried out with AWI and CBI Industries to examine the potential of high-power electron-beam welding for joining heavy-section steels.

2.3.1 Microstructure of Rapidly Quenched Type 308 Stainless Steel Weld Filler Metal and Its Implications on Rapid Solidification Processes – S. A. David and J. M. Vitek

In an earlier investigation at Oak Ridge National Laboratory (ORNL), it was found that during laser welding of austenitic stainless steels (type 308) at high welding speeds, a fully austenitic weld metal microstructure was produced. This is in contrast to the duplex austenitic and ferrite ($\gamma + \delta$) structure observed in the weld metal of the same steel after using conventional welding processes. The observed modification in the microstructure during laser welding at high speeds was attributed to the change in mode of solidification from primary delta ferrite to primary austenite at high solidification rates. In order to investigate further the effect of solidification rate on microstructure, the structure of type 308 stainless steel was evaluated after rapid quenching by the hammer-arc process. A large degree of variation was found from a fully austenitic structure to the duplex ferrite plus austenite structure commonly found in welded material. The lack of large-scale segregation, as determined by electron microprobe analysis, indicates that the structural variations are due to cooling rate changes rather than compositional fluctuations. The results also show that this material is very sensitive to cooling rate in the range prevalent in the hammer-arc process.

2.3.2 Electron-Beam Welding of Heavy-Section 3Cr-1.5Mo Alloy – J. F. King, S. A. David, J. E. Sims, and A. M. Nasreldin

Electron-beam welding is a process that potentially could have advantages for the fabrication of heavy-section steel components such as pressure vessels. The penetrating ability of the beam produces welds with high depth-to-width ratios at relatively high travel speeds, making it possible to weld thick sections with one or two passes without filler metals and other consumables. A study was undertaken to investigate the feasibility of using a high-power electron-beam welding machine to weld heavy-section steel of 3Cr-1.5Mo-0.1V alloy. Single-pass welds were made in 102-mm-thick (4-in.) plates of this alloy. The main emphasis of this work concentrated on determining the mechanical properties of the this work concentrated on determining the mechanical properties of the resulting weldment, characterizing the microstructure of the various weldment regions, and comparing these results with those from other welding

processes. As a result of this investigation it has been shown that single-pass, full-penetration electron-beam weldments of high integrity can be made in 102-mm-thick 3Cr-1.5Mo-0.1V steel. These weldments have a fusion zone and heat-affected zone microstructure that is predominantly martensitic. The weld metal produced by the electron-beam process has a slightly higher hardness and tensile strength than the base metal in this alloy after post-weld heat treatment. Charpy impact properties of the weld metal were found to match those of the base metal and were better than the results obtained from current weldments produced by the submerged arc and shielded metal arc welding processes. Electron-beam weldments in the 3Cr-1.5Mo-0.1V steel readily pass Section IX of the ASME Code bend tests. These results indicate that electron-beam welding offers an attractive alternative for heavy-section steel joining.

2.3.3 Metastable Equilibrium of Ferrite in Type 308 Stainless Steel and the Concept of Effective Quench Temperature – J. M. Vitek and S. A. David

For a wide range of iron-chromium-nickel alloys, ferrite is often retained at low temperatures because of non-equilibrium cooling conditions. Types 308 and 308 CRE stainless steels with different initial states were aged, and the composition of ferrite was evaluated as a function of aging time and temperature. During aging at any temperature the ferrite partially dissolves and concurrently changes its composition, approaching a limiting value (Fig. 2.3.1). This adjustment in composition occurs independently of the transformation of ferrite to sigma phase. The change in omposition is a result of an approach to equilibrium, either stable equilibrium at the highest temperatures or metastable equilibrium at the lower temperatures.

Elevated-temperature structures are routinely studied at room temperature by assuming that such structures can be quenched-in by appropriate means. The possibility is often ignored that microstructures change during quenching, and that the final product is not truly representative of the structure at the quench temperature. An effective quench temperature can be determined by means of compositional analyses of the constituent phases in a structure. The idea of such an effective quench temperature is applied to welded or rapidly quenched type 308 austenitic stainless steels.

YE-12914

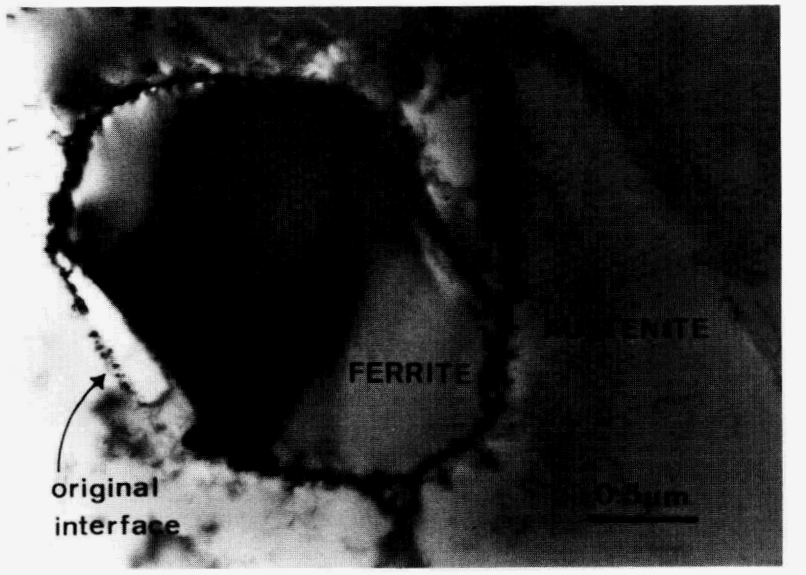

(*a*)

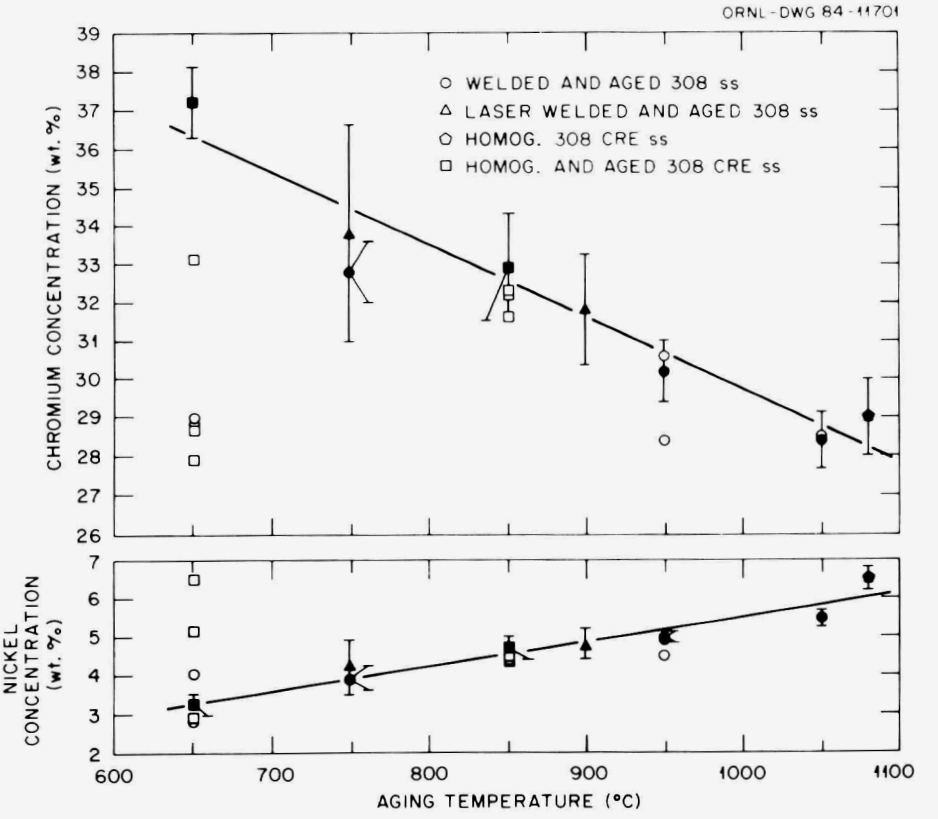

(*b*)

Fig. 2.3.1. (*a*) Electron micrograph of homogenized and aged (850°C, 1 h) type 308 CRE stainless steel showing recession of ferrite-austenite interface that results from aging. (*b*) Plot of ferrite composition as a function of aging temperature for various aging times. Solid symbols with error bars are for longest aging times at each temperature and were used to determine the trend line shown for composition versus temperature.

3. STRUCTURAL CERAMICS

P. F. Becher

This report describes progress within the structural ceramics task for the period of July 1, 1984, to December 31, 1985. The work reported includes transformation toughening behavior in ceramics and the effects of microstructure and composition; it has involved collaborative efforts with the Chemical Technology and Chemistry Divisions of Oak Ridge National Laboratory (ORNL), 3M Corporation, and CSIRO at Melbourne, Australia. This work is intimately coupled to our studies of colloidal processing of transformation-toughened ZrO_2-alumina composites and the influence of surface charge regulation to control sintering and microstructure and hence toughness and mechanical properties in multiphase systems. This latter critical research endeavor comprises a recent growth area in our program and is an evolution based on our findings of the critical nature of controlling sinterability and microstructure on the toughening behavior of the zirconia-toughened ceramic composites as reported last time. This progression has also been realized by the completion of much of our research on the processing and mechanical behavior of diboride ceramics that had previously constituted a major part of our efforts.

3.1 TRANSFORMATION TOUGHENING BEHAVIOR[1,2] – P. F. Becher and P. Angelini

Transformation toughening involves a phase/crystal structure change that can be triggered by the stress at the crack and tip that in turn alters the crack tip stress. In many ways this is similar to the plastic deformation in the vicinity of crack tips in metals. However, the phase tranformation, rather than dislocation motion and plastic deformation, is the mechanishm by which the crack tip stress is altered and the toughness increased. The tetragonal crystal structure of both ZrO_2 and HfO_2 can be transformed to the monoclinic structure, involving an expansion in volume, when subjected to a tensile stress. When this occurs in ZrO_2

particles dispersed in a matrix near a crack tip, the volume expansion of the ZrO_2 introduces local compressive stresses and reduces the tensile stress acting on the crack tip.

As in the case of metals where plastic deformation is initiated at a well-defined stress level (the yield stress), the phase transformation is triggered at a stress level known as the critical transformation stress - σ_c^T. The lower the value of σ_c^T, the easier it is to transform the ZrO_2, and the size, r_T, of the region around the crack tip where the transformation occurs increases as follows:

$$r_T = (K_{IC}^M/\sigma_c^T)^2 \quad , \tag{1}$$

where K_{IC}^M is the fracture toughness of the matrix in which the ZrO_2 is dispersed.

When we lower σ_c^T and thus increase r_T, the fracture toughness contribution from transformation toughening, ΔK_{IC}^T increases:

$$\Delta K_{IC}^T = AV_f r_T^{1/2} \quad , \tag{2}$$

where V_f is the volume fraction of tetragonal ZrO_2 that transforms and A is a term describing stress, strain, and elastic parameters. Because these are composite systems the total fracture toughness is

$$K_{IC}^C = K_{IC}^M + \Delta K_{IC}^T \quad , \tag{3}$$

and the fracture toughness is increased.

Studies by G. M. Begun of the Chemistry Division using laser Raman spectroscopy techniques show that the transformation zone size around the cracks in partially stabilized zirconia (PSZ) ceramics, which contain tetragonal ZrO_2 precipitates in a cubic ZrO_2 matrix, do indeed increase as the toughness increases in the manner predicted by Eqs. (2) and (3). This is seen in Fig. 3.1.1.

Additional studies have shown that r_T increases as the value of σ_c^T decreases as predicted by Eq. (1). The question that remained was how to

ORNL–DWG 84-17727R

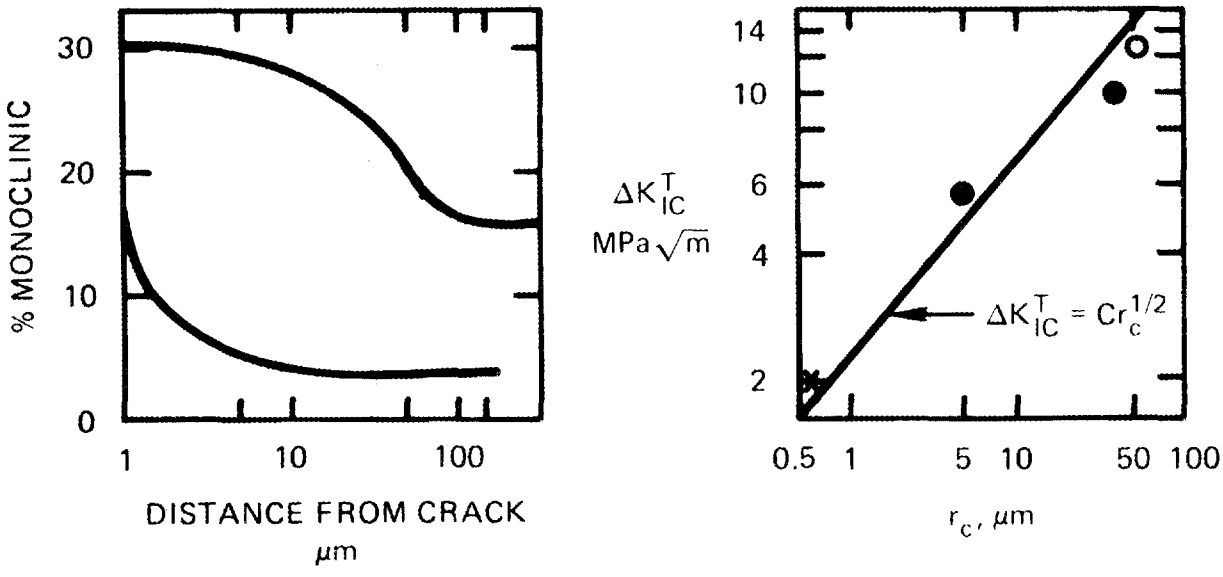

Fig. 3.1.1. Transformation zone size (r_T) dependence of fracture toughness of PSZ ceramics. Laser Raman spectroscopy results confirm $(r_T)^{1/2}$ dependence of ΔK_{IC}^T predicted by Eq. (2).

further define σ_c^T in terms of the stability of the tetragonal ZrO_2. We know that such tetragonal particles in a matrix can be transformed by lowering the sample temperature, T, below M_S, which is the temperature where the tetragonal phase begins to spontaneously transform to the monoclinic phase. In studies[2] by P. F. Becher, M. V. Swain,[3] and M. K. Ferber,[4] analytical descriptions were derived by considering the thermodynamics of the tetragonal to monoclinic transformation for particles in a matrix. Briefly, the total chemical free energy change for the stress-induced transformation of such a tetragonal particle in a matrix can be described as

$$dG^{t-m} = (T - M_S)dS \ , \qquad (4)$$

where dS is the entropy change associated with the transformation. Under the above conditions, the strain energy that must be supplied by the application of a tensile stress must be equal to dG^{t-m}:

$$\sigma_c^T = dG^{t-m}/e^T = (T - M_S)dS/e^T \ , \tag{5}$$

and from Eq. (5) we see that σ_c^T will decrease as $(T - M_S)$ or dS decrease. By substituting Eq. (5) into Eq. (2) using Eq. (1), one obtains

$$\Delta K_{IC}^{T} = AV_f K_{IC}^{M}/(T - M_S)dS \ , \tag{6}$$

which predicts that the fracture toughness increases as M_S approaches T or vice versa as long as T is greater than M_S. The value of the term $(T - M_S)$ tells us how easy it is to transform the tetragonal ZrO_2; the smaller the value of $(T - M_S)$ is, the lower is the σ_c^T needed to start the transformation and the greater is the toughness. This is consistent with the behavior of PSZ ceramics at room temperature, Fig. 3.1.2, and similarly the toughness at various temperatures. This description of the transformation is also consistent with the toughening behavior of ZrO_2-toughened aluminas.

One can introduce other chemical compounds into the tetragonal ZrO_2 to make it more or less stable (i.e., to lower or raise its M_S temperature). Increasing amounts of compounds such as Y_2O_3 and CeO_2 lower M_S, while HfO_2 raises M_S. Studies by P. F. Becher with W. D. Bond of the Chemical Technology Division, E. F. Funkenbusch of 3M Corporation, and G. M. Begun show that such alloying additions have a profound effect on M_S, σ_c^T, and fracture toughness obtained by transformation toughening in both zirconia ceramics containing the tetragonal phase and other ceramics, such as alumina, which contain dispersed tetragonal ZrO_2 particles. These studies are now addressing the mechanisms by which these alloying compounds alter the tetragonal to monoclinic phase transformation.

One feature of the analysis derived for the contribution of transformation toughening, which involves a stress-induced phase transformation in ZrO_2, reveals that the overall toughness achieved is the sum of the

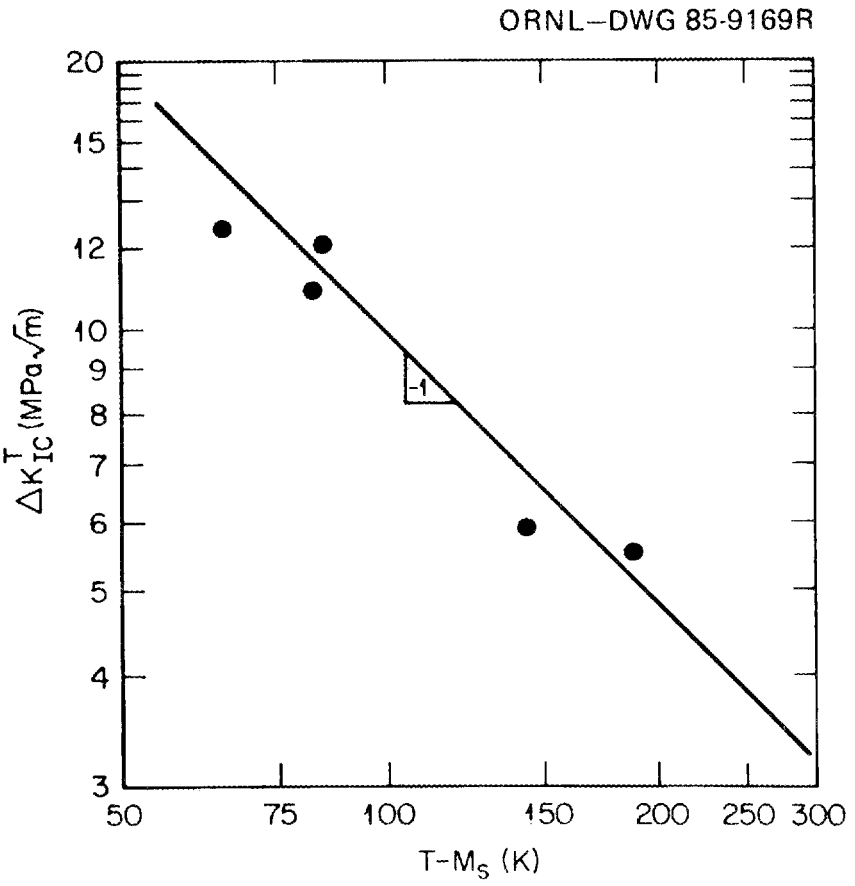

Fig. 3.1.2. The stability of tetragonal ZrO_2 phase is characterized by the $(T - M_S)$ term in Eqs. (4) and (5). The fracture toughness of PSZ ceramics thus increases as M_S approaches T (22°C in this case). Data confirm toughening behavior described by Eq. (6).

matrix toughness and the toughening related to the transformation of ZrO_2 particles around an advancing crack. The models derived are descriptive of the experimentally observed behavior of transformation-toughened ceramics in the Materials Sciences Program studies.[1,2] Further consideration of these results indicates that greater toughening can be achieved by increasing the toughness of the matrix, allowing us to consider additional concepts. One concept is to first toughen the matrix by reinforcing it with strong, microscopic SiC whiskers (based on studies by G. C. Wei, P. F. Becher, and T. N. Tiegs). Such an approach, when combined with transformation toughening, should result in a ceramic composite with greater toughness than that achieved with either transformation toughening or whisker reinforcement alone.[5]

In order to confirm this, composites were developed and characterized in a joint effort by researchers in the Materials Sciences and Conservation Programs on ceramics.[5] Mullite, an alumina silicate compound, reinforced with SiC whiskers was developed to include ZrO_2 particles as the transformation-toughening media. As seen in Fig. 3.1.3, transformation toughening of the mullite increases the toughness from approximately 2 to 3 MPa·m$^{1/2}$ about 1.5 fold. However, when combined with whisker reinforcement, the toughness increases to approximately 7 MPa·m$^{1/2}$ or nearly 3.5 fold. In fact, the combining of the two toughening mechanisms results in greater toughness than that obtained by either mechanism by itself, confirming the analytical predictions.

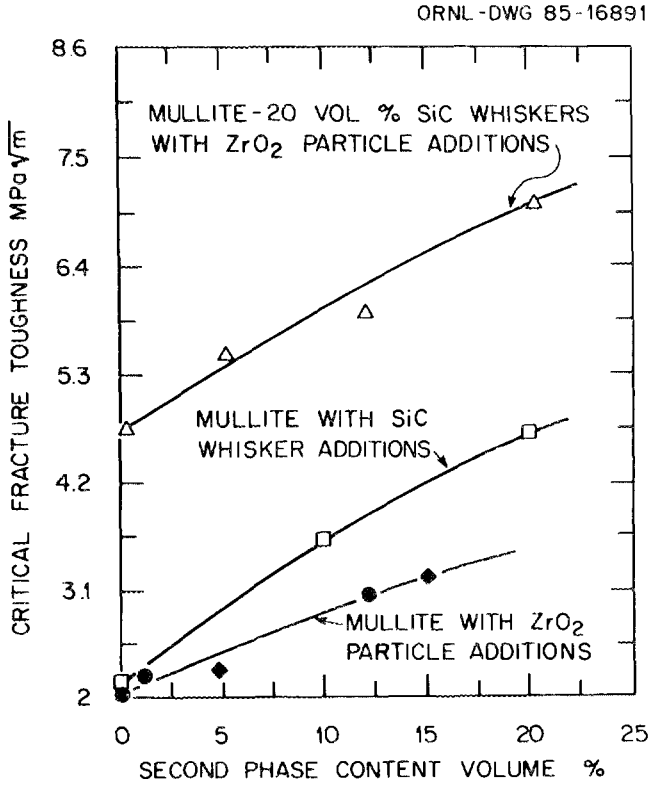

Fig. 3.1.3. Fracture toughness data for mullite-based composites illustrate the greater toughness achieved by use of multiple toughening mechanisms (i.e., SiC-whisker-reinforced matrix plus ZrO_2 toughening) than that achieved by either mechanism by itself.

These findings provide a basis for developing ceramic composites with excellent mechanical performance – high fracture strength and toughness – for energy-related applications. The demonstrated ability to combine toughening mechanisms greatly expands the approaches to "designing" the properties of ceramics, which has resulted in considerable interest in the ceramic research and industrial communities.

3.1.1 Subcritical Crack Growth in Partially Stabilized ZrO_2(MgO) (ref. 6) – P. F. Becher

Slow crack growth at 22°C in partially stabilized zirconia is enhanced in water as compared with air (~50% R.H.). On the basis of Region I data, at a K_{Ia} level of 6 MPa·m$^{1/2}$ the as-fired PSZ exhibits a crack velocity of approximately 4×10^{-14} m/s in air versus approximately 1×10^{-3} m/s in water. The aged PSZ exhibits a less pronounced effect of environment – crack velocities in water are only slightly enhanced as compared with those in air (e.g., at $K_{Ia} = 4.5$ MPa·m$^{1/2}$, velocities are approximately 2×10^{-7} m/s and 1×10^{-8} m/s, respectively).

There is a significant decrease in slow crack growth resistance as a result of aging the sintered PSZ at 1400°C for 8 h in air. Not only is the entire slow crack growth V-K_{Ia} curve shifted to lower K_{Ia} levels after aging, but the Region I slope, n, is decreased about two-fold and the intercept, A, is increased dramatically. These changes are associated with an increase in monoclinic phase content in the aged PSZ. Thus this aging treatment not only diminishes the critical fracture toughness but also decreases the time to failure under applied tensile stress ($\sigma_{Ia} < \sigma_{IC}$).

3.1.2 References

1. Summary of material contained in a paper by P. F. Becher, M. K. Ferber, and M. V. Swain, in press, *J. Mater. Sci.*, 1986.

2. P. F. Becher, "Toughening Behavior in Ceramics Associated with the Transformation of Tetrogonal ZrO_2 – Overview," accepted for publication in *Acta Metall.*

3. Materials Sciences Division, CSIRO, Melbourne, Australia.

4. University of Illinois, Urbana.

5. Summary of material contained in a paper by P. F. Becher and T. N. Tiegs to be submitted to *J. Am. Ceram. Soc.*, 1986.

6. P. F. Becher, "Subcritical Crack Growth in Partially Stablized $ZrO_2(MgO)$," *J. Mater. Sci.* 21, 297–300 (1986).

3.2 BEHAVIOR OF POLYCRYSTALLINE TITANIUM DIBORIDE CERAMICS – P. Angelini, S. Baik, and P. F. Becher

Diboride ceramics have considerable interest as a result of their metal-like electrical conductivity and extremely high hardness, which approaches that of cubic boron nitride. As noted in our previous report, diborides are difficult to fabricate into dense components and are extremely brittle. While previous work showed that diborides could be densified with nickel additions, little was known of the details of the evolution of secondary phases during densification. That evolution now has been analyzed. Furthermore, studies that addressed the effects of the second phase on the mechanical properties have now been completed. Finally, we have completed studies of the influence of impurities on the densification of submicron powders in a joint effort with the Chemistry Division staff. These results are summarized in the following sections.

3.2.1 Processing and Microstructural Development in Liquid Phase Sintered and Pure TiB_2 Ceramics[1] – P. Angelini, P. F. Becher, J. Bentley, J. Brynestad,[2] M. K. Ferber,[3] C. B. Finch,[4] and P. S. Sklad

The fracture toughness and fracture strength of hot-pressed TiB_2 liquid phase sintered with nickel increased as a function of residual nickel content. Fracture strength was also found to increase with decreasing TiB_2 grain size. Electron microprobe analysis of similarly formed TiB_2-Ni compacts revealed the presence of a titanium oxide. Analysis of exuded material revealed a multicomponent system with the major phases being Ni_3B and Ni_2B. Minor phases included TiC, TiB_2, an intergranular Ti_xB_y, and a silicon-rich phase. A model for the liquid phase sintering reactions was developed. The model is based on reactions

between the titanium component (which results during the dissolution of TiB_2 with nickel) and dissolved oxygen or B_2O_3 (present as either impurities or oxide surface layers on TiB_2 powder).

3.2.2 Effect of Impurities on the Densification of Submicrometer TiB_2 Powders[5] – C. B. Finch,[4] P. F. Becher, P. Angelini, S. Baik, C. E. Bamberger,[2] and J. Brynestad[2]

As noted in other publications, the mechanical behavior of polycrystalline TiB_2 is quite sensitive to the grain size and grain-boundary-phase content achieved during densification. In the present study, it is shown that densification of submicrometer TiB_2 powder synthesized via reaction of titanium with BCl_3 could be achieved at 1400°C or higher by hot pressing, resulting in fine-grained materials with excellent mechanical properties. However, the ability to densify these powders is significantly affected by the impurities present. Nickel and iron contaminants in the as-synthesized powder were found to significantly lower the hot-pressing temperatures required to achieve full density. When the total content of these transition-metal species was reduced to well below 0.1 wt % it was not possible to achieve hot-pressed densities greater than 88% of theoretical, even at 1600°C. Previous observations reveal these two species segregate significantly to the TiB_2 grain boundaries and that enhanced densification is achieved with nickel additions by liquid phase formation. The current findings show that combined nickel plus iron levels of 0.3 wt % or more result in substantially enhanced densification. This behavior could be a result of liquid phase formation at interfaces or at least of enhanced boundary transport resulting from presence of the segregants at the grain boundaries.

Oxygen contamination, on the other hand, is a serious detriment to achieving densification. The current observations indicate that oxide species on the TiB_2 surfaces, and not TiO_2 or B_2O_3 second-phase particles, promote particle coarsening/neck formation by either vapor or surface transport instead of allowing densification to proceed when the oxygen content of the powder exceeds 1.5 wt %. The accompanying reduction in residual oxygen content when particle coarsening and desintering occur suggests that vapor transport plays an important role.

Incorporation of carbon into the TiB_2 has a dramatic influence on grain growth and densification by either sintering or hot pressing. Both normal and exaggerated grain growth are inhibited by carbon additions. This, of course, will promote densification because pore entrapment by grain-boundary migration is minimized. However, from the behavior of the TiB_2 powders with high (>1.5 wt %) oxygen levels, it is also obvious that the carbon also acts to sufficiently reduce the oxygen levels in the very early stages of sintering (e.g., by CO evolution) to allow densification to proceed to completion.

3.2.3 Effect of Residual Nickel Content on the Grain Size Dependent Mechanical Properties of TiB_2 (ref. 6) – P. F. Becher, C. B. Finch,[4] and M. K. Ferber[3]

The mechanical behavior of dense polycrystalline TiB_2 containing a Ni_3B boundary phase is influenced by the amount of this phase retained in the structure. Because the Ni_3B phase is a liquid at a hot pressing temperature of 1450°C, it is exuded from the compact; the final Ni_3B content can thus be controlled (e.g., by the time held at temperature under the ram pressure). The resultant fracture strength and toughness of the polycrystalline TiB_2 are observed to decrease as the retained nickel content is lowered below approximately 1.5 wt % for dense TiB_2 with an average grain size of either approximately 5 or approximately 12 microns as a result of changes in residual thermal expansion anisotropy stresses.

3.2.4 Study of the Kondo Effect and Intrinsic Electrical Conduction in Titanium Diboride[7] – R. K. Williams, P. F. Becher, and C. B. Finch

Electrical resistivity data for seven dense polycrystalline TiB_2 samples are reported. The data, which extend from 4.2 to 300 K, all show resistivity minima in the range 34 to 47 K, and this is attributed to the Kondo effect. Although the residual resistivity values varied by only a factor of about 2, the strength of the Kondo effect changed by a factor of 15. These differences are related to the effects of processing variables. The ideal resistivity of TiB_2 was calculated from the measurements and was found to vary about as T^5 at low temperatures. These values can be

adequately described by the Bloch-Grüneisen equation, and the characteristic temperature obtained from resistivity, 720 K, is in reasonably good agreement with the Debye temperature from specific heat measurements. A comparison of the electronic scattering part of the Bloch-Grüneisen constant shows that TiB_2 is a somewhat better conductor than titanium, and the electronic band structures of ZrB_2 and zirconium help to explain this difference.

3.2.5 Transport Properties of High-Purity, Polycrystalline Titanium Diboride[8] - R. K. Williams, R. S. Graves, and F. J. Weaver

Thermal conductivity data for several TiB_2 samples are presented, and the results for one sample extend from 80 to 400 K. These results show that the thermal conductivity attains a maximum value of about 130 W/m K at 140 K. An analysis of the results shows that this is caused by the electronic component of the thermal conductivity and that phonon conduction probably is significant also. Seebeck coefficient values agreed with the results of previous studies. The electrical resistivity of one sample was also determined to 1800 K. The results can be described by the Bloch-Grüneisen equation if the effect of thermal expansions is included.

3.2.6 Effect of Oxygen Contamination on Pressureless Sintering of Submicrometer TiB_2 (ref. 9) - S. Baik and P. F. Becher

The detrimental influence of oxygen as an impurity element during TiB_2 processing has been documented. In this study, attempts were made to correlate quantitatively the amount of oxygen present in the original powder with the pressureless sintering kinetics and final sintered microstructure. Due to the highly pyrophoric characteristics of submicron powder, the amount of oxygen present in the various stages of processing steps can vary a great deal, depending on the powder processing routes, contact media, and final firing conditions.

The results show that if the powder was exposed to air, water, or alcohol (or any organic solvent) containing oxygen, the final density achieved by pressureless sintering never exceeded 80% of theoretical density (TD). On the other hand if the powder was processed in contact with

nonpolar dispersants such as toluene, xylene, or hexane, oxygen contamination was limited to less than 3 wt %, and 98% TD could be obtained. However, the pronounced effect of oxygen contents is not limited only to the sintering kinetics; it also influences the final grain size. For instance, the powder contaminated with 2.9 wt % O_2 could be sintered to more than 95% TD at 1900°C with grain size of 20 to 50 μm, whereas those with 1.4% O_2 sintered to the same density but had much smaller grain size, 2 to 10 μm. The mechanism by which oxygen increases grain growth kinetics can be explained in conjunction with the beneficial effect of carbon as a grain growth inhibitor.

3.2.7 References

1. Summary of a paper to be published in *Proceedings of the 2d International Conference on Science of Hard Materials*.

2. Chemistry Division.

3. University of Illinois, Urbana.

4. Solid State Division.

5. C. B. Finch, P. F. Becher, P. Angelini, S. Baik, C. E. Bamberger, and J. Brynstad, "Effect of Impurities on the Densification of Submicron TiB_2 Powders," *Adv. Ceram.* **1**(1), 50–54 (1986).

6. Summary of a paper published in *J. Mater. Sci. Lett.* **5**, 195–97 (1986).

7. R. K. Williams, P. F. Becher, and C. B. Finch, "Study of the Kondo Effect and Intrinsic Electrical Conduction in Titanium Diboride," *J. Appl. Phys.* **56**(8), 2295–2302 (1984).

8. R. K. Williams, R. S. Graves, and F. J. Weaver, "Transport Properties of High Purity, Polycrystalline Titanium Diboride," *J. Appl. Phys.* **59**(5), 1552–6 (1986).

9. Summary of a paper to be published in *J. Am. Ceram. Soc.*

3.3 CERAMIC PROCESSING SCIENCE – A. Bleier and S. Baik

Thus far we have seen that when ceramics are appropriately formulated as to composition and fabricated to achieve full densification and the desired microstructure, the final components exhibit mechanical and other properties that are unique and/or markedly improved. An understanding of

how final composition, including alloying, and microstructural details in sintered components specifically influence toughness, strength, and other physical properties clearly allows us to describe critical compositional and microstructural parameters for desired applications. However, these insights do not tell us how to process desired dense ceramics routinely and reproducibly. Whereas pragmatism can lead to an improved understanding of important areas such as toughening mechanisms, it is inefficient in describing how to avoid defects and is incapable of predicting next-generation components. Thus, we also are systematically investigating the generic and specific mechanisms and processes underpinning the science of ceramic processing, especially those regarding control of powders and other aspects related to compositional uniformity and microstructural evolution. These problems are not always clearly defined for "single phase" ceramics and are certainly very poorly defined and often acute for ceramic composites (e.g., ZrO_2-toughened Al_2O_3).

We have thus launched a program of experimental and theoretical study into the processing of ceramics from powder precursors. Critical objectives are (1) to understand the fundamental principles controlling the green density of particulate compacts, (2) to identify the generic processing parameters that ultimately influence the evolution of fired microstructures, and (3) to develop predictive capabilities for extending the underlying physicochemical principles to any desirable ceramic system. Studies focus on powder synthesis, powder dispersion and suspension stability, and powder consolidation, with the goal of preparing readily densifiable green components. Components derived by aqueous processing of alumina and zirconia are emphasized.

The synthesis of uniform monoclinic zirconia, the pressure casting of alumina, and the implications of interfacial acid-base reactions on the consolidation of oxide powders constitute major research efforts. In the first one, nucleation and growth are manipulated with temperature and time to produce zirconia with a narrow size distribution, a modal diameter between 10 and 300 nm,[1] and a high specific surface area resulting from particulate porosity, Fig. 3.3.1. This ability permits critical examination of mechanical behavior related to grain size of zirconia,

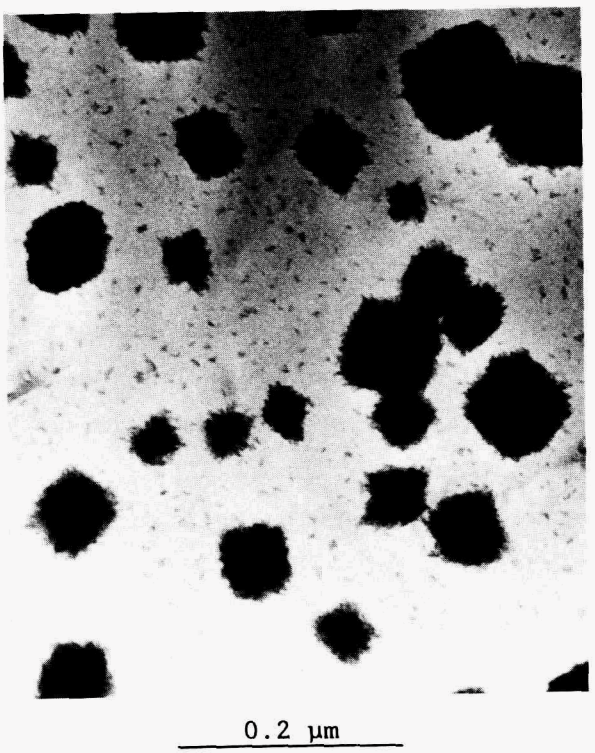

Fig. 3.3.1. Uniform ZrO_2 powder is produced by hydrothermal treatment of $ZrO(NO_3)_2$ at 98°C. The very fine particles are dimers and trimers composed of 3-nm ZrO_2 crystallites.

and distribution of the yttria stabilizer in transformation-toughened materials. Growth of particles in Fig. 3.3.1 has been clearly demonstrated to be one of "controlled" agglomeration of 3-nm m-ZrO_2 crystal.

The second effort focuses on processing alumina within a broad pH range in either the absence or the presence of anionic polymer; the electrochemical properties of powder, those of polymer, and their adsorption mechanisms are evaluated. Desirably low suspension viscosity at powder volume fractions exceeding 20% corresponds to surface charge saturation in polymer-free systems and to the degree of charge and the configuration of adsorbed polymer in those systems containing anionic deflocculant (Fig. 3.3.2); these factors are obtained from rheological studies, potentiometric titrations, and adsorption isotherms.[2] Finally,

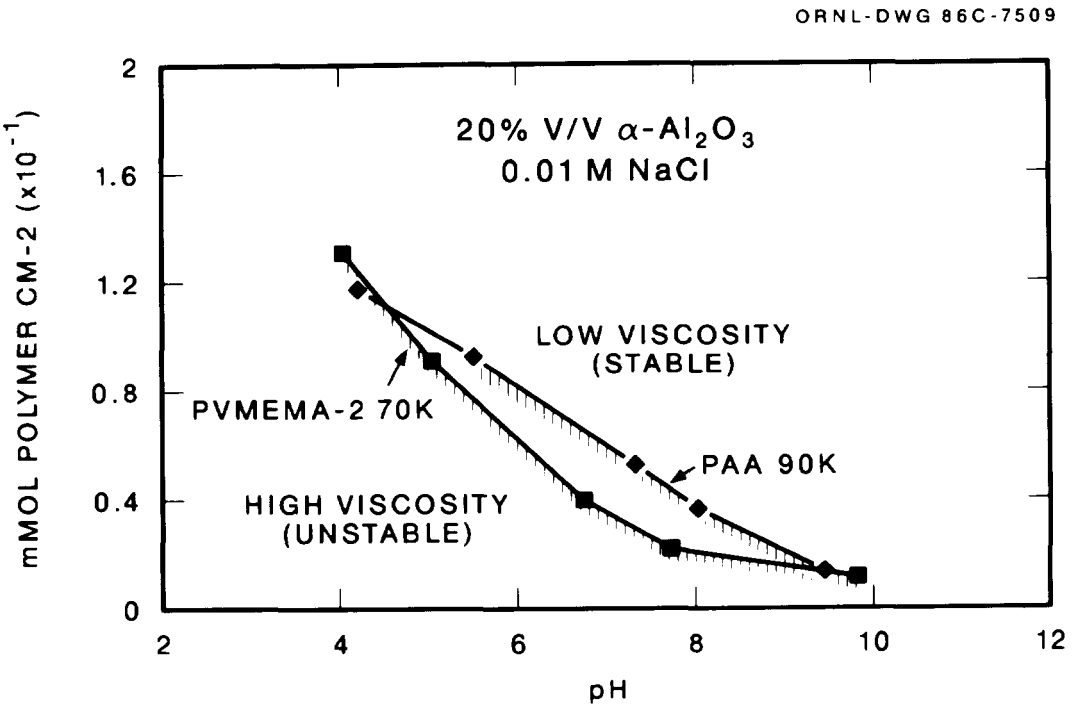

Fig. 3.3.2. Stability diagrams for Al_2O_3 suspensions in the presence of anionic polyacrylic acid (PAA) and polyvinyl methylethermaleic acid (PVMEMA) reveal conditions for forming stable low-viscosity suspension systems as a function of polymer content and pH of the suspension. Hatching (below each curve) represents conditions where extensive flocculation (agglomeration) occurs.

theoretical models[3] based on thermodynamic and heterocoagulation considerations indicate that not only chemical reactivity of oxide powders but also the solids content of suspensions can lead during consolidation to a critical reduction in electrostatic repulsion (Fig. 3.3.3), such that irreversible green microstructures are produced in single-component or composite pieces. These structures would subsequently affect the evolution of fired microstructures.

they relate to the *predictability* and *control* of ceramics processing for each area cited. The results are elucidating generic relationships among processing, green state, and fired microstructures by identifying fundamental principles. Broad predictive capabilities are leading to critical experiments for processing any desired oxide system, whether or not polymer additives are tolerable. A significant added advantage is that this effort is integrated with the structural mechanical studies described earlier.

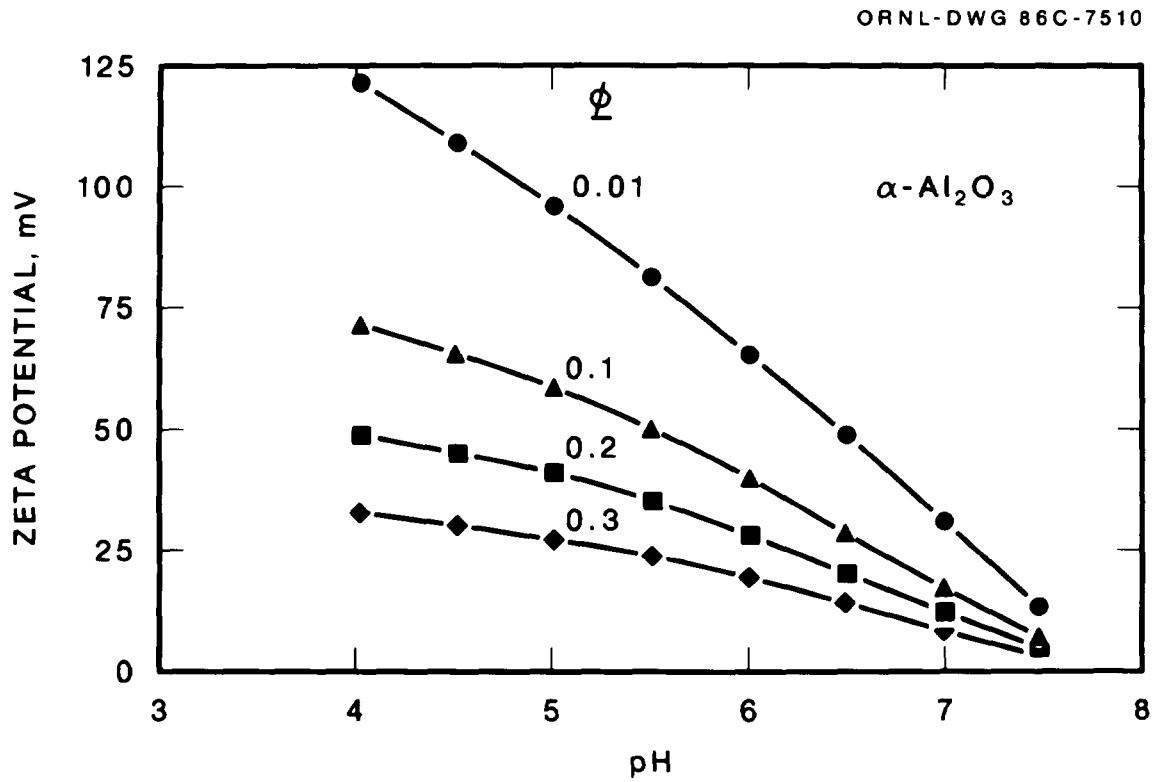

Fig. 3.3.3. Volume fraction of solids (ϕ) influences zeta potential in concentrated suspensions. The data reveal that each alumina's suspension, regardless of the value of ϕ, has an isoelectric point of pH approximately 8, but the effective repulsive potential decreases a given pH (<8) as ϕ increases.

3.3.1 Colloidal Preparation of Al_2O_3-ZrO_2 Composites[4] - S. Baik, A. Bleier, and P. F. Becher

Aqueous colloidal routes for processing binary suspensions containing Al_2O_3 and ZrO_2 were designed and tested in order to achieve homogeneous microstructures. Effects of particle size and size ratio of each component, pH, and electrolyte concentration of composite suspensions on sedimentation, green density, and ZrO_2 distribution in green compacts were defined. Processing conditions for prohibiting differential sedimentation without impairing green density can be optimized by controlling the Al_2O_3 to ZrO_2 particle size ratios. Overall suspension behavior for these composite systems was modelled by using the Derjaguin-Landau-Verwey-Overbeek approach, modified to account for surface acidity, ionic complexation, and

charge regulation. The specific role of colloidal forces was found to explain heterocoagulation and homocoagulation phenomena, such that green and fired microstructures could be explained and often predicted. Degrees of agglomeration and, therefore, ultimate states of mixing and consolidation were found to be sensitive to pH, i.e., ionic strength.

3.3.2 Surface Segregation of Sintering Additives or Impurities in α-Al_2O_3 (ref. 5) – S. Baik and C. L. White

Sintering of ceramic materials to theoretical densities often requires the addition of small amounts of sintering additives, less than 0.25 wt % MgO in Al_2O_3 for example. At the same time, certain impurities such as CaO in Al_2O_3 powder have to be controlled below a certain concentration level in order to achieve desirable shape and density through the sintering process. Unfortunately, the mechanisms behind such important industrial practices have not yet been understood. Now, it is generally accepted that magnesium helps sintering of Al_2O_3 by preventing pore-boundary breakaway up to the final stage of sintering so that pores can be removed by boundary diffusion. This research is characterizing the segregation behavior of impurities/dopants on the pore surface by heating α-Al_2O_3 single crystals (sapphire) doped with known amounts of magnesium and/or calcium. The enrichment of such dopants on various surfaces is observed by Auger electron spectroscopy (AES). Low-energy electron diffraction (LEED) apparatus is also used to study two-dimensional surface structural changes when such segregation occurs.

As shown in Fig. 3.3.4, calcium was found to segregate very strongly on the α-Al_2O_3 $(10\bar{1}0)$ plane above 1300°C. Between 800 and 1200°C, a relatively low level of calcium ($\leq$1 at. %) was observed, and its concentration was not sensitive to the total annealing time. At 1300° and above, calcium enrichment on the surface increased dramatically up to the level that one of every five aluminum ions is replaced by calcium ions, which corresponds to a surface-to-bulk enrichment factor, X^s_{Ca}/X^b_{Ca}, of about 5×10^3. In the range 1300 to 1500°C, X^S_{Ca}/X^S_{Al} generally follows the equilibrium segregation behavior, which can be expressed by the Langmuir isotherm:

$$\frac{X^s}{1 - X^s} = \frac{X^b}{1 - X^b} \exp - \frac{\sigma H_s}{k_T} , \quad (1)$$

where X^s and X^b represent surface and bulk concentration, and σH_s represents a heat of surface segregation that is estimated at 2.5 ± 0.5 eV/atom.

The sharp increase in surface calcium concentration above 1300°C was concurrent with the 2-D surface phase transformation as observed by LEED. The 1 × 2 structure started appearing above 1000°C and changed to

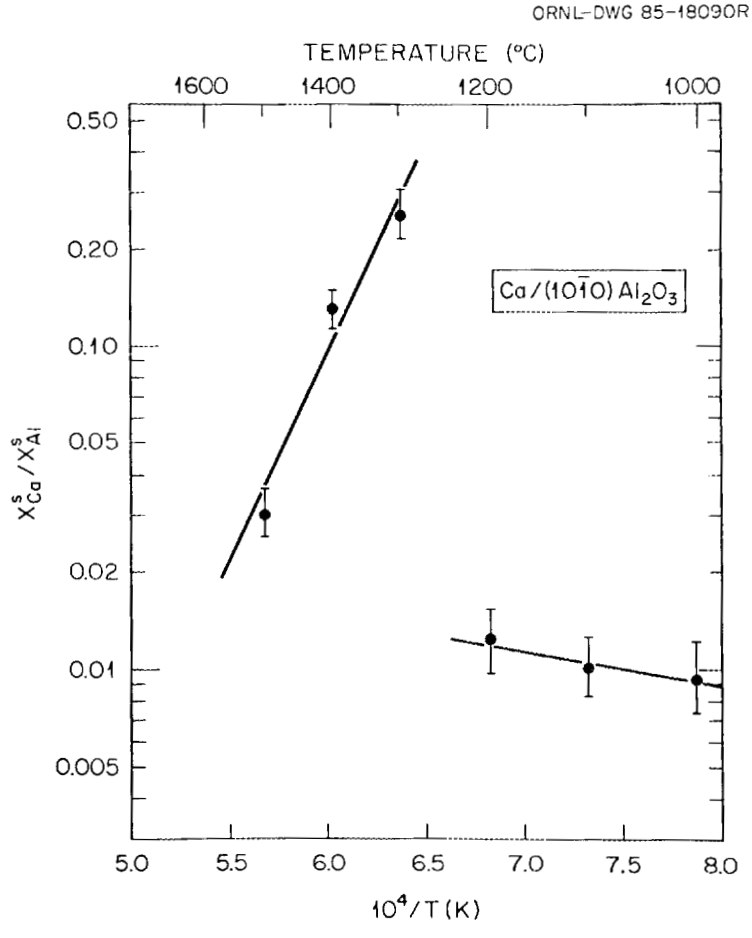

Fig. 3.3.4. Calcium enrichment occurs on the (10$\bar{1}$0) surface of single-crystal Al_2O_3 doped with 50 ppm CaO. After annealing at 1300°C, approximately one quarter of the aluminun sites on the surface are replaced by calcium ions.

the 2 × 2 structure at 1300°C. The mechanisms for the generation of such structures observed in the LEED patterns developed on the Al_2O_3 $(10\bar{1}0)$ plane, and whether strong calcium segregation induced the surface phase transformation, are currently under study. However, from the fact that annealing times, thus kinetics, play an insignificant role in calcium concentration and surface phase formation, it is highly possible that strong calcium segregation is likely to be induced by 2-D phase transformation and subsequent change in surface energy.

3.3.3 References

1. S. Spooner, P. Angelini, A. Bleier, P. F. Becher, W. D. Bond, and J. Brynestad, "Investigation of the Synthesis and Processing of Submicron Ceramic Powders by TEM and Small Angle X-Ray Scattering (SAXS)," p. 3 in *Extended Abstracts American Ceramic Society 87th Annual Meeting*, American Ceramic Society, Columbus, Ohio, 1985.

2. (*a*) A. Bleier, C. G. Westmoreland, and M. A. Janney, "Rheology of Concentrated Alumina Suspensions Containing Anionic Polymer," Summer Meeting, American Institute of Chemical Engineers, Seattle, August 1985. (*b*) J. Cesarano, I. A. Aksay, and A. Bleier, "Interaction of Polymethacrylic Acid with α-Al_2O_3 in Aqueous Suspensions," Paper No. 344, 59th Colloid and Surface Science Symposium, American Chemical Society, Potsdam, N.Y., June 1985.

3. (*a*) W. C. Hasz and A. Bleier, "Surface Reactivity of Silica and Alumina Ceramic Powders," in *Advances in Materials Characterization II*, Materials Science Research, vol. 19, ed. R. L. Snyder, R. A. Condrate, Sr., and P. F. Johnson, Plenum Press, New York, 1985, pp. 189– 201. (*b*) M. Strauss, T. Ring, A. Bleier, and H. K. Bowen, "Coagulation in Processing of Ceramic Suspensions: Powder Size Distribution Effects," *J. Appl. Phys.* **58**(10), 3871–79 (1985).

4. Abstract of a paper presented at the Materials Research Society 1986 Spring Meeting and to be published in the proceedings entitled *Better Ceramics Through Chemistry*.

5. Summary of a paper to be published in *J. Am. Ceram. Soc.*

4. RADIATION EFFECTS

L. K. Mansur

The Radiation Effects Task aims to develop an understanding of the mechanisms by which neutron irradiation and ion beam treatments alter physical and mechanical properties of metals and alloys. While microstructural characterization forms a large part of the effort, development of a fundamental understanding of mechanisms is the major pursuit. The scope includes processes associated with the evolution of microstructure and microcompositon. An integrated theoretical and experimental approach is brought to bear on major problem areas.

The chief observational technique used is analytical electron microscopy for the direct observation of microstructural and microcompositional changes. For producing damage or altered materials, both neutron and ion irradiations are used. The Fast Flux Test Facility (FFTF), Experimental Breeder Reactor-II (EBR-II), High Flux Isotope Reactor (HFIR), and Oak Ridge Research Reactor (ORR) are the reactors used. Charged-particle bombardments are carried out with our dual 5-MV Van de Graaff- 0.4-MV Van de Graaff accelerator facility. Nuclear microanalysis techniques that use accelerated ions to probe chemical composition as a function of depth in the target are being exploited. We are increasing our efforts in ion beam mixing and ion implantation to more fully exploit the experimental research capabilities developed in this task. In addition, a straining chamber is being developed for embrittlement studies using proton beams on the 5-MV Van de Graaff accelerator. Together with a new tritium trick facility and the reactors, this will allow more mechanistic research into embrittlement than has heretofore been undertaken. Recently, we have begun an irradiation program in ceramics. Though ceramics are more complex, and relatively little is known about their irradiation response, this research benefits from our extensive theoretical and experimental work on metals and alloys.

The theory of radiation effects receives major emphasis in this task. We have made major contributions to the framework of the rate theory description. Modeling the effects of charged-particle bombardment has been an important activity. In alloys, precipitates are also often an important feature of the microstructure. The theory has been further developed to treat a variety of mechanisms affecting damage response in alloys with precipitates. Recently, we have attacked a new problem that can be regarded as a profound phase instability - radiation-induced amorphization - with a new theoretical approach. Important progress has been made to improve the rate theory description of microstructural evolution based on point defect reactions. Emphasis recently has been placed on the roles of gas in affecting swelling and microstructural evolution, especially with reference to helium transmutation production. We have developed a more comprehensive computer model to include many of the phenomena whose descriptions have been worked out previously. A major achievement has been to develop a new theoretical framework, cascade diffusion theory, to account for the discrete nature of point-defect production as it affects local point-defect fluxes. It has revealed a new mechanism for irradiation creep and has been useful in interpreting our recent pulsed irradiation experiments.

This task is performed in the Materials Science Section of the Metals and Ceramics Division, a unit that includes applied research on related problems in programs for magnetic fusion reactors and ion beam modification work. The fusion reactor program is part of a national alloy development program supported by the Office of Fusion Energy coordinated by Oak Ridge National Laboratory (ORNL). Research also covers the related area of ion beam modification supported by the Office of Basic Energy Sciences. Work on this program complements the activities of the ORNL Solid State Division, now focussed on the new National Low-Temperature Neutron Irradiation Facility (NLTNIF) and on research in beam-solid interactions. Our facilities have been used by a number of industrial organizations and laboratories in connection with the applied programs and by

numerous universities supported by the Basic Energy Sciences Program and by other programs. Numerous collaborations are maintained. International cooperation is maintained through exchanges of personnel, collaborative research, and information exchange with the British, German, French, and Japanese materials establishments.

4.1 NEUTRON AND CHARGED-PARTICLE IRRADIATIONS

4.1.1 Radiation Embrittlement at Elevated Temperatures – K. Farrell

A new research program in this task addresses radiation embrittlement at elevated temperatures, specifically intergranular failure and associated loss in ductility. This encompasses helium embrittlement (abbreviated HeE) and the newly recognized phenomenon of radiation-induced solute segregation and precipitation (labeled RIS/P). Helium embrittlement involves the stress-assisted growth and interconnection of helium bubbles on grain boundaries. Although some aspects of HeE are well established, there are some large gaps in our knowledge. Signs that some metals might have inherent resistance to HeE have not been pursued. The roles of plastic strain and of helium migration rates are unknown. The effects of impurities have been ignored despite much evidence from other grain boundary disciplines indicating segregated impurities as a primary cause of intergranular weakness. The latter takes on particular significance when RIS/P is considered.

Radiation-induced solute segregation and precipitation is believed to arise by correlated drifts of solute atoms with the fluxes of radiation-produced point defects to sinks such as dislocations, voids, and grain boundaries. The degree of segregation is much worse (and also covers other segregants) than in thermal segregation, and it can cause phase changes in systems that would otherwise remain stable. This segregation means that grain boundary regions will have altered compositions. Consequently, mechanical properties will change. Our experiments will identify and characterize RIS/P embrittlement and distinguish it from contributions by matrix hardening and HeE. The work covers the temperature range 0.3 to

0.5 T_m, where significant overlap of mechanisms is expected. This temperature range is highly pertinent to the operating temperatures of fusion and fission components.

In this context, we are investigating HeE and RIS/P and their interactions on heavily irradiated, complex commercial-type alloys as well as on selected, simple model systems. Additionally, migration of helium is being measured. The efforts making up this integrated program are described below.

4.1.1.1 Embrittlement of Commercial-Type Alloys

During the processing and irradiation of our simpler alloys, we began the study of complex technological alloys. Three alloys were made available in heavily irradiated condition from the Breeder Reactor Alloy Development program. Two of these alloys, designated D21 and D25, are based on the austenitic fcc Fe-Cr-Ni system, hardened with fine precipitates of γ' phase. These fail intergranularly with little strain, at the irradiation temperature of about 600°C; they also break along the grain boundaries at room temperature, which is not characteristic of HeE. The third alloy, HT-9, is a Fe-12Cr-1Mo alloy with a bcc tempered martensite structure. It remains tough after irradiation. Specimens of these materials were broken in our Auger electron spectrometer in ultrahigh vacuum with a stage designed for this purpose, and the chemical compositions of the newly opened fracture surfaces were measured. The findings are described in other summaries in this section.

In the γ' alloys, the chemical complexity of the grain boundary regions prevents unambiguous identification of the cause of embrittlement. However, other investigators of these alloys claim that the culprit is the γ' phase, Ni_3Si. Since Ni_3Si is known to be created and/or redistributed readily under irradiation, it warrants further investigation in simple systems where its segregation behavior and embrittling effects can be assessed without interference from other processes. Accordingly, we prepared some simple nickel-based and iron-based alloys containing the γ' formers silicon, aluminum, and titanium. These model alloys are now undergoing neutron irradiation. One of them, Ni-4 wt % Si, has also been

subjected to ion bombardments under tensile stress in cooperation with researchers at KFA Jülich as described elsewhere in this section (see Sect. 4.1.4).

4.1.1.2 Helium and Lithium Doping

The method of tritium absorption and decay to helium-3 known as the "tritium trick" is being used to dope helium into bulk creep specimens without causing displacement damage and associated RIS/P. This will help us separate the effects of solute segregation and hardening during irradiation from the effects of helium transport alone to grain boundaries. Doping is done at elevated temperatures, 600°C for steels, to simulate appropriate irradiation temperatures. Safety considerations restrict the tritium pressure to a maximum of 1 atmosphere. This is more than adequate for doping materials such as zirconium and titanium that have high solubilities for tritium. But in steels the solubility of tritium is small at 1 atmosphere pressure; less than 1 appm helium can be introduced during a three-week treatment. This limitation has discouraged researchers from using this technique for steels, the assumption being that there will not be enough helium bubbles to cause embrittlement. This assumption is not totally true. It is valid only if there are many traps, i.e., damage microstructure, that restrict migration and coalescence of helium and vacancies. Without such trapping, we estimate that as little as 1 appb should provide ample bubbles to ensure HeE. In keeping with this view, we are finding many grain boundary helium bubbles in specimens doped to an estimated helium level of 0.2 appm. Encouraged by these findings, we are now doping to even lower levels. These specimens will allow us to study the hitherto unexplored region of HeE at very low helium concentrations.

We also are placing emphasis on large helium concentrations of the order of hundreds of appm relevant to future fusion reactors. To obtain these quantities in steels by using the tritium trick, a novel modification is being explored. This applies an electrical glow discharge during tritium exposure, boosting the uptake of tritium.

In furtherance of our thesis that trace impurities, as well as RIS/P products, may affect embrittlement, we are investigating selected impurity

elements. The first is lithium. Lithium may have had adverse but unrecognized effects on the results of many early HeE tests on steels. In these tests the helium was generated by burnup of the boron-10 isotope, which also produced lithium-7 as a sister product. Boron is a common impurity or alloy addition. The lithium by-product has been regarded as benign. We are finding otherwise on the basis of special melts of our test materials doped with ppm levels of lithium and creep tested. The preliminary results on austenitic alloys and iron show intergranular embrittlement that increases with decreasing strain rate. These features are similar to those of HeE, but these specimens do not contain helium. Tests with implanted helium will help separate the effects of helium and lithium.

4.1.1.3 Neutron Irradiations

The alloys for the RIS/P studies and some materials doped with lithium are now being irradiated in the FFTF and in the Oak Ridge Research Reactor (ORR) as described elsewhere in this section. Included in these irradiations are some materials intended to test fragmentary evidence indicating that bcc ferritic alloys are more resistant to HeE than fcc stainless steels, and that hcp titanium and zirconium are even more resistant than iron. If this apparent trend is substantiated, we will examine mechanisms underlying the differences.

4.1.1.4 Helium Migration

Very little is known about the migration of helium in metals, a topic that is crucial to understanding HeE. Even the available data are subject to severe experimental limitations and to deserved criticism. To provide more information pertinent to the present research, the movement of helium is being measured by using ion beam analysis techniques. First results are described elsewhere in this report.

4.1.1.5 New Facilities

To continue the ion bombardments under applied stress begun at KFA Jülich, we have built a stressing device for the Oak Ridge National

Laboratory (ORNL) accelerator facility. This device is undergoing final tuning and commissioning and is described elsewhere in this report.

The idea of using a glow discharge system to promote the absorption of tritium in steels and in other metals of low tritium solubility requires demonstration and parameterization. It is undesirable and unnecessary to do this preliminary experimentation in the tritium facility. Therefore a mockup hydrogen charging apparatus in which to map operating conditions using hydrogen gas has been fabricated. This unit also provides the necessary hydrogen-treated control specimens to match the tritiated specimens in our embrittlement experiments. (This apparatus can be used with other gases and offers applications in the fields of hydrogen embrittlement, nitriding, and carburizing.)

Specimens doped with helium by the tritium trick remain slightly contaminated with tritium. They must be handled and tested in enclosures with special venting. For mechanical tests we are sharing space in a large enclosure with the Fusion Reactor Materials program. We are now building two dedicated vacuum-creep machines for installation in this enclosure. These machines are designed for easy access to the specimen and for rapid specimen exchange to further minimize operator exposure to tritium.

4.1.2 Complementary AES and AEM of Grain Boundary Regions in Irradiated γ' Alloys[1] — K. Farrell, N. Kishimoto,[2] R. E. Clausing, L. Heatherly, and G. L. Lehman[3]

As an initial part of our radiation embrittlement program we are investigating some instances of brittle intergranular failure discovered in some developmental alloys. These alloys are based on the austenitic 55Fe-25Ni-10Cr-1 wt % Mo system. Several percent of each of the γ'-forming elements Al, Si, and Ti are added to produce a fine dispersion of the Ni_3X γ' phase in the heat-treated condition. One of these alloys, now identified as D25, was described in the annual progress report for 1984 (ORNL/TM-9357, pp. 103–104). There, data from Auger electron spectroscopy (AES) of the brittle fracture surfaces showed depletion of Fe at the surface, and enrichment of Mo, Si, Ti, and P. Below the fracture surface, at depths of 80 to 150 nm, the Fe, Ni, and Si concentrations

approached the bulk alloy levels. Transmission electron microscopy examination revealed that the grain boundaries were covered with precipitate particles. Analytical electron microscopy (AEM), using energy-dispersive X-ray analysis, and electron diffraction patterns have now identified the precipitates. They are predominantly the FeMo Laves phase interspersed with the Ni-, Si-, and Ti-rich G phase, and a sprinkling of γ' particles. These phases account for the segregation found in the AES examination. Unfortunately, they cannot be recognized exclusively as the cause of brittle fracture because two other possible candidates are also observed. One of these is gas bubbles on the grain boundaries and the particle-matrix interfaces. The other is a narrow region each side of the grain boundaries that is denuded of the fine γ' dispersion prevalent throughout the grains. Either of these features could provide a low-resistance path for fracture.

Study of a second alloy, designated D21, which contains more Ni and Ti and less Mo than D25, is now complete. A bar graph of the bulk analysis of D25 is shown in Fig. 4.1.1 together with AES analyses of the intergranular fracture surfaces. The elements Si, Ti, Ni, and Al are segregated at the fracture surfaces at the expense of Fe and Cr. After sputtering away the top layers to a depth of 250 nm, the segregation disappears. Transmission electron microscopy shows complete coverage of grain boundaries with precipitate particles. There are also gas bubbles and γ'-denuded regions about 200 nm wide. The precipitates are identified as primarily the Ni-, Si-, and Ti-rich G phase with small fractions of Laves and γ'. An example of an AEM trace across overlapping G phase particles on a grain boundary is given in Fig. 4.1.2. The enrichment in Ni, Si, and Ti and the depletion of Fe and Cr agree with those detected by AES and are obviously connected with the grain boundary phases. There is also an indication in Fig. 4.1.2 of segregation of Ni at distances from the grain boundary phases corresponding to the widths of the γ'-denuded regions. As with D25, a specific cause of embrittlement cannot be distinguished.

These studies illustrate the complementary nature of AES and AEM and the good quantitative agreement available between the two techniques. They also demonstrate the need to go beyond local chemical analyses to

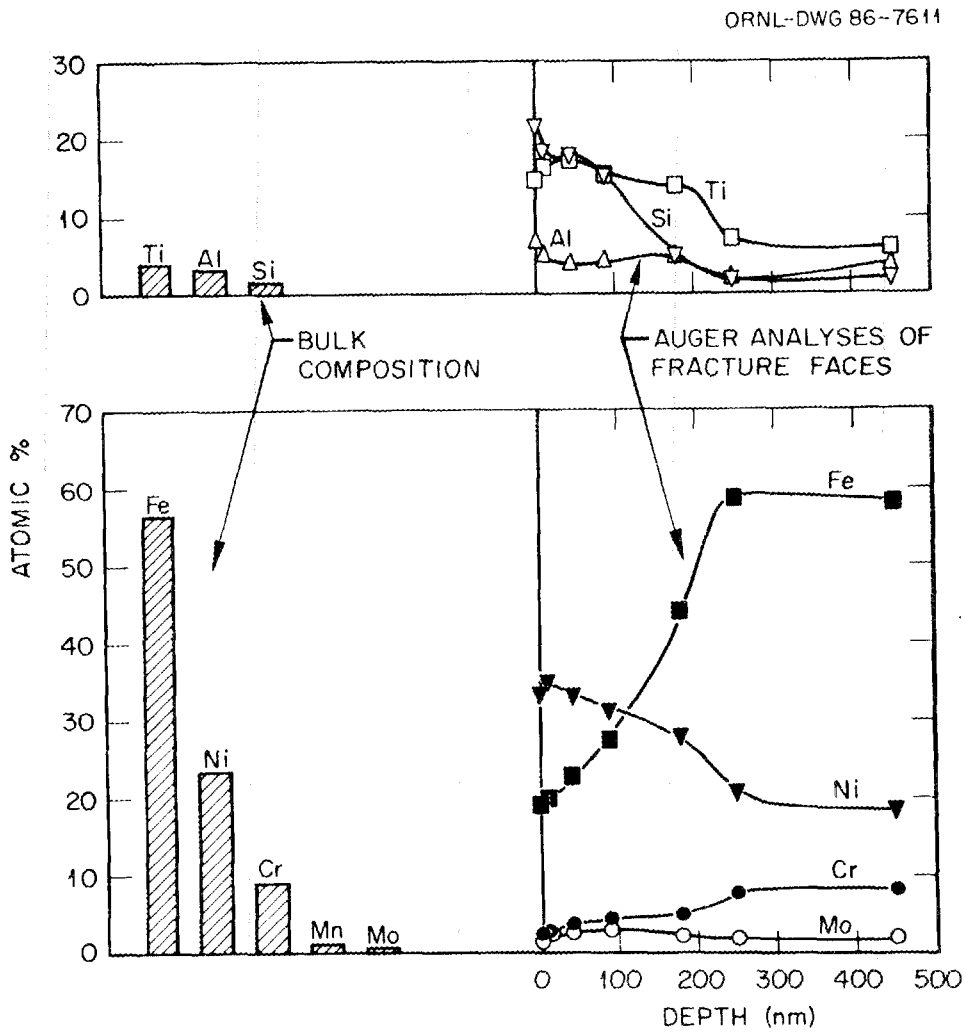

Fig. 4.1.1. Chemical compositions of intergranular fracture surfaces compared with bulk compositions.

seek the mechanism(s) of embrittlement. And above all, they emphasize the unsuitability of complex alloys for unraveling the mysteries of embrittlement phenomena.

4.1.3 Radiation Effects Possibly Leading to Embrittlement in the Alloy HT-9 – R. E. Clausing, L. Heatherly, Jr., R. G. Faulkner,[4] and K. Farrell

Radiation-induced segregation that contributes to embrittlement can occur as the result of point-defect gradients and solute-defect coupling. Since point-defect gradients occur at defect sinks, the solute segregation occurs predominantly in the vicinity of extended defects such as free surfaces, grain boundaries, interphase boundaries, dislocations, and voids

ORNL-PHOTO 1731-86

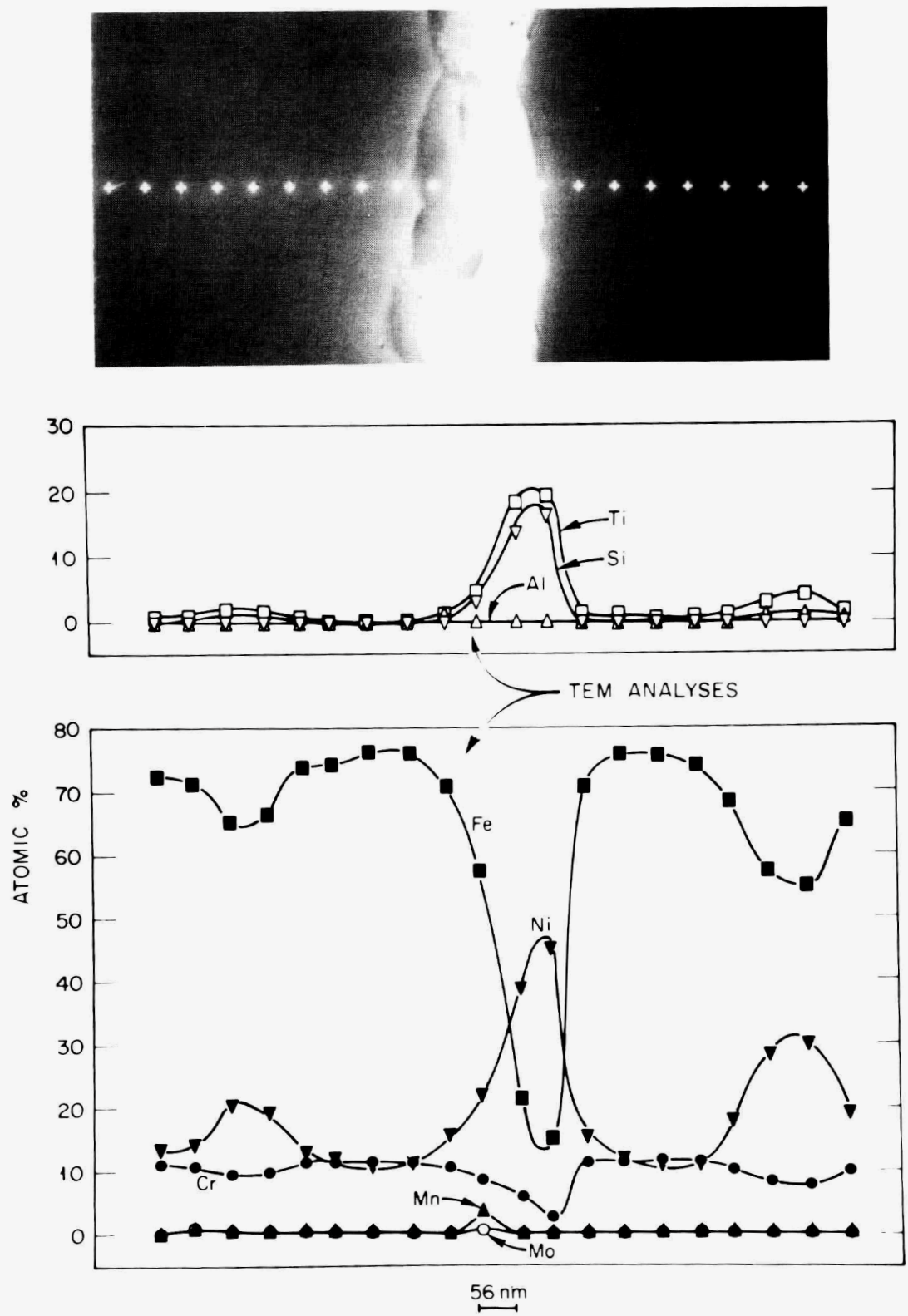

Fig. 4.1.2. Analytical electron microscopy trace across precipitate phases on a grain boundary.

and gives rise to enrichment or depletion of particular alloying or impurity elements. Significant enrichment may give rise to formation of precipitates. These microchemical changes may affect the properties of these alloys. In cases where an alloy shows embrittlement associated with grain or phase boundaries, the compositional changes in the vicinity of the boundaries may play an important role in the reduction of ductility.

In this respect, we are studying the chemical compositions of grain and other microstructural boundaries in irradiated alloys known to suffer embrittlement or loss of ductility due to irradiation. We have studied several austenitic Fe-Ni-Cr alloys previously. Ferritic/martensitic steels appear to be possible alternates to Fe-Ni-Cr alloys for fusion reactor first walls and fast reactor core materials due to their apparently superior performance in fast neutron fluxes. However, these alloys have been shown to suffer a significant increase in the ductile to brittle transition temperature (DBTT) as the result of irradiation. The increase in DBTT is accompanied by an increase in the proportion of grain boundary fracture. It is known that thermally induced segregation to interfaces in these alloys can cause increases in the DBTT. It has also been postulated that the high density of interfaces in the ferritic/martensitic steels may be responsible for their otherwise apparently good resistance to radiation-induced loss of ductility at elevated temperatures. (By sharing the segregation with so many sinks, the segregation to any one surface is reduced.)

We are studying the segregation in irradiated specimens of the ferritic/martensitic HT-9 alloy, Fe-12Cr-1Mo. The study is difficult both because the microstructure is complex and because it is difficult to expose microstructural boundaries for analysis by scanning Auger electron spectroscopy because of the often ductile fracture habit. Thinning of irradiated specimens for transmission electron microscopy has also been a problem. Through the use of a low-temperature impact fracture apparatus we have, however, exposed a limited amount of grain boundary and lath packet boundary area for analysis. We also have had limited success with hydrogen embrittlement as a way of exposing microstructural interfaces.

Annealed and tempered specimens were irradiated for 15,000 hours in EBR-II to a fluence of 2.8×10^{26} n/Em^2 (14 dpa) at 408, 519, and 564°C.

Control specimens were given similar thermal treatments. Lath and lath packet boundaries were found to be strongly enriched in phosphorous, silicon, and chromium in the specimen irradiated at 408°C as shown in Fig. 4.1.3. The nickel was low at the fracture surface but increased to 6 to 8 at. % in a region beyond 10 nm from the fracture surface. No significant variation from bulk composition was detected on areas exhibiting ductile fracture features. Little segregation of any kind was detected for the higher-temperature irradiations. The 408°C thermal control specimen showed some interfacial segregation, but it was not as great nor did it extend as far into the specimen as in the irradiated material.

This work is not yet complete, but we believe that the results are consistent with the suppositions that radiation-enhanced segregation contributes to the increase in the DBTT and that the very fine microstructure of these materials may help limit segregation during irradiation.

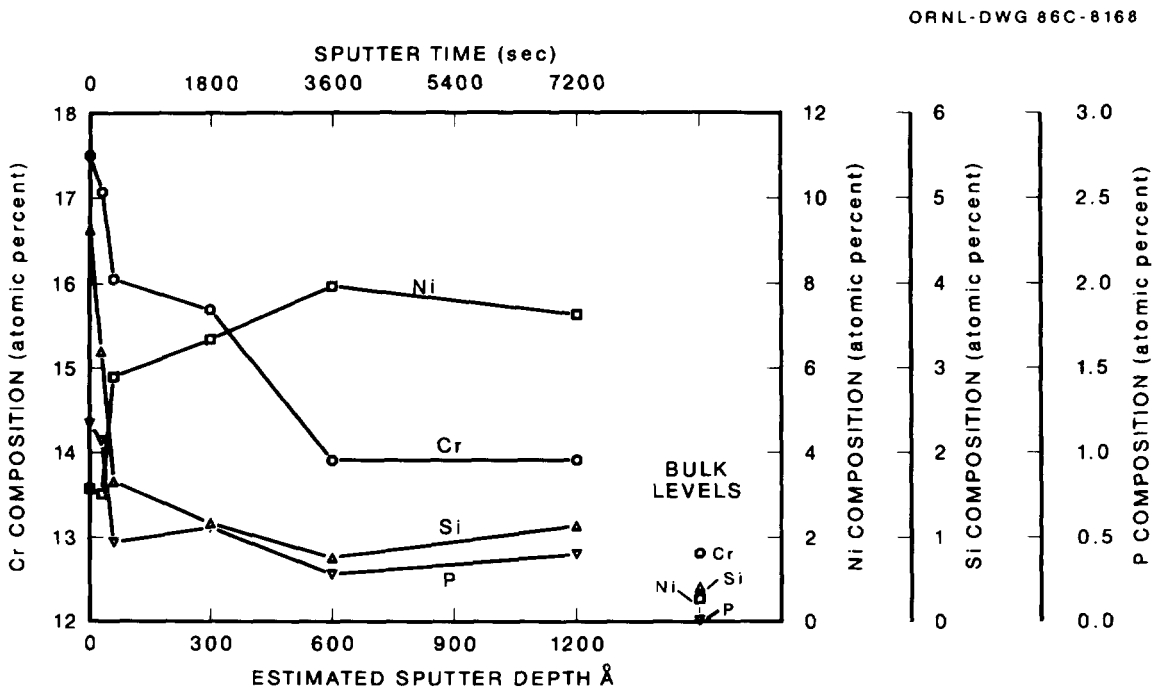

Fig. 4.1.3. Composition as a function of depth from the fracture surface of an HT-9 specimen irradiated at 408°C. The area chosen for analysis was thought to be a lath packet boundary.

4.1.4 Radiation-Induced Segregation in Light-Ion-Bombarded Ni–8% Si (ref. 5) – N. H. Packan, L. Heatherly, W. Kesternich,[6] and H. Schroeder[6]

Radiation-induced segregation (RIS) is an active research area because RIS processes are capable of undermining the performance of structural alloys exposed to radiation. An element often added to austenitic stainless steels to suppress void swelling, silicon, is also particularly active in RIS. Numerous studies of the model system nickel-silicon have established that silicon readily concentrates at defect sinks such as dislocation loops, cavities, and the external surface, even by doses well below 1 dpa. In high-nickel commercial type alloys, we have indeed found that radiation-induced embrittlement is a problem. Generation of an intermetallic phase like Ni_3Si at grain boundaries as a result of RIS might lead to embrittlement, especially in the presence of transmuted or injected helium. These investigations accordingly have sought to quantitatively assess RIS to grain boundaries in a simple alloy, compare it with RIS to the external surfaces, and look for changes in mechanical behavior with and without helium injection.

The material studied was Ni–8 at. % Si, in the form of tensile specimens of overall size 28 mm × 8 mm × 0.060 mm thick (8 × 2 × 0.060 mm in the gage section), annealed 10 min at 1073 K in vacuum. Bombardments generating bulk damage levels of 0.1 to 0.3 dpa have been conducted with either 7-MeV protons or 28-MeV alpha particles from the compact cyclotron at the Jülich Nuclear Research Facility, Jülich, West Germany. The temperature was 750 K, expected to be the peak temperature for RIS effects. Certain specimens were preimplanted with 250 to 1000 appm helium at 973 K, while all the alpha-bombarded specimens incurred 750 appm helium per 0.1 dpa in the course of their damage-generating irradiation.

Postirradiation tensile tests at Jülich conducted at 293 and 723 K revealed no substantial differences between the proton-bombarded specimens and unbombarded controls, both exhibiting fully ductile (chisel-edged) fracture profiles and at least 25% elongation (Fig. 4.1.4). The alpha-bombarded specimens also showed ductile fracture with somewhat lower (17–18%) elongation values. Only the specimens that were deliberately

ORNL-PHOTO 0496-86

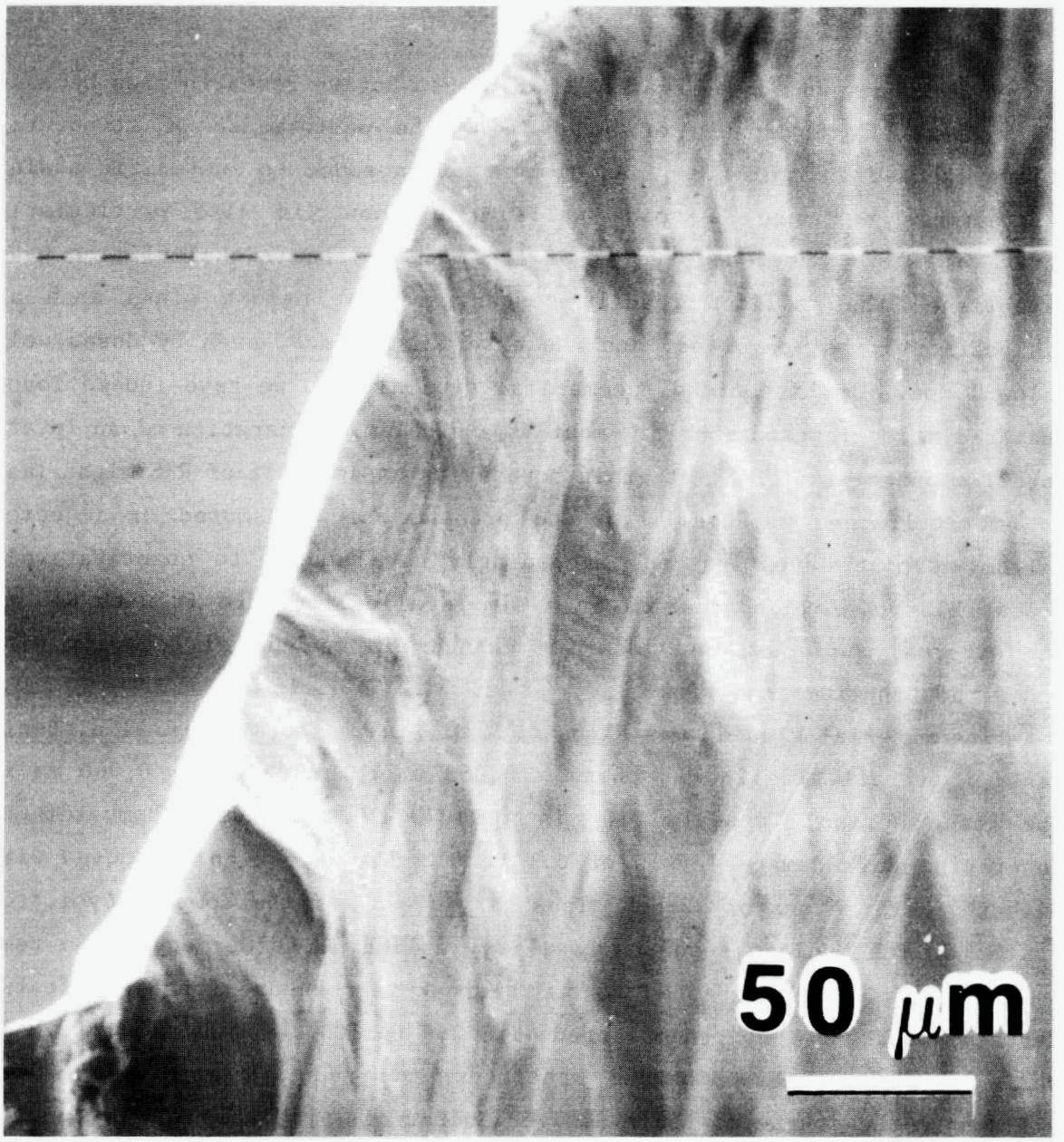

Fig. 4.1.4. Ductile fracture exhibited by Ni-8 at. % Si bombarded with 7-MeV protons at 750 K to a dose of 0.1 dpa and subsequently tested at 723 K.

embrittled by the 973-K preimplantation of helium fractured in an intergranular mode when pulled at 973 K inside ORNL's scanning Auger microprobe, thereby exposing grain boundary surfaces for depth-profile analysis. It was found that RIS of silicon to outer surfaces gives rise to a strongly enriched (20 to 30% Si) surface layer 20 to 30 nm thick followed by a shallow depletion zone for the next 1.0 to 1.5 μm, in agreement with previous studies in the literature. In contrast, silicon segregation to grain boundaries varied from boundary to boundary but generally exhibited a more gradually decreasing silicon profile and no depletion zone. Observations of silicon profiles and Ni_3Si formation at grain boundaries have also been obtained by analytical transmission electron microscopy (TEM) at ORNL.

By using very fine electron-beam probes of about 2-nm diameter, microchemical profiles across the grain boundaries were measured by energy-dispersive X-ray analysis, and the formation of ordered γ' phase (Ni_3Si) was investigated by TEM dark-field imaging. At irradiation doses of about 0.15 dpa, γ' layers of 10- to 30-nm thicknesses were formed at almost all grain boundaries (Fig. 4.1.5). The γ' layers were found to be generally asymmetric, with γ' phase located only on one side of the grain boundaries. There was an exception for coherent twin boundaries, where the γ' phase always grew symmetrically into both grains. The γ' layers did not appear to consist of a continuous solid phase but revealed fine-scale substructure.

Additional experiments are planned to correlate the extent of radiation-induced segregation to grain boundaries with mechanical behavior in this and other alloys. The ability to bombard ribbon specimens under a specific static tensile stress provided by our new straining chamber will be employed in these experiments.

4.1.5 Irradiations in the Fast Flux Test Facility – N. H. Packan and K. Farrell

Three sets of experiments have been or are being carried out by using available space in the Materials Open Test Assembly (MOTA) Facility of the Fast Flux Test Facility (FFTF) reactor. The common purpose is to study

ORNL-PHOTO 0498-86

Fig. 4.1.5. Dark-field transmission electron micrograph of Ni_3Si phase coating dislocation loops and a grain boundary in Ni–8 at. % Si bombarded with 7-MeV protons at 750 K to a dose of 0.13 dpa.

the effects of irradiation on microstructure and, for some specimens, mechanical properties in a variety of new materials and research alloys. The list of materials comprises five different Fe-Cr-Ni alloys; eight Fe-Cr-C compositions; three types of metallic glasses; three varieties of nickel aluminides; and two groups of fourteen alloys featuring controlled additions of Si, Ti, B, P, C, and Nb to Fe-13Cr-15Ni and Fe-13Cr-15Ni-2Mo-2Mn base compositions.

In the first experiments, "disk packet" tubes containing transmission electron microscopy (TEM) disks were irradiated in cycles 4 through 6 for periods of 109.5 effective full power days (cycle 4) to 366.2 EFPD (cycles 4-6). For irradiation temperatures in the range 470 to 490°C, doses of 0.2 through 35 dpa were attained (fluence range 2.7×10^{20} to 7.8×10^{22} n/cm^2). Generally higher doses (15 through 44 dpa) were experienced by specimens in the 550 to 585°C regime. Microstructural examinations of these disks will now be made by the respective investigators: L. L. Horton for the ternaries and ferritics, N. H. Packan for the metallic glasses and nickel aluminides, and E. H. Lee for the two Fe-Ni-Cr base alloy sets.

The second experiments utilized a small collection of nickel binary alloys (Ni-1% Al, Ti, Si, or 8% Si) and a few of the Fe-13Cr-15Ni alloy series developed for phase stability studies in the form of miniature fracture bars designed to be broken in our ultrahigh-vacuum Auger spectroscopy system to allow chemical analyses of fracture surfaces free from atmospheric contamination. These specimens fit within the TEM tubes and were irradiated in cycles 5 and 6, 256.7 EFPD, in spaces vacated by some of the above-mentioned first sets of TEM disks. The fracture bars attained doses of 3 and 23 dpa at 470°C, 2 dpa at 490°C, 27 dpa at 550°C, and 25 dpa at 585°C.

The third specimen set is in the FFTF currently (cycles 7 and 8, from August 17, 1985, until summer 1986). In this series, small flat tensile specimens have been substituted for the miniature fracture bars of cycles 5 and 6. Mechanical properties data from the specimens will complement the TEM microstructure and fractographic analyses made on the same materials in cycles 5 and 6. This work will help isolate the effects of helium and solute segregation on radiation-induced embrittlement.

4.1.6 Effect of Minor Alloying Elements on Phase Stability in Fe-13Cr-15Ni Prototype Alloys – E. H. Lee and L. K. Mansur

Minor alloying elements have been traditionally added to the austenitic stainless steels to improve alloy properties. Since the discovery of cavity swelling in alloys exposed to the irradiation environment in a reactor, a study of the effects of alloy composition has been an important subject in radiation effects programs. A major impact of minor elements is the formation of precipitate phases that lead directly to changes of swelling and mechanical properties. It has also been recognized that other alloy properties can be greatly improved through proper control of precipitate phases that occur during irradiation. The present work aims to understand the nature of precipitate phases and to establish a systematic scheme to generate desired precipitate phases. Twenty-eight alloys were fabricated with varying additions of seven important minor elements (C, Si, P, Ti, Mn, Mo, Nb) to the Fe-13Cr-15Ni base alloy. Extensive thermal aging and fabrication studies were conducted to provide a baseline on which to accurately compare the effect of irradiation. Dual ion irradiations were carried out with the ORNL dual-beam accelerator system by employing 4-MeV nickel or iron ions and 200- to 400-keV alpha particles for simultaneous helium implantation. Irradiation experiments in the FFTF and the ORR, and mechanical property testing, are also in progress. Important highlights of the experimental findings are summarized in the following subsections.

4.1.6.1 Fabrication Study

Precipitate phases that were formed during alloy melting and solidification processes were mostly oxides (Cr_2O_3, SiO, TiO, NbO, and presumably also CO), a small fraction of carbides (TiC, MC, NbC), various sulfides (Ti_xS_y, CrS), and phosphide (M_2P). The analysis revealed that a substantial amount of residual oxygen was removed as slag by forming oxides with Ti, Si, and C during fabrication. This aspect is an important factor because gas atoms influence the cavity formation. The strong effect of oxygen on swelling was confirmed by an oxygen implantation experiment with the ORNL accelerator facility (to be reported subsequently).

Although the alloys with Ti, Si, and/or C show very little or no cavity swelling, the cavity swelling was initiated when the oxygen eliminated during fabrication was replenished by implantation. Figures 4.1.6 and 4.1.7 demonstrate this effect of oxygen in alloy B3 (Fe-13Cr-15Ni-0.8Si) and in alloy B5 (Fe-13Cr-15Ni-0.2Ti-0.04C), respectively.

4.1.6.2 Thermal Aging Study

Thermal aging has been carried out at 600°C and 675°C for intervals of 24 h, 500 h, 6 months, and 1 year. Crystal structures and compositions of phases produced upon thermal aging were determined as well as typical morphology and orientation to matrix. Four carbides ($M_{23}C_6$, eta, MC, NbC) and three non-carbides (Laves, TiO, phosphides) were identified. The distribution of precipitate phases varied considerably with alloying additions. Notable findings are that no stoichiometric compound was found in thermal aging products and that the stability of phases was dictated by supersaturation of solute elements that are essential for the phase formation. The phase distributions are generally in agreement with the Gibbs free energies of formation, but kinetic factors often limit the formation of energetically favorable phases. In such cases, ion irradiation accelerates the formation of energetically favorable phases as discussed below.

4.1.6.3 Ion Irradiation Study

During irradiation atomic bonds are constantly broken and reconstructed, and radiation-enhanced diffusion may facilitate the approach to an equilibrium state. On the other hand, preferential solute-defect interaction causes non-equilibrium phases also to form. Much has been reported in the literature on non-equilibrium phase formation during irradiation. Our recent work has identified and confirmed the irradiation-induced acceleration toward equilibrium precipitate phases. The first type includes phases normally formed during thermal processing (M_2P, TiO, MC, NbC, $M_{23}C_6$, eta), while the second type consists invariably of silicon and/or nickel-rich radiation-induced phases (G, gamma prime, Ni-rich gamma, CrSi).

H-78202 H-87654

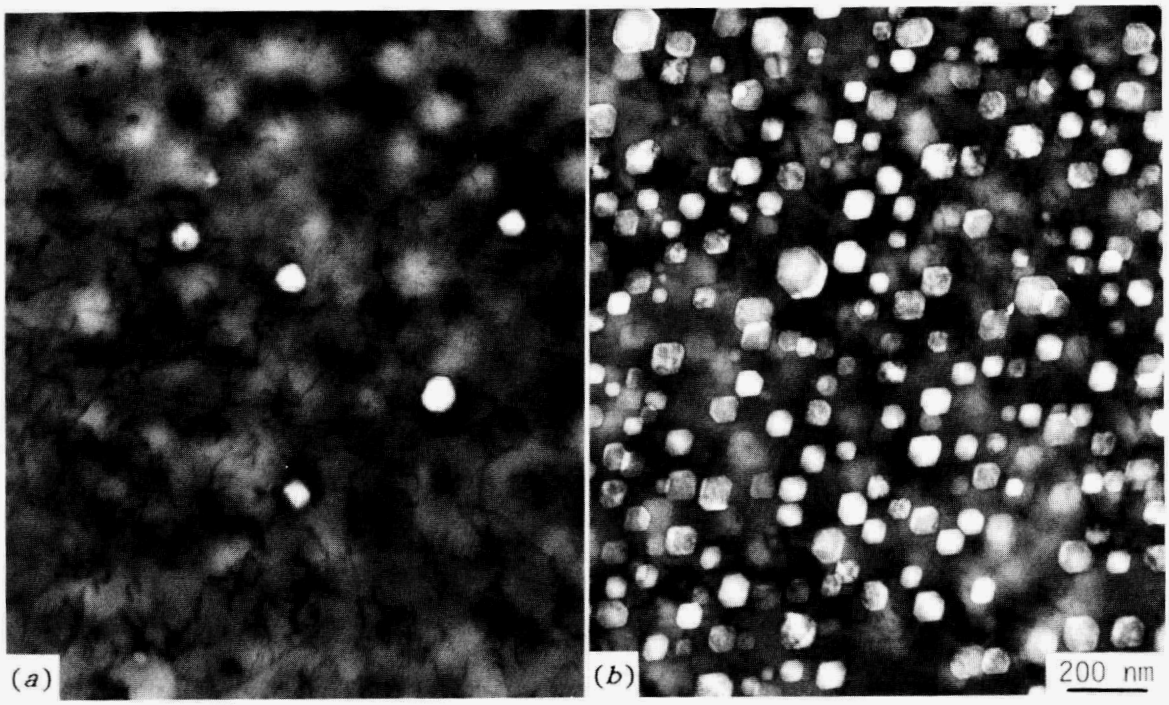

Fig. 4.1.6. Alloy B3 irradiated at 675°C (*a*) to 69 dpa and (*b*) to 101 dpa with 300 appm oxygen preinjection at room temperature.

H-78248 H-87638

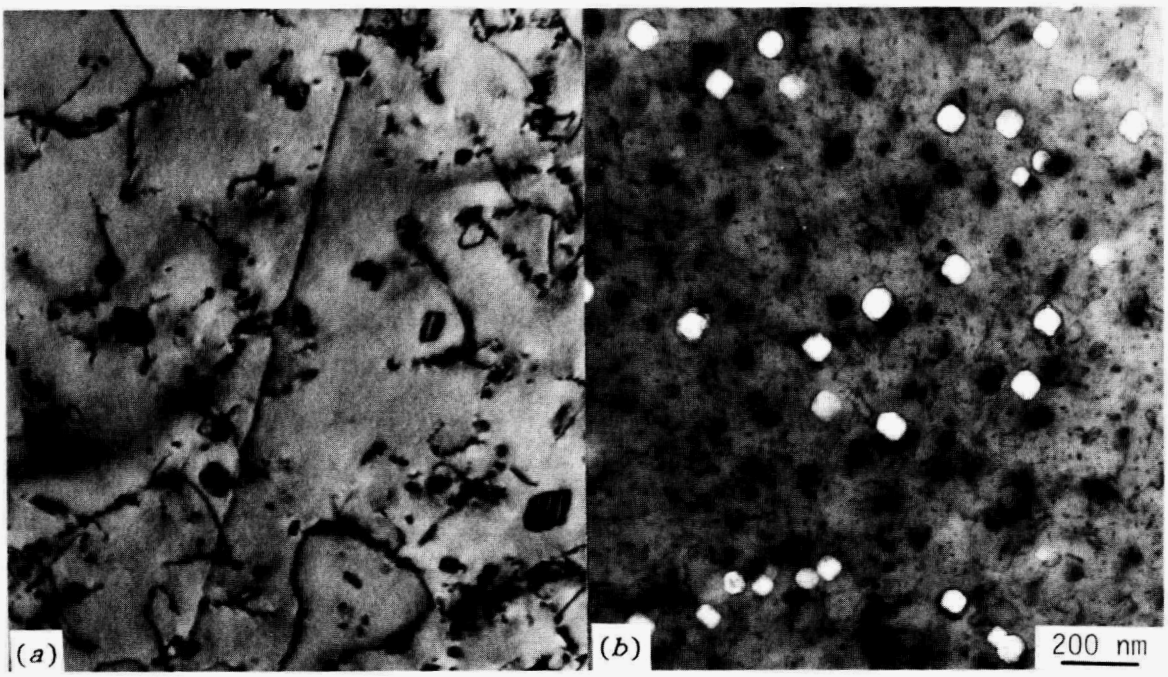

Fig. 4.1.7. Alloy B5 irradiated at 675°C to (*a*) 65 dpa and (*b*) to 69 dpa with 300 appm oxygen preinjection at room temperature.

In general, TiC and NbC phases were enhanced by radiation because damage-induced dislocations and radiation-enhanced diffusion facilitated their nucleation, but $M_{23}C_6$ and eta phases declined as a result of the formation of the two active carbides. However, the stability of carbides was greatly affected when M_2P or TiO were enhanced by irradiation. This interdependence was mainly due to the change in supersaturation of carbon and titanium and to the free energies of formation of interrelated phases. Both M_2P and TiO are Ti-rich phases, and their formation depleted titanium from the solution and freed carbon, which in turn enhanced $M_{23}C_6$ but suppressed the Ti-rich MC phase. Although TiO is energetically preferred over TiC, the latter was dominant during thermal aging because of its fast kinetics. Titanium oxide was found to be the equilibrium phase by Gibbs free energy calculations but did not form under thermal conditions in the presence of the long-lived metastable TiC phase. However, when radiation was introduced, TiO formation became predominant. Figure 4.1.8 compares TiC and TiO in alloy B5 (Fe-13Cr-15Ni-0.2Ti) after thermal aging and irradiation at 675°C, respectively.

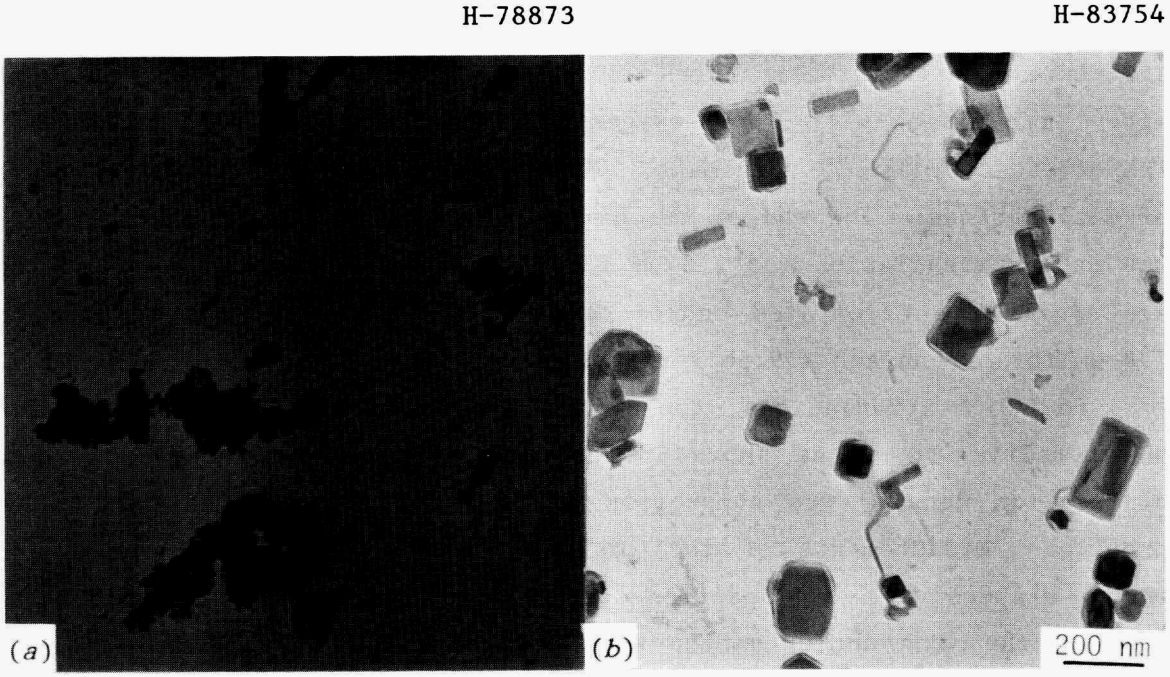

Fig. 4.1.8. Carbon replicas showing TiC and TiO particles in alloy B5. (*a*) After 6 months aging at 675°C. (*b*) After 65-dpa irradiation at 675°C.

This work has established the nature of precipitate phases occurring during fabrication, thermal aging, and irradiation, and it provides a reference scheme for the manipulation of phase relationships in irradiated alloys. Energetic considerations provide the new insight that irradiation may accelerate the approach to equilibrium where processes such as solute segregation, which favor non-equilibrium phases, are not predominant. This offers the possibility that irradiation may be used as a tool to study equilibrium phase relationships in systems whose kinetics are too sluggish to exhibit anything but metastable states after thermal processing.

4.1.7 **Radiation Damage in Ion-Irradiated MgO** (ref. 7) – L. L. Horton, J. Bentley, and M. B. Lewis

While ion irradiations have been used extensively to study damage phenomena in metals, little work has been reported for ceramic materials. This is due to the complexity of this class of materials and the difficulty of the specimen preparation procedures required to study the resulting damage with transmission electron microscopy (TEM). In the current investigation, ion irradiations have been used to study radiation damage in MgO. This material was selected because of the interest in it for fusion reactor applications and the relatively simple NaCl crystal structure. The microstructures found in specimens of single-crystal MgO after irradiation with 2-MeV oxygen or 4-MeV iron ions were examined by TEM of cross-sectional specimens. The observed damage consisted primarily of dislocations. The end of the damage occurred at a depth of 2.4 μm for the oxygen irradiation and 2.8 μm for the iron irradiation. These values are similar to calculated end-of-range values (EDEP-1 Computer Code) of 1.8 μm for oxygen and 1.9 μm for iron.

For both irradiations, the damage appeared to have two bands where the density peaked, as shown in Fig. 4.1.9. Between these bands, the dislocation density was suppressed as compared with the balance of the profile. Measurements of the implanted iron concentration profile by energy-dispersive X-ray spectroscopy, Fig. 4.1.10, demonstrated that the peak in the iron concentration was located at 2.2 μm, approximately the center of the low dislocation region. The peak in the measured iron concentration was 0.46 at. %, whereas the calculated maximum concentration

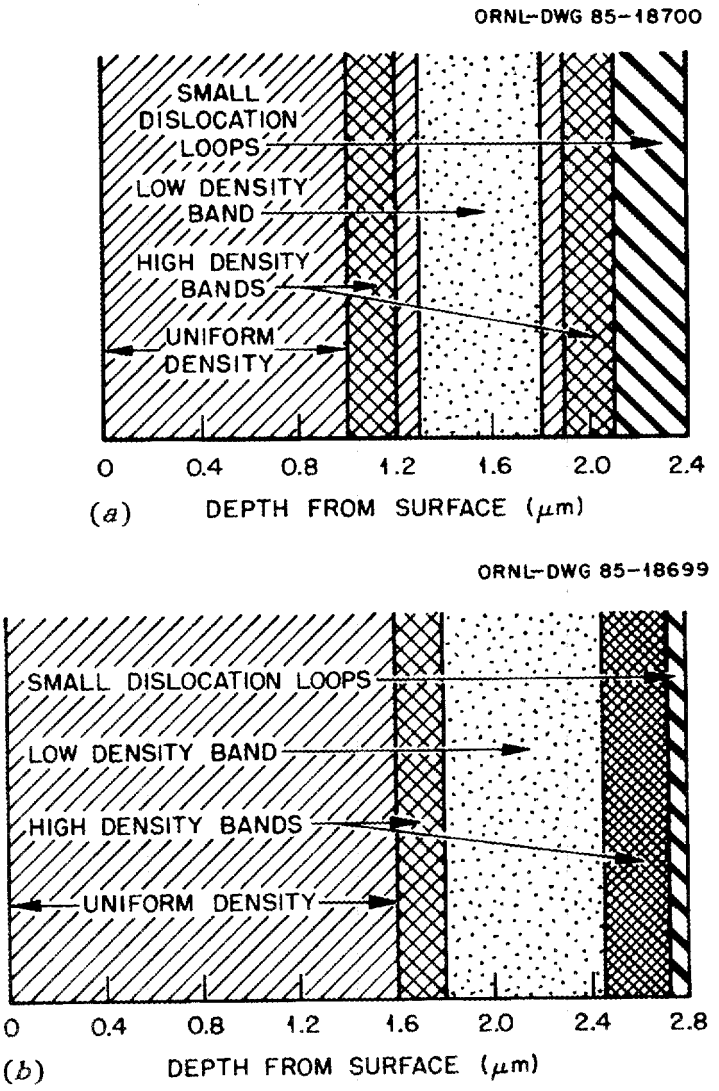

Fig. 4.1.9. Schematics of the damage as a function of depth from the irradiated surface. The density of the shaded regions corresponds to the relative apparent density of the damage. (*a*) Oxygen irradiation. (*b*) Iron irradiation.

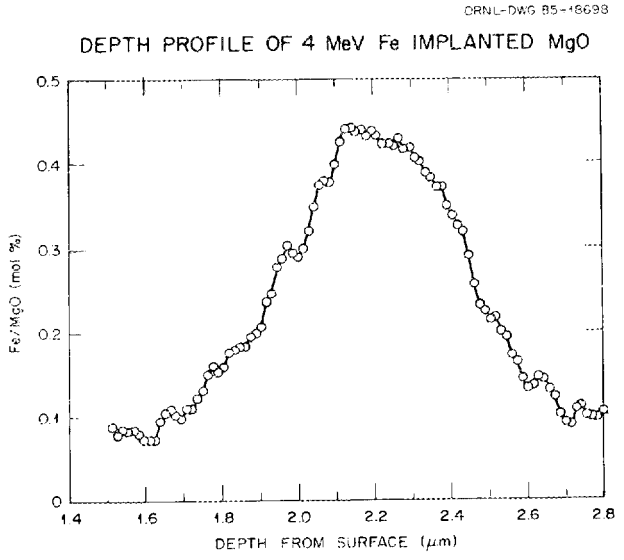

Fig. 4.1.10. Plot of the concentration ratio of iron to MgO in iron-irradiated MgO as measured by an energy-dispersive X-ray spectroscopy line scan.

is 0.9 at. % at a depth of 1.5 μm. The FWHM (full width at half maximum) for the experimental profile was 0.6 μm, but the calculated value is only 0.36 μm. Surprisingly, electron energy loss spectroscopy of the damaged region from the oxygen irradiation demonstrated no measurable variations in the nominal 50 at. % oxygen concentration. The explanation for this is not clear. With simultaneous implantation of helium ions, an additional region with low dislocation density was observed at 0.9 to 1.1 μm, the calculated location of the implanted helium.

The experimental damage and implanted ion profiles correlated as expected, which suggests that the deeper-than-calculated damage is produced directly by the energetic ions rather than by stress or knock-on oxygen atoms. Consistent with the greater ion range, the maximum concentration measured for the iron ions was about 60% of the calculated value. The results suggest either an error in the range calculations or channeling of the implanted ions. The observations of bands with low dislocation density at the calculated or experimentally determined locations of the implanted ions indicates a possible influence of the charged defects on the dislocation evolution. These observations suggest avenues for future investigation utilizing TEM as well as additional characterization techniques.

4.1.8 Microstructural Response of Ceramics to Neutron Irradiation — L. L. Horton

There is increasing interest in the mechanisms responsible for radiation damage in ceramic materials. Of special interest are low irradiation temperature studies and investigations of the effects of gas, especially helium and hydrogen, on the microstructural evolution. These problems are particularly important for potential fusion reactor applications. Currently there are few comprehensive studies of damage microstructures in neutron-irradiated ceramics. In order to establish a foundation for understanding the damage mechanisms, transmission electron microscopy disks of several different ceramics have been placed in the Oak Ridge Research Reactor (ORR) and in the Fast Flux Test Facility (FFTF). These experiments were prepared in conjunction with Dr. Frank Clinard, Los Alamos National Laboratory. The specimen materials include $MgAl_2O_4$,

Al_2O_3, MgO, MgO doped with Ni, and MgO doped with Li. In the ORR, the Ni and Li dopants will generate helium as a result of transmutation reactions, allowing a partial determination of the effects of helium on the microstructures. These specimens were included in the joint ORR JAERI-ORNL experiment (MFE 6J and 7J) at irradiation temperatures of 60, 200, 300, and 400°C and a damage rate of 3.8 dpa/year (based on 316 stainless steel). In addition, specimens are included as part of the Fusion Program FFTF experiment at irradiation temperatures of 425 and 470°C (tubes KF01 and LA01) at damage rates of 30 and 15 dpa/year, respectively.

4.1.9 The Role of Phosphorous in Suppressing Swelling in Austenitic Fe-Ni-Cr Base Alloys During Irradiation[8] – E. H. Lee and L. K. Mansur

It has been observed that phosphorous-modified austenitic stainless steels exhibit resistance to cavity swelling during irradiation.[9] This property has attracted much attention because swelling is one of the most important problems in alloys intended for fission and fusion reactor structural materials applications. Several mechanisms have been suggested to explain the role of phosphorous during irradiation. One claim is that phosphorous is a fast diffuser and thus reduces the vacancy supersaturation during irradiation, leading to swelling suppression.[10] Experimental evidence, however, does not support this idea because swelling suppression is observed to occur only when phosphorous atoms are incorporated into needle-shaped phosphide precipitates. Enhanced point-defect recombination at particle-matrix interfaces has also been suggested to explain the swelling suppression, but our analysis does not give an effect as large as observed experimentally.[11]

A set of phosphorous-modified alloys based on the Fe-13Cr-15Ni ternary was investigated with 4-MeV iron ions and 200- to 400-keV alpha-particle irradiation. The results reveal that (1) addition of phosphorous alone does not suppress swelling, Fig. 4.1.11; (2) swelling suppression occurs when a high concentration of phosphide particles forms; (3) the higher the particle concentration the higher the bubble concentration, and swelling is delayed; (4) the particle-matrix interfaces serve as sites for the nucleation of the very fine dispersion of helium bubbles,

ORNL-PHOTO 1533-86

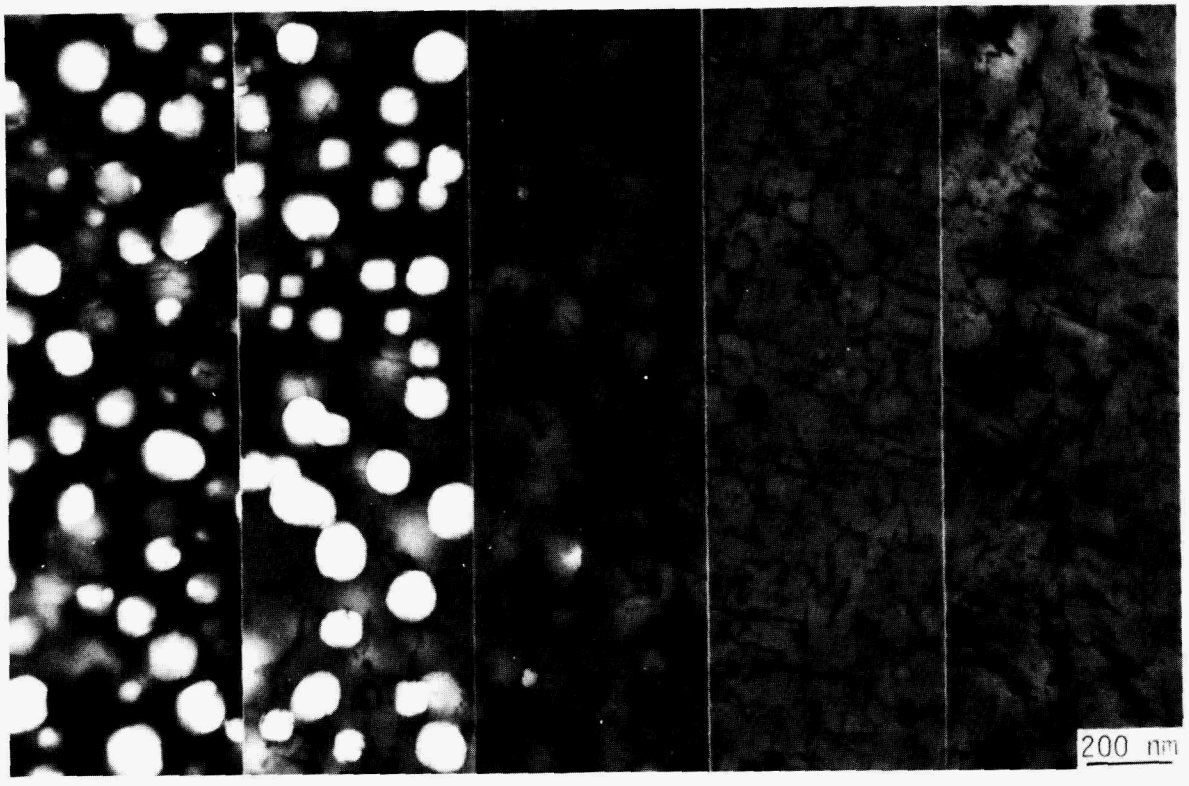

Fig. 4.1.11. Microstructures after 70 dpa Ni^{++}-ion irradiation at 675°C. (*a*) B1 (Fe-13Cr-15Ni). (*b*) B9 (Fe-13Cr-15Ni-0.05P). (*c*) B10 (Fe-13Cr-15Ni-0.05P-0.8Si). (*d*) B11 (Fe-13Cr-15Ni-0.05P-0.2Ti). (*e*) B12 (Fe-13Cr-15Ni-0.05P-0.8Si-0.2Ti).

Fig. 4.1.12; and (5) cavities must reach a critical size before rapid point-defect-driven swelling can occur, as manifested by bimodal cavity size distributions.

The experimental findings are consistent with the theory of swelling, which predicts that a critical number of gas atoms is required in each cavity before the initiation of bias-driven cavity growth. Since a high number density of cavities lowers the number of helium atoms per cavity, the irradiation time for the cavities to accumulate the critical number of gas atoms for bias-driven growth is correspondingly increased. Very high numbers of cavities are associated with the high precipitate-matrix interfacial area of these phosphides. A recent experiment utilizing a high helium injection rate confirms the predicted eventual cavity swelling in these alloys when sufficient helium atoms are supplied. These results indicate that cavity swelling can be delayed through the manipulation of

H-84534

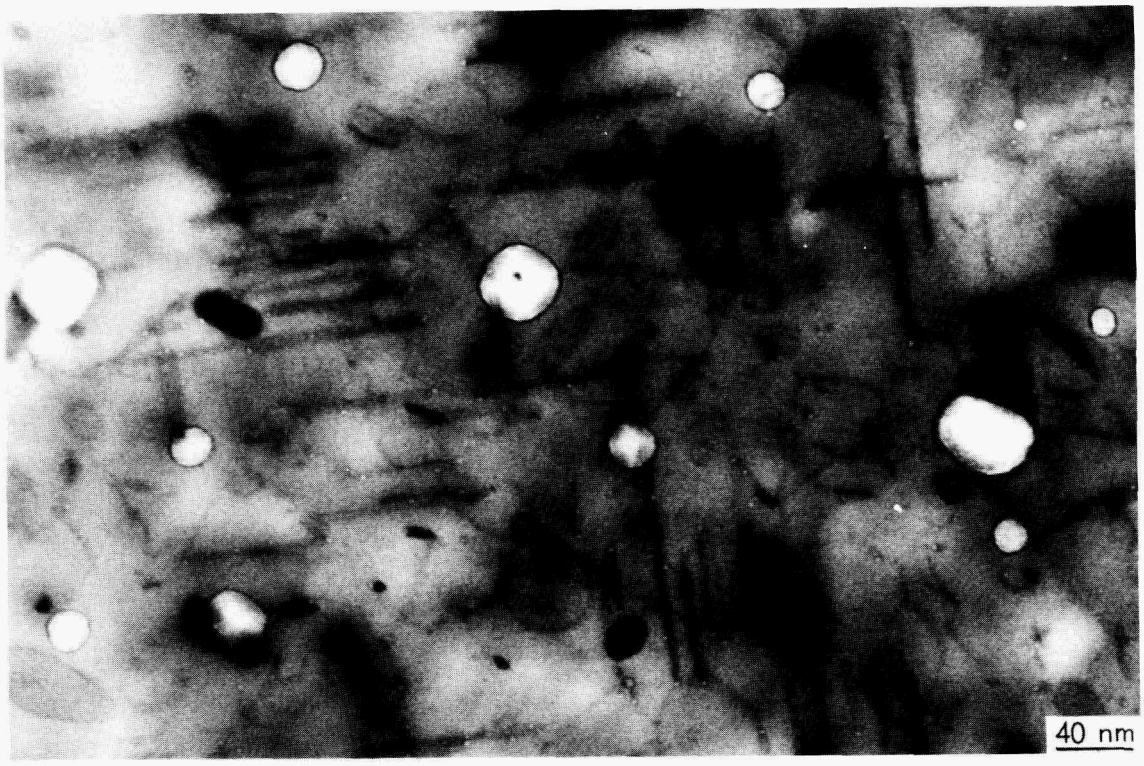

Fig. 4.1.12. Alloy B12 irradiated to 40 dpa without helium and additionally to 40 dpa with 180 appm helium at 675°C. Large cavities and small bubbles at precipitate-matrix interfaces are seen, revealing bimodal cavity size distribution.

precipitate phases. By a particular combination of thermomechanical treatment and compositional modifications based on phosphide additions, we have been able to extend the period prior to the onset of swelling up to 120 dpa with the concurrent accumulation of 2480 appm of helium, Fig. 4.1.13.

4.1.10 Helium Effects in 12Cr-1MoVW Ferritic Steel - L. L. Horton and J. M. Vitek

Ferritic steels are being considered for fusion reactor applications involving high damage levels with the simultaneous production of helium (10 to 15 at. ppm/dpa). Present neutron and ion irradiation experiments have indicated that helium plays an important role in the microstructural response of ferritic steels to irradiation. Such studies have shown early

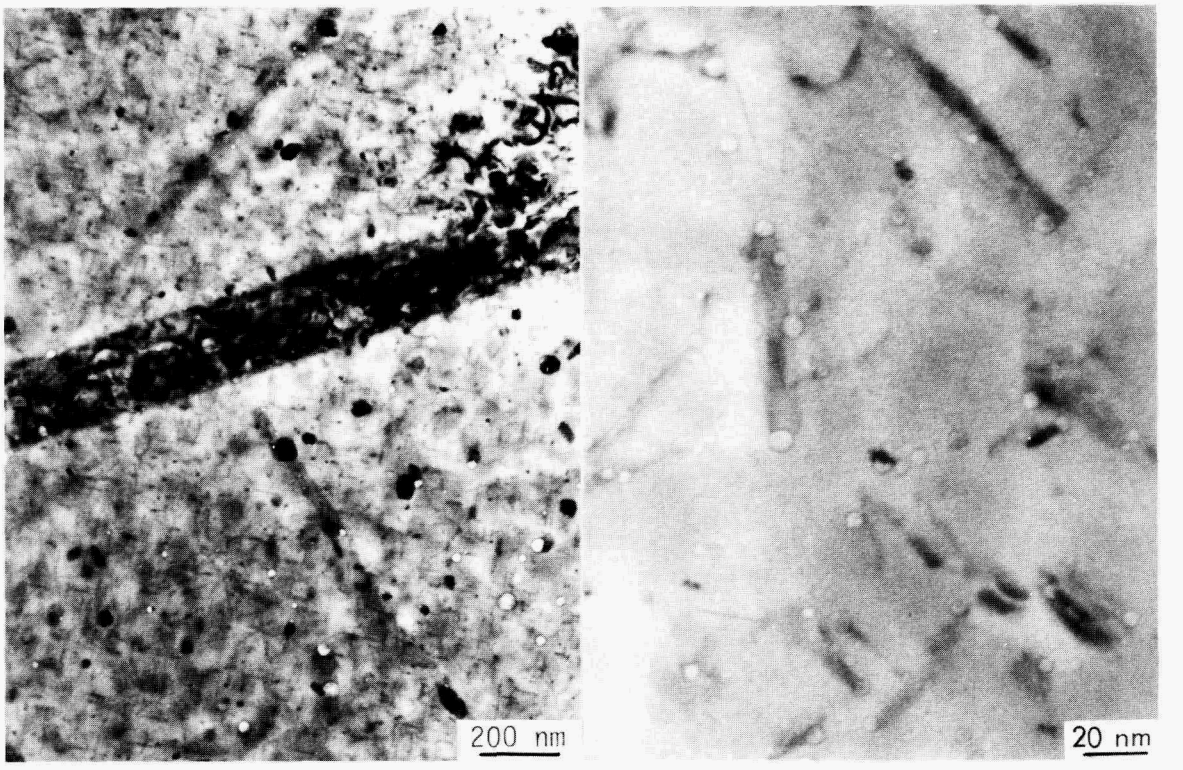

Fig. 4.1.13. Low and high magnification microstructures of a cold-worked stainless steel type alloy irradiated to 128 dpa/2480 appm helium at 675°C.

stages of swelling at a dose of 40 dpa. Significantly, both neutron and ion irradiations to 40 dpa have yielded similar results. To study the effects of helium on the damage microstructures, a series of ion irradiation experiments have been performed. Specimens of HT-9, a 12Cr-1MoVW ferritic steel, were irradiated to 40, 100, and 200 dpa with 4-MeV Fe^{++} ions. During the heavy ion bombardment, the specimens were simultaneously implanted with helium ions. The energy of the helium ions was ramped between 0.2 and 0.4 MeV, resulting in an even helium implantation over the 3-m region corresponding to the peak in the damage from the iron ions. Two helium concentration levels were selected, 3 and 12 at. ppm/dpa. The lower helium level allows comparison with fission reactor irradiations, while the higher level corresponds to the helium concentrations expected for ferritic steels exposed to fusion reactor environments. An irradiation temperature of 500°C, the peak swelling temperature for ion irradiations of this material, was selected.

At 40 dpa, both levels of helium yielded similar microstructures. Cavity formation was quite limited, with no significant amounts of swelling [Fig. 4.1.14(*a*)]. As expected, this microstructure is similar to the microstructures observed after neutron irradiation. There is a narrow zone near the lath boundaries with few or no cavities. Thus, the narrow laths have a lower concentration of cavities than wider laths have. There were additional lath-to-lath variations in the cavity concentration that had no apparent microstructural cause. The cavities show no preference for precipitate-matrix interfaces. At 100 dpa, however, as shown in the micrographs in Fig. 4.1.14(*b* and *c*), the higher level of helium yielded a substantially higher concentration of small bubble-like cavities than did the lower helium levels. For the 12 at. ppm/dpa helium concentration, these bubbles were found on the lath boundaries and at precipitate-matrix interfaces.

The overall swelling in the 100-dpa specimens does not appear to be dramatically higher than observed at 40 dpa, suggesting a continued low

ORNL-PHOTO 0461-86

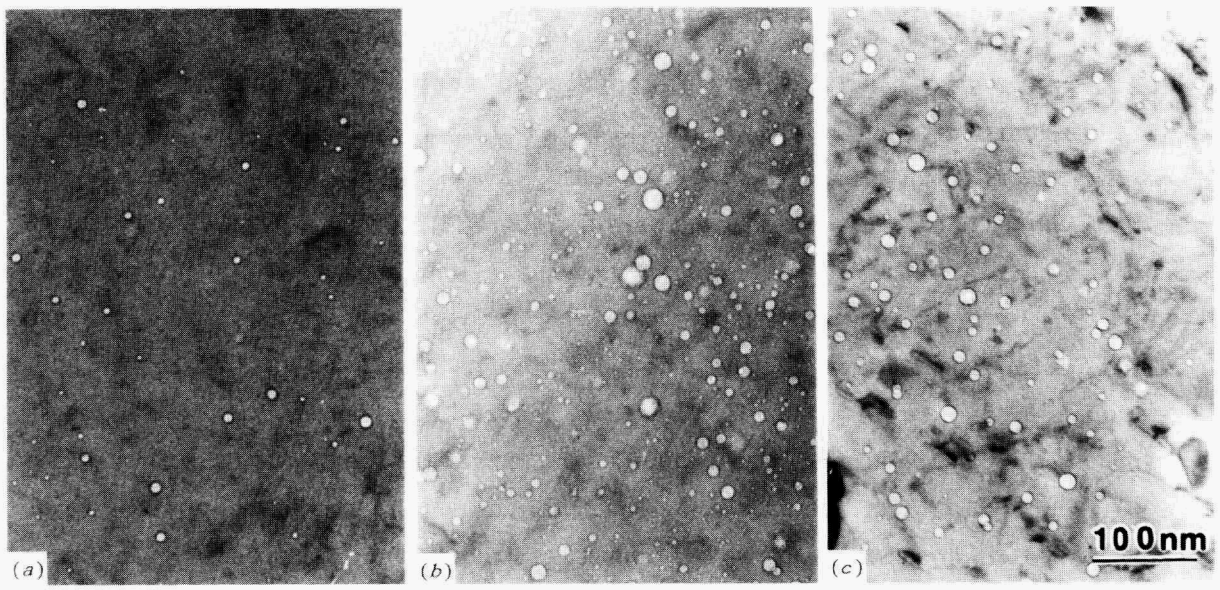

Fig. 4.1.14. Cavity formation in ion-irradiated 12Cr-1MoVW ferritic steel. T_I = 500°C. (*a*) 40 dpa, 12 appm He/dpa. (*b*) 100 dpa, 12 appm He/dpa. (*c*) 100 dpa, 3 appm He/dpa.

rate of swelling in these alloys, even with high levels of helium. Examination of the 200-dpa specimens is in progress. These results will provide insight concerning the behavior of 12Cr1MoVW ferritic steel under fusion reactor conditions at high damage and helium levels and also will provide valuable data for continued modeling efforts of the radiation response of this complex class of materials.

4.1.11 Ion Bombardment Damage in a Modified Fe-9Cr-1Mo Steel[12] – K. Farrell and E. H. Lee

A class of ferritic steels undergoing development and investigation for potential applications in high-temperature power generators is the Fe-0.1C-9Cr-1Mo-0.1Si-0.4Mn system modified by 0.2 wt % additions of niobium and vanadium and used in the normalized-and-tempered condition. The microstructure consists of small, lath-shaped α-ferrite grains of mean width about 0.5 μm, containing subboundary-type dislocation networks and many random dislocations. This microstructure imparts good toughness to the steel.

To explore the response of this type of steel to radiation-induced swelling under conditions expected in the first wall of a fusion reactor, we simulated such conditions with accelerator bombardments using simultaneous beams of iron, helium, and hydrogen (deuterium) ions. The effects of the gaseous ions on swelling were isolated by performing some of the bombardments with iron ions alone. The nominal level of atomic displacements was 100 dpa at temperatures of 400, 450, 500, 550, and 600°C. For the multiple-beam bombardments, the helium was incorporated at a rate of 10 at. ppm/dpa and the deuterium at 45 at. ppm/dpa. Microstructural damage was examined by TEM at the peak damage depth of 0.9 μm.

Bombardments with iron ions alone caused the formation of dislocation tangles which coarsened with increasing irradiation temperature until, at 600°C, there was no obvious change from the as-heat-treated condition. A few heterogeneously distributed cavities were found at 500 and 550°C; the associated levels of swelling were less than 0.05%. Multiple-beam bombardments introduced high concentrations ($>10^{21}/m^3$) of very small (2 to 4 nm diam) cavities. Some examples of these cavities are shown in Fig. 4.1.15. These cavities were uniformly distributed at the lower

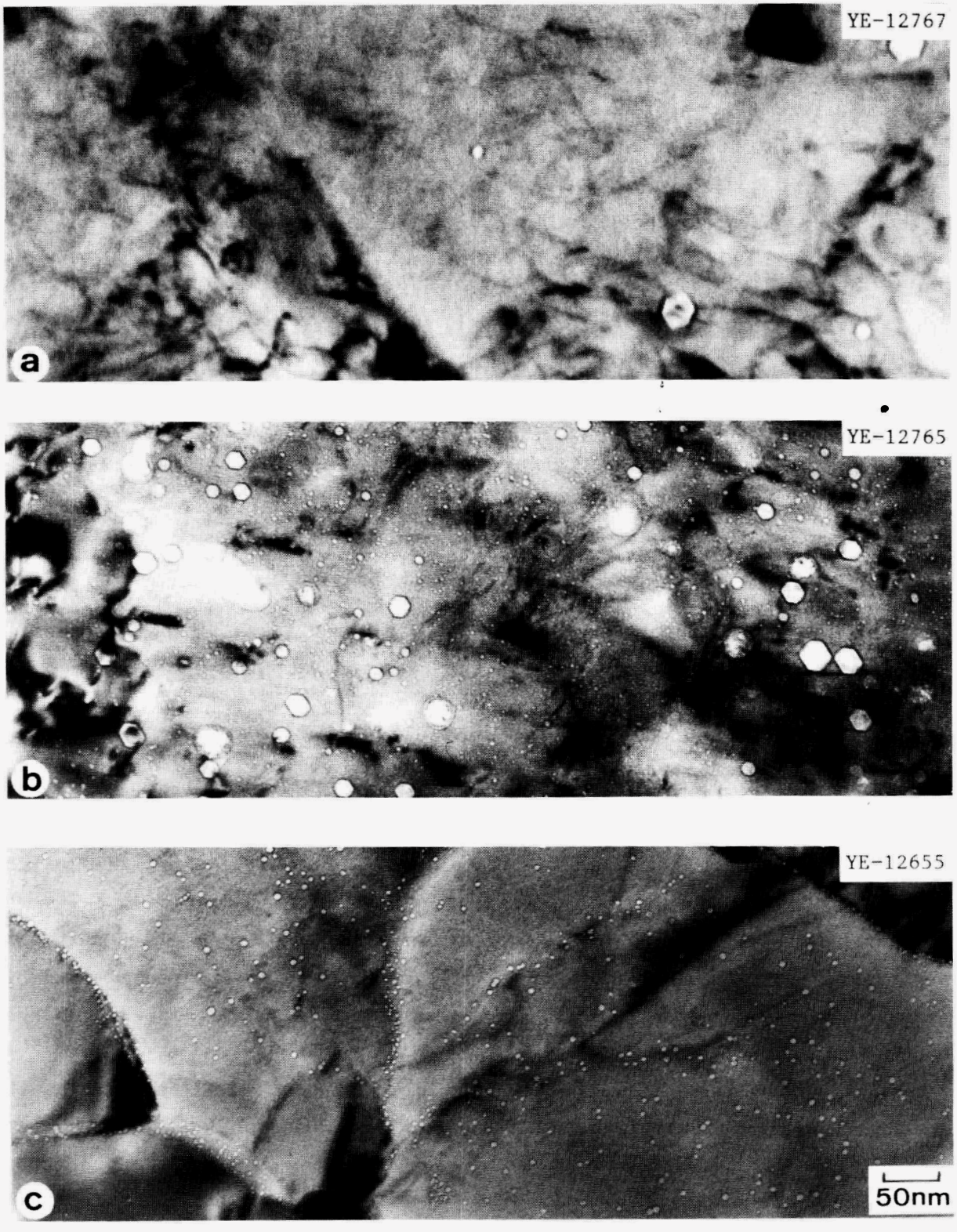

Fig. 4.1.15. Cavity distributions after bombardment to (*a*) 93 dpa at 500°C with Fe ions and (*b*) 121 dpa at 500°C with Fe + He ions. (*c*) Uniform size cavities after 95 dpa at 600°C with Fe + He + D ions.

irradiation temperatures but were preferentially associated with dislocations and grain boundaries at 550 and 600°C. At 500 and 550°C a small fraction of the cavities were relatively large but not as large as those in the specimens irradiated with iron ions only. Swelling reached a maximum of only about 0.4% at 500°C. An irradiation with Fe + He beams caused cavities similar to those produced by Fe + He + D beams, indicating that helium is the principal promoter of the small cavities.

Analysis of these data in terms of gas concentration and theories of cavity nucleation and growth suggested that the small cavities are stabilized by helium as near-equilibrium bubbles. The larger cavities at 500 and 550°C, and those in the helium-free specimens, experienced bias-driven growth. A critical cavity size of 2 to 4 nm is implied. The commendably low swelling in this alloy is thought to be due only in part to the original high concentrations of dislocations and grain boundaries in the tempered martensite structure. The major factor is considered to be the inherent swelling resistance displayed generally by bcc ferritic alloys, possibilities for which are discussed. Attention is drawn to the presence of many helium bubbles on grain boundaries, which raises the question of intergranular failure under creep conditions.

4.1.12 Irradiation Creep in a Simple Ferritic Alloy at Low Temperatures – L. L. Horton

Few comprehensive data sets are currently available for irradiation creep, especially for ferritic materials. Correlation of creep- and irradiation-induced microstructures is essential for accurate modeling of creep behavior. At low irradiation temperatures, creep should be particularly interesting for ferritic alloys because these materials exhibit swelling and significant dislocation evolution at lower temperatures than do austenitic alloys.

To study this area, pressurized creep tubes were included in the JAERI-ORNL joint experiment in the Oak Ridge Research Reactor (ORR). A special heat of high-purity Fe-16Cr was fabricated at ORNL for the tubes. A high-purity binary alloy was selected in order to study the irradiation response in an alloy with a simple pre-irradiation microstructure, a condition that simplifies the subsequent interpretation of the results

required for modeling. The chromium content of the alloy was dictated by the low corrosion requirements for materials placed in the cooling water of the ORR. Tubes pressurized to 10, 20, 50, 80, and 100 MPa were placed in the reactor in June 1985 in experiments ORR-MFE 6J and 7J at irradiation temperatures of 60, 200, 300, and 400°C. This low temperature range is of particular interest for ferritic materials. No previous irradiation data cover this range, yet these temperatures are of interest for fusion reactor materials, and theory indicates that dimensional instability may well occur in this range. The projected damage rate is 3.8 dpa/year. Corresponding nonstressed tubes and transmission electron microscopy disks were also included in the experiment. Planned postirradiation analyses include correlation of the creep results with the transmission electron microscope evaluations of the damage microstructures.

4.1.13 Effects of Rapidly Pulsed Ion Bombardment on Microstructure and Phase Stability in a Ti-Modified Stainless Steel[13] – E. H. Lee, N. H. Packan, M. B. Lewis, and L. K. Mansur

The influence of beam pulsing is a topic of interest both in radiation effects and in ion-beam modification research. Our heavy-ion bombardment facility with beam chopping capability is a powerful tool to study the kinetics of the defect processes induced by pulsing. In our earlier work, the effect of pulsed irradiation was studied by using a solenoid-actuated beam chopper that could interrupt the beam for intervals as short as 0.5 s. In the current experiments, a recently developed electrical chopper has been used to produce beam interruptions as short as 10 microseconds – times approaching the interstitial and much less than the vacancy lifetimes for these irradiation conditions.

Solution-annealed (1373 K) titanium-modified austenitic stainless steel (Fe-15Cr-15Ni-2Mo-2Mn-1Si-0.2Ti-0.05C in wt %) was studied with pulsed-beam irradiation in the ORNL dual-ion Van de Graaff accelerator facility. The bombardments employed either 4-MeV nickel ions alone or simultaneously with 0.2- to 0.4-MeV helium ions. Pulsed ion beams were generated with equal on/off intervals, and pulse periods of 10^{-3} s and 10^{-5} s on/off were used in this experiment. Specimen disks 3 mm in diameter by 0.35 mm thick were subjected to irradiation doses of 1, 40, and 70 dpa at 948 K near the peak swelling temperature.

The greatest effect of pulsing was manifest at the loop growth stage; at higher doses its effects were subtle and mainly appeared in precipitate development. Figure 4.1.16 depicts, for a dose of 1 dpa, the variation of average loop diameters as a function of pulse duration. As the pulsing frequency is increased, from right to left in the figure, the average loop diameters initially decrease slightly, showing minima somewhat below 1-s pulses, but increase again for further reduced periods. The greatest refinements occur for pulse periods that correspond roughly to the calculated vacancy lifetimes (10^{-3} s and 10^{-1} s for helium-implanted and helium-free material, respectively). For a pulse interval of 10^{-5} s, the average loop diameters approach those of continuous irradiation, which may indicate that the effects of very fast pulsing are indistinguishable from the inherent cascade-induced fluctuations produced during ion irradiation, a finding consistent with our recent theory development. With increased dose the interstitial loops unfault and interact to form a dislocation network whose density is quite independent of pulsing conditions.

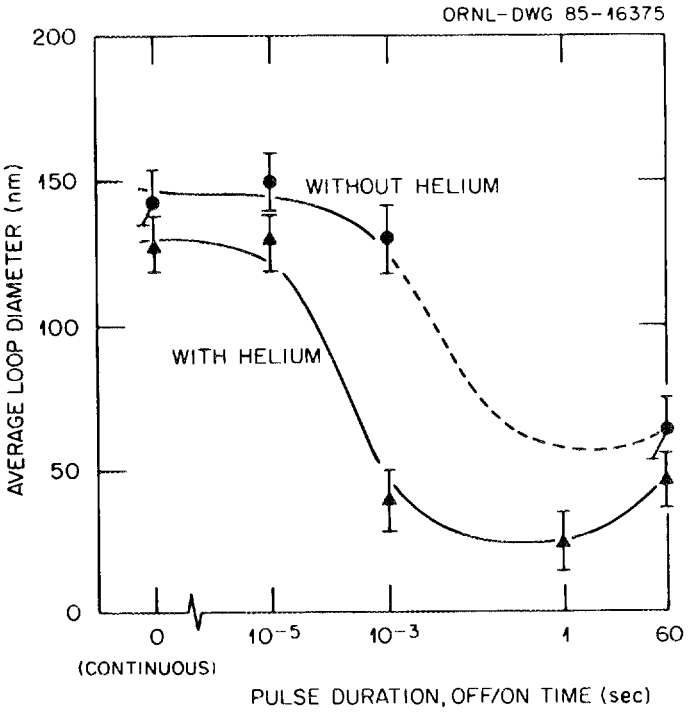

Fig. 4.1.16. Dependence of loop average diameter on pulse period for both single- and dual-beam bombardments.

At higher doses (40– 70 dpa), pulsed irradiation influenced the balance between thermally stable phases like MC and the radiation-induced G phase. Pulsing at any frequency reduced the amount of G phase, which depends upon radiation-induced segregation for a high local buildup of silicon and nickel. Long pulse periods promoted the thermally stable MC phase, while shorter periods such as 10^{-3} s aided eta and $M_{23}C_6$ development.

While helium bubbles were present for all pulsing conditions, growth of cavities from the class of small bubbles to large bias-driven voids occurred only for continuous irradiation. Such a result is consistent with the idea that void growth is aided by symbiotic attachment to growing G precipitates and retarded if helium has to be distributed among a higher number of sinks. We have developed the theoretical and experimental bases of these processes in our previous work. Pulsing at both high and low frequencies inhibited G phase and generated more loops, bubbles, and MC precipitates, all of which are effective dispersed traps for helium. While the irradiation conditions employed in this experiment are relevant to fusion reactor first-wall parameters, the findings are also of use from the point of view of ion-beam modification research. Pulsed irradiation amounts to a sequence of irradiation and anneal periods, the details of which can broadly influence the final damage microstucture. Accordingly, pulsed ion-beam treatments at deliberately chosen frequencies are an additional tool to control the microstructure and phase stability in the implanted region.

4.1.14 References

1. Synopsis of paper to be presented at Second International Conference on Fusion Reactor Materials, Chicago, Apr. 13–17, 1986.

2. On leave from National Research Institute for Metals, Tsukuba, Japan.

3. Oak Ridge Associated Universities, now with Japan Electron Optics Ltd., Boston.

4. Loughborough University of Technology, Loughborough, United Kingdom.

5. Summary of papers: "The Influence of Radiation-Induced Segregation on Ductility of a Nickel-Silicon Alloy," by N. H. Packan, H. Schroeder, and W. Kesternich, and "Radiation-Induced Segregation to Grain Boundaries in a Ni-Si Alloy Studied by Transmission Electron Microscopy," by W. Kesternich, N. H. Packan, and H. Schroeder, both presented at the Second International Conference on Fusion Reactor Materials, Chicago, April 13–17, 1986; and "Radiation-Induced Segregation in Light-Ion Bombarded Ni–8% Si," by N. H. Packan, L. Heatherly, W. Kesternich, and H. Schroeder, to be presented at the 13th International Symposium on the Effects of Radiation on Materials, Seattle, June 23–25, 1986.

6. Institute for Solid State Research, Jülich Nuclear Research Facility, Jülich, Federal Republic of Germany.

7. Summary of a paper given at the symposium Irradiation Effects Associated with Ion Implantation, AIME Fall Meeting, Toronto, Oct. 13–17, 1985; proceedings to be published in *Nucl. Instrum. Methods Phys. Res. B* (1986).

8. Summary of the paper "A Mechanism of Swelling Suppression in Phosphorous-Modified Austenitic Steels," to be published in *J. Nucl. Mater.*

9. E. H. Lee, L. K. Mansur, and A. F. Rowcliffe, *J. Nucl. Mater.* **122&123**, 299–304 (1984).

10. F. A. Garner and H. R. Brager, *J. Nucl. Mater.* **133&134**, 511–14 (1985).

11. A. D. Brailsford and L. K. Mansur, *J. Nucl. Mater.* **103&104**, 1403 (1981).

12. Summary of paper published in *Effects of Radiation on Materials, Twelfth International Symposium*, ASTM STP-870, ed. F. A. Garner and J. S. Perrin, American Society for Testing and Materials, Philadelphia, 1985, pp. 383–93.

13. Summary of a paper given at the symposium Irradiation Effects Associated with Ion Implantation, AIME Fall Meeting, Toronto, Oct. 13–17, 1985; proceedings to be published in *Nucl. Instrum. Methods Phys. Res. B* (1986).

4.2 THEORY AND MODELING

4.2.1 Time-Dependent Rate Theory for Diffusional Defect Processes[1] – A. D. Brailsford[2] and L. K. Mansur

The kinetic theory of microstructural evolution based on point-defect reactions has proved of use in an ever-enlarging realm of phenomena. However, essentially all of the work has been done with tools that retain crucial aspects of steady-state theory. Even where time-dependent problems are treated, the microstructural sink strengths used in conjunction with time-varying concentrations are those that are appropriate to steady-state conditions. For example, a number of researchers have investigated theoretically the consequences of pulsed irradiations, implicitly assuming the forms appropriate to steady-state theory. That work was carried out in response to the emergence of designs for fusion reactors that were developed for pulsed operation.

Our recent development of cascade diffusion theory,[3] an otherwise general time- and space-dependent theory summarized in the previous progress report in this series, employed an effective medium that was ascribed the same loss characteristics as appropriate for steady-state theory. While this theory provides a more faithful physical description of the situation in an irradiated material (both in terms of local spatial concentrations and in terms of time dependence) than does a steady-state approach, our assumptions on the forms of the sink strengths needed to be justified. For these reasons we have developed the general structure of a truly time-dependent rate theory and explored its differences with steady-state forms.

After ascertaining the form of the time-dependent loss rate, it is found that there are corrections to the steady-state forms, including a dependence on the entire irradiation history. However, by evaluating a number of cases corresponding to situations of interest, we have found that the corrections do not lead to physically significant differences. Thus the present work provides an effective medium theory of general time-dependent (but spatially uniform) form, gives a justification for the

point-defect loss rate structure of cascade diffusion theory, and provides a justification for the previous use of the steady-state forms of rate theory employed in irradiation pulsing analyses.

4.2.2 Cascade-Induced Fluctuations and the Transition from the Stable to the Critical Cavity Radius for Swelling[4] - M. R. Hayns[5] and L. K. Mansur

In a material subject to energetic neutron or heavy-ion irradiation, knock-on events lead to point-defect generation in cascades. Previous theoretical work by one of us and coworkers[6] has demonstrated the enormous magnitudes of the resulting spatial and temporal fluctuations in local point-defect concentrations and fluxes. Subsequently, a new mechanism of irradiation creep, cascade-induced creep, was revealed by this work and shown to be of large magnitude.[7] On the other hand, such fluctuations were shown to have relatively little effect on the growth of large cavities when compared with the swelling results predicted by a conventional rate theory picture where fluctuations are not considered. In related work it was also shown that an averaged rate theory approach is valid for the growth of cavities in a periodically varying environment that does not include cascade-induced fluctuations, i.e., where the irradiation is pulsed in time but spatially uniform.[8]

In the present paper we address the possible importance of cascade-induced fluctuations on the early stages of cavity formation. This work is based on the existence of a critical radius above which cavity growth is driven by the dislocation-cavity bias. Where gas is present in a material, the existence of both stable radii, r_c^s (smaller than the critical radius), and critical radii, r_c^c, has been established theoretically and experimentally.[9-13] It is obvious in principle that fluctuations in the point-defect flux at a cavity may induce growth or shrinkage excursions. The question explored here is whether such excursions could be of sufficient magnitude to be important in transferring cavities from the stable to the critical cavity radius.

As shown in Fig. 4.2.1, r_c^s approaches r_c^c as the contained number of gas atoms n_g approaches the critical number, n_g^*, and the gap that fluctuations must bridge decreases. We first establish the required number

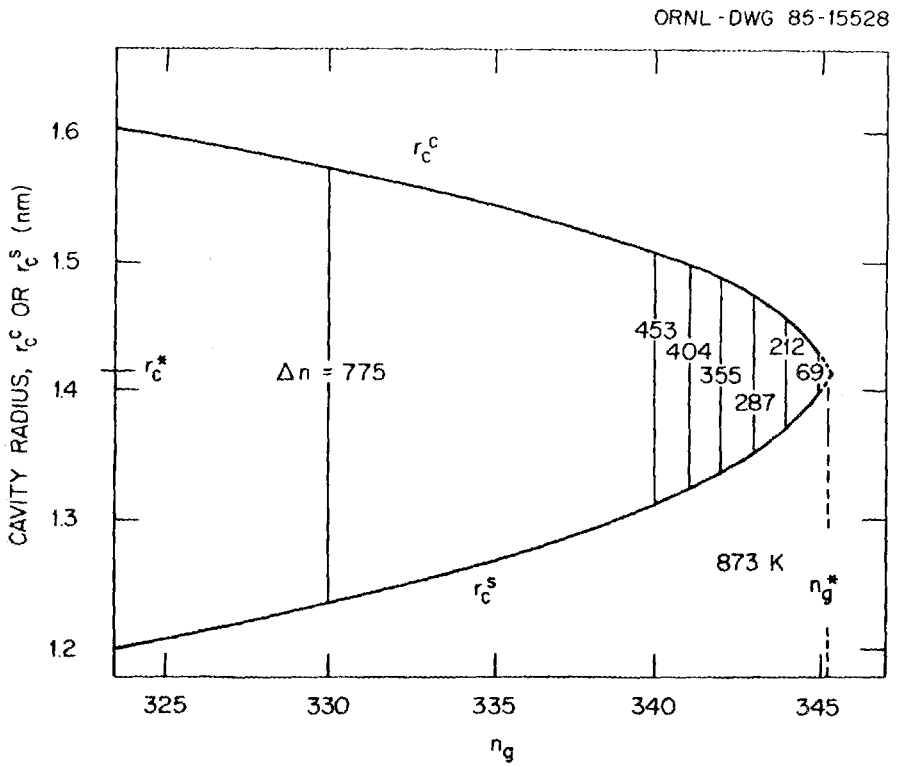

Fig. 4.2.1. Variation of the stable and critical radii as a function of the contained number of gas atoms near n_g^* and r_c^* for a typical reactor irradiation of nickel.

of vacancies corresponding to the difference between r_c^s and r_c^c as a function of n_g and temperature. Under conditions of typical reactor irradiations, it is found that $n_g^* = 345$ and the minimum critical radius $r^* = 1.42$ nm. Shown also are the number of vacancies, Δn, needed for conversion corresponding to several values of n_g. The cavity is only likely to be converted when the magnitude of cascade-induced fluctuations is significant with respect to Δn.

Two methods were used to assess the importance of fluctuations. The first method is based on a derived expression for variance in the number of point defects collected at a cavity.[6] This reflects an average behavior of the cavity population. It is found that the variance is generally small with respect to the number of vacancies needed to produce an experimentally significant excursion from stable to critical radius.

Figure 4.2.2 shows the ratio of the variance in the number of defects collected at a cavity to the average number as a function of r_c^s for a range of dislocation densities of interest for a gap in radius of $r_c^c - r_c^s$ of 0.1 nm. The second method is a very approximate evaluation of upper limits and corresponds to the largest excursions that a very few cavities in the population may experience. Here again it is found that cascade-induced growth excursions produce differences that are experimentally insignificant with respect to the case where fluctuations are ignored. Figure 4.2.3 is an upper limit estimate of the possible effect of cascade-induced fluctuations in point-defect flux in triggering early nucleation of cavities in typical reactor irradiations of nickel. It is therefore concluded that the main mechanism underlying the achievement of bias-driven cavity growth is gas accumulation rather than fluctuations in point-defect flux.

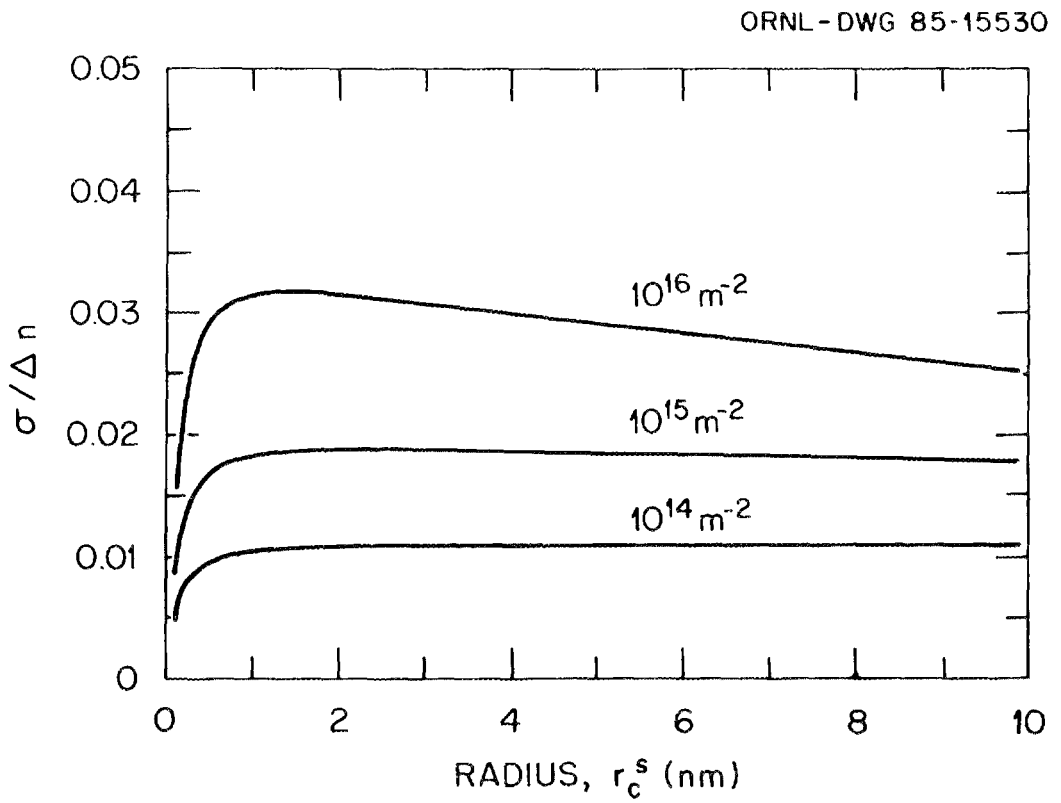

Fig. 4.2.2. The ratio of the variance in the number of vacancies collected to the number required to convert a stable cavity to bias-driven growth.

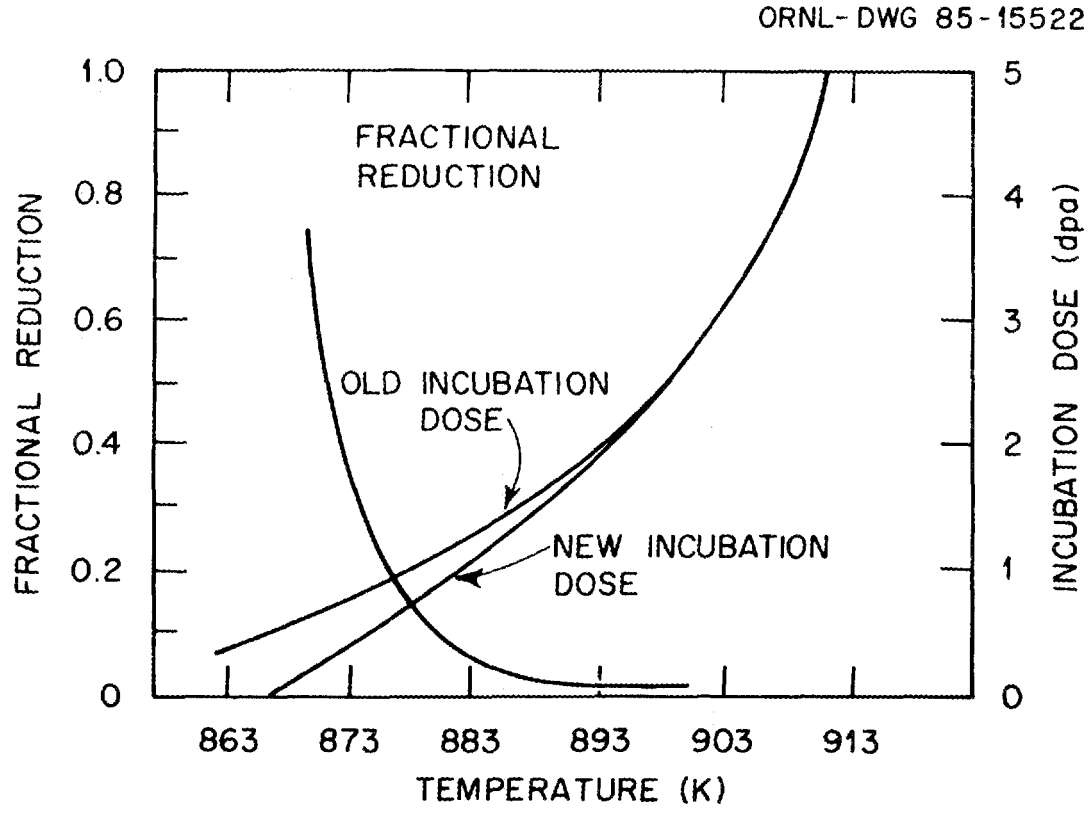

Fig. 4.2.3. Fractional change in dose to the onset of bias-driven swelling due to cascade-induced fluctuations, as a function of temperature. The two curves for incubation dose compare calculations in which fluctuations are included and excluded.

Criteria are suggested by which to judge whether cascade-induced fluctuations may be important in other physical processes occurring in ion beam or neutron irradiations.

4.2.3 Mechanisms of the Electron-Irradiation-Induced Amorphous Transition in Intermetallic Compounds[14] – D. F. Pedraza

Amorphization under particle bombardment is a remarkable case of phase instability where the crystalline structure itself is destroyed. The aim of this work was to investigate theoretically the mechanisms responsible for the crystalline to amorphous transition in electon-irradiated intermetallic compounds. A buildup of radiation-induced lattice defects is proposed as the cause for lattice instability that can give rise to the transition. An analysis of experimental observations reveals that, when amorphization takes place, no microstructural evolution

based on the aggregation of like-point defects occurs. It is therefore suggested that buildup of a different type of defect to a critical value, which will destabilize the crystalline structure, should occur. In order to destabilize the lattice via the irradiation-induced point defects, it is necessary to have a mechanism that retains them in the lattice by hindering direct recombination and opposing like-defect aggregation. The model proposed for the defect responsible consists of an interstitial and a vacancy associated within a certain interaction distance. This defect, called a complex (see Fig. 4.2.4), can allow a partial relaxation of the stress field of the interstitial. Complex buildup is a path for propagating topological disorder, one of the conditions that may lead to an amorphous state.

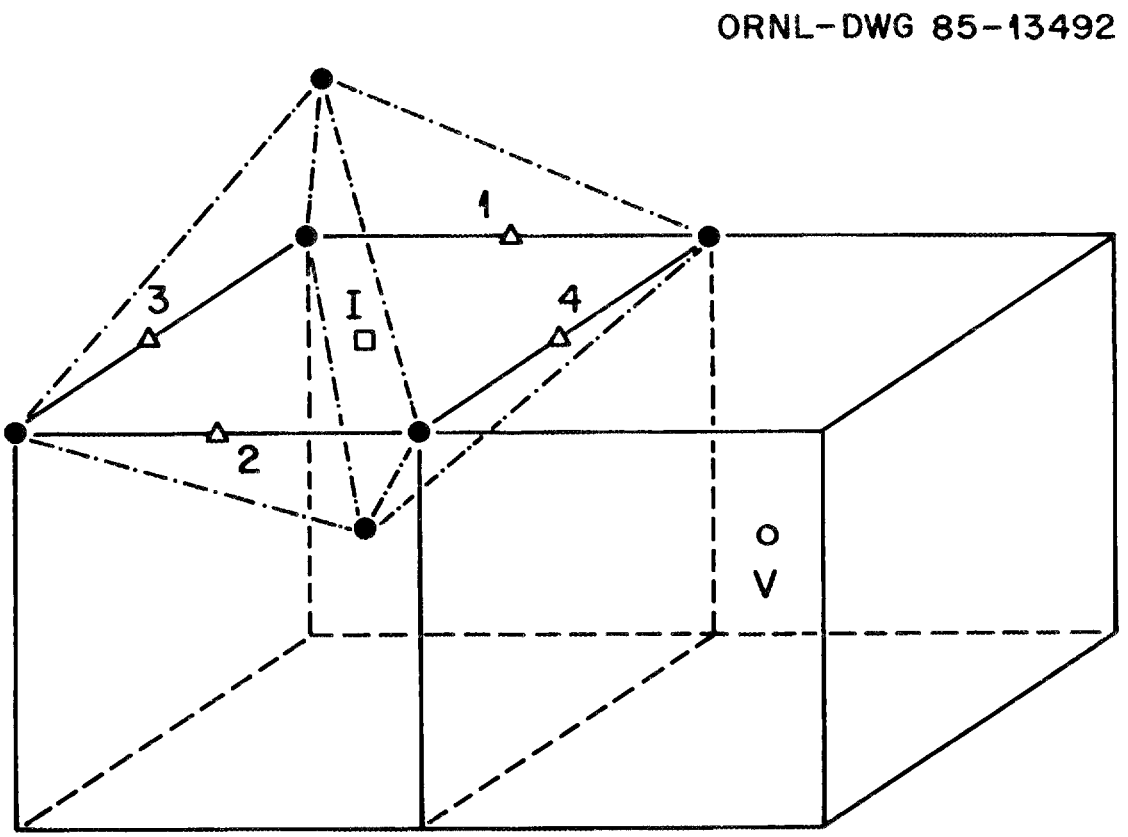

Fig. 4.2.4. Vacancy-interstitial complex configuration. Out of the six atoms surrounding the interstitial at I, at least five are of the same species (different from the interstitial).

We have assumed that vacancies remain essentially immobile. In fact, if they could annihilate at the sinks, insufficient defect buildup would occur. The temperature range where vacancies remain immobile is thus a natural constraint for the occurrence of amorphization. Two mechanisms of complex buildup were considered, one where the interstitials also are immobile. The defect concentrations in that case are limited by the pair production rate vs the rate of close pair recombination, part of the latter being suppressed in favor of complex formation. In the other mechanism, the true interstitial mobility determines the rate of complex formation. However, the lifetime of a complex is determined by two factors, viz. the binding energy that opposes thermal decomposition and the stability against indirect recombination, i.e., the annihilation of a second interstitital at the vacancy that belongs to the complex.

We next proposed that in order for any region containing n_o atoms to become amorphous, it is necessary that a critical complex concentration be reached. Considering further that owing to their nature complexes are immobile defects, we have used a Poisson distribution for the probability that any region becomes amorphous, as a function of the mean complex concentration. A rate theory approach was used for calculating the buildup of complexes and of free vacancies and interstitials. This allowed us to investigate the effect of temperature, dose, and preirradiation microstructure. The dose necessary to produce complete amorphization (within 3%) was calculated for the case of electron-irradiated TiNi. Also, the dose required to produce a given amorphous fraction as a function of temperature was calculated. The results are shown in Fig. 4.2.5 together with data by Mori and Fujita.[15]

A very interesting result – which emphasizes the role of vacancies – was obtained in connection with the microstructure. It was shown that increasing the dislocation density and/or decreasing the film thickness, both amounting to increasing the sink strength for interstitials, accelerates the amorphous transition. The faster kinetics follows from a more rapid increase of complexes as the above-mentioned indirect recombination process is diminished.

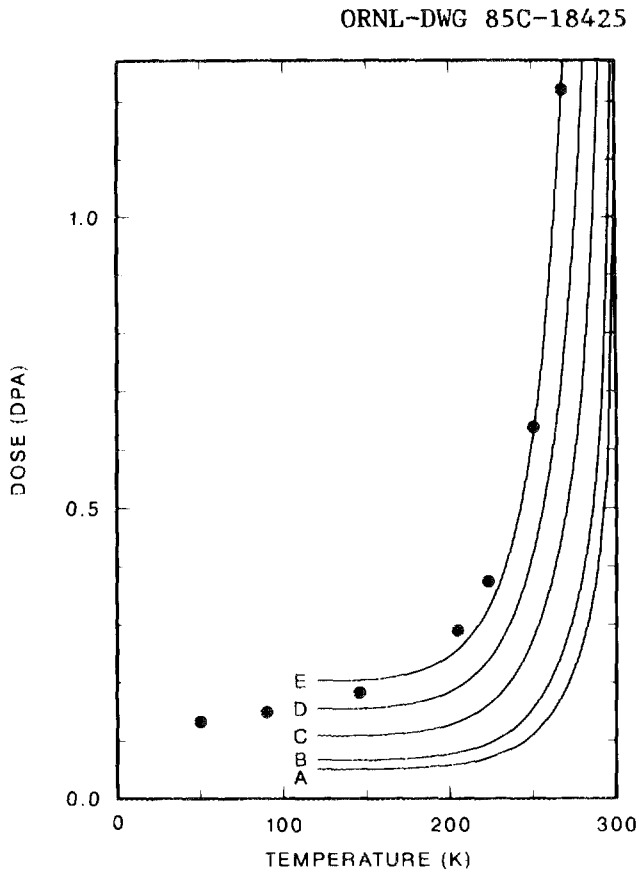

Fig. 4.2.5. Dose required to produce various amorphous fractions, as a function of temperature. A, 0.10; B, 0.20; C, 0.50; D, 0.80; and E, 0.97. Experimental points are from ref. 15.

We have simulated two different hypotheses of complex formation, one where it is symmetric with respect to the two components and one where it is asymmetric. In the latter case, the limit where just one of the atomic species can form complexes has been analyzed. The results simply show that in the latter case the amorphization kinetics is slower and the cut-off temperature for amorphization lower. An inspection of the rate equations reveals that other asymmetries might exist and be incorporated into the model while allowing both species to form complexes, e.g., different diffusivities, binding energies, or indirect recombination probabilities. The possibility of an asymmetry extending to all intermetallic compounds of a given binary system might explain, at least partly, why not all of them can become amorphous under irradiation.

4.2.4 The Effect of Point Defects on the Amorphization of Metallic Alloys During Ion Implantation[16] — D. F. Pedraza and L. K. Mansur

Conventional amorphization procedures start from either the gaseous phase (e.g., vapor deposition onto cold substrates) or the liquid phase

(e.g., splat quenching and melt spinning techniques), both based on very fast cooling rates. Particle bombardment techniques, on the other hand, start with crystalline solids. It has been suggested that ion irradiation produces conditions far more severe than those that arise on very fast quenching. This is tantamount to asserting that a state of disorder similar to that encountered in the liquid is produced locally by the collision cascades, which then "freeze" at an ultrafast rate. This means that after a certain dose, the entire crystalline target will have experienced displacement cascades and thus become amorphous.

However, as pointed out elsewhere in this section, electron irradiation also can induce the crystalline-to-amorphous transition. In this instance, no displacement cascades are produced. Instead, the amorphization phenomenon has to be related to the behavior of the radiation-induced point defects. Comparing the effects produced by each particle type may provide an understanding of the effect of point defects and also of effects due to displacement cascades. Our brief review of published observations provides a phenomenological background. This review singles out the absence of a radiation-induced microstructural evolution based upon like-point defect aggregation. The existence of a mechanism that prevents this aggregation and also inhibits mutual recombination, in order to produce a highly defective lattice, is postulated. As for electrons, the complex defect consisting of a vacancy-interstitial pair is again invoked, assuming here that the self-interstitial occurs in a dumbbell configuration. Similar calculations of the amorphous fraction versus dose and of the dose necessary for complete amorphization to those carried out in the work summarized previously for TiNi are conducted here. It is shown that the amorphization kinetics is not sensitive to the particular self-interstitial configuration.

For ions it is proposed that complexes may also form directly in the cascade athermally, in addition to forming by diffusional processes as in the electron case. The possibility of amorphization occurring directly as a result of cascade collapse also exists. In principle, both mechanisms may operate concurrently. Two experimental facts indicate that defect formation occurs mainly in the cascade region. One is that amorphization

occurs at lower doses under ions than under electron irradiation and the other is that, at variance with the electron case, amorphization progresses while the rest of the crystal remains ordered. This means that the cascade efficiency for producing free point defects is fairly low.

The in-cascade formation of complexes can be viewed as taking place partly at the expense of in-cascade recombination. It may be suggested, therefore, that the complex production rate could be much larger than under electron irradiation. Furthermore, due to the cascade geometry, defect configurations more complex than those already proposed might form. We have accounted for other possible stable complex configurations by assuming the formation of clusters of the simpler complex. A rate theory approach has been used here as well for calculating amorphization kinetics. Figure 4.2.6 illustrates two model calculations for the case of TiNi; s = 1 indicates a simple enhancement effect of individual complexes

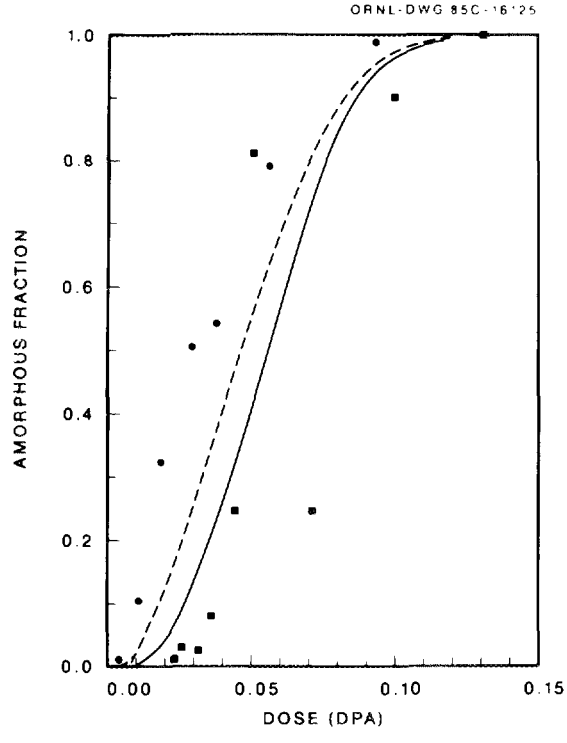

Fig. 4.2.6. Amorphous fraction versus ion dose at 300 K. Solid line: simple complex configuration (s = 1). Dashed line: two-complex clusters and single complexes (s = 2). ■ Experimental data by Brimhall et al. • Experimental data by Moine et al.

brought about by the production of displacement cascades, and $s = 2$ assumes that both individual complexes and two-complex clusters are produced in the cascade. An equal total cascade efficiency for both cases has been considered. The theoretical calculations are presented together with experimental data by Brimhall et al.[17] and by Moine et al.[18] It is seen that the theoretical curves attain virtually complete amorphization in coincidence with the experimental results. Parameter values assumed in the calculations are given in the full paper.

The mechanism of direct complex production in the cascade, in addition to the production of complexes by a diffusional process, results in ions being more efficient than electrons in inducing amorphization. The greater efficiency of ions in producing amorphization is supported by experimental observations. For instance, some compounds that are easily rendered amorphous under ion bombardment (e.g., Zr_3Al, FeTi) are resistant under electron irradiation.

An important point should be highlighted in this connection. In other studies comparing microstructural damage by ions and electrons where no amorphous transition occurs, it has been generally found that electrons are more effective per unit displacement in producing microstructual defects such as dislocation loops and cavities. The opposite seems to be the case when amorphization takes place, as ions seem to be more effective than electrons. This can be interpreted to support a very high efficiency for direct complex formation in cascades.

4.2.5 The Effect of Microstructure on the Minimum Critical Radius and Critical Number of Gas Atoms for Swelling[19] – W. A. Coghlan[20] and L. K. Mansur

Under irradiation, vacancies and transmutation product gas combine to form clusters that progressively increase in size. Initially these cavities grow slowly as bubbles, where the accumulation of vacancies is dictated by the absorption of gas atoms. After they reach a certain size, however, they may grow more rapidly, driven by the excess vacancy flux caused by the dislocation-cavity bias. The radius where this transformation in growth mechanism occurs is known as the critical radius, the value of which depends on the number of gas atoms in the cavity. It has

been shown theoretically that, as the number of gas atoms in a cavity increases, the critical radius decreases until a minimum is reached at which the critical radius vanishes. This value is called the minimum critical radius, r_c^*, and the number of gas atoms required is the critical number of gas atoms, n_g^* (ref. 21). These concepts have been corroborated experimentally in a number of studies, most recently in some detail quantitatively.[22-25]

Several material properties in addition to the irradiation conditions of dose rate and temperature strongly dictate the magnitudes of the minimum critical size and critical number of gas atoms. In this paper we show that the dislocation density has a remarkably strong effect. Over a wide range of dislocation density, the minimum critical radius increases linearly with dislocation density. We also show that the dislocation-cavity bias has a very strong and nonlinear effect. Since the bias depends on dislocation density and arrangement, both bias and dislocation density are explored together here.

Figure 4.2.7 shows the calculated dependence of the minimum critical radius, r_c^*, on bias for both ideal and Van der Waals gas laws for typical conditions pertaining to neutron irradiation of stainless steel. Figure 4.2.8 shows the very strong dependence of n_g^* on temperature for two different dislocation densities. It takes approximately an order of magnitude more gas atoms in a cavity to initiate bias-driven growth at 650°C than it does at 600°C. It can be seen also that n_g^* is dependent on the gas law used, particularly at the lower temperatures. Figure 4.2.9 plots the minimum critical radius against dislocation density for several different temperatures. The higher the temperature, the larger the dependence on dislocation density. These strong sensitivities imply that the time to the onset of bias-driven swelling is sensitive to the same variables. The effect of temperature is well known and has been discussed earlier. For systems that have small bias, the minimum critical radius decreases rapidly with increasing bias. The effect of dislocation density is also strong. Dislocation density and bias are not independently variable in a real system, however.

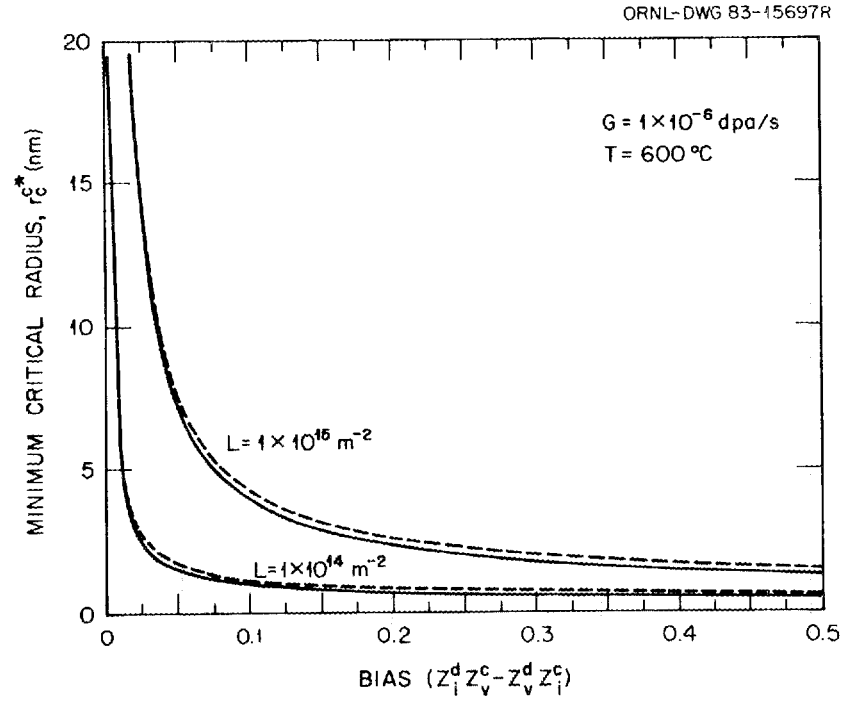

Fig. 4.2.7. Minimum critical radius as a function of bias at 600°C. The solid lines are calculated for cavities containing an ideal gas, and the dashed lines are calculated for a Van der Waals gas.

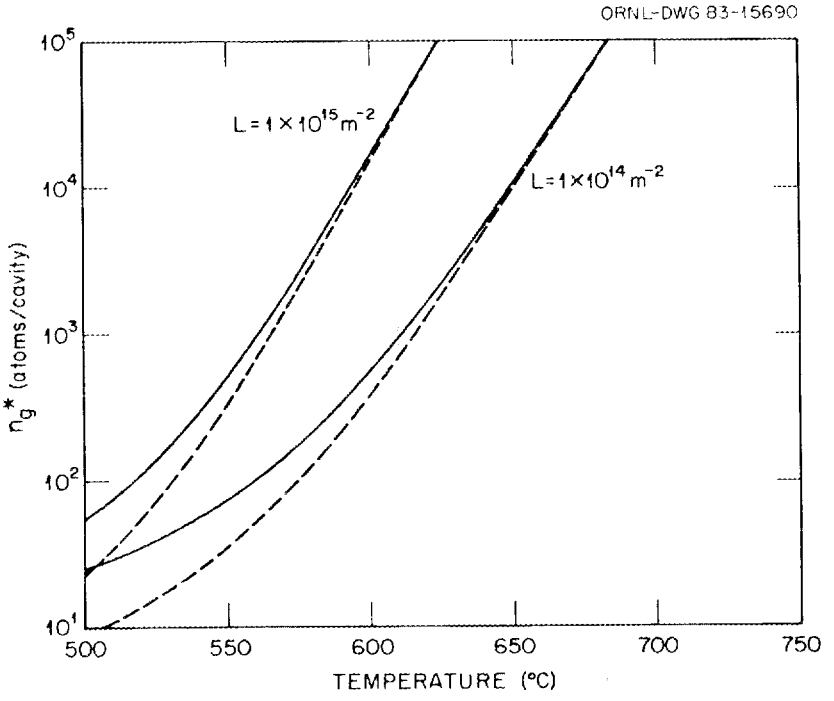

Fig. 4.2.8. Critical number of gas atoms versus temperature. The solid lines are for ideal gas, and the dashed lines are for a Van der Waals gas.

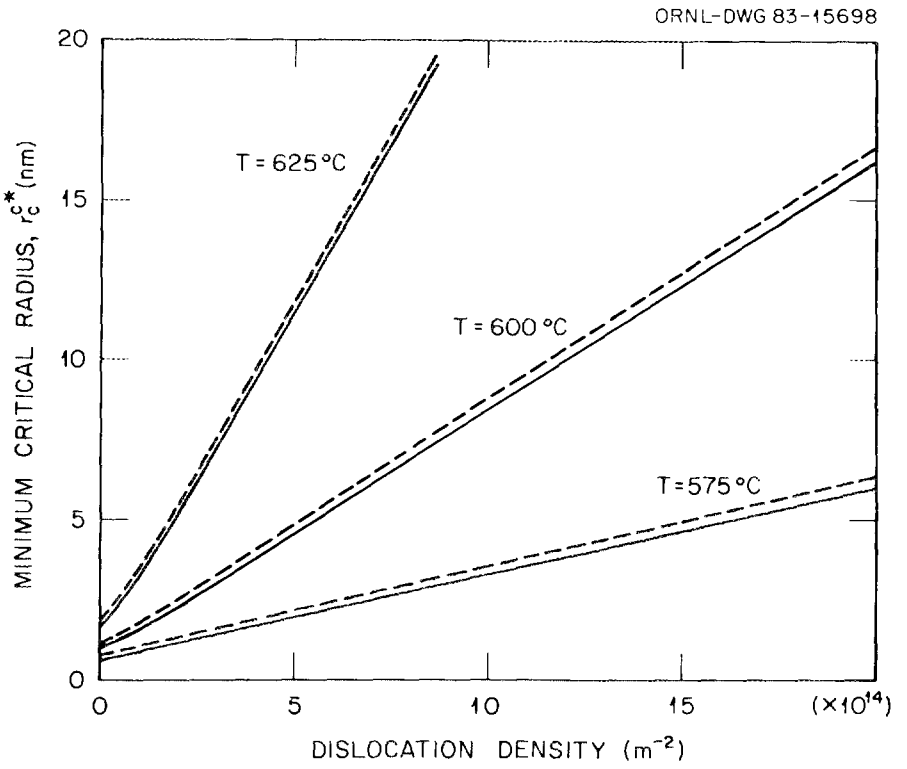

Fig. 4.2.9. Minimum critical radius as a function of dislocation density for ideal (solid line) and Van der Waals gas laws (dashed line).

The interaction of dislocation density and bias can be visualized by considering two materials with the same dislocation density but with the dislocations distributed in different ways. If the dislocations are distributed uniformly, the overall bias is larger. However, if most of the dislocations are found in dense tangles or cell walls, the average bias is reduced because of the mutual cancellation of the long-range strain fields of the dislocations. In the material with the nonhomogeneous dislocations, the average significantly increases the minimum critical radius, thus giving rise to a more swelling-resistant material. A second consequence also arises. Cavity swelling is expected to be patchy. For example, in a material having a cell structure, the region between the cell boundaries has low local dislocation density and therefore relatively high bias, leading to low critical radii and low critical numbers of gas atoms. In the dense region, the material has a high dislocation density

and a low bias leading to large critical radii. According to Fig. 4.2.7, bias-driven cavities are therefore expected to grow first in the cell interiors and only later in the cell walls. Early work by Stiegler et al.,[26] for example, on neutron-irradiated aluminum supports this expectation. Cavities were seen most often where the dislocation density was lowest.* More recent work also describes patchy swelling in cold-worked type 316 stainless steel.[27]

4.2.6 Development of Analytical Solutions for Helium Bubble Parameters Using a Hard Sphere Equation of State[28] – R. E. Stoller and G. R. Odette[29]

Considerable theoretical and experimental work has verified the role of helium-stabilized bubbles as the precursor to void formation in fast-neutron-irradiated stainless steels. The concept of the critical bubble radius or critical number of helium gas atoms required to induce bubble-to-void conversion has received particular attention because the length of the incubation time preceeding measurable swelling can be correlated with the time required for small helium/vacancy clusters to reach this critical size. As discussed elsewhere in this section, the value of the critical radius or critical number under irradiation is sensitive to a number of physical and environmental parameters. When the critical radius is computed for a given set of parameters and irradiation conditions, the value is also sensitive to the equation of state used to describe the behavior of the helium. The use of the ideal gas law permits one to obtain simple analytical expressions for the critical number, the critical radius, and the stable bubble radius under irradiation. Use of the Van der Waals equation of state improves the calculation considerably, as discussed elsewhere in this section. This is particularly true when high compressibilities result from small critical radii. The use of more complex equations of state typically requires resorting to iterative techniques to compute the helium bubble parameters.

In the present work a hard sphere equation of state (HSEOS) was used to compute the various bubble parameters, and the results were systematically compared with those computed by using the ideal gas law. The

*This does not contradict the fact that often the initial bubbles are formed on dislocations, which then may climb away.

comparison indicated that, when using the HSEOS to compute the critical parameters, the functional dependencies of the ideal gas expressions were preserved. This led to the development of two "master curves" that describe the deviation from ideal gas behavior as a function of the vacancy supersaturation, S, where:

$$S = \frac{D_V C_V - D_i C_i}{D_V C_V^e} \quad . \tag{1}$$

In Eq. (1), $D_V C_V$ and $D_i C_i$ are the vacancy and interstitial fluxes due to the irradiation and $D_V C_V^e$ is the self diffusion coefficient. For the ideal gas case, the critical number is given by

$$n_g^* = \frac{32 F_V}{27} \left(\frac{\gamma}{kT}\right)^3 \left(\frac{\Omega}{\ln S}\right)^2 \quad , \tag{2}$$

and the critical radius is

$$r_c^* = \frac{4\gamma\Omega}{3kT \ \ln S} \quad , \tag{3}$$

where Ω is the atomic volume, γ is the surface free energy, and F_V is a geometric factor that allows for nonspherical cavities. The cavity volume is given as $F_c r^3$; hence for a sphere $F_V = 4\pi/3$.

The solutions for the critical parameters using the HSEOS are given in Eqs. (4) and (5). As stated above, the results are similar to Eqs. (2) and (3) with the geometrical coefficients replaced by two functions that depend on the vacancy supersaturation.

$$n_g^* = f_1(\Phi) \ F_V \left(\frac{\gamma}{kT}\right)^3 \left(\frac{\Omega}{\Phi}\right)^2 \tag{4}$$

$$r_c^* = f_2(\Phi) \ \frac{\gamma\Omega}{kT \ \Phi} \tag{5}$$

The functions $f_1(\Phi)$ and $f_2(\Phi)$ are polynomials in $\Phi = \ln(S)$

$$f_1(\Phi) = a_0 + a_1\Phi + a_2\Phi^2 \ . \ . \ . \ + a_{10}\Phi^{10} \tag{6}$$

$$f_2(\Phi) = b_0 + b_1\Phi + b_2\Phi^2 \ . \ . \ . \ + b_{10}\Phi^{10} \tag{7}$$

whose coefficients are given in the full paper. The influence of the equation of state on the critical number and critical radius is shown in Fig. 4.2.10, where the ratio of the HSEOS to ideal gas values is plotted as a function of S. Under fast reactor conditions, a supersaturation of 10 would be obtained at about 500 C. For temperatures less than 500 C, Fig. 4.2.10 indicates that the error in using the ideal gas law to compute the critical number exceeds a factor of 2. Thus the use of the ideal gas law in a predictive computer model would result in a similar error for the dose required for bubble-to-void conversion.

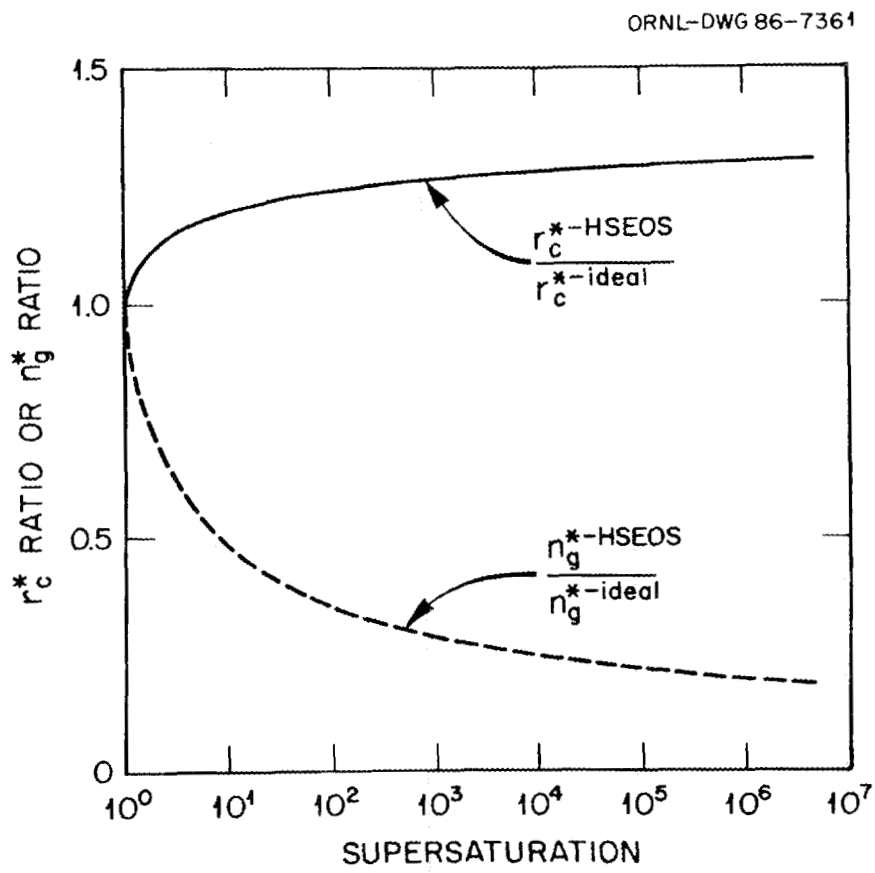

Fig. 4.2.10. Ratio of the critical bubble parameters computed with the HSEOS to the ideal gas values.

In addition to the critical bubble parameters, the ability to compute the bubble radius, r_c^s, as a function of the helium content is also required to model the swelling incubation regime. The use of the HSEOS requires finding the root of a twelfth-order equation; iterative methods are necessary and one must be sure of finding the correct root. An effort was made to relate the ideal gas bubble radius to the value computed with the HSEOS. Figure 4.2.11 shows the ratio of the ideal gas to HSEOS bubble radius as a function of a reduced radius:

$$R = \left[\frac{r_c^{s\text{-ideal}}}{\frac{kT}{\gamma}}\right]^{1/3} \tag{8}$$

for four vacancy supersaturations with the case for no irradiation, i.e., $S = 1$ overlaying the other curves. This led to a third master curve which can be used to find the real gas bubble radius directly from the ideal gas value. This master curve has also been fit with a polynomial

$$f_3(R) = c_0 + c_1R + c_2R^2 \ . \ . \ . + c_3R^{10} \ , \tag{9}$$

and the coefficients are given in the full paper. By using Eq. (9), the bubble radius can be computed as

$$r_c^s\text{-HSEOS} = \frac{r_c^{s\text{-ideal}}}{f_3(R)} \ . \tag{10}$$

Eqs. (8–10) are valid over the entire range of reasonable bubble radii ($r_c^s > 0.2$ nm).

The solutions given in Eqs. (4–5) provide the improved accuracy of the hard sphere equation of state while regaining the computational simplicity of the ideal gas law. Along with Eq. (10), they eliminate time-consuming iterative calculations of key helium bubble parameters which would otherwise be required. The results obtained here can be used in detailed models of void swelling and microstructural evolution to simplify the simulation of the void nucleation regime.

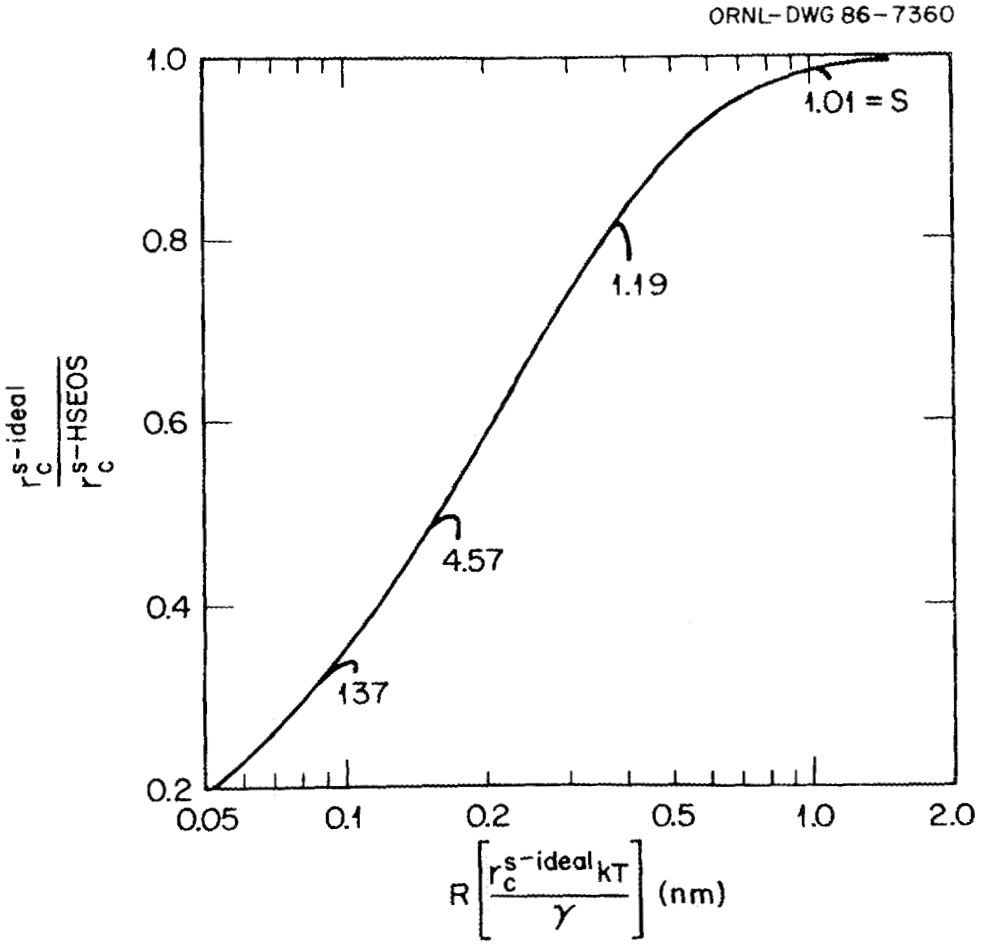

Fig. 4.2.11. Master curve for obtaining the stable bubble radius from the ideal gas value (r_c^S) by using HSEOS.

4.2.7 A Composite Model of Microstructural Evolution in Austenitic Stainless Steel Under Fast Neutron Irradiation[30] – R. E. Stoller and G. R. Odette[29]

A rate-theory-based model has been developed that includes the simultaneous evolution of the dislocation and cavity components of the microstructure of irradiated stainless steels. Previous work has generally focused on developing models for void swelling while either neglecting the time dependence of the dislocation structure or introducing phenomenological forms for it. These models have broadened our understanding of the

physical processes that give rise to swelling, e.g., the role of helium and void formation from critically sized bubbles. That work has also demonstrated some predictive capability by successful calibration to fit the results of fast reactor swelling data. However, considerable uncertainty about the values of key parameters in these models limits their usefulness as predictive tools. The present work represents an effort to remove some of these uncertainties by self-consistently generating the time dependence of the dislocation structure, both faulted loops and network dislocations. The model's predictions reveal the closely coupled nature of the evolution of the various microstructural components and generally track the available fast reactor data in the temperature range of 350 to 700°C for doses up to 100 dpa. As the theoretical model has become more complex, parameter choices were constrained to a more limited range of values in order to obtain agreement between theory and experiment.

The major innovation has been the development of a model of dislocation evolution that includes both thermal and irradiation-driven terms. For the network dislocations, the thermal terms are a high temperature climb (Bardeen-Herring) source term and an annihilation term due to stress-assisted directional diffusion of vacancies. Models of this type have been developed for the study of creep processes. The thermal evolution model was calibrated by using AISI 316 stainless steel tensile data obtained at 450, 550 and 650°C. Good agreement was obtained with the data using reasonable model parameters. Under irradiation, the growth and unfaulting of Frank faulted loops provide an additional source of network dislocations, and the dislocation network can be annihilated by bias-driven climb by absorption of point defects. The major parameters in the dislocation evolution model are the net interstitial biases of the network dislocations (Z_i^n) and the faulted loops (Z_i^l).

The dislocation evolution model has been coupled with a previously developed model of void swelling in which void formation is controlled by the growth of helium bubbles to a critical size at which the bubbles convert to voids. The void swelling model had been successfully used to fit

20% cold worked AISI 316 stainless steel swelling data from fast reactor irradiation experiments. In that work the dislocation density had been treated as an input parameter that was temperature dependent but not dose dependent.[31] Typical results from the composite model are shown in Fig. 4.2.12.

The predictions of the model compare favorably with fast reactor data as shown in Fig. 4.2.13 (refs. 32 and 33). The theoretical model presented here provides a tool for studying the evolution of the major microstructural features in fast-neutron-irradiated stainless steel. The predictions of the model reveal that the individual microstuctural components do not evolve independently but that their evolution is coupled via their mutual effects on the point-defect concentrations. In addition, the more complex model developed here was found to be more sensitive to

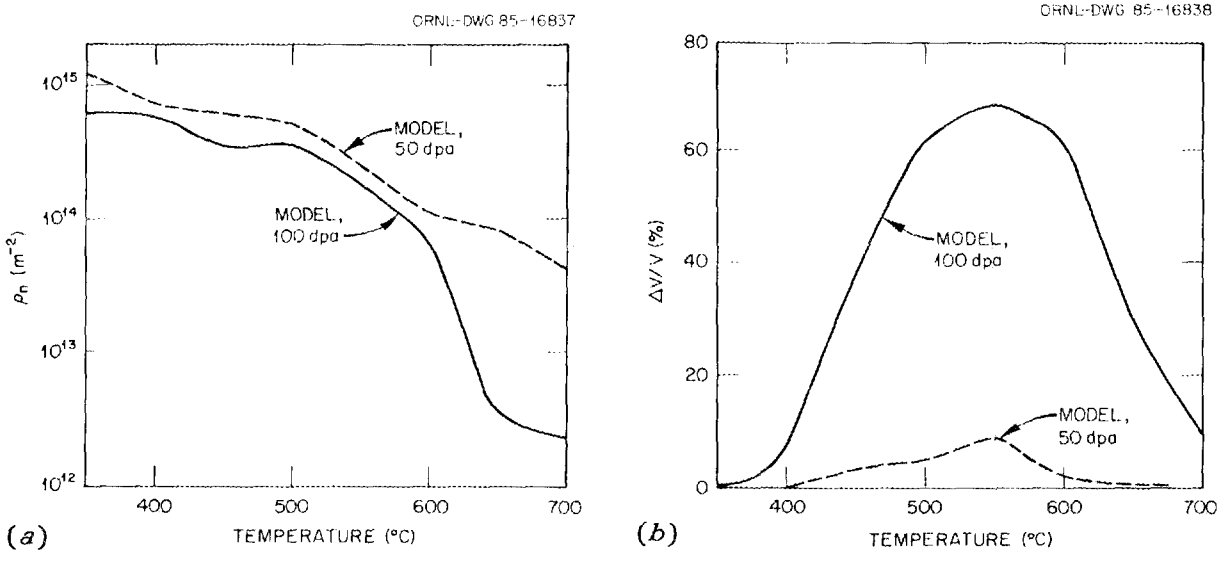

Fig. 4.2.12. Temperature dependence of model predictions of swelling (*a*) and network dislocation density (*b*) at 50 and 100 dpa.

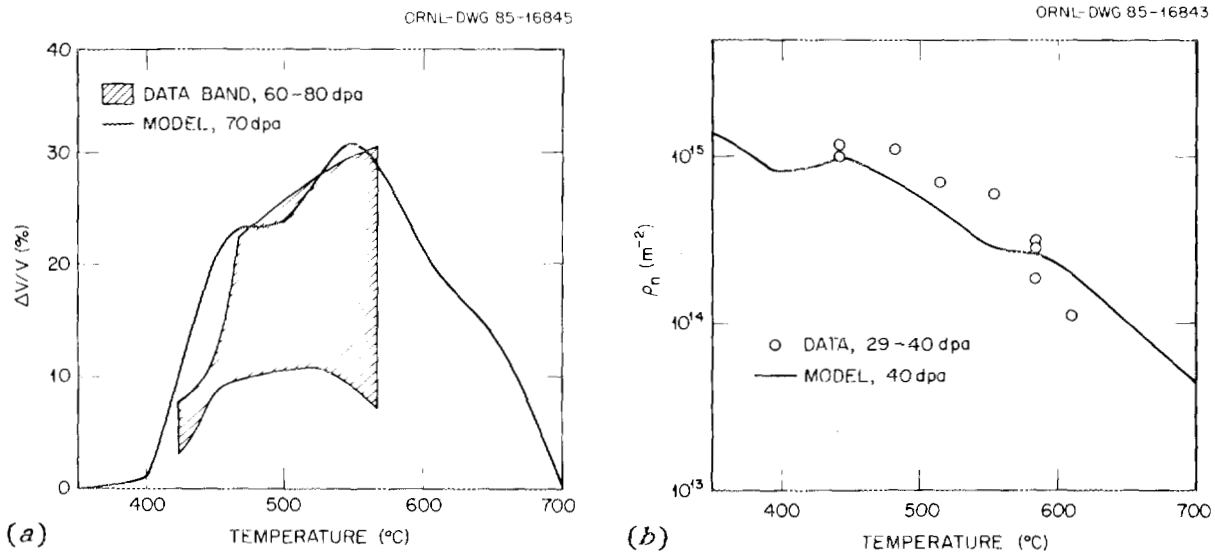

Fig. 4.2.13. Comparison of composite model predictions of swelling (*a*) and network dislocation density (*b*) with fast reactor data.

certain parameter variations than simpler models because of these couplings. This indicates that the new model may provide a more reliable predictive tool than those that do not fully include the time dependence of the dislocation components.

4.2.8 An Analysis of Carbide Precipitation in Vanadium and Niobium During Aging and Ion Bombardment[34] – A. J. Pedraza[35] and D. Pedraza

The surface of a solid is the region where gas molecules may be adsorbed and eventually transferred to the bulk by a diffusion process. It is also the region where stresses can be more easily relaxed. Thus, the volume and shape changes that occur during the precipitation of a new phase can be more easily accommodated in the near surface region. During ion bombardment, the large fraction of point defects created provides additional means for accommodating these changes.

The volume changes that occur during the precipitation of carbides in vanadium and niobium are particularly high, e.g., 18.4% change is involved in V_2C formation and 17.4% in Nb_2C precipitation. These carbides are known to precipitate in the near surface region of alloys whose bulk carbon contents would cause no internal precipitates. We first analyzed surface precipitation in vanadium during aging and showed that it is a process that can be distinguished from bulk precipitation. A thermodynamic analysis of the vanadium-carbon system and an estimate of the plastic energy required for accommodating that change were performed in order to calculate the carbon concentrations necessary for surface and for bulk precipitation. A carbon concentration of 0.2 at. % produces bulk precipitation of V_2C in the range 523 to 823 K, while only about 0.05 at. % is necessary for surface precipitation. The mass balance equation shows that irradiation-induced carbide precipitation in vanadium depletes the matrix carbon concentration in its vicinity practically to zero. It is concluded that precipitation limited to the surface region can occur in high purity vanadium if an external carbon source is available. A similar conclusion is reached in the case of niobium, partly based on an estimate of the plastic energy required for accommodating the volume change due to carbide precipitation.

These analyses provide a basis to distinguish between surface and radiation-induced precipitates. Two main classes of behavior can arise during ion bombardment. When the highest damage region is very close to the surface, no internal precipitates are produced and radiation-induced point defects enhance surface precipitate growth. When peak damage is produced farther from the surface, internal precipitates are formed and compete with the surface precipitates for carbon atom capture. The mass balance equation shows that in vanadium irradiated with 3-MeV V^+ ions the precipitates formed in the highest damage region compete with the surface precipitates for the capture of carbon coming from an external source, for example, the vacuum chamber atmosphere. In contrast to surface precipitates that have practically only one carbon source, the radiation-induced matrix precipitates may also obtain carbon from the bulk. If the peak damage region is very close to the surface, as is the case with niobium

bombarded with 150-keV H^+, no internal precipitates are produced and radiation-induced point defects enhance the growth of surface precipitates. The delicate balance between carbon availability, transformation stresses, and radiation effects may significantly alter the precipitation characteristics of both the surface and the internal damaged region, relative to thermal aging.

4.2.9 References

1. Summary of paper published in *Acta Metall.* **33**, 1425–37 (1985).
2. Research Staff, Ford Motor Company, Dearborn, Mich.
3. L. K. Mansur, A. D. Brailsford, and W. A. Coghlan, *Acta Metall.* **33**, 1407–23 (1985).
4. Summary of a paper given at the symposium Irradiation Effects Associated with Ion Implantation, AIME Fall Meeting, Toronto, Oct. 13–17, 1985; proceedings to be published in *Nucl. Instrum. Methods Phys. Res. B* (1986).
5. Safety and Reliability Directorate, Culcheth, Warrington, U.K.
6. L. K. Mansur, A. D. Brailsford, and W. A. Coghlan, *Acta Metall.* **33**, 1407 (1985).
7. L. K. Mansur et al., *J. Nucl. Mater.* **103&104**, 1257 (1981).
8. A. D. Brailsford and L. K. Mansur, *Acta Metall.* **33**, 1425 (1985).
9. K. C. Russell, *Acta Metall.* **26**, 1615 (1978).
10. R. Stoller and G. R. Odette, *Effects of Radiation on Materials: Eleventh International Symposium*, ASTM STP 782, ed. H. R. Brager and J. S. Perrin, American Society for Testing and Materials, p. 275.
11. L. K. Mansur and W. A. Coghlan, *J. Nucl. Mater.* **119**, 1 (1983).
12. L. L. Horton and L. K. Mansur, "Experimental Determination of the Critical Cavity Radius in Fe-10Cr for Ion Irradiation," *Effects of Radiation on Materials: Twelfth International Symposium*, ASTM STP 870, American Society for Testing and Materials (in press).
13. E. H. Lee and L. K. Mansur, *Phil. Mag. A* **51**, 493 (1985).
14. Summary of a paper submitted for publication in *J. Mater. Res.*
15. H. Mori and H. Fujita, *Jpn. J. Appl. Phys.* **21**, L494 (1982).

16. Summary of a paper given at the symposium Irradiation Effects Associated with Ion Impalantation, AIME Fall Meeting, Toronto, Oct. 13–17, 1985; proceedings to be published in *Nucl. Instrum. Methods Phys. Res. B* (1986).

17. J. L. Brimhall, H. E. Kissinger, and A. R. Pelton, *Ion Implantation and Ion Beam Processing of Materials*, ed. G. K. Hubler, O. W. Holland, C. R. Clayton, and C. W. White, North Holland, New York, 1984, p. 163.

18. P. Moine et al., *Nucl. Instrum. Methods B* **7/8**, 20 (1985).

19. Summary of a paper presented at the symposium Effects of Radiation on Materials: Twelfth Symposium, ASTM STP 870, ed. F. A. Garner and J. S. Perrin, American Society for Testing and Materials, Philadelphia, 1985, pp. 481–92.

20. Department of Mechanical and Aerospace Engineering, Arizona State University, Tempe.

21. For a review, see L. K. Mansur and W. A. Coghlan, *J. Nucl. Mater.* **119**, 1 (1983).

22. A. Hishinuma and L. K. Mansur, *J. Nucl. Mater.* **118**, 91 (1983).

23. E. H. Lee and L. K. Mansur, *Phil. Mag. A* **52**, 493 (1985).

24. L. L. Horton and L. K. Mansur, p. 344 in *Effects of Irradiation on Materials*, 12th International Symposium, ASTM STP 870, ed. F. A. Garner and J. L. Perrin, American Society for Testing and Materials, Philadelphia, 1985.

25. E. H. Lee, L. K. Mansur, and A. F. Rowcliffe, "The Effect of Phosphorous on the Swelling and Precipitation Behavior of Austenitic Stainless Steels During Irradiation," *J. Nucl. Mater.* (in press).

26. J. O. Stiegler, K. Farrell, C.K.H. DuBose, and R. T. King, *High-Fluence Neutron-Irradiation Damage in Aluminum*, IAEA-SM-120/F, pp. 215–232.

27. G. R. Odette, P. J. Maziasz, and J. A. Spitznagel, *J. Nucl. Mater.* **103&104**, 1289 (1981).

28. Summary of a paper published in *J. Nucl. Mater.* **131**, 118–25 (1985).

29. Department of Chemical and Nuclear Engineering, University of California, Santa Barbara.

30. Summary of a paper to be presented at the 13th International Symposium on the Effects of Radiation on Materials, June 1986.

31. R. E. Stoller and G. R. Odette, *Effects of Irradiation on Materials: Eleventh International Symposium*, ASTM STP 782, American Society for Testing and Materials, Philadelphia, 1982, pp. 275–94.

32. F. A. Garner, *Optimizing Materials for Nuclear Applications*, symposium proceedings, the Metallurgical Society of AIME, New York, 1985.

33. J. I. Bramman et al., *Radiation Effects in Breeder Reactor Structural Materials*, International Conference, the Metallurgical Society of AIME, New York, 1977, pp. 479–507.

34. Summary of a paper given at the symposium Irradiation Effects Associated with Ion Implantation, AIME Fall Meeting, Toronto, Oct. 13–17, 1985; proceedings to be published in *Nucl. Instrum. Methods Phys. Res. B* (1986).

35. Department of Materials Science and Engineering, University of Tennessee, Knoxville.

4.3 FACILITY AND TECHNIQUE DEVELOPMENT

4.3.1 Isotopic Alloying to Tailor Helium Production Rates in Mixed-Spectrum Reactors[1] – L. K. Mansur, A. F. Rowcliffe, M. L. Grossbeck, and R. E. Stoller

An important aspect of research into the effects of irradiation on structural materials at elevated temperatures is the interaction of transmutation-produced helium with displacement damage. Helium is an insoluble inert gas typically produced to levels of a few tenths appm/dpa in fast reactor irradiations and to levels of up to tens of appm/dpa in fusion reactor environments. It has been found that this gas may contribute to dimensional instability and degradation of mechanical properties of irradiated structural materials and may strongly affect microstructural development and phase stability. In planned fusion reactors, the 14-MeV component of the (D,T) fusion neutron spectrum ensures the simultaneous production of displacement damage and high helium concentrations in all

the materials used for the first wall, the blanket structure, and related components of a fusion reactor. Until a 14-MeV neutron machine suitable for fusion materials research is constructed, materials scientists must utilize fission reactors and accelerators to investigate radiation damage effects and to develop improved materials.

The purpose of the present paper is to examine an approach that allows the helium generation to be varied widely in alloys of identical chemical composition, during side-by-side irradiation in mixed-spectrum reactors. In mixed spectra, the fast neutron component of the spectrum produces high levels of damage, accompanied by some transmutation products including helium, while the slow component of the neutron spectrum produces high levels of helium by the two-step reaction

$$^{58}\mathrm{Ni}(n,\gamma)^{59}\mathrm{Ni}(n,\alpha)^{56}\mathrm{Fe} \tag{1}$$

Since ^{58}Ni is responsible for high helium production, the idea is to systematically deplete or enrich it in favor of other stable isotopes of nickel, while maintaining the overall nickel chemical composition constant.

In general, helium production in mixed-spectrum reactors can be described by

$$n = n_t + n_f = \sum_{\ell} \sum_{i} (p_{\ell}^{i} + s_{\ell}^{i}) q_{\ell}^{i} r_{\ell} \ , \tag{2}$$

where n is the number of helium atoms per atom of alloy and t denotes time. The quantities $n_t = \sum_{\ell} \sum_{i} p_{\ell}^{i} q_{\ell}^{i} r_{\ell}$ and $n_f = \sum_{\ell} \sum_{i} s_{\ell}^{i} q_{\ell}^{i} r_{\ell}$ are the fractional helium levels produced by slow and fast reactions, respectively. Hence, p_{ℓ}^{i} *and* s_{ℓ}^{i} are the helium generating functions for slow and fast reactions giving the cumulative number of helium atoms produced per initial atom of isotope i of element ℓ at time t. The symbol q_{ℓ}^{i} is the initial fraction of atoms of isotope i of element ℓ to all atoms of element ℓ in the alloy, and r_{ℓ} is the atom fraction of element ℓ in the alloy, so that $\sum_{i} q_{\ell}^{i} = \sum_{\ell} r_{\ell} = 1$.

The quantities q_ℓ^i are of primary interest here. The crux of isotopic alloying is to manipulate q_ℓ^i at will, not simply accepting the naturally occurring distribution of stable isotopes. We might make use of the naturally occurring mixture and one or more mixtures enriched or depleted in an isotope of interest. The mixtures are combined in various proportions to achieve systematic variations. In general, q_ℓ^i is given by

$$q_\ell^i = \sum_j a^i_{j,\ell} b_{j,\ell} \tag{3}$$

Here $a^i_{j,\ell}$ is the atom fraction of isotope i in the isotopic mixture j of element ℓ. Similarly, $b_{j,\ell}$ is the atom fraction that isotope mixture j comprises of total atoms of element ℓ of the alloy. Again, $\sum_i a^i_{j,\ell} = \sum_i b_{j,\ell} = 1$.

To apply this formalism to nickel-bearing alloys, we may take all p_ℓ^i as negligible, except for p^{58}_{Ni}, the production term corresponding to Eq. (1). It can be shown that

$$p^{58}_{\mathrm{Ni}} = f\ \sigma_\alpha/\sigma_T\ , \tag{4}$$

where f is the cumulative fraction of ^{59}Ni that has been eliminated by all types of reactions up to fluence ϕt, σ_α is the spectral averaged (n, α) cross section of ^{59}Ni, and σ_T is the total reaction cross section of ^{59}Ni. The quantity f is given by

$$f = \frac{\sigma_T(1 - e^{-\sigma\gamma\phi t}) - \sigma_\gamma(1 - e^{-\sigma_T\phi t})}{\sigma_T - \sigma_\gamma} \tag{5}$$

The functions f and its first and second derivatives are plotted in Fig. 4.3.1 for the High Flux Isotope Reactor Peripheral Target Position spectral-averaged cross sections. Figure 4.3.1(a) shows f. This is the shape of the helium accumulation function by slow neutron reactions that arises in all calculations for specific alloys. At a total fluence of 2×10^{28} n/m^2 the helium accumulation is only a few percent from saturation (unity). To obtain the helium accumulated per initial atom of ^{58}Ni, this function need only be multiplied by σ_α/σ_T or 0.126 for the present case. Figure 4.3.1(b) shows f'. This gives directly the fraction of ^{59}Ni

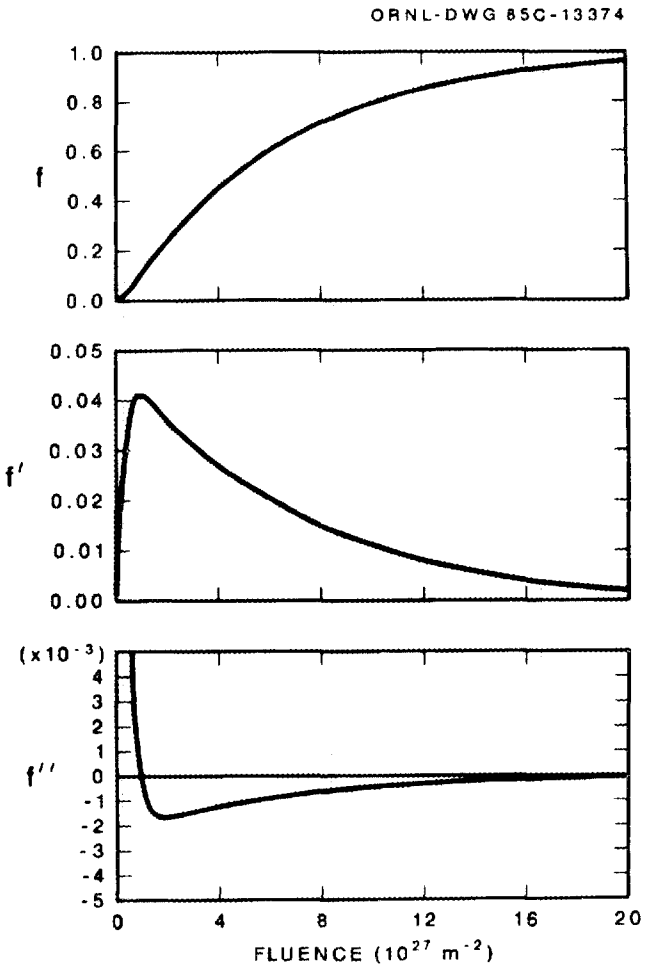

Fig. 4.3.1. The functions f, f', and f'' versus fluence for a wide range of fluence. (*a*) The cumulative fraction f of ^{59}Ni to initial ^{58}Ni transformed to other species, (*b*) the instantaneous fraction f' of ^{59}Ni, and (*c*) f'' its derivative.

to initial ^{58}Ni at any fluence. For the current cross-section values, the peak value of ^{59}Ni is about 4%. Figure 4.3.1(*c*) shows the behavior of f''.

We have recently obtained two special isotopic mixtures of nickel from the Operations Division of Oak Ridge National Laboratory that are highly enriched in ^{60}Ni and in ^{58}Ni, respectively. Using these isotopes, we are pursuing two broad categories of experiments:

1. Experiments formulated on the basis of radiation effects theory and mechanisms, which address fundamental aspects of helium effects in nickel-bearing alloys.
2. Experiments designed to assess the response of nickel-bearing structural alloys to the high levels of displacement damage and helium expected in a fusion reactor environment.

Both types of experiments, mechanistic and scoping, could also be carried out with materials that do not normally contain nickel but to which nickel is added to increase helium production. It then becomes additionally necessary to determine the effects of the nickel addition on the physical metallurgy of the alloy system. Examples of experiments that are being initiated are described in the paper.

4.3.2 Development of a Stressed Specimen Chamber for Through-Range Proton Irradiation of Ribbon Specimens — N. H. Packan and R. A. Buhl

Embrittlement of materials under irradiation is a problem attracting ever-increasing attention. There is a need for experiments that can probe this area rapidly and with reliable control over irradiation conditions, including the vital parameter of applied stress. To provide such a capability we are developing a stressed specimen chamber that will permit through-thickness damage of ribbon specimens 25 to 30 μm thick by using a 4-MeV proton beam from our Van de Graaff accelerator. During irradiation, the specimens will be under a chosen static load applied by one or more weights (Fig. 4.3.2). Postirradiation studies will employ a variety of techniques, including mechanical testing, Auger analysis of fracture surfaces, and electron microscopy.

Early tests revealed problems in removing the substantial heat from the volume bombarded by the protons. A number of major modifications are being made revolving around a novel method of helium cooling within the chamber. Admittance of helium to the chamber is via jets directed at the specimen and at the beam line foil window. For efficient cooling, helium is being exhausted through a porous insert situated directly behind the specimen in the temperature control block. The temperature control block

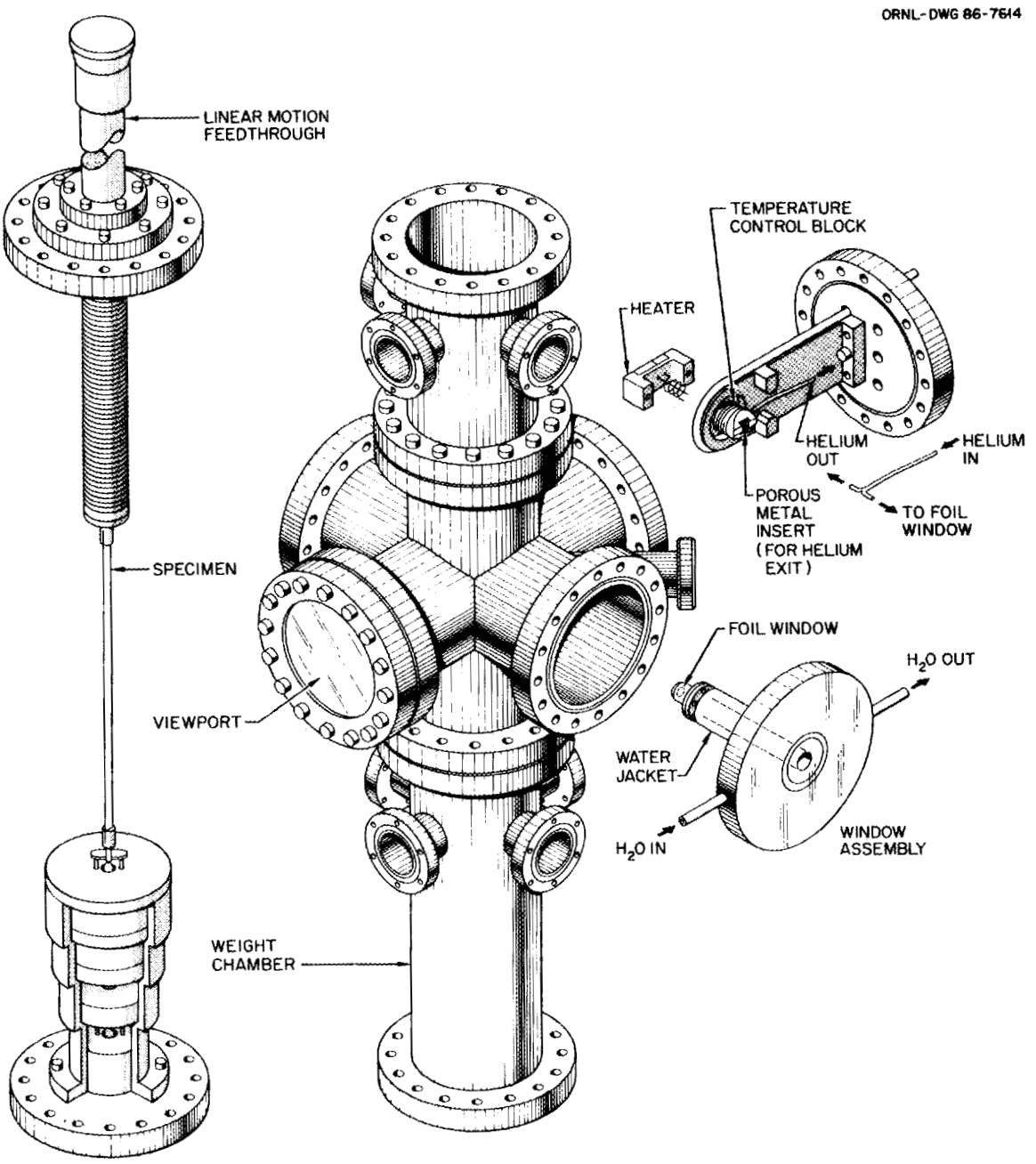

Fig. 4.3.2. Assembly view of the stressed-specimen chamber. A central region, about 4 mm high, of the 3-mm-wide by 300-mm-long ribbon specimen is bombarded by a beam of 4-MeV protons.

is additionally cooled by a coil containing refrigerated helium gas, and it can be heated by a resistance heater. Tests are in progress to define the optimum procedures for temperature control and the maximum proton beam intensity that can be handled.

4.3.3 Migration Behavior of Helium Under Displacive Irradiation in Stainless Steel, Nickel, Iron, and Zirconium[2] - M. B. Lewis and K. Farrell

Helium is an inevitable by-product of the irradiation of reactor structural materials with energetic neutrons. In future fusion reactor devices, helium may accumulate at a rate of several hundred atomic parts per million per year in heavily irradiated metals and ceramic materials. The energy of solution of helium in crystalline solids is large and, because helium does not form chemical compounds with its host, it tends to accumulate at pre-existing or radiation-induced crystal defects. Furthermore, calculations indicate that the binding energy of helium atoms with metal vacancies is high, greater than about 2 eV. This is higher than for binding with other helium atoms, self-interstitial atoms, impurities, and dislocations. Therefore, helium is expected to become preferentially bound with vacancies.

Entrapment of helium affects its migration behavior. In the absence of vacancies and other traps, helium can migrate interstitially with an activation energy less than 0.5 eV. Consequently, long-range helium transport is feasible at or below room temperature if the concentration of traps is low. Otherwise, the mobility of helium is limited by the density of traps and by the events occurring at the traps. Measurements of helium migration are needed to test these models and to improve our fundamental understanding of the problems of helium embrittlement and radiation-induced swelling, which involve migration and trapping of helium.

Accordingly, we have used helium ion implantations at elevated temperatures and nuclear microanalyses to gather preliminary data on helium migration during hot irradiations in stainless steel, nickel, α-iron, and α-zirconium. These metals were chosen because they represent the bases of the major alloys used in fusion reactor first walls and fission reactor core construction. They also display a wide range of responses to radiation damage. Stainless steels and nickel are highly susceptible to swelling and helium embrittlement, whereas ferritic steels are more resistant, and α-zirconium is comparatively immune unless considerable helium is introduced. One purpose of these experiments was to seek a correlation of helium migration with the known damage responses.

The targets were implanted with monoenergetic beams of helium-3 at energies of 200 keV or 300 keV. These implantation energies were chosen to ensure an ion range large enough (>0.5 μm) to avoid near surface defects and contaminants but low enough to allow concentration versus depth profiles to be measured readily.

Following the implantation the targets were quickly brought to room temperature and transferred to another target chamber for determination of concentration-depth profiles. These profiles were measured by a method of nuclear reaction microanalysis using a 0.5-MeV deuterium beam. Alpha particles from the $He^3(d,\alpha)p$ reaction were energy analyzed at a reaction angle of 65 or 70° from the deuterium beam direction.

An example of the results of the measurements is shown in Fig. 4.3.3. These data are for helium implantation in zirconium at temperatures where

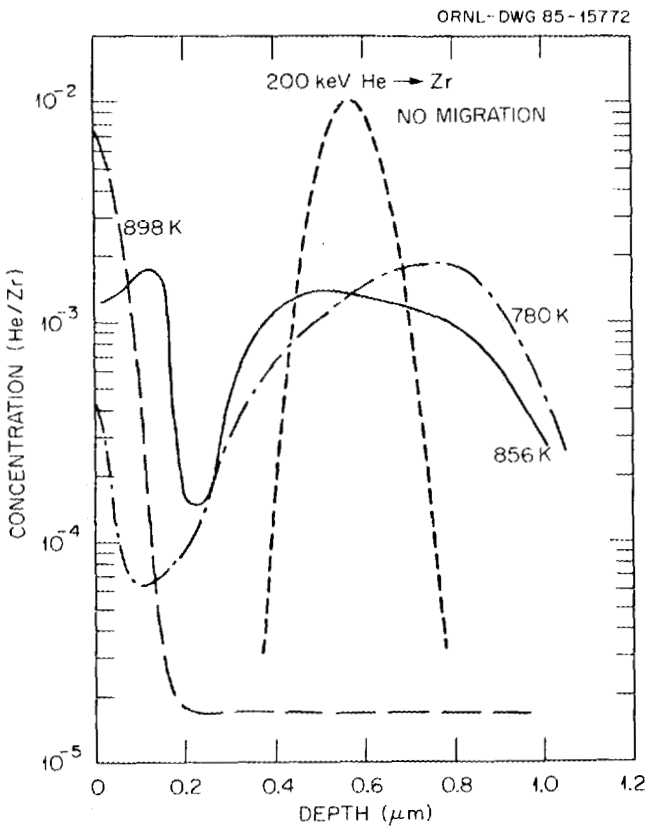

Fig. 4.3.3. Helium-3 concentration versus depth below the irradiated surface following the implantations at the temperatures shown. "No migration" refers to the theoretical profile of the initial implantation.

most of the helium experiences long-range migration during the implantation. As is evident in the figure, when the helium escapes the region (≈0.6 micron) where it was initially implanted, it is recaptured at the target surface. Although most defects such as vacancies are generated near the end of the ion range (≈0.6 micron), a fraction of the defects are also generated at the surface. One possible explanation of the present results is that those defects generated at the surface by the ion beam do not anneal as rapidly as those in the bulk; a surface film such as oxygen may either inhibit the recombination of vacancies and interstitials or act as a trap itself. Work with other metals as well as oxygen-bearing targets is in progress in order to better understand this phenomenon. In nickel and stainless steel, it was found that helium exhibited essentially no migration at the temperatures studied, while in iron the behavior was between that of zirconium and that of nickel.

4.3.4 Ion Source Development – M. B. Lewis

A duoplasmatron ion source has been installed on the 5-MV Van de Graaffe generator. This source can be mounted in place at the conventional "910 heavy ion" source with minimal modification to the rest of the accelerator terminal; only a polarity reversal of the anode power supply and current meter is necessary. Owing to the effective use of a magnetic mirror between the cathode and the anode, the ion densities can be as high as 6×10^{14} ions/cm^2, and the source can produce proton beam currents up to a milliampere. This source is being used to produce 4-MeV proton currents up to about 50 μA/cm^2 on 40-μm-thick targets, which are to be under stress during the irradiation in our new stressed-specimen chamber. This source can also produce up to 4-MeV oxygen beams of several microamperes.

Modifications have also been made on the heavy-ion source to increase the lifetime of the source. A hole approximately 5 mm in diameter has been drilled in the wall of the anode. When this hole is filled with a metal plug (e.g., iron) the plug acts as a long-term reservoir for metal ions. Electron bombardment of the surface of the plug removes carbon and

keeps the surface clean and chemically active to react continually with CCl_4 and produce metallic chlorides. Testing of this source is still in progress.

4.3.5 Liquid-Nitrogen-Cooled Fracture Apparatus for Auger Analysis of Irradiated Specimens

– L. Heatherly, Jr., R. E. Clausing, and N. Kishimoto[3]

In order to observe grain boundary segregation in alloys exposed to neutron irradiation, specimens are fractured in our recently developed fracture chamber under ultrahigh vacuum conditions and analyzed with a scanning Auger microprobe.

Some alloys that are of interest to our program fracture intergranularly only at liquid nitrogen temperature. For this reason, a liquid-nitrogen-cooled fracture device has been fabricated and added to our ultra-high-vacuum specimen fracture and introduction stage. This device is compatible with the existing equipment; however, the cooled specimens are fractured by bending rather than by tension.

The specimen to be fractured at low temperature is loaded into one of our standard grips with part of the specimen protruding. This assembly is then slid into a box that is attached to a liquid-nitrogen reservoir. After the specimen temperature approaches 77 K, the cold box is driven downward, causing a plunger to break off the protruding part of the sample. The carriage is used to remove the assembly from the cold box and to transfer the specimen to the scanning Auger microprobe for analysis.

Several specimens including both neutron-irradiated and reirradiated ferritic materials have been successfully fractured and analyzed by using the liquid-nitrogen-cooled stage. This stage allows exposure of the grain boundaries of some materials when that would not otherwise be possible.

4.3.6 References

1. Summary of a paper submitted to *J. Nucl. Mater.* This research was sponsored both by the Office of Basic Energy Sciences and by the Office of Fusion Energy.

2. Summary of a paper given at the symposium Irradiation Effects Associated with Ion Implantation, AIME Fall Meeting, Toronto, Oct. 13–17, 1985; proceedings to be published in *Nucl. Instrum. Methods Phys. Res. B* (1986).

3. On leave from National Research Institute for Metals, Tsukuba, Japan.

4.4 RELATED RESEARCH

4.4.1 Measurements of Beryllium Migration in the ISX-B Tokamak – M. B. Lewis and R. A. Langley[1]

A beryllium limiter was installed in the ISX-B tokamak to test the applicabiity of beryllium as a plasma-side component for possible use in the Joint European Torus (JET). The ISX-B tokamak was operated for more than 3000 high-power, neutral-beam-injected discharges with the beryllium limiter. In order to assess the transport of beryllium in the tokamak and attached diagnostics, both stainless steel and silicon samples were placed at various strategic positions and used as catcher plates.

Nuclear reaction analysis was used to measure the beryllium deposited on the plates and to provide a measure of the beryllium transport in the tokamak. The reaction used was the ^{9}Be (p,α) ^{6}Li reaction at E_p = 330 keV. Surface barrier detectors were used to measure the alpha-particle energy at a reaction angle of 150°. A typical spectrum is shown in Fig. 4.4.1. The area of the 1.22-MeV alpha group was used to calculate the film thicknesses. Most of the beryllium films were in the thickness range 2 to 25 mg/m^2.

4.4.2 Reference

1. Fusion Energy Division.

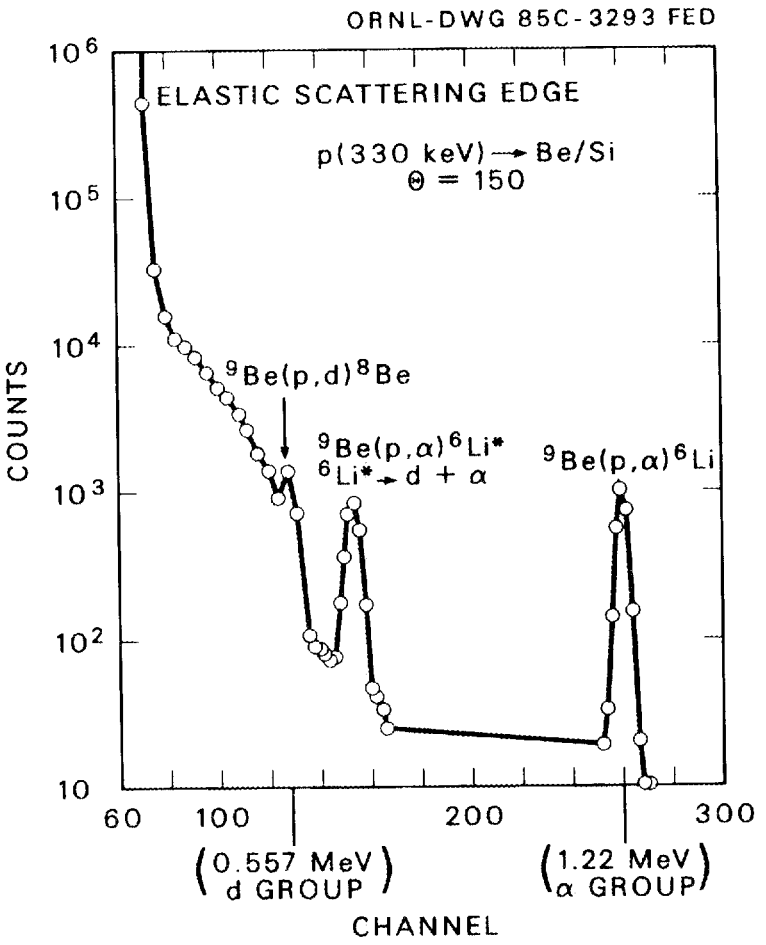

Fig. 4.4.1. Typical nuclear reaction spectrum for 330-keV p incident on a sample from the ISX-B tokamak. The distinct peaks result from a thin beryllium film on the silicon substrate of the sample.

5. STRUCTURE AND PROPERTIES OF SURFACES AND INTERFACES

C. J. McHargue

Although ion implantation doping has had its greatest success in semiconductor technology, it has been used in recent years to alter the physical and chemical properties of metals and the optical and electrical properties of insulators. Relatively little has been reported on changes in the mechanical and chemical properties of ceramics as a result of ion implantation.

Implantation for metallurgical purposes requires implanted concentrations of a few to several atomic percent (fluences of 10^{16}–10^{17} ions/cm^2). At such high fluences, effects such as sputtering and composition-dependent phase stability become important considerations. Similar concentrations are required to alter the surface mechanical properties of ceramics.

Implantation and radiation damage in ceramics are much more complex and less studied than in semiconductors or metals. In the displacement cascade, one must deal with at least two sublattices, which may have different displacement energies. The types of defects that can be produced are strongly influenced by the requirements of local electrical charge neutrality, the local stoichiometry, and the nature of the chemical bonding of the particular lattice. Similarly, the local structure is strongly sensitive to the chemical nature of impurities or dopants. In addition, ionizing effects may introduce lattice defects, whereas in metals such effects are generally unimportant.

Members of the Metals and Ceramics and Solid State Divisions are studying the structural and mechanical property changes associated with ion beam treatment of a variety of ceramics.

The task on structure and mechanics of interfaces and thin films focuses its efforts on development and use of experimental techniques for quantitative characterization of parameters that control mechanical behavior. Specification of the state of strain and interface structure is

central in developing an understanding of adherence, for example. The methods used in this task represent a different approach to interface study and thin film research: the approach is to develop the "toughness" by manipulating both interfacial interactions and the film's deformation behavior. Measurements of the damping capacity of thin films, evaluations of the energy losses due to plastic deformation in small material volumes; and determination of the chemical composition, atomic structure, and state of strain at interfaces can all be done quantitatively by using techniques that are being developed or that presently exist at Oak Ridge National Laboratory (ORNL).

5.1 ION BEAM MODIFICATION OF CERAMIC SURFACES

A systematic study of implantation parameters (temperature, fluence, ion species) has given us the ability to prepare a variety of surface structures in single-crystal α-Al_2O_3 and α-SiC.

5.1.1 Amorphization of α-Al_2O_3 and α-SiC (ref. 1) — C. J. McHargue, G. C. Farlow,[2] C. W. White,[3] J. M. Williams,[3] G. M. Begun,[4] and P. S. Sklad

The structures of the near-surface regions of α-Al_2O_3 and α-SiC single crystals after implantation were determined by Rutherford backscattering-channeling (RBS), transmission electron microscopy (TEM), and Raman spectroscopy (for α-SiC). In order to normalize the data for a variety of implant species, energies, and fluences, the damage in the aluminum or silicon sublattice (from RBS measurements) was examined as a function of defect production (displacements per atom, dpa).

The effect of substrate temperature on the resultant structure is shown in Figs. 5.1.1 and 5.1.2. The RBS spectra of Fig. 5.1.1 are from crystals implanted with 4×10^{16} Cr/cm^2 (150 keV) at 77, 300, and 640 K. This fluence corresponds to 5.1 dpa. Disorder in the aluminum sublattice at the peak damage position is about the same for substrate temperatures of 300 and 640 K. The spectra show considerable recovery in the immediate surface layer for the higher substrate temperature. The degree of substitutionality of chromium was about the same for these temperatures (34% at 640 K, 29% at 300 K). The 77-K implant gave a scattering curve typical of

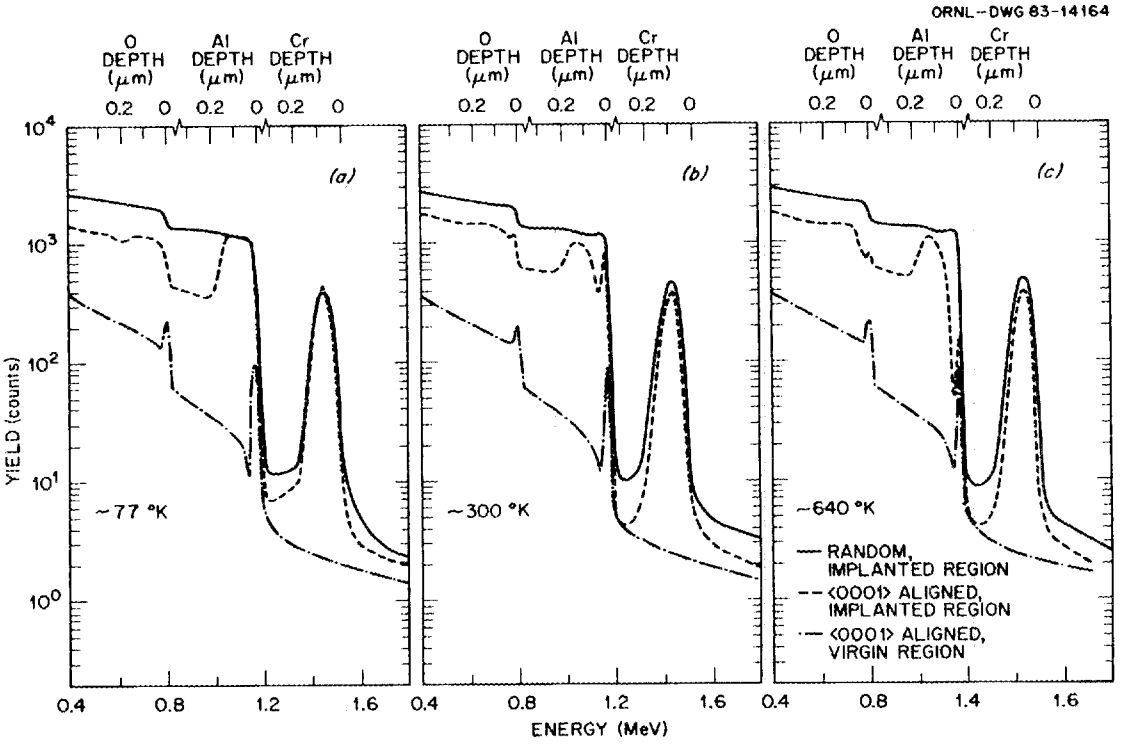

Fig. 5.1.1. Backscattering spectra from α-Al_2O_3 implanted with 4×10^{16} Cr/cm^2 (5.1 dpa) at 77, 300, and 640 K.

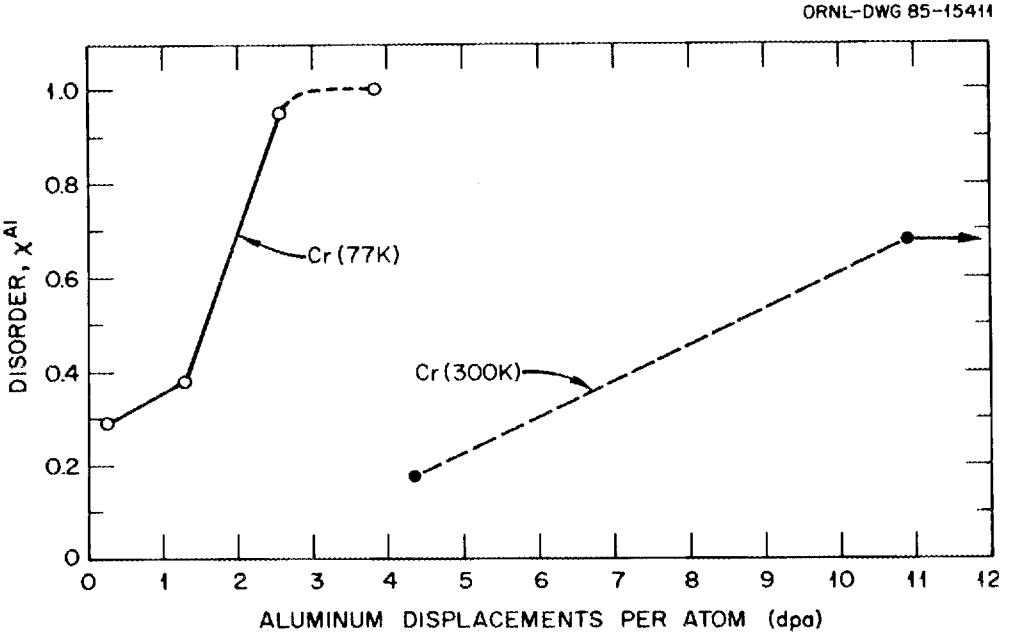

Fig. 5.1.2. Disorder in the aluminum sublattice (χ^{Al}) as a function of fluence (dpa) for chromium implanted into α-Al_2O_3 at 77 and 300 K.

an amorphous layer that extended to about 120 nm - well beyond the peak concentration of chromium. The amorphous nature of this region was confirmed by TEM observations.

The effect of increasing fluence is also shown in Fig. 5.1.2 for chromium implanted into Al_2O_3. Disorder in the aluminum sublattice, χ^{Al}, remains constant at a value of 0.66 for the fluence range of 10.9 to 109 dpa for specimens implanted at 300 K. The saturation suggests that the defects are mobile at these high damage levels such that defects are annihilated at the same rate as they are produced. Burnett and Page[5] report that α-Al_2O_3 implanted with 6×10^{17} Cr/cm^2 (300 keV) at 300 K had an amorphous surface layer; hence the curve in Fig. 5.1.2 must again increase to a value of unity. The fluence for their specimen corresponded to more than 600 dpa, and the chromium-to-aluminum ratio was approximately unity. The critical fluence for amorphization by chromium at 77 K (about 3 dpa) is 200 times less than at 300 K (greater than 600 dpa).

The data for a number of chemical species implanted into α-Al_2O_3 are summarized in Fig. 5.1.3. Zirconium and zinc (not shown) are the only cations to produce amorphous α-Al_2O_3 at 300 K in our studies. The RBS for zirconium (170 keV) gave a value of 0.75 for χ^{Al} after a fluence of

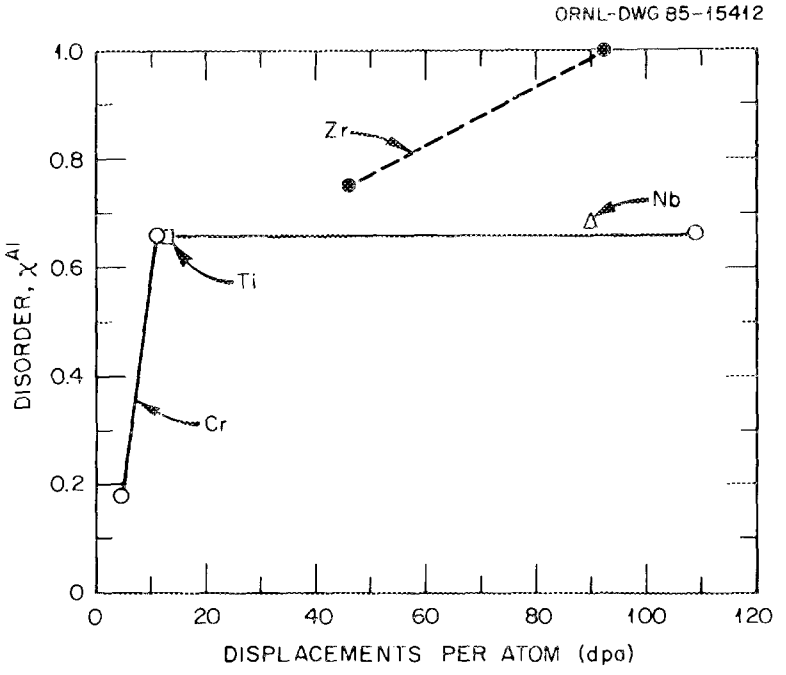

Fig. 5.1.3. Disorder in the aluminum sublattice (χ^{Al}) as a function of fluence (dpa) for α-Al_2O_3 implanted with Cr, Ti, Nb, and Zr at 300 K.

$2 \times 10^{16}/cm^2$ (46 dpa) but a value of 1.0 after a fluence of $4 \times 10^{16}/cm^2$ (92 dpa). The RBS spectra showed that there was no tendency for zirconium to occupy substitutional lattice sites even at the lower fluence. In order to determine that the zirconium effect was not associated with changes in the cascade nature due to the higher mass, implants were made with niobium (having approximately one higher mass unit). The value of χ^{Al} for a fluence of 90 dpa was 0.68 (compared with 1.0 for zirconium at dpa of 92). Thus, it appears that zirconium stabilizes the defects to prevent recovery processes or prevents the disordered regions within cascades from reordering. In the range of fluences studied (to 110 dpa), the disorder in the aluminum sublattice is approximately the same for Cr, Ti, and Nb. The corresponding value for χ^{O} was about 0.9.

The fluence required to amorphize covalently bonded α-SiC was more than 1000 times lower at 300 K than that required for Al_2O_3. [Room temperature (300 K) is approximately 0.13 T_m for Al_2O_3 and 0.11 T_d, decomposition temperature, for SiC.] Figure 5.1.4 shows the peak disorder in the silicon sublattice, χ^{Si}, as a function of fluence (dpa). The energies of the nitrogen (62 keV) and chromium (280 keV) were chosen to give the

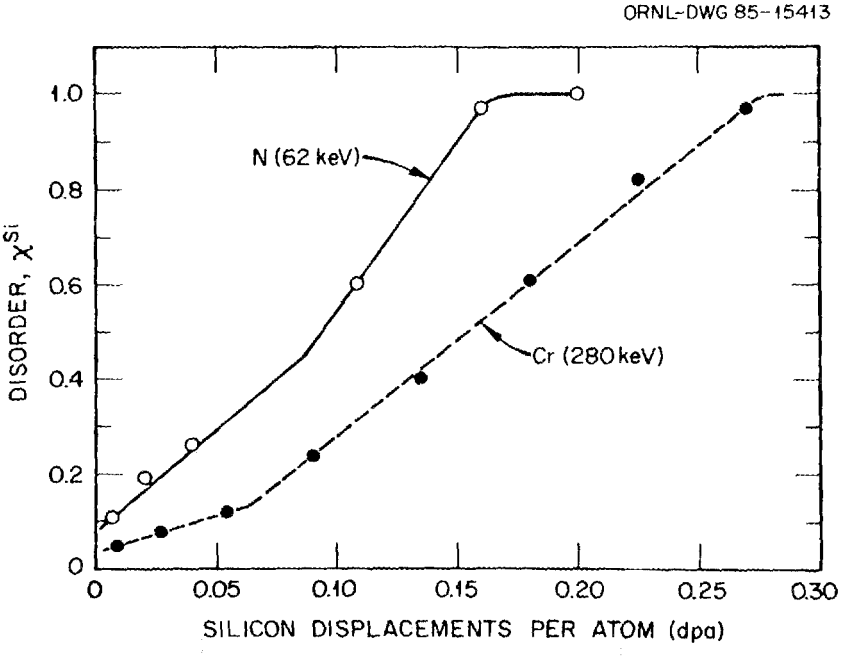

Fig. 5.1.4. Disorder in the silicon sublattice (χ^{Si}) as a function of fluence (dpa) for α-SiC implanted with nitrogen (62 keV) and chromium (280 keV) at 300 K.

ions approximately the same range in the target. There was a change in the slope of the curves indicating an acceleration in the rate of disordering after some initial period. These data also show a difference in disorder for the different ion species although the total defect production was similar.

As in the case of α-Al_2O_3, raising the substrate temperature allows recovery processes to occur or bonds to reform and delays the onset of amorphization in α-SiC. The RBS spectra for samples implanted with nitrogen (62 keV, 8×10^{16}/cm^2) or chromium (260 keV, 1×10^{16}/cm^2) at 1023 K (750°C) show that neither specimen became amorphous. The values of χ^{Si} and dpa were 0.85 and 16.8, respectively, for the nitrogen implants and 0.6 and 9.0, respectively, for the chromium implants. These dpa levels are 45 and 100 times those that produced amorphous structures at 300 K.

5.1.2 Regrowth of Amorphous Phases in Ion-Implanted Ceramics[6] —

C. J. McHargue, G. C. Farlow,[2] C. W. White,[3] J. M. Williams,[3] P. S. Sklad, H. Bohn,[7] and G. M. Begun[4]

In the temperature range 800 to 960°C, the amorphous layer in Al_2O_3 crystallizes to γ-Al_2O_3. The microstructure consists of long columnar subgrains that have a preferred crystallographic orientation with respect to the substrate (probably $\langle 111 \rangle_\gamma \parallel \langle 0001 \rangle_\alpha$). At long times (e.g., 96 h at 800°C), the γ-phase transforms to α or is consumed by a growth front of α moving from the substrate. At temperatures of 1190°C and above, the amorphous phase crystallizes into α-Al_2O_3, apparently by epitaxial growth from the original crystalline-amorphous interface.

Figure 5.1.5 shows the width of the amorphous layer in nitrogen-implanted α-SiC (8×10^{16} N/cm^2, 62 keV) as a function of annealing temperature. Above 1500°C the amorphous phase of SiC rapidly crystallized into α-SiC of the same orientation as the substrate. The regrown material contains a large number of stacking faults, dislocations, and other defects. At temperatures in the range 800 to 1500°C, a small amount (~10%) of epitaxial regrowth occurs at the original crystalline-amorphous interface but ceases after a short time. The remaining amorphous phase appears relatively stable; however, in basal plane short-range order increases although there is no discernable increase in order along the c-axis. Chromium-implanted samples (1×10^{16} Cr/cm^2, 260 keV) behaved in a similar manner.

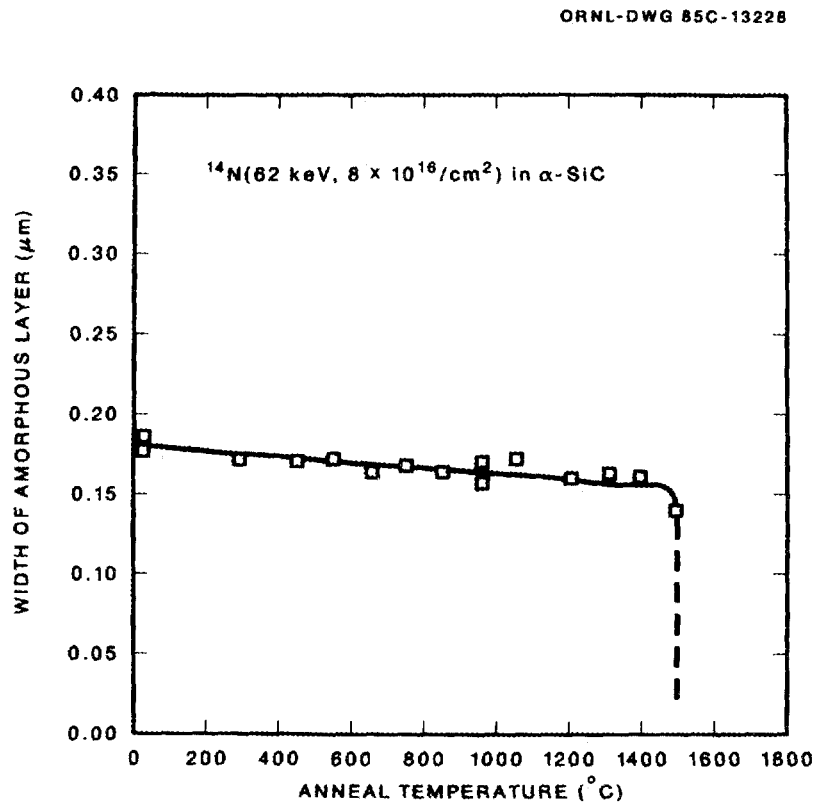

Fig. 5.1.5. Effect of annealing temperature on the width of the amorphous layer in SiC implanted with 8×10^{16} N/cm^2 (62 keV).

5.1.3 **Reactivity of Amorphous SiC** (ref. 8) - C. J. McHargue, J. M. Williams,[3] M. B. Lewis, and B. R. Appleton[3]

A comparison was made of the chemical etching rates and the oxidation rates of crystalline and amorphous SiC samples. The amorphous phase was produced by implantation of chromium to fluences of 6.2×10^{15} to 2.7×10^{16} Cr/cm^2 (280 keV) at room temperature.

The chemical etching studies were carried out in a boiling saturated solution of 50% $K_3Fe_2(CN)_6$ plus 50% KOH. The amount of material removed was determined by measuring the step height between the etched and unetched regions.

The data for material removal by a 1-min etch are summarized in Table 5.1.1. The measurements are the averages of five traces across the respective interfaces. The etching rate for the amorphous SiC was 2.4 to 4.1 times the rate for the crystalline counterpart.

Table 5.1.1. Material removed by a 1-min etch in a solution of 50% $K_3Fe(CN)_6$ plus 50% KOH

Specimen	Type of sample	Fluence (Cr^+ ions cm^{-2})	Material removed		Ratio[a]
			Implanted (nm)	Unimplanted (nm)	
Norton NC-203					
0020	Polycrystalline	2.7×10^{16}	134	36	3.7
Carborundum Company					
0045	Polycrystalline	2.0×10^{16}	255	105	2.4
0047	Polycrystalline	2.0×10^{16}	141	40	3.5
0016	Single crystal	2.7×10^{16}	80	28	3.0
0079	Single crystal	6.2×10^{16}	83	20	4.1

[a]Ratio of implanted material removed to unimplanted material removed.

The implanted chromium concentration in the removed layer was calculated from the E-DEP-1 computer program. The chromium concentration in the layers removed from the single crystals was about 1.2 mol % and from the polycrystalline specimens about 2.1 mol %. There are no data available to indicate whether this amount of chromium could account for the difference between the etching rate of implanted SiC and that of unimplanted SiC. In view of the corresponding differences in oxidation rates reported below, it seems likely that the observed effects are due to structural differences rather than to compositional differences.

Specimens were exposed to flowing oxygen for 1 h at 1300°C for the oxidation studies. As noted in Sect. 5.1.2, no significant recrystallization should occur in the amorphous SiC at that temperature.

A specimen of sintered α-SiC (Carborundum Company) was examined in an Auger spectrometer to obtain a qualitative measure of the relative oxide film thickness over the implanted and umimplated areas. Auger spectra were taken at various intervals during sputtering, and the time required for the carbon signal to appear was assumed to indicate the oxide layer thickness. The spectra exhibited marked changes between 12 and 13 min for

the unimplanted area and between 40 and 41 min for the implanted region. The intensity of the oxygen signal decreased, and a carbon signal was detected for the first time. These data indicate the oxide film on the implanted amorphous material to be about three times as thick as that on the unimplanted (crystalline) area.

Figures 5.1.6(*a*) and (*b*) contain the RBS spectra for 1.6-MeV α-particles reflected from the unimplanted region and implanted region respectively of oxidized (for 1 h at 1300°C) sintered α-SiC (Carborundum Company). The silicon, oxygen, and carbon edges are indicated at the top of each graph. The energy scale can be converted to a depth scale for each species. It is immediately obvious that the oxygen peak is substantially wider for the implanted sample. On the assumption that the oxygen-containing phase has the density of SiO_2, the width of the oxygen peak was converted into an oxide thickness. Values of 130 and 78 nm were derived for the implanted area and unimplanted area, respectively, giving a ratio of the thicknesses of the oxide layers of 1.67.

The scattering spectra from the silicon atoms exhibit two distinct regions corresponding to scattering from silicon in the oxide (surface or

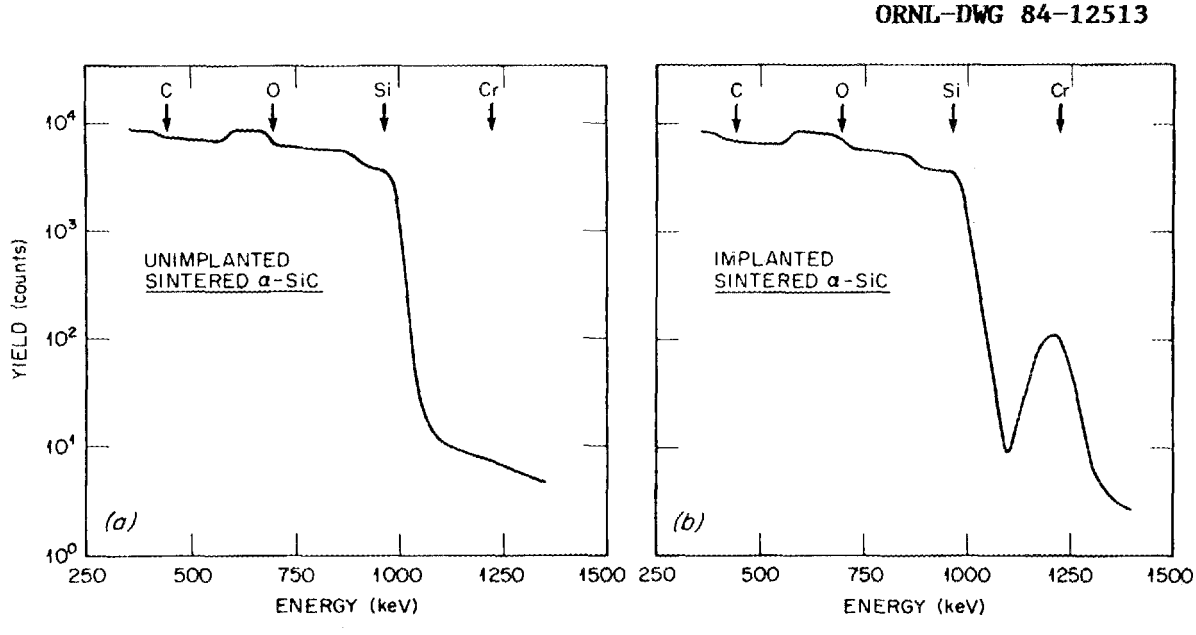

Fig. 5.1.6. Backscattering spectra for (*a*) unimplanted and (*b*) implanted (Cr) α-SiC oxidized for 1 h at 1300°C in flowing oxygen. The energy positions of the chromium, silicon, oxygen, and carbon edges are denoted by arrows.

higher energy scattered α-particles) and from silicon in the carbide (lower energy region). The width of the oxide region calculated from the width of the silicon in SiO_2 spectra agrees with that given above.

When the RBS data are deconvoluted, the ratio of the oxygen to silicon in the oxide (less dense phase) is approximately 2 for both the implanted and the unimplanted samples. This indicates twice as many oxygen atoms per unit volume as there are silicon atoms; thus, we can conclude that the oxide is SiO_2.

5.1.4 Charge State of Iron Implanted into α-Al_2O_3 – C. J. McHargue, P. S. Sklad, G. C. Farlow,[2] C. W. White,[3] and A. Perez[9]

We have previously noted significant differences in the microstructure of Al_2O_3 implanted with various ionic species and annealed in oxidizing or reducing atmospheres. To learn more about the local chemical effects and defect structure, we have initiated a collaborative study between ORNL and the Department de Physique des Materiaux, University Claude Bernard, Lyon, France. A. Perez and co-workers employ conversion electron Mössbauer spectroscopy (CEMS) to obtain information about the electronic structure, position in matrix, and local symmetry of implanted ions. In our study, Al_2O_3 was implanted with ^{57}Fe (4×10^{16} Fe/cm^2, 100 keV) at room temperature. The RBS spectra indicate that about 50% of the iron ions occupied substitutional lattice sites. The internal electron conversions associated with the 14.4 keV γ-ray transition in ^{57}Fe were determined at Lyon.

The isomer shifts (proportional to the density of electrons at the nucleus) and quadrupole splittings (measurement of the electric field gradient at the nucleus) indicated that the implanted iron was present as Fe^{2+} (62%), Fe^{3+} (11%), and Fe^0 (27%). The metallic iron (zero charge state) was present as clusters having less than 6-nm diameters.

Further studies will determine if the distribution of charge states varies with fluence and the changes induced by annealing in oxidizing and reducing atmospheres.

5.1.5 Ion Beam Mixing – C. J. McHargue, G. C. Farlow,[2] B. R. Appleton,[3] and C. W. White[3]

In a study with G. J. Clark and J.E.E. Baglin of IBM, T. J. Watson Research Center, Yorktown Heights, N.Y., a test was made of the proposal

that metal films on insulations will mix if the reaction enthalpy is negative and will not if it is positive.[10] Thin films were deposited on substrates of Al_2O_3, ZrO_2, SiO_2, YPO_4, SiC, and Si_3N_4. Mixing was attempted with 200-keV xenon ions using fluences of 1 or 2 × 10^{16} ions/cm^2 and substrate temperatures nominally of 300 K.

We consider balanced chemical equations for reactions of the metal and substrate where the products of the reaction are known metal oxides, silicides, silicates, aluminates, or other compounds containing the elements of which the metal and substrate consist. The standard enthalpies of formation, ΔH_f, for each reaction are then summed to give the enthalpy change for the reaction ΔH_r, under standard conditions. If ΔH_r is negative for any one reaction between metal and substrate we say the enthalpy rule predicts mixing. If ΔH_r is positive for all the reactions between metal and insulator, we say that the enthalpy rule predicts no mixing and probably some sort of segregation behavior. In fact, the enthalpies for the reactions of any given metal-insulator pair that we considered were either all positive or all negative. (Strictly speaking, if we are looking for possible chemical reactions, we should consider the free energy change rather than the enthalpy change. The entropy contribution for solid-solid reactions is so small that the signs of the free energy and enthalpy changes are the same.)

The specific materials combinations and results are summarized in Table 5.1.2. Stoichiometric mixing was observed in each instance predicted by the enthalpy rule. Mixing was also observed for two cases where the rule predicted no mixing, chromium on SiO_2 and zirconium Al_2O_3. Thus, it seems that the enthalpy rule is a useful but not complete concept.

5.1.6 Surface Mechanical Properties of Ion Implanted Ceramics —

C. J. McHargue, C. S. Yust, W. C. Oliver, G. C. Farlow,[2] and C. W. White[3]

An ultralow-load microindentation tester (Nanoindenter) was obtained from Nano Instruments, Inc., and installed. The resolution of the displacement system is 0.16 nm, and the resolution of the loading system is 0.4 μN. The data are obtained as load-displacement curves. The elastic recovery that occurs in ceramics (high hardness to modulus ratio) required that some modifications be made in the testing procedures originally developed for metallic specimens.

Table 5.1.2. Mixing map showing substrates and films examined according to the interfacial reaction observed[a]

Films	Substrates					
	Al_2O_3 (single crystal)	ZrO_2 (single crystal)	SiO_2	YPO_4 (single crystal)	SiC (single crystal)	Si_3N_4
Ni	X	X	X	X	M	NM
Au	NM	X	X	X	X	
Cu	SA	SA	SA	SA	SA	
Cr	BM	NM	M(20°C) NM(600°C)	NM	M	
Ti	BM?	NM	M	NM	X	
Zr	BM	X	M	X	X	
Si	BM	M	X	NM	X	
Nb	SM	X	M	X	X	
Pd	SA	X	SA	X	X	
V	SM	X	X	X	X	
W	NM	X	SA	X	X	
Al	X	X	BM?	NM	SA	
Ta	X	X	SM	X	X	

[a]X = system not completed; SA = segregation-agglomeration of the film; SM = stoichiometric mixing; BM = ballistic mixing; NM = no mixing, no change in the RBS spectra; ? = ambiguous identification.

Figure 5.1.7 illustrates how the relative hardness ($H_{implanted}/H_{unimplanted}$) varies as a function of depth for a sample of Al_2O_3 implanted with 4×10^{16} Al/cm^2 (90 keV) and 6×10^{16} O/cm^2 (55 keV) at 77 K. The surface was amorphous to a depth of 155 nm. Since the elastic-plastic zones extend to a depth of 7 to 14 times the penetration depth, the shape of the hardness profile should not be identical to the distribution of the implanted species. The data show that the hardness of the amorphous Al_2O_3 was about 55% that of the crystalline Al_2O_3 (ref. 11).

The modulus of elasticity was calculated from the unloading portion of the load-indenter displacement curves for the virgin crystal and the

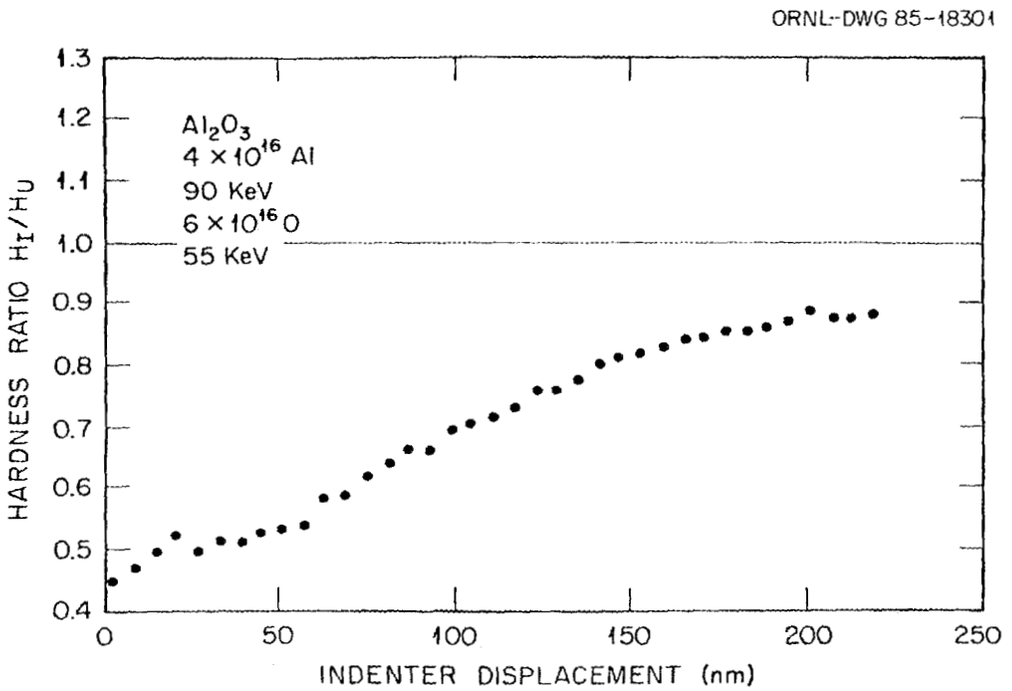

Fig. 5.1.7. Relative hardness of amorphous/crystalline Al_2O_3 from microindentation tests.

amorphous Al_2O_3. A value of 539 GPa was found for the c-axis oriented crystal and a value of 479 GPa for the sample with the amorphous surface. Because of contributions from the substrate below the amorphous region, this is not the true value for the elastic modulus of amorphous Al_2O_3, but it indicates that the value is certainly much less than the value for the crystalline material.

Pin-on-disk wear tests of niobium-implanted TiB_2 produced severe adhesive wear of the diamond pin but little damage to the TiB_2. The small amount of material removed from the wear track was the result of grain boundary cracking, which allowed entire grains to fall out. The microstructure showed much less grain boundary cracking in the implanted region relative to the unimplanted region. The observations suggest that the residual compressive stresses that accompany implantation counteract the tensile component of the applied stress, thereby reducing the amount of cracking.

Testing in an oxygen atmosphere reduced the wear of the diamond pin by a factor of 10 relative to testing in nitrogen. However, the wear mode was again adhesive wear of the pin with little damage to the TiB_2 disk.[12]

Pin-on-disk wear tests have recently been initiated on the amorphous phases of Al_2O_3 and SiC that were produced by ion implantation.

5.1.7 References

1. Summary of material contained in the following papers:

(a) C. W. White, G. C. Farlow, C. J. McHargue, P. Angelini, P. S. Sklad, M. B. Lewis, and B. R. Appleton, *Nucl. Instrum. Methods Phys. Res. B* **7/8**, 473–78 (1985).

(b) C. J. McHargue, G. C. Farlow, C. W. White, J. M. Williams, P. Angelini, and G. M. Begun, *Mater. Sci. Engr.* **69**, 391–95 (1985).

(c) C. J. McHargue, B. R. Appleton, and C. W. White, *Nucl. Instrum. Methods Phys. Res. B* **10/11**, 569–73 (1985).

(d) C. J. McHargue, C. W. White, B. R. Appleton, P. S. Sklad, P. Angelini, and C. S. Yust, in *Application of Ion Plating and Ion Implantation to Materials*, American Society for Testing and Materials (in press).

(e) C. J. McHargue, G. C. Farlow, G. M. Begun, J. M. Williams, C. W. White, B. R. Appleton, P. S. Sklad, and P. Angelini, *Nucl. Instrum. Methods Phys. Res.* (in press).

2. Wright State University, Dayton, Ohio. Work done while a guest from the University of Tennessee.

3. Solid State Division.

4. Chemistry Division.

5. P. J. Burnett and T. F. Page, *J. Mater. Sci.* **19**, 3524–45 (1984).

6. Summary of material contained in the following papers:

(a) G. C. Farlow, C. W. White, C. J. McHargue, P. S. Sklad, and B. R. Appleton, *Proceedings Materials Research Society Symposium, Boston, Mass, December 2–7, 1985*, in press.

(b) H. Bohn, C. J. McHargue, J. M. Williams, and G. M. Begun, *J. Mater. Res.*, in press.

7. Guest from KFA Jülich, Federal Republic of Germany.

8. Abstracted from *Mater. Sci. Engr.* **69**, 391–95 (1985).

9. Department de Physique des Materiaux, University Claude Bernard, Lyon, France.

10. G. C. Farlow, B. R. Appleton, L. A. Boatner, C. J. McHargue, C. W. White, G. J. Clark, and J.E.E. Baglin, pp. 137–45 in *Materials Research Society Symposium Proceedings*, vol. 45, 1985.

11. W. C. Oliver, C. J. McHargue, G. C. Farlow, and C. W. White, *Proceedings Materials Research Society Symposium, Boston, Mass., December 2-7, 1985*, in press.

12. Summary of papers:

(a) C. J. McHargue, C. S. Yust, P. Angelini, P. S. Sklad, and M. B. Lewis, to be published in *Proceeedings Second International Conference on the Science of Hard Materials, September 1984.*

(b) C. S. Yust, C. J. McHargue, C. L. White, P. Angelini, and P. S. Sklad, to be published in *Proceedings EUROTRIB '85.*

5.2 STRUCTURE AND MECHANICS OF INTERFACES AND THIN FILMS – R. A. McKee

During this reporting period we have completed the construction of our dynamic resonance apparatus, taken preliminary mechanical property data for two thin film systems by using this device, developed high-temperature and vacuum techniques for epitaxial nickel film growth on sapphire, and grown thin (100-nm) Al_2O_3 films for adherence property studies by using chemical vapor deposition (CVD) techniques.

5.2.1 Dynamic Resonance – R. A. McKee and F. A. List

The dynamic resonance method of measuring elastic properties of solids uses mechanical resonance data and is a technique that has great promise for quantitative characterization of thin films and coatings. We have developed this technique for thin films and are in the process of testing and evaluating its capabilities. An illustration of its capabilities, as we have developed it for thin films, can be seen in Fig. 5.2.1; the data shown are for a 100-nm nickel film supported on sapphire. We wish to emphasize that, without a destructive test, we are able to (1) determine that the film is adherent to the sapphire substrate and (2) measure the elastic constants of this 100-nm nickel film. Several papers are in preparation or are being published concerning this work.

5.2.1.1 Measurements of Mechanical Properties of Thin Films and Interfaces by the Dynamic Resonance Method[1] – F. A. List and R. A. McKee

We describe a simple experimental apparatus capable of simultaneous measurements of elastic and anelastic properties of film-substrate

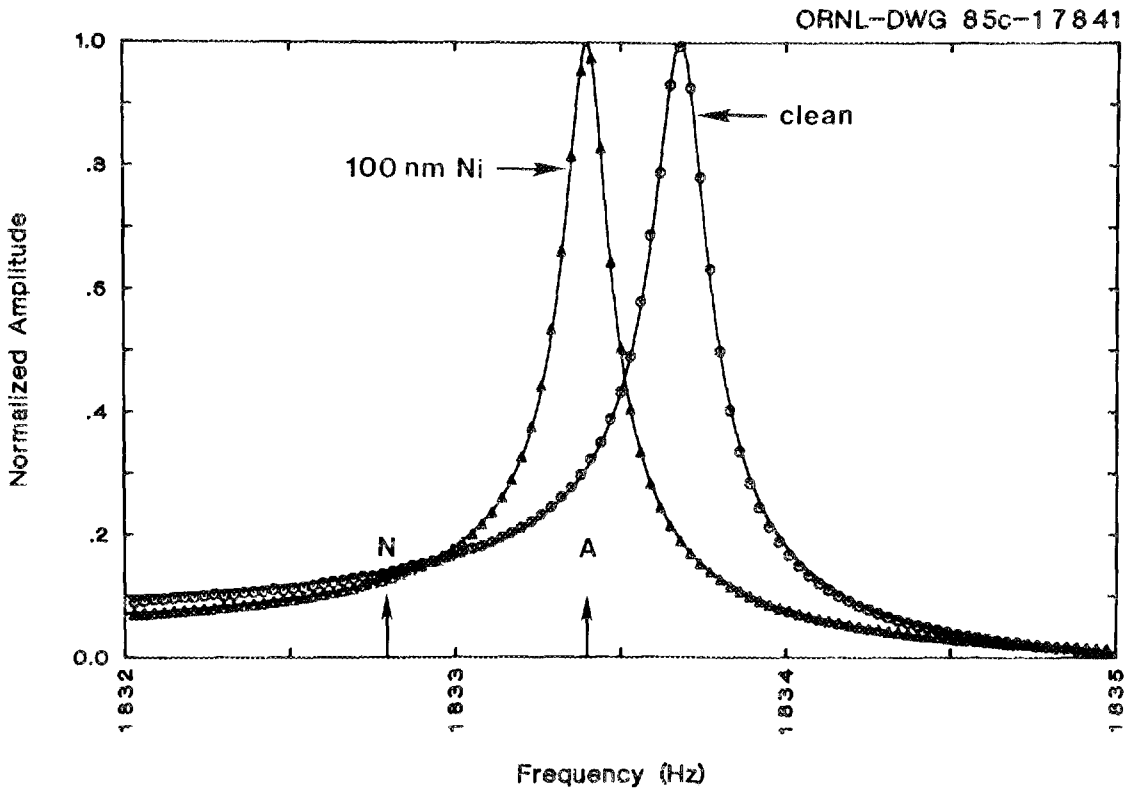

Fig. 5.2.1. Dynamic response of a rectangular sapphire bar at 100°C before (o) and after (Δ) coating with 100.1 nm of nickel on each side. The resonant frequencies for an adherent (1833.794 ± 0.05 Hz) and a nonadherent (1833.794 ± 0.025 Hz) nickel film are indicated with arrows labeled A and N, respectively.

composites in controlled atmospheres (10^{-6}–10^{4} Pa) from 25 to 1000°C. The apparatus employs the technique of dynamic resonance in which the mechanical response of a material can be determined over a wide range of frequency (0.1–100 kHz) with resolution ±1 mHz. We present experimental results for thin films (~100 nm) of nickel and gold on sapphire substrates. These results demonstrate the sensitivity of the apparatus to both the nature of the film-substrate interface and the intrinsic mechanical properties of the supported film.

5.2.1.2 Adherence and Mechanical Properties of Gold and Nickel Thin Films on Sapphire[2] – R. A. McKee and F. A. List

The mechanical aspects of adherence at thin film-substrate interfaces are especially important in applications of thin film technology. As a result, the study of thin film mechanical properties has attracted

considerable interest. In order to develop a better understanding of the interrelationships between thin film mechanical properties and adherence, we have developed a variation of the dynamic resonance technique for studying thin film properties. This technique, as we have developed it, is sufficiently sensitive to provide a nondestructive determination of thin film (10–100 nm) adherence and to provide a quantitative measurement of thin film elastic properties. Using this device, we have studied the loading effect of a nonadherent 50-nm gold film on sapphire and measured the Young's modulus of an adherent 100-nm nickel film on sapphire from room temperature to 500°C. These data illustrate the continuity or discontinuity in shear strain at the film-substrate interfaces, i.e., adherent or nonadherent films, and provide a measure of the effective modulus for a [111] textured nickel film on the rhombohedral plane of sapphire.

5.2.1.3 Mechanical Properties of Metallic Films on Sapphire[3] – F. A. List and R. A. McKee

A knowledge of interfacial mechanical properties is of considerable importance in the areas of oxidation, corrosion, metallization, and composite materials. We have developed an experimental apparatus capable of simultaneous measurements of elastic and anelastic properties of materials in controlled atmospheres (10^{-7} to 10^{5} Pa) from 25 to 1200°C. This apparatus employs the technique of dynamic resonance in which a material's resonance spectrum can be determined over the range 10^{2} to 10^{5} Hz with resolution of 0.001 Hz. This resolution has enabled us to determine the mechanical properties of films as thin as approximately 10 nm.

We present resonance results for thin films (100 nm) of Ni, Cr, Au, and Ag on sapphire substrates. These results suggest that Ni and Cr films on sapphire are adherent (i.e., cyclic strain is continuous at the film-substrate interface) over a range of temperature about the film growth temperature, whereas films of Au and Ag show nonadherent behavior at all temperatures studied.

5.2.2 Adherence Properties – R. A. McKee, F. A. List, and R. E. Druschel

This portion of the research task is centered around the idea that adherence properties of thin films and coatings can be improved

systematically, if thin film mechanical properties can be measured quantitatively and energy dissipation mechanisms characterized. We are studying a number of metallic and dielectric thin film systems toward this end.

5.2.2.1 Adherence Properties of Thin Films and Coatings[4] – R. A. McKee

The fundamental issues of adherence phenomena for metal–metal and metal–ceramic interfaces are reviewed from both theoretical and experimental approaches. The relationships between apparent chemical bonding and energetic beam interactions (ions, electrons, and photons) are discussed for metal films on ceramics. Finally, elastic and anelastic property measurements are presented for Ni, Cr, and Au films on sapphire, and these data and this particular approach to the problem of mechanical energy dissipation in thin films are discussed as they relate to adherence of thin films.

5.2.2.2 Oxide Scale Adhesion – R. E. Druschel and R. A. McKee

As part of a broad effort toward characterizing mechanical properties and adherence of thin films (5–100 nm), the specific problem of adherence of Al_2O_3 films on metal alloys is being studied by using both CVD-deposited and thermally formed films.

During this period the techniques for CVD formation of alumina have been developed by using the oxidation of trimethyl aluminum at the surface of a chosen substrate. This is a low-temperature (200 to 400°C) process that has a number of advantages for laboratory studies, and film uniformity has been demonstrated at the 3 to 5% level for a 100-nm film over a substrate surface 5 cm in extent. This is a requirement for our subsequent mechanical resonance studies of the film's elastic, anelastic, and adherence properties.

Figure 5.2.2 is an electron micrograph of one of the films that we have developed thus far. This particular case resulted in an amorphous film that recrystallized to the cubic phase and finally to the α or corundum phase on heating. Subsequent work in this portion of our studies will be to manipulate the film microstructural development by changing substrate temperature and deposition rate. The CVD-formed films are

M2-1863

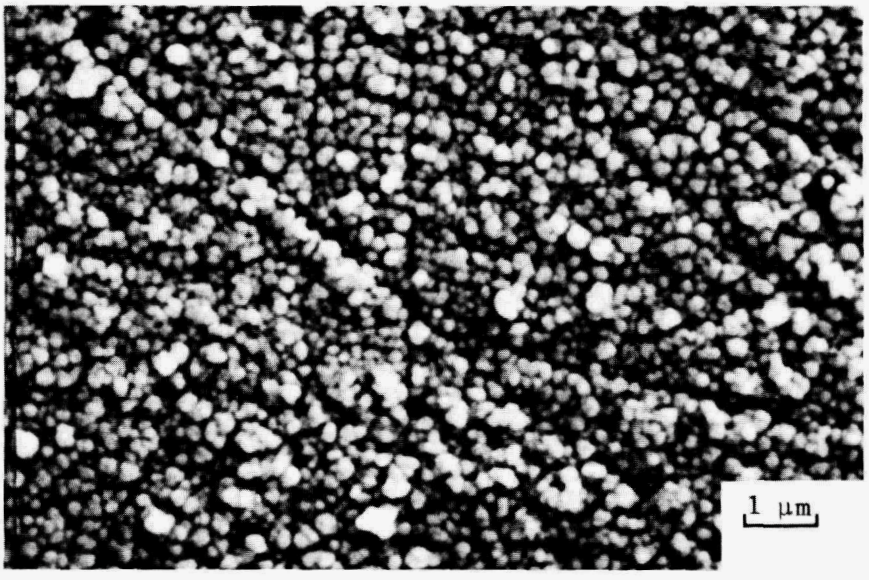

Fig. 5.2.2. Amorphous Al_2O_3 film formed on platinum at 400°C. The film is approximately 100 nm thick.

important in our work because we can easily dope the film with specific reactive elements for investigation of their influences on interface and grain boundary sliding. A critical issue in our research on adherence is, therefore, to determine if the specific role of dissipation mechanisms such as grain boundary sliding can be quantified as they relate to a film's ability to absorb mechanical energy without delamination.

5.2.2.3 Nickel Epitaxy on Sapphire – R. A. McKee, S. Baik, and D. S. Easton

We are attempting to prepare thin single-crystalline nickel films on sapphire substrates by vapor deposition. This investigation is in support of our general mechanical property studies of thin films, and its specific aim is to determine whether there exists any epitaxial correlation between deposited nickel films and the optimum deposition conditions for achieving defect-free single-crystalline nickel films. To date we have found that epitaxy does develop for this system; our preliminary results suggest that the following epitaxial relationships can be observed:

$$Ni\langle 111\rangle \;//\; -Al_2O_3\ \langle 0001\rangle$$

$$Ni\langle 110\rangle \;//\; -Al_2O_3\ \langle 10\bar{1}2\rangle$$

These relationships have been determined by using X-ray diffraction techniques. The degree of single-crystalline perfection has also been determined by measuring diffraction line broadening in comparison with the substrate diffraction peaks. Our general observations are that we will be able to reliably grow these thin film structures.

5.2.3 Collaborative Studies

5.2.3.1 Metallic Glass Coatings – R. A. McKee and P.B.D. Phipps[5]

We are studying the mechanical properties of metallic glasses as a joint project with IBM Corporation, San Jose. The system of primary interest to IBM is Ni_3P, and we are measuring the adherence characteristics and the elastic-anelastic properties of the metallic glass as it changes its crystalline form while supported on a sapphire substrate. This work was initiated this year and is in a "proof of principle" stage; IBM is furnishing the samples, and we are making the measurements.

5.2.3.2 Metal-Sulfide Interfacial Microstructure – R. A. McKee, Thao A. Nguyen,[6] and Linn W. Hobbs[6]

Professor Hobbs and his student, Thao Nguyen, are working on the interfacial structure of Fe/FeS by using high-resolution electron microscopy. We are collaborating to characterize the defect structure and morphology of the FeS that grows on iron when it is exposed to sulfur vapor at elevated temperatures. We are supplying specimens and helping with the interpretation of the growth kinetics-microstructural development. A paper[7] is being prepared to report some of the results that we have obtained so far.

5.2.4 References

1. F. A. List and R. A. McKee, submitted to *Rev. Sci. Instr.* (1985).

2. R. A. McKee and F. A. List, submitted to *J. Thin Solid Films* (1985).

3. F. A. List and R. A. McKee, submitted to *J. Mater. Res. Soc.* (1985).

4. R. A. McKee, invited Gordon Conference talk, July 1985.

5. IBM Corporation, San Jose, Calif.

6. Massachusetts Institute of Technology, Cambridge, Mass.

7. R. A. McKee, Thao A. Nguyen, and Linn W. Hobbs, paper in preparation for *J. Elect. Soc.* (1986).

6. COLLABORATIVE RESEARCH CENTERS

6.1 SHARED RESEARCH EQUIPMENT PROGRAM (SHaRE) – E. A. Kenik

The past 18 months has been a productive period for the SHaRE program, which has experienced growth in the number of collaborators, research areas, and publications. The program allows participants from universities, industrial research, and other national laboratories access to the wide range of often unique microanalytical facilities. The program is aimed at collaborative research in materials science in areas pertinent to the DOE-ORNL mission, and it emphasizes areas under current investigation in the Metals and Ceramics Division. Facilities and techniques included under SHaRE are analytical and high-voltage electron microscopy, Auger spectroscopy, nuclear microanalysis, X-ray diffraction, and rapid solidification facilities. The 300-kV Philips EM430 analytical electron microscope has been in operation approximately one year, and an atom probe/field ion microscope has recently been installed. Several SHaRE projects are in support of advanced materials development programs in the Metals and Ceramics Division, such as long-range-ordered alloys, nickel-based aluminides, high-temperature ferritic alloys, and high-performance ceramics.

During this period, the Division of Materials Sciences, Office of Basic Energy Sciences, provided funds through Oak Ridge Associated Universities (ORAU) to support the SHaRE activity. Program funds are used for travel and living expenses of SHaRE participants while at ORNL and for the support of G. L. Lehman, an electron microscopist. His responsibility is to familiarize SHaRE participants with the electron microscope and computer facilities and to participate in SHaRE research when appropriate. His presence has allowed the high level of SHaRE participation with minimal interference with in-house programs. Mr. Lehman resigned in November 1985 to take a position with JEOL USA, Inc.

A steering committee reviews all proposed SHaRE projects and defines SHaRE program policy. The members in FY 1984 were:

E. A. Kenik, ORNL;

P. S. Sklad, ORNL;

R. F. Davis, North Carolina State University, Raleigh;

J. J. Hren, University of Florida, Gainesville;

G. L. Lehman, ORAU;

R. Wieseheugel, ORAU.

In FY 1985, one change was made in the steering committee: C. B. Carter, Cornell University, replaced J. J. Hren. In FY 1986, two changes were made in the committee: R. J. Bayuzick, Vanderbilt University, replaced C. B. Carter, and K. Newport, ORAU, replaced R. Wieseheugel.

In the past year and one half, 27 SHaRE projects have been active, involving approximately 55 participants. These projects follow.

H. U. Anderson, University of Missouri-Rolla, with J. Bentley: TEM Studies of Doped Transition Metal Oxides.

R. J. Arsenault, University of Maryland, with J. O. Stiegler and E. A. Kenik: HVEM (High-Voltage Electron Microscope) Studies of Composite Strengthening.

R. J. Bayuzick, Vanderbilt University, with E. A. Kenik: Studies of Microstructures of Niobium Alloys Resulting from Large Degrees of Supercooling.

R. B. Benson, Jr., North Carolina State University, with J. Bentley: Defect Structures Using AEM in Implanted Aluminum and in Implanted III-V Semiconducting Compounds.

W. B. Carter, Georgia Institute of Technology, with R. E. Clausing: Ion Implantation and Plating to Improve Mechanical, Corrosion, and Oxidation Characteristics of Metal Surfaces.

B. A. Chin, Auburn University, with C. T. Liu: Effect of Strain Rate on Fracture Behavior of Long-Range-Ordered Alloys.

R. F. Davis, North Carolina State University, with J. Bentley: TEM of Deformed and Undeformed Single Crystalline and Polycrystalline NbC and SiC.

J. J. Hren, University of Florida, with E. A. Kenik: HVEM Studies of Microstructural Evolution of Spherical Precipitated Al_2O_3 During Calcination.

P. H. Holloway, University of Florida, with R. E. Clausing: Scanning Auger Microprobe Analysis of In Situ Fractured SiC.

W. A. Jemian, Auburn University, with S. A. David: Control of Ferrite Morphology in Welding Austenitic Stainless Steel.

A. Krawitz, University of Missouri-Columbia, with E. A. Kenik: Plastic Deformation of Tungsten Carbide in WC-Co and WC(Co,Ni) Cemented Carbide Compositions.

K. R. Lawless, University of Virginia, with J. V. Cathcart and E. A. Kenik: In Situ HVEM Studies of Oxidation of Nickel Aluminides.

L. L. Marcus, University of Texas, with E. A. Kenik: The Effects of Stress and Composition on the Hydride Solvus Temperature in Titanium Alloys.

D. Northwood, University of Windsor, Canada, with E. A. Kenik: HVEM and AEM Studies of Hydrogen Storage Materials.

S. R. Nutt, National Bureau of Standards, with J. A. Horton: In Situ TEM (Transmission Electron Microscope) Investigation of Titanium Fracture.

P. J. Reucroft, University of Kentucky, with J. Bentley: Chemical and Physical Characterization of Dispersed Metal Particles in Porous Media.

E. Schulson, Dartmouth University, with J. A. Horton and C. T. Liu: Structure of Rapidly Solidified and of Consolidated Ni_3Al Using Analytical Electron Microscopy.

J. J. Wert, Vanderbilt University, with P. S. Sklad: The Role of Structure in the Wear Process.

C. B. Carter, Cornell University, with P. Angelini, P. S. Sklad, and J. Bentley: AEM of Aluminas and Segregation to Grain Boundaries.

I. Baker, Dartmouth College, with J. A. Horton: In Situ Straining Experiments on Ni_3Al in the Electron Microscope.

G. M. Pharr, Rice University, with W. C. Oliver: High Resolution Microhardness of Subgrain Boundaries and Dislocation Cell Walls.

C. C. Koch, North Carolina State University, with J. A. Horton: AEM of Rapidly Solidified or Undercooled Nickel and Iron Aluminides.

P. P. Camus, University of Pittsburgh, with M. K. Miller: Quantitative Microchemical Analysis Using the Atom Probe Field Ion Microscope.

M. G. Burke, University of Pittsburgh, with M. K. Miller: The Coarsening Behavior of Spinodally Decomposed Fe-Be Alloys.

C. A. Allison, Oklahoma State University, with E. A. Kenik and R. Stoller: Electron Irradiation Damage in Transition Metal Carbides.

I. M. Curelaru, University of Utah, with R. E. Clausing: XPS Studies of Electronic Structure of Electrode Materials for High Energy Batteries.

F. Ebrahimi, University of Florida, with R. Clausing and P. J. Maziasz: Effect of Composition on Irradiation Embrittlement of Pressure Vessel Steels.

Some 35 papers based on SHaRE research have been published in the past 18 months, and approximately 30 presentations have been made at technical meetings. Results from research on some of these SHaRE projects listed above are described elsewhere in this report.

6.2 OAK RIDGE SYNCHROTRON ORGANIZATION FOR ADVANCED RESEARCH (ORSOAR) — C. J. Sparks, Jr.

Transportation of our beamline from Oak Ridge and installation at the National Synchrotron Light Source (NSLS) were completed in June 1985. Our earlier developments in X-ray optics paid off. The sagittal focusing crystal arrangement works beautifully. It images the small horizontal source size of the radiation in the NSLS X-ray ring. To date we have achieved the best focus and the most intense X-ray flux of any beamline at the NSLS. Now that others have seen the advantages of our optics, their interest in implementing them will lead to further refinements and widespread usage. The dissemination of information among the many scientists is one of the important advantages of a large facility like the NSLS.

Our annual meeting of users was held at Brookhaven National Laboratory on May 24, 1985, immediately following the annual NSLS users meeting. Nineteen users attended the meeting. A decision was reached to commit part of the beam time to user collaboration during the early debugging process and before the April 1986 date. This date is the official beginning of the operational status of the beamlines, after which it is mandatory to share facilities for 25% of the schedule with the NSLS.

We provided several of our users with beam time so that they can prepare themselves for productive research and, in some cases, to acquaint them with the advantages of synchrotron radiation. Following is a list of some of these interactions.

1. POWDER DIFFRACTION STUDY OF HETEROGENEOUS CATALYSTS
with Robert J. DeAngelis, Department of Metallurgical Engineering and Materials Science, University of Kentucky.

A number of catalysts were examined including Co and Ni on silica, and Y_2O_3 stabilized zirconia, prepared at various pH's. This was the first powder diffraction done at the X-14 beamline.

2. AN X-RAY DIFFRACTION STUDY OF THE SPATIAL DISTRIBUTION OF STRAIN AROUND NIOBIUM HYDRIDE PRECIPITATES IN A NIOBIUM MATRIX
with Stuart R. Stock, School of Materials Engineering, Georgia Institute of Technology.

The strains in the niobium matrix surrounding a niobium hydride precipitate were mapped by using a 25-μm-diam beam and by monitoring the shift in the (110) Bragg peak of the niobium. From measurements of the peak shape and peak shift, the components of the strain tensor in the niobium matrix can be determined as a function of distance from the precipitate. We have enough intensity to achieve 0.5-μm spatial resolution for quantitative measurement of the strain fields at crack tips. This has not been done before.

3. THIN SURFACE LAYERS FORMED BY ION IMPLANTATION AND ION PLATING
with W. Brent Carter and Stuart R. Stock, School of Materials Engineering, Georgia Institute of Technology.

The structure of an amorphous subsurface layer of phosphorous-implanted poly- and single-crystalline iron was examined with low angle (2–10°) X-ray diffraction. Data were taken at various X-ray energies and incident angles. Unimplanted iron specimens were also examined for comparison. The production of amorphous surface layers by implantation of metalloid ions into crystalline transition metals holds considerable promise for improved corrosion resistance.

4. POWDER PATTERNS FROM QUASICRYSTALS EXHIBITING ICOSAHEDRAL SYMMETRY
with John Budai, Solid State Division, Oak Ridge National Laboratory.

One of the recent interesting discoveries is the report of an aluminum-manganese alloy exhibiting diffraction patterns of fivefold symmetry. These quasicrystals were prepared by rapid cooling methods. For the first time, an aluminum-manganese alloy prepared by ion implantation was shown to exhibit the same icosahedral symmetry as shown by X-ray diffraction patterns.

The ion-implanted samples are unique in forming the quasicrystals as surface structures with certain symmetry axes oriented normal to the crystal surface. The race is on to obtain a single crystal large enough for X-ray measurements to determine if it is truly fivefold symmetry or a faulting effect.

5. TRACE ELEMENT FLUORESCENCE TOMOGRAPHY
with Lee Grodzins and Paul Boisseau, Department of Physics,
Massachusetts Institute of Technology.

X-ray fluorescence induced by monochromatic X-ray beams is a well known technique for trace element analysis in bulk samples. We have a stated interest in developing intense microbeams of monochromatic X rays for high-spatial-resolution diffraction and trace element detection. Micrometer-diameter beams can also be used as in CAT scans for image reconstruction of trace elements in the interior of small samples. We report here on the first experiments using synchrotron radiation and a 150-μm-diam beam to measure trace elements at less than 500 ppm concentrations. The success of these simple experiments shows that, with the ORNL beamline, tomographic fluorescence techniques can be effective at 25 μm resolution to measure trace concentrations of less than 10 ppm level in the titanium-zinc region in millimeter-size samples.

Images reconstructed from iron and titanium fluorescence scans on fibers axially imbedded in plastic cylinders clearly showed their location. The 50 × 50 image reconstruction spanned about 1 cm^2 of area in the plane of the beam. The results of an iron scan across the abdomen of a honey bee indicated that iron is highly concentrated on the dorsal side of the abdomen, in the body wall, and in various organs. This information pertains to the influence of the earth's magnetic field on the guidance system of bees.

Appendix A

SCIENTIFIC AND PROFESSIONAL ACTIVITIES

P. Angelini:
- Visiting Research Scientist, Max Planck Institute, Stuttgart, W. Germany (June 1985–June 1986)

P. F. Becher:
- Cochairman, International Symposium on "Advanced Structural Ceramics," sponsored by Materials Research Society
- Member, American Society for Metals (ASM), Oak Ridge Chapter, Symposium Organizing Committee on "Composite Materials for Structural Applications"
- Secretary-Elect, Basic Science Division, American Ceramic Society (ACS)

J. Bentley:
- Adjunct Associate Professor, Department of Materials Science and Engineering, University of Tennessee
- Adjunct Professor, Department of Mechanical Engineering and Materials Science, Vanderbilt University
- Board of Review, *Metallurgical Transactions*

A. Bleier:
- Contributing Editor, *Communications of the American Ceramic Society*
- Abstractor for *Ceramics Abstracts*, ACS
- Chairman Elect, P&B Fellowship Committee, American Chemical Society
- Symposium Chairman, Fine Particle Society

W. H. Butler:
- Manager, ORNL Computer Planning (1984-1985)

A. DasGupta:
- Adjunct Professor, Department of Metallurgy and Materials Engineering, Lehigh University
- Vice Chairman, The Metallurgical Society of AIME (TMS-AIME) Chemistry and Physics of Metals Committee
- TMS-AIME Physical Metallurgy Committee

S. A. David:
- Adjunct Professor, Department of Metallurgy, University of Pittsburgh
- Adjunct Professor, Department of Welding Engineering, Ohio State University, Columbus
- Conference Chairman, "International Conference on Trends in Welding Research," Gatlinburg, Tenn., May 18–22, 1986
- Chairman, Conference Committee, ASM Joining Council
- Member, Organizing Committee, World Materials Congress 1988
- TMS-AIME Solidification Committee
- American Welding Society Committee C7 on High-Energy Beam Processing

D. S. Easton:
- TMS-AIME Mechanical Properties Committee
- Task Group, American Society for Testing and Materials (ASTM) Physical/Mechanical Properties of Superconductors
- TMS-AIME Composites Committee
- Executive Board, Tennessee Valley Chapter of the American Vacuum Society
- Exhibits Chairman, Tennessee Valley Chapter of the American Vacuum Society

L. L. Horton:
- Council Secretary, Electron Microscopy Society of America (EMSA)
- Organizer, Symposium on "Composite Materials for Structural Applications," Oak Ridge Chapter, ASM, March 22, 1985

E. A. Kenik:
- Adjunct Professor, Department of Mechanical Engineering and Materials Science, Vanderbilt University
- Director, Steering Committee, ORNL-ORAU SHaRE Program
- ASM Structures Committee
- Member, EMSA Education Committee
- Member, Review Committee, DOE University Research Instrumentation Program
- Project Advisor, Management Advisory Group Member - NASA Center for Space Processing of Engineering Materials

C. T. Liu:
- Cochairman, International Symposium on "High-Temperature Ordered Intermetallic Alloys," sponsored by Materials Research Society
- U.S. Superalloys Delegation, 2nd Japan-USA Superalloys Conference, sponsored by TMS-AIME
- TMS-AIME Alloy Phases Committee

L. K. Mansur:
- ORNL Graduate Fellow Selection Panel
- Invited Speaker, Japan-U.S. Workshop on Fusion Reactor Materials, Tsukuba, Japan
- Review Board Member, *Journal of Materials for Energy Systems*

D. L. McElroy:
- Adjunct Professor, Department of Materials Science and Engineering, University of Tennessee
- ASTM Technical Committee C16 on Thermal Insulation
- Secretary, ASTM Subcommittee C16.30 on Thermal Measurements
- Board of Governors, Symposium on Expansion of Solids
- Editorial Board, *International Journal of Thermophysics*
- Alternate Chairman, The Governing Board of International Thermal Conductivity Conference, 1981

C. J. McHargue: Professor, Department of Materials Science and Engineering, University of Tennessee
Past Chairman, ASM/TMS-AIME Nuclear Metallurgy Committee
International Metals Committee, ASM
Chairman, ASM Materials Science Division Materials Processing Committee
ASM, Materials Science Division Council
Materials Research Society, Membership Committee
Los Alamos Meson Physics Facility (LAMPF) Proposal Advisory Committee
TMS-AIME Program Committee-Planning and Liaison
Member, Organizing Committee and Coeditor of proceedings, *Irradiation Effects Associated with Ion Implantation*, held in conjuction with TMS-AIME-ASM, Toronto, Canada, October 14-15, 1985

M. K. Miller: Member, Steering Committee, International Field Emission Symposium
Co-Organizer, 32nd International Field Emission Symposium, July 15-19, 1985, Wheeling, W.Va.

N. H. Packan: Chairman, ASTM Subcommittee E10.08, "Procedures for Neutron Radiation Damage Simulation"

P. S. Sklad: Adjunct Associate Professor of Materials Science, Department of Mechanical and Materials Engineering, Vanderbilt University
Vice-Chairman, Education Committee, EMSA
Organizer and Chairman, 1985 EMSA Symposium "Ion Implantation and Near-Surface Examination"

C. J. Sparks: Chairman, National Synchrotron Light Source Executive Committee of the Association of Users, DOE, Brookhaven National Laboratory
Steering Committee, ORNL-ORAU Synchrotron Collaborative Research Center
U.S. National Committee for Crystallography, the National Research Council
Cornell High Energy Synchrotron Source Proposal Review Committee
Program Advisory Committee, National Synchrotron Light Source, DOE, Brookhaven National Laboratory

G. M. Stocks: Member, Supercomputers Advisory Committee, Office of Energy Research, DOE
Contributor to *The Role of Supercomputers in Energy Research Programs*, DOE report drafted by National Magnetic Fusion Energy Computer Center, Lawrence Livermore Laboratory, 1985
Member, Advisory Board for "Collaborative Computational Project on Electronic Structure Calculations," Science and Engineering Research Council, United Kingdom

C. L. White: Adjunct Professor, Department of Mechanical Engineering and Materials Science, Vanderbilt University
TMS-AIME Mechanical Metallurgy Committee
TMS-AIME Operations Subcommittee
TMS-AIME Book Publications Committee
ASM-MSD Council
ASM-MSD Flow and Fracture Committee
ASM-MSD Surfaces and Interfaces Committee

D. W. Yarbrough: Organizer and Session Chairman, Symposium on "Properties, Testing, and Utilization of Materials for Energy Conservation in Industrial Applications" for the National Meeting of the American Institute of Chemical Engineers, Philadelphia, August 20–23, 1984
Chairman, Nineteenth International Thermal Conductivity Conference

C. S. Yust: Chairman, Best Paper Award Committee, Nuclear Division, ACS

FELLOWS OF PROFESSIONAL SOCIETIES
(with years of election)

American Association for the Advancement of Science

B. S. Borie	1965
J. S. Faulkner	1975
H. L. Yakel	1980

American Ceramic Society

P. F. Becher	1979
C. S. Yust	1978

American Nuclear Society

L. K. Mansur	1984

American Physical Society

J. S. Faulkner	1978
G. S. Painter	1978
G. M. Stocks	1983

American Society for Metals

C. J. McHargue	1972
D. L. McElroy	1977
J. V. Cathcart	1979
S. A. David	1984
C. T. Liu	1984
L. K. Mansur	1985

The Metallurgical Society of AIME

C. J. McHargue 1978

Institute of Metals (London)

K. Farrell 1970

Appendix B

PRESENTATIONS AT TECHNICAL MEETINGS

Compiled by Faye Roseberry

Seminar, Karlsruhe Nuclear Research Center, Federal Republic of Germany, July 9, 1984:

N. H. Packan, "Pulsed Dual-Ion Irradiations of Stainless Steels"

Conference on Ceramic Substrates, Cornell University, Ithaca, New York, July 15–18, 1984:

A. Bleier, "Effects of Powder Surface Chemistry on the Fabrication of Ceramic Thin Films"

Fourth Analytical Electron Microscopy Workshop, Lehigh University, Bethlehem, Pennsylvania, July 16–20, 1984:

P. Angelini* and J. Bentley, "Thermal Expansion Coefficient Determination by CBED"

J. Bentley, "The Utility of Replica Techniques for X-Ray Microanalysis of Second Phase Particles"

J. Bentley,* P. Angelini, and P. S. Sklad, "Secondary Fluorescence Effects of X-Ray Microanalysis"

J. Bentley,* G. L. Lehman, and A. T. Fisher, "Structural Characterization by Intensity Measurements of Electron Diffraction Patterns"

M. G. Burke,* M. K. Miller, S. S. Brenner, and W. A. Soffa, "A Combined AEM/FIM Study of Precipitation in an Fe–25 at. % Be Alloy"

A. G. Dhere*, P. J. Reucroft, R. J. De Angelis, and J. Bentley, "Characterization of Supported Metal Catalysts by Imaging, Microdiffraction and Microanalysis Techniques"

---

*Speaker.

E. A. Kenik* and P. J. Maziasz, "Application of Extraction Replicas and Analytical Electron Microscopy to Precipitate Phase Studies"

M. K. Miller, M. G. Burke,* S. S. Brenner, and W. A. Soffa, "A TEM/FIM Study of Modulated Microstructures in the Fe-Be System"

P. S. Sklad,* J. Bentley, P. Angelini, and G. L. Lehman, "Reliability of the Quantification of EELS Measurements"

J. M. Vitek (presented by D. B. Williams), "An EDS Round-Robin Evaluation of Type 308 Austenitic Stainless Steel"

Polymers, Ceramics, and Other Insulators Session at Ion Beam Modification of Materials Meeting, Cornell University, Ithaca, New York, July 16-20, 1984:

G. C. Farlow,* C. W. White, C. J. McHargue, and B. R. Appleton, "Annealing of Implanted Al_2O_3 in a Reducing Environment"

M. B. Lewis, "Long-Range Recoil Extension of Heavy Ion Damage in Ceramics"

C. W. White,* G. C. Farlow, C. J. McHargue, P. S. Sklad, P. Angelini, and B. R. Appleton, "Formation of Amorphous Layers in Al_2O_3 by Ion Implantation"

J. M. Williams,* B. R. Appleton, C. J. McHargue, P. S. Sklad, G. M. Begun, P. Angelini, and R. F. Davis, "Ion Implantation Effects in SiC"

31st International Field Emission Symposium, Paris, France, July 16-20, 1984:

P. P. Camus, W. A. Soffa, S. S. Brenner, and M. K. Miller,* "Quantification of Interconnected Microstructures by FIM"

M. K. Miller, "Imaging Atom Probe Computer Experiments"

M. K. Miller,* J. Bentley, S. S. Brenner, and J. A. Spitznagel, "Long Term Thermal Aging of Type CF 8 Stainless Steel"

M. K. Miller,* M. G. Burke, and S. S. Brenner, "Morphological Interpretation of Modulated Microstructures"

Seminar, Martin Marietta Laboratory, Baltimore, Maryland, July 17, 1984:

P. F. Becher, "Toughening Processes in Ceramic Composites"

Ninth International Conference on Atomic Physics, Seattle, Washington, July 23-27, 1984:

G. B. Armen,* M. H. Chen, B. Craseman, J. C. Levin, G. S. Brown, and G. E. Ice, "Threshold M-Shell Excitation Accompanying K Ionization of Argon"

J. C. Levin,* G. B. Armen, M. H. Chen, B. Craseman, G. E. Ice, and G. S. Brown, "Measurements of Post-Collision Interaction in Auger Decay of Deep Hole States"

Seminar, Oulu University, Oulu, Finland, July 26, 1984:

J. M. Vitek, "Welding of Austenitic Stainless Steels"

Seminar, Saclay Nuclear Research Center, Paris, France, July 26, 1984:

N. H. Packan, "Pulsed Dual-Ion Irradiations of Stainless Steels"

Gordon Research Conference on Frontiers of Science, New London, New Hampshire, July 29-Aug. 3, 1984:

P. F. Becher, "Toughening Effects in SiC Whisker Reinforced Oxides"

Second Conference in Series on Characterization of Ceramics and Glasses, New York State College of Ceramics at Alfred University, Alfred, New York, July 30-Aug. 4, 1984:

S. Baik,* D. E. Fowler, R. Raj, and J. M. Blakely, "Auger Spectroscopy and Leed Studies of Surface Segregation in Doped Sapphire"

W. C. Hasz and A. Bleier,* "Surface Reactivity of Silica and Alumina Ceramic Powders"

International Union on Crystallography 13th Congress and General Assembly, Hamburg, Federal Republic of Germany, August 9-18, 1984:

H. L. Yakel, "Anomalous Scattering Studies of Average Distribution Parameters in Sigma and Tau Phases"

Electron Microscopy Society of America 42d Annual Meeting, Detroit, Michigan, August 13-17, 1984:

P. Angelini* and J. Bentley, "Secondary Fluorescence Effects on X-Ray Microanalysis"

J. Bentley* and P. Angelini, "X-Ray Microanalysis of Ion-Implantation Profiles in Backthinned Specimens"

C. K. H. DuBose, "Safety in the Materials Science Microscopy Laboratory"

L. L. Horton, "Experimental Determination of the Critical Cavity Radius in Fe-10% Cr for Ion Irradiation"

P. S. Sklad,* P. Angelini, C. J. McHargue, and J. M. Williams, "Analytical Electron Microscopy of SiC Implanted with Cr Ions"

Eighth European Congress on Electron Microscopy, Budapest, Hungary, August 13-18, 1984:

J. M. Vitek, "Round Robin EDS Evaluation of Fully Austenitic Stainless Steel"

17th International Conference on Low Temperature Physics, Karlsruhe, Federal Republic of Germany, August 15-22, 1984:

H. R. Kershner, D. K. Christen, A. DasGupta, S. T. Sekula, B. C. Cai, and Y. T. Chou, "Flux-Line Pinning by the Grain Boundary in Niobium Bicrystals"

Fifth RISO International Symposium on Metallurgy and Materials Sciences, RISO National Laboratory, Roskilde, Denmark, September 3-7, 1984:

M. H. Yoo,* J. C. Ogle, J. H. Schneibel, and R. W. Swindeman, "SANS and TEM Studies of Carbide Precipitation and Creep Damage in Type 304 Stainless Steel"

Fifth International Conference on Rapidly Quenched Metals, Würzburg, Federal Republic of Germany, September 3-7, 1984:

S. A. David* and J. M. Vitek, "Microstructure of Rapidly Quenched 308 Stainless Steel Weld Filler Metals and Its Implications on Rapid Solidification Processes"

D. M. Kroeger,* C. C. Koch, C. G. McKamey, and J. O. Scarbrough, "A Study of Temper Embrittlement in an Iron-Based Metallic Glass"

1984 International Conference on New Developments in Stainless Steel Technology, Detroit, Michigan, September 17-20, 1984:

J. H. Schneibel,* C. L. White, G. F. Petersen, and R. A. Padgett, "Creep Fracture in an Austenitic Stainless Steel Containing Titanium and/or Antimony"

International Conference on Surface Modification of Metals by Ion Beams, University of Heidelberg, Federal Republic of Germany, September 17-21, 1984:

C. J. McHargue,* G. C. Farlow, C. W. White, J. M. Williams, P. Angelini, and G. M. Begun, "The Amorphization of Ceramics by Ion Beams"

C. J. McHargue,* J. M. Williams, M. B. Lewis, and B. R. Appleton, "The Reactivity of Ion Implanted SiC"

1984 Fall Meeting of The Metallurgical Society of AIME, Detroit, Michigan, September 17–21, 1984:

E. A. Kenik, "HVEM In Situ Studies of Strain Localization in Al-Li Alloys"

L. Martinez* and J. H. Schneibel, "On the Measurement of Surface Free Energies of Solids"

Seminar, Physics Laboratory, University of Athens, Greece, September 21, 1984:

P. Angelini, "Analytical Electron Microscopy of Ion Implanted Al_2O_3"

Second International Conference on the Science of Hard Materials, Rhodes, Greece, September 23–28, 1984:

P. Angelini,* P. F. Becher, J. Bentley, J. Brynestad, M. K. Ferber, C. B. Finch, and P. S. Sklad, "Processing and Microstructural Development in Liquid Phase Sintered and Pure TiB_2 Ceramics"

C. J. McHargue,* C. S. Yust, P. Angelini, P. S. Sklad, and M. B. Lewis, "The Surface Mechanical Properties and Wear Behavior of Ion Implanted TiB_2"

Energy Conversion and Utilization Technologies Workshop on Production and Fabrication of Ordered Intermetallic Alloys, Oak Ridge, Tennessee, September 25–26, 1984:

C. T. Liu,* C. L. White, and J. A. Horton, "The Role of Boron Additions on Grain-Boundary Chemistry and Tensile Properties of Ni_3Al Containing 24 and 26 at. % Al"

Seminar, Max-Planck-Institut, Stuttgart, Federal Republic of Germany, October 1, 1984:

P. Angelini, "Characterization and Properties of TiB_2"

Seminar, University of Pittsburgh, Pittsburgh, Pennsylvania, October 25, 1984:

S. A. David, "Effect of Initial Microstructure on the Transformation Characteristics of Type 308 Stainless Steel Weld Filler Metal"

Stanford Synchrotron Radiation Laboratory 1984 Users Group Meeting, Stanford, California, October 26, 1984:

H. L. Yakel, "Optimizing Estimates of Long-Range Order Parameters with Anomalous Bragg X-Ray Scattering Data"

Seminar, Lockheed Research Laboratory, Palo Alto, California, October 26, 1984:

C. L. White, "Boron Segregation and Ductilization of Grain Boundaries in Ni_3Al"

American Ceramic Society Fall Meeting, San Francisco, California, October 28–31, 1984:

C. B. Finch,* S. Baik, A. Bleier, and P. F. Becher, "Processing and Sintering of Submicrometer TiB_2 Powders"

C. L. White, "Study of Solute Segregation at Interfaces Using Auger Electron Spectroscopy"

Seminar, Max-Planck Institut, Stuttgart, Federal Republic of Germany, October 29, 1984:

J. M. Vitek, "Investigation of Ferrite Stability in Duplex Austentic Steels Using Analytical Electron Microscopy (AEM)"

Appalachian Region Electron Microscopy Society Meeting, Knoxville, Tennessee, November 2, 1984:

P. Angelini, J. Bentley, A. T. Fisher, J. A. Horton, Jr., E. A. Kenik,* G. L. Lehman, and P. S. Sklad, "Comparison of Performance of an Analytical Electron Microscope at 300 and 100 kV"

Seminars, Institute Laue Langevin, Grenoble, France, and Research Center, Fiat, Torino, Italy, November 5 and 9, 1984:

M. H. Yoo, "SANS and TEM Studies of Carbide Precipitation and Creep Damage in Type 304 Stainless Steel"

State University of New York, Stony Brook, Department of Materials Science and Engineering, November 6, 1984:

C. J. Sparks, Jr., "X-Ray Microprobe Characterization of Materials: The Case for Undulators on Advanced Storage Rings"

Conference on Application of Accelerators in Research and Industry, North Texas State University, Denton, Texas, November 12–14, 1984:

C. J. McHargue,* G. C. Farlow, C. W. White, B. R. Appleton, P. Angelini, and H. Naramoto, "The Structure and Properties of Ion-Implanted Al_2O_3"

Seminar, University of Tennessee, Department of Metallurgical Engineering, Knoxville, Tennessee, November 20, 1984:

C. L. White, "Boron Segregation and Ductilization of Grain Boundaries in Ni_3Al"

Materials Research Society 1984 Fall Meeting, Boston, Massachusetts, November 26–30, 1984:

P. Angelini, J. Bentley, A. T. Fisher, J. A. Horton, Jr., E. A. Kenik,* G. L. Lehman, and P. S. Sklad, "Comparison of Performance of an Analytical Electron Microscope at 300 and 100 kV"

G. M. Stocks,* A. P. Maclin, and W. M. Temmerman, "The Electronic Structure of Transition Metal Aluminides"

G. M. Stocks,* J. Wadsworth, and B. L. Gyorffy, "First Principles Approach to the Calculation of Short-Range Order in Metallic Alloys"

G. M. Stocks,* J. Wadsworth, and B. L. Gyorffy, "First Principles Theory of Fermi-Surface Driven Concentration Waves in Cu_cPd_{1-c} Alloys"

R. K. Williams,* R. S. Graves, F. J. Weaver, and D. L. McElroy, "Physical Properties of Ni_3Al Containing 24 and 25 Atomic Percent Al"

30th Annual Conference on Magnetism and Magnetic Materials, San Diego, California, American Institute of Physics/Magnetics Society of IEEE, November 27–30, 1984:

D. D. Johnson,* F. J. Pinski, and G. M. Stocks, "Self-Consistent Electronic Structure of Disordered $Fe_{0.65}Ni_{0.35}$"

Second USA–Japan Superalloys Seminar, Shizuoka, Japan, December 6–12 and 21, 1984:

C. T. Liu, "Design of Ordered Intermetallic Alloys for High-Temperature Use"

Dislocations and Properties of Real Materials, The Royal Society of London, England, December 11–12, 1984:

M. H. Yoo, "Slip-Interface Interaction at Elevated Temperatures"

Arizona State University Centennial Symposium on High-Resolution Electron Microscopy, Scottsdale, Arizona, January 7–11, 1985:

D. N. Braski* and J. V. Cathcart, "The Effect of Y_2O_3 Dispersoid in 80Ni–20Cr Alloy on the Early Stages of Oxidation at 1273K"

A. G. Dhere,* R. J. De Angelis, P. J. Reucroft, and J. Bentley, "Twinned Colloidal Gold Particles"

Seminar, University of Tennessee, Knoxville, Tennessee, January 8, 1985:

J. H. Schneibel* and G. F. Petersen, "The Influence of Impurities on Grain Boundary Sliding in Nickel"

Seminar, Stanford University, Stanford, California, January 28, 1985:

W. C. Oliver, "Ultra Low Load Hardness Testing"

Seminar, IBM, San Jose, California, January 29, 1985:

W. C. Oliver, "Ultra Low Load Hardness Testing"

Seminar, Hewlett Packard, San Jose, California, January 30, 1985:

W. C. Oliver, "Ultra Low Load Hardness Testing"

Seminar, University of Tennessee, Knoxville, Tennessee, February 19, 1985:

P. F. Becher, "Stress-Induced Phase Transformations Yield Toughened Ceramics"

Annual Meeting of the American Institute of Mining, Metallurgical, and Petroleum Engineers, New York, New York, February 24-28, 1985:

S. A. David* and V. P. Kujanpää, "Correlation Between Solidification Parameters and Weld Microstructure"

J. H. Schneibel* and L. Martinez, "On the Measurement of Surface Free Energies of Solids"

J. H. Schneibel,* L. Martinez, and C. L. White, "Comparison of Cavitation in Stainless Steels with Different Creep Ductilities"

G. M. Stocks,* J. S. Faulkner, M. Boring, F. J. Pinski, and D. D. Johnson, "Abinitio Theory of the Electronic Structure of the Hume-Rothery Alloys"

C. L. White, "Kinetic Mechanisms for S and Sb Segregation to Free Surfaces in Ni-1 wt % Sb at 700°C"

Symposium on Noble Metal Alloys, New York, New York, February 25-27, 1985:

G. M. Stocks,* M. Boring, D. M. Nicholson, F. J. Pinski, D. D. Johnson, J. S. Faulkner, and B. L. Gyorffy, "Self-Consistent Electronic Structures of α-Phase Hume-Rothery Electron Compound Alloys Cu_cZn_{1-c}, Cu_cGa_{1-c}, and Cu_cGe_{1-c}"

Seminar, Vacuumschmelze, Hanau, Federal Republic of Germany, March 6, 1985:

J. M. Vitek, "The Effect of Cooling Rate on the Structure of Austenitic Stainless Steels"

Seminar, American Society for Metals Visting Lecture Program, Madras, India, March 11, 1985:

S. A. David, "Solidification Behavior, Microstructure and Modification of Austenitic Stainless Steel Weld Metal"

S. A. David,* D. N. Braski, and C. T. Liu, "Welding of Ductile Long-Range-Ordered Alloys"

Seminar, Quantum Chemistry and Solid-State Theory, Part II of 1985 Sanibel Symposia, sponsored by the University of Florida, St. Augustine, Florida, March 18–23, 1985:

J. S. Faulkner, "Electronic States in Disordered Solids, III. Applications to Materials Science"

Seminar, Arizona State University, Tempe, Arizona, March 21–26, 1985:

L. K. Mansur, "How Swelling Begins in Irradiated Metals (and What Can be Done About It)"

American Physical Society Meeting, Baltimore, Maryland, March 25–29, 1985:

A. Al-Lehaibi, J. C. Swihart,* W. H. Butler, and F. J. Pinski, "Electron-Phonon Interaction Effects in Tantalum"

W. H. Butler, "Electron-Phonon Scattering Using the Coherent-Potential Approximation"

A. Chowdhary,* D. Nicholson, and L. Schwartz, "Electronic Structure of Amorphous Ni-B and Ni-P Alloys"

A. P. Maclin* and G. M. Stocks, "Electronic Structures of Aluminum-Rich Al_cLi_{1-c} Alloys"

D. M. Nicholson* and G. M. Stocks, "Electronic Structure of $Ni_{1-x}Mo_x$ Alloys"

D. M. Nicholson,* G. M. Stocks, D. D. Johnson, F. J. Pinski, and B. L. Gyorffy, "Local Density Theory of Random Alloys"

G. S. Painter* and F. W. Averill, "The Total Energy Hypersurface and Force Field in Transition Metal Clusters as Calculated in the Local Spin Density Approximation"

G. M. Stocks and F. J. Pinski,* "Use of Integration in the Complex Energy Plane in Multiple Scattering Greens Function Methods: An Optimal Contour"

J. C. Swihart* and W. H. Butler, "Theory and Calculation of Electrical Conductivity in Random Alloys"

Corrosion 85, National Association of Corrosion Engineers, Boston, Massachusetts, March 25–29, 1985:

C. T. Liu* and J. V. Cathcart, "Ordered Intermetallic Alloys Based on Ni_3Al for High-Temperature Applications"

Seminar, Characterization of Chemically Processed Ceramics, Rutgers University, Piscataway, New Jersey, March 26, 1985:

A. Bleier, "Surface, Colloidal, and Chemical Properties of Ceramic Powders"

Seminar, University of California, Los Angeles, California, March 26–29, 1985:

L. K. Mansur, "How Swelling Begins in Irradiated Metals (and What Can be Done About It)"

Seminar, Cambridge University, Cambridge, England, and Central Electricity Generating Board, Berkley, England, April 1, 1985:

M. H. Yoo, "Interfacial Segregation and Fracture at Elevated Temperature"

New Directions in X-Ray Scattering Workshop, Lawrence Livermore Laboratory, Asilomar, California, April 3–5, 1985:

G. E. Ice, "Experimental X-Ray Scattering Cross Sections for H^2 and Rare Atomic Gases"

American Ceramic Society, Northeast Section Meeting, Boston, Massachusetts, April 11, 1985:

C. J. McHargue, "Ion Beam Modification of Ceramics"

Seminar, Rice University, Houston, Texas, April 12–15, 1985:

W. C. Oliver, "Hardness Measurements With Indents As Shallow As 20 nm"

Seminar, Materials Science and Engineering Department, University of Tennessee, Knoxville, Tennessee, April 30, 1985:

M. K. Miller, "Atom Probe Field Ion Microscopy"

American Vacuum Society Meeting, Sheraton West, Knoxville, Tennessee, April 30–May 2, 1985:

W. C. Oliver, "The Use of Ultra-Low Load Testing to Mechanically Characterize Thin Films"

Seminar, University of Illinois, Urbana-Champaign, Illinois, May 3, 1985:

P. F. Becher, "Stress-Induced Phase Transformations Yield Toughened Ceramics"

87th Annual Meeting of the American Ceramic Society, Cincinnati, Ohio, May 5–9, 1985:

P. Angelini, C. B. Finch, P. F. Becher,* J. Bentley, and P. S. Sklad, "Evaluation of Liquid Phase Sintering Mechanisms in TiB_2–Ni Ceramics by TEM and Electron Microprobe Analyses"

S. Baik,* P. Angelini, P. F. Becher, C. E. Bamberger, and J. Brynestad, "The Effect of Impurities on Sintering of Submicrometer TiB_2 Powders"

P. F. Becher,* G. Begun, S. B. Waters, W. H. Warwick, and M. K. Ferber, "Temperature Dependence of Fracture Toughness in M_gO-PSZ and ZrO_2 (Y_2O_3) Toughened Alumina"

J. Cesarano,* I. A. Aksay, and A. Bleier, "Polyelectrolyte Adsorption on α-Al_2O_3 and Aqueous Suspension Stability"

S. Spooner,* P. Angelini, P. F. Becher, A. Bleier, W. D. Bond, and J. Brynestad, "Investigation of the Synthesis and Processing of Submicron Ceramic Powders by TEM and Small Angle X-Ray Scattering (SAXS)"

Seminar, Thomas J. Watson Research Center, IBM Corporation, Yorktown Heights, New York, May 21, 1985:

C. J. Sparks, Jr., "X-Ray Microprobe Characterization of Materials"

Meeting on Application of Ion Plating and Ion Implantation to Materials, Atlanta, Georgia, June 3–5, 1985:

C. J. McHargue,* G. C. Farlow, C. W. White, B. R. Appleton, J. M. Williams, P. S. Sklad, P. Angelini, and C. S. Yust, "Surface Property Modification of Ceramics by Ion Beams"

Symposium on Surface and Colloid Science in Computer Technology, part of the 5th International Conference on Surface and Colloid Science, Clarkson College of Technology, Potsdam, New York, June 24–28, 1985:

A. Bleier* and P. Angelini, "Synthesis and Colloidal Properties of Uniform Monoclinic Zirconia"

J. Cesarano, I. A. Aksay, and A. Bleier,* "Interaction of Polymethacrylic Acid with α-Al_2O_3 in Aqueous Suspension"

Workshop on the Relation Between Mechanical Properties and Microstructure Under Fusion Irradiation Conditions, Ebeltoft, Denmark, June 27–July 2, 1985:

N. H. Packan, "The Effect of Pulsed Irradiation on Microstructural Evolution"

32d International Field Emission Symposium, Wheeling, West Virginia, July 15–20, 1985:

J. A. Horton* and M. K. Miller, "A TEM-APFIM Investigation of Boron Doped Ni_3Al"

M. K. Miller, "The ORNL Atom Probe"

M. K. Miller, "The ORNL Atom Probe Software Package"

M. K. Miller,* L. L. Horton, and S. Spooner, "A Comparison of Characteristic Distance Measurements by AP, TEM, and SANS"

Gordon Research Conference on Corrosion, London, New Hampshire, July 25, 1985:

R. A. McKee, "Adherence Properties of Thin Films and Coatings"

Gordon Research Conference on Ceramics Science, Plymouth, New Hampshire, July 28-August 2, 1985:

A. Bleier, "Chemical and Thermodynamical Forces in Powder Consolidation"

J. Cesarano, I. A. Aksay, and A. Bleier,* "Polyelectrolyte Adsorption on Alumina and Aqueous Suspension Behavior"

International Conference on the Physics and Chemistry of Boron and Boron-Rich Borides, The University of New Mexico, Albuquerque, New Mexico, July 29-31, 1985:

H. L. Yakel, "Recent Developments in the Structural Crystallography of Boron and the Higher Borides"

Workshop on Micromechanics of Fracture in Metallic Materials, Bretton Woods, New Hampshire, sponsored by the the U.S. Department of Energy, July 29-August 2, 1985:

C. T. Liu and C. L. White,* "Grain-Boundary Segregation and Fracture Behavior of Nickel Aluminides"

43d Annual Meeting, Electron Microscopy Society of America, Louisville, Kentucky, August 5-9, 1985:

J. Bentley,* M. K. Miller, S. S. Brenner, and J. A. Spitznagel, "Identification of G-Phase in Aged Cast CF 8 Type Stainless Steel"

M. G. Burke* and M. K. Miller, "A Comparison of TEM and APFIM to the Interpretation of Modulated Microstructures"

A. G. Dhere,* P. J. Reucroft, R. J. De Angelis, and J. Bentley, "Nickel Oxide Morphology in Nickel-Silica Catalysts"

A. T. Fisher* and P. Angelini, "Preparation of Backthinned Ceramic Specimens"

C. P. Haltom, "Mechanical Prethinning and Thinning of Unique Materials for TEM"

L. L. Horton, "Specimen Preparation for Near-Surface Examination"

E. A. Kenik, "Segregation to Boundaries in an Antimony-Containing Stainless Steel"

K. F. Russell* and L. L. Horton, "Specimen Preparation of Near Surface Ion Irradiated Samples"

P. S. Sklad, "Analytical Electron Microscopy of Surface Modified Ceramics"

W. H. Smith (presented by C. K. H. DuBose), "Electrolytic Extractions of Precipitates from Steel Alloys"

Materials Science Series Seminar, Oak Ridge Gaseous Diffusion Plant, Oak Ridge, Tennessee, August 13, 1985:

L. K. Mansur, "Swelling in Irradiated Metals and Alloys (and What Can be Done About It)"

American Institute of Chemical Engineers Summer Meeting, Seattle, Washington, August 25–28, 1985:

J. Cesarano, I. A. Aksay, and A. Bleier,* "Polyelectrolyte Adsorption on Alumina and Aqueous Suspension Behavior"

A. Bleier* and M. A. Janney, "Rheology of Concentrated Alumina Suspensions Containing Anionic Polymer"

1985 Calorimetry Conference, Pacific Grove, California, August 25– 30, 1985:

R. K. Williams, "The Thermal Conductivity of Metals and Alloys at High Temperatures"

1985 International Conference on Magnetism, San Francisco, California, August 26–30, 1985:

D. D. Johnson*, G. M. Stocks, B. L. Gyorffy, F. J. Pinski, and J. Staunton, "A First-Principles Calculation of the Magnetic Properties of Paramagnetic fcc Iron"

North Atlantic Treaty Organization Advanced Study Institute Symposium on Amorphous and Liquid Materials, Mendola (Trentino), Italy, August 26–September 7, 1985:

D. M. Nicholson, "Nagel-Tauc and Ziman Theory Viewed in the Light of Modern Electronic-Structure Calculations"

EMAG '85, Institute of Physics, University of Newcastle-upon-Tyne, England, September 2–5, 1985:

P. Angelini* and J. Bentley, "Microanalysis by Electron Energy Loss Spectroscopy at 100 to 300 kV"

Technical Meeting of the Southern Tier Chapter of American Society for Metals, Corning, New York, September 9, 1985:

P. F. Tortorelli, "SEM Studies of Selected Corrosion Reactions"

Symposium, Kernforschungsanlage Jülich, Federal Republic of Germany, September 9, 1985:

C. J. McHargue, "Damage Accumulation in Ceramics During Ion Implantation"

2d International Symposium on Environmental Degradation of Materials in Nuclear Power Systems - Water Reactors, Monterey, California, September 9-12, 1985:

S. S. Brenner, M. K. Miller,* and J. A. Spitznagel, "Microanalytical Investigations of Light Water Reactor Materials Using the Atom Probe"

Seminar, EUROTRIB '85, Congres International de Tribologie, Lyon, France, September 9-12, 1985:

C. S. Yust,* C. J. McHargue, C. L. White, P. Angelini, and M. B. Lewis, "Wear of Ion Implanted TiB_2 Surfaces"

Seminar, Columbia University, New York, New York, September 10, 1985:

C. T. Liu, "Boron Segregation and Dynamic Embrittlement in Ni_3Al Alloys"

Symposium, Universite Claude, Bernard, Lyon, France, September 12, 1985:

C. J. McHargue, "Damage Accumulation in Ceramics During Ion Implantation"

NATO Advanced Study Institute on Erosion and Growth of Solids Stimulated by Atom and Ion Beams, Heraklion, Crete, Greece, September 16-27, 1985:

C. J. McHargue, "Effects of Implantation on Subsequent Erosion Behavior of Solids"

Seminar, Rutgers University, New Brunswick, New Jersey, September 24, 1985:

P. F. Becher, "Advances in Ceramic Composites: Whisker Reinforced and ZrO_2 Toughened Ceramics"

Seminar, Dupont DeNemours Company, Wilmington, Delaware, September 25, 1985:

P. F. Becher, "Advances in Ceramic Composites: Whisker Reinforced and ZrO_2 Toughened Ceramics"

Workshop on Atomic Transport and Defects in Metals by Neutron Scattering, Kernforschungsanlage Jülich, Federal Republic of Germany, October 2-4, 1985:

D. Schwahn and M. H. Yoo,* "Studies of Heterogeneities in Micrometer-Range with Double Crystal Diffractometer"

Seminar, Pennsylvania State University, University Park, Pennsylvania, October 3, 1985:

S. A. David, "Solidification Behavior, Microstructure, and Modification of Austenitic Stainless Steel Weld Metal"

Symposium on Applications of Local Density Functional Theory in Chemistry, Southeast-Southwest Regional Meeting of the American Chemical Society, Memphis, Tennessee, October 9–11, 1985:

G. S. Painter, "The Bonding Properties of Transition Metal Clusters Within the Local Spin Density Method"

Metallurgical Society of AIME Fall Meeting, Toronto, Canada, October 13–17, 1985:

J. Bentley, "A Review of the Application of Analytical Electron Microscopy to Ion-Implanted Materials"

A. DasGupta,* L. C. Smedskjaer, D. G. Legnini, and R. W. Siegel, "Positron Annihilation Studies in Boron-Doped Ni_3Al"

D. S. Easton,* C. G. McKamey, D. M. Kroeger, and O. B. Cavin, "A New Metastable Phase from Amorphous Ni_{40}-Zr_{60}"

M. R. Hayns and L. K. Mansur,* "Cascade-Induced Fluctuations and the Transition from the Stable to the Critical Cavity Radius for Swelling"

L. L. Horton,* J. Bentley, and M. B. Lewis, "Radiation Damage in Ion-Irradiated MgO"

E. H. Lee, N. H. Packan,* M. B. Lewis, and L. K. Mansur, "Effects of Rapidly Pulsed Ion Bombardment on Microstructure and Phase Stability in a Ti-Modified Stainless Steel"

M. B. Lewis* and K. Farrell, "Migration Behavior of Helium Implanted Into Nickel, Iron, Titanium, and Zirconium"

C. T. Liu,* C. L. White, and J. H. Schneibel, "Effect of Hafnium Additions on Creep Behavior of Nickel Aluminides"

L. K. Mansur,* A. D. Brailsford, and W. A. Coghlan, "Fluctuations of Defect Concentrations During Ion Bombardment as Described by Cascade Diffusion Theory"

C. J. McHargue,* G. C. Farlow, G. M. Begun, J. M. Williams, C. W. White, B. R. Appleton, P. S. Sklad, and P. Angelini, "Damage Accumulation in Ceramics During Ion Implantation"

W. Oliver* and C. T. Liu, "The Hardness of Ni_3Al Very Near Grain Boundaries"

A. J. Pedraza and D. F. Pedraza,* "An Analysis of Carbide Precipitation in V and Nb During Aging and Ion Bombardment"

D. F. Pedraza* and L. K. Mansur, "The Effect of Point Defects on the Amorphization of Metallic Alloys During Ion Implantation"

C. L. White,* R. A. Padgett, C. T. Liu, and S. M. Yalisove, "Surface and Grain Boundary Segregation in Relation to Inter-Granular Fracture: Boron and Sulfur in Ni_3Al"

M. H. Yoo* and H. Trinkaus, "Role of Interfaces in Cavity Formation"

1985 Metals Congress, American Society for Metals Annual Meeting, Toronto, Canada, October 13–18, 1985:

S. A. David* and J. M. Vitek, "Solidification Structure and Microstructural Stability of Austenitic Stainless Steel Welds"

P. S. Sklad,* P. Angelini, and J. T. Houston, "Analytical Electron Microscopy of Ion Implanted SiC"

Topical Symposium on Recent Developments in Ceramic Science, Albuquerque, New Mexico, October 14–15, 1985:

P. F. Becher, "Stress-Induced Phase Transformations Yield Toughened Ceramics"

A. Bleier, "Particle Agglomeration"

19th International Thermal Conductivity Conference, Cookeville, Tennessee, October 21–23, 1985:

W. H. Butler, "Is It Possible to Calculate Thermal Conductivities of Metals and Alloys from First Principles?"

Seminar, Pennsylvania State Univeristy, University Park, Pennsylvania, November 8, 1985:

P. F. Becher, "Toughening Effects in SiC Whisker Reinforced Oxides"

American Society for Metals Seminar, Savannah River Chapter, Savannah, Georgia, November 14, 1985:

M. K. Miller, "Atom Probe Field Ion Microscopy"

American Ceramic Society Division Meeting, Basic Sciences Division, Baltimore, Maryland, November 17–19, 1985:

S. Baik, "Surface Segregation Model: Is it Real?"

Annual Meeting of the American Vacuum Society, Houston, Texas, November 19–22, 1985:

C. L. White, "Recent Development Concerning Segregation and Fracture at Grain Boundaries"

4th Japan Institute of Metals International Symposium (JIMIS-4), Minakami Spa, Japan, November 25–29, 1985:

J. H. Schneibel* and G. F. Petersen, "Grain Boundary Sliding in Wires with Bamboo Structure"

1985 Materials Research Society Meeting, Boston, Massachusetts, December 2–5, 1985:

P. B. Allen,* T. P. Beaulac, F. A. Khan, W. H. Butler, F. J. Pinski, and J. C. Swihart, "Calculations of Resistivity and Superconducting T_c in Metals"

J. Bentley, "Axial Electron Channeling Microanalysis of $L1_2$ Alloys"

A. G. Dhere,* R. J. De Angelis, P. J. Reucroft, J. Bentley, G. E. Ice, A. Habenshcuss, ""Morphological Developments of Nickel Particles in Supported Metal Catalysts"

L. L. Horton, "Defect and Microstructural Analyses in Ferromagnetic Materials"

E. A. Kenik, "Measurements of Equilibrium and Nonequilibrium Segregation by X-Ray Microanalysis"

F. A. List and R. A. McKee,* "Mechanical Properties of Metallic Films on Sapphire"

C. G. McKamey,* D. S. Easton, and D. M. Kroeger, "Evidence for the Formation of a Metastable Crystalline Phase During Crystallization of Zr-Ni Metallic Glasses of Approximately 57-63.2 at. % Zr"

D. M. Nicholson,* A. Chowdhary, and L. Schwartz, "Nagel-Tauc and Ziman Theory Viewed in the Light of Modern Electronic-Structure Calculations"

R. D. Nixon,* R. R. Davis, and J. Bentley, "Kinetics and Mechanisms of Creep in Hot Isostatically Pressed Niobium Carbide"

W. C. Oliver,* C. J. McHargue, G. C. Farlow, and C. W. White, "The Hardness of Ion Implanted Ceramics"

P. S. Sklad, "Ion Implantation and Near Surface Examination"

Y. K. Simpson,* C. B. Carter, P. S. Sklad, and J. Bentley, "Grain-Boundary, Glassy-Phase Identification and Possible Artifacts"

Meeting, The Aerospace Corporation, Los Angeles, California, December 3, 1985:

C. T. Liu, "Recent Development in Nickel Aluminides for High-Temperature Structural Uses"

Appendix C

PUBLICATIONS

Compiled by Faye Roseberry

P. Angelini, P. F. Becher, J. Bentley, C. B. Finch, and P. S. Sklad, "Processing and Microstructural Characterization of TiB_2 Liquid Phase Sintered with Ni and Ni_3Al," pp. 299-305 in *Defect Properties and Processing of High-Technology Nonmetallic Materials*, proceedings of symposium held in Boston on Nov. 14-18, 1983, ed. J. H. Crawford, Jr., Y. Chen, and W. A. Sibley, Elsevier, New York, 1984 (*Materials Research Society Symposia Proceedings*, vol. 24).

P. Angelini and J. Bentley, "Secondary Fluorescence Effects on X-Ray Microanalysis," pp. 582-83 in *Proceedings 42d Annual Meeting of the Electron Microscopy Society of America, Detroit, Michigan, August 13-17, 1984*, ed. G. W. Bailey, San Francisco Press, San Francisco, 1984.

P. Angelini and J. Bentley, "Thermal Expansion Coefficient Determination by CBED," pp. 93-96 in *Analytical Electron Microscopy 1984*, proceedings of workshop held at Bethlehem, Pa., July 16-20, 1984, sponsored by the Microbeam Analysis Society, ed. D. B. Williams and D. C. Joy, San Francisco Press, San Francisco, 1984.

G. B. Armen, T. Åberg, K. R. Karim, J. C. Levin, B. Craseman, G. S. Brown, M. H. Chen, and G. E. Ice, "Threshold Double Photoexcitation of Argon with Synchrotron Radiation," *Phys. Rev. Lett.* **54**(3), 182-85 (January 1985).

F. W. Averill and G. S. Painter, "Orbital Forces in the Density-Functional Formalism: Application to the Copper Dimer," *Phys. Rev. B* **32**(4), 2141-48 (Aug. 15, 1985).

S. Baik, D. E. Fowler, J. M. Blakely, and R. Raj, "Segregation of Mg to the (0001) Surface of Doped Sapphire," *J. Am. Ceram. Soc.* **68**(5), 281-86 (May 1985).

S. Baik and R. Raj, "Effect of Silicon Activity on Liquid-Phase Sintering of Nitrogen Ceramics," *J. Am. Ceram. Soc.* **68**(5), C-124-26 (May 1985).

S. Baik and R. Raj, "Suppression of Frothing by Silicon Addition During Oxynitride Glass Synthesis," *J. Am. Ceram Soc.* **68**(7), C-168-70 (July 1985).

P. F. Becher, "Processing of Transformation Toughened Al_2O_3-$ZrO_2(Y_2O_3)$ Composites," pp. 9-10 in *Ceramics: Science of Processing*, U.S. DOE Basic Energy Sciences Bulletin, Materials and Molecular Research Division, Lawrence Berkeley Laboratory, University of California, Berkeley, August 1984.

P. F. Becher and M. K. Ferber, "Grain-Size Dependence of the Slow-Crack Growth Behavior in Noncubic Ceramics," *Acta Metall.* **33**(7), 1217-21 (July 1985).

J. Bentley, "The Utility of Replica Techniques for X-Ray Microanalysis of Second-Phase Particles," pp. 223-26 in *Analytical Electron Microscopy 1984*, proceedings of workshop held in Bethlehem, Pa., July 16-20, 1984, sponsored by Microbeam Analysis Society, ed. D. B. Williams and D. C. Joy, San Francisco Press, San Francisco, 1984.

J. Bentley and P. Angelini, "X-Ray Microanalysis of Ion-Implantation Profiles in Backthinned Specimens," pp. 578-79 in *Proceedings of 42d Annual Meeting of the Electron Microscopy Society of America, Detroit, Michigan, August 13-17, 1984*, ed. G. W. Bailey, San Francisco Press, San Francisco, 1984.

J. Bentley, P. Angelini, and P. S. Sklad, "Secondary Fluorescence Effects on X-Ray Microanalysis," pp. 315-17 in *Analytical Electron Microscopy 1984*, proceedings of workshop held in Bethlehem, Pa., July 16-20, 1984, sponsored by Microbeam Analysis Society, ed. D. B. Williams and D. C. Joy, San Francisco Press, San Francisco, 1984.

J. Bentley, E. A. Kenik, P. Angelini, A. T. Fisher, P. S. Sklad, G. L. Lehman, and J. A. Horton, Jr., "Comparison of Performance of an Analytical Electron Microscope at 300 and 100 kv," pp. 363-68 in *Advanced Photon and Particle Techniques for the Characterization of Defects in Solids*, proceedings of symposium held in Boston Nov. 27-29, 1984, ed. J. B. Roberto, R. W. Carpenter, and M. C. Wittels, Materials Research Society, Pittsburgh, 1985 (*Materials Research Society Symposia Proceedings*, vol. 41).

J. Bentley, G. L. Lehman, and A. T. Fisher, "Structural Characterization by Intensity Measurements of Electron Diffraction Patterns," pp. 143-46 in *Analytical Electron Microscopy 1984*, proceedings of workshop held at Bethlehem, Pennsylvania, July 16-20, 1984, sponsored by the Microbeam Analysis Society, ed. D. B. Williams and D. C. Joy, San Francisco Press, San Francisco, 1984.

J. Bentley, M. K. Miller, S. S. Brenner, and J. A Spitznagel, "Identification of G-Phase in Aged Cast CF 8 Type Stainless Steel," pp. 328-29 in *Proceedings of the 43rd Annual Meeting of the Electron Microscopy Society of America, Louisville, Kentucky, August 5-9, 1985*, ed. G. W. Bailey, San Francisco Press, San Francisco, 1985.

J. Bentley, L. D. Stephenson, R. B. Benson, Jr., P. A. Parrish, and J. K. Hirvonen, "Second Phase Formation in Aluminum Annealed after Ion Implantation with Molybdenum," pp. 151–56 in *Ion Implantation and Ion Beam Processing of Materials*, proceedings of symposium held in Boston Nov. 14–17, 1983, ed. G. K. Hubler, O. W. Holland, C. R. Clayton, and C. W. White, North-Holland, New York, 1984 (*Materials Research Society Symposia Proceedings*, vol. 27).

A. Bleier, "The Science of the Interactions of Colloidal Particles and Ceramics Processing," pp. 71–81 in *Emergent Process Methods for High-Technology Ceramics*, proceedings of conference held at North Carolina State University, Raleigh, Nov. 8–10, 1982, ed. R. F. Davis, H. Palmour III, and R. L. Porter, Plenum Press, New York, 1984 (*Materials Science Research*, vol. 17).

A. Bleier, "The Science of the Interaction of Colloidal Particles and Ceramics Processing," *J. Mater. Ed.* 7(3), 435–52 (1985).

A. D. Brailsford and L. K. Mansur, "Time Dependent Rate Theory for Diffusional Defect Processes," *Acta Metall.* 33(8), 1425–37 (1985).

D. N. Braski and K. Farrell, "Elevated-Temperature Heavy Ion Damage in $(Co_{0.78}Fe_{0.22})_3V$ Ordered Alloy," *J. Nucl. Mater.* **136**, 48–58 (1985).

M. G. Burke and M. K. Miller, "A Comparison of TEM and APFIM to the Interpretation of Modulated Microstructures," pp. 70–71 in *Proceedings of the 43rd Annual Meeting of the Electron Microscopy Society of America, Louisville, Kentucky, August 5–9, 1985*, ed. G. W. Bailey, San Francisco Press, San Francisco, 1985.

M. G. Burke, M. K. Miller, S. S. Brenner, and W. A. Soffa, "A Combined AEM/FIM Study of Precipitation in an Fe-25 at. % Be Alloy," pp. 157–60 in *Analytical Electron Microscopy 1984*, proceedings of workshop held at Bethlehem, Pa., July 16–20, 1984, sponsored by the Microbeam Analysis Society, ed. D. B. Williams and D. C. Joy, San Francisco Press, San Francisco, 1984.

W. H. Butler, "Resistivity of Alloys," pp. 215–30 in *High-Temperature Alloys: Theory and Design*, proceedings of conference sponsored by the Alloy Phases Committee of the Metallurgical Society of AIME and the Metals and Ceramics Division, Oak Ridge National Laboratory, held in Bethesda, Md., Apr. 9-11, 1984, ed. J. O. Stiegler, The Metallurgical Society of AIME, Warrendale, Pa., 1984.

W. H. Butler, "Theory of Electronic Transport in Random Alloys: Korringa-Kohn-Rostoker Coherent-Potential Approximation," *Phys. Rev. B* **31**(6), 3260–77 (March 1985).

P. P. Camus, W. A. Soffa, S. S. Brenner, and M. K. Miller, "Quantification of Interconnected Microstructures by FIM," *J. Phys.* C9(12), 265–71 (December 1984).

C. H. Carter, Jr., J. Bentley, and R. F. Davis, "The Occurance of Defects in Silicon Carbides as a Result of Processing Mode and Applied Stress," pp. 351–64 in *Defect Properties and Processing of High-Technology Nonmetallic Materials*, proceedings of symposium held in Boston, November 1983, ed. J. H. Crawford, Jr., Y. Chen, and W. A. Sibley, North-Holland, New York, 1984 (*Materials Research Society Symposia Proceedings*, vol. 24).

C. H. Carter, Jr., R. F. Davis, and J. Bentley, "Kinetics and Mechanisms of High-Temperature Creep in Silicon Carbide: I, Reaction-Bonded," *J. Am. Ceram. Soc.* **67**(6), 409–17 (June 1984).

C. H. Carter, Jr., R. F. Davis, and J. Bentley, "Kinetics and Mechanisms of High-Temperature Creep in Silicon Carbide: II, Chemically Vapor Deposited," *J. Am. Ceram. Soc.* **67**(11), 732–40 (November 1984).

Li Chang, A. Cerezo, G. D. W. Smith, M. K. Miller, M. G. Burke, S. S. Brenner, K. A. Taylor, T. Abe, and G. B. Olson, "Ageing of Fe-Ni-C Martensite," *J. Phys.* C9(12), 409–16 (December 1984).

W. A. Coghlan and L. K. Mansur, "Effect of Microstructure on the Minimum Critical Radius and Critical Number of Gas Atoms for Swelling," pp. 481–92 in *Effects of Radiation on Materials*, ASTM STP 870, proceedings of the Twelfth International Symposium, Williamsburg, Va., June 18–20, 1984, ed. F. A. Garner and J. S. Perrin, American Society for Testing and Materials, Philadelphia, 1985.

A. DasGupta, J. A. Horton, and C. T. Liu, "Phase Formation and Stability in the Pseudobinary Ni_3Al-Ni_3V Alloy System," pp. 115–23 in *High-Temperature Alloys: Theory and Design*, proceedings of conference sponsored by the Alloy Phases Committee of the Metallurgical Society of AIME and the Metals and Ceramics Division, Oak Ridge National Laboratory, held in Bethesda, Md., Apr. 9–11, 1984, ed. J. O. Stiegler, The Metallurgical Society of AIME, Warrendale, Pa., 1984.

S. A. David and J. M. Vitek, "Microstructure of Rapidly Quenched Type 308 Stainless Steel Weld Filler Metal and Its Implications on Rapid Solidification Processes," pp. 847–50 in *Rapidly Quenched Metals*, vol. I, proceedings of Fifth International Conference on Rapidly Quenched Metals held in Würzburg, Germany, Sept. 3–7, 1984, ed. S. Steeb and H. Warlimont, North-Holland, Amsterdam, 1985.

R. F. Davis, C. H. Carter, Jr., S. Chevacharoenkul, and J. Bentley, "The Occurrence and Behavior of Dislocations During Plastic Deformation of Selected Transition Metal and Silicon Carbides," pp. 97–124 in *Deformation of Ceramics II*, proceedings of Second International Conference on Plastic Deformation in Ceramics held at Pennsylvania State University, University Park, Pa., July 1983, ed. R. E. Tressler and R. C. Bradt, Plenum Publishing Corporation, New York, 1984.

R. F. Davis, J. E. Lane, C. H. Carter, Jr., J. Bentley, W. H. Wadlin, D. P. Griffis, R. W. Linton, and K. L. More, "Microanalytical and Microstructural Analyses of Boron and Aluminum Regions in Sintered Alpha Silicon Carbide," *Scanning Electron Microsc.* **1984**(III), 1161–67 (1984).

A. G. Dhere, P. J. Reucroft, R. J. De Angelis, and J. Bentley, "Nickel Oxide Morphology in Nickel-Silica Catalysts," pp. 378–79 in *Proceedings of the 43rd Annual Meeting of the Electron Microscopy Society of America, Louisville, Kentucky, August 5–9, 1985*, ed. G. W. Bailey, San Francisco Press, San Francisco, 1985.

A. G. Dhere, P. J. Reucroft, R. J. De Angelis, and J. Bentley, "Characterization of Supported Metal Catalysts by Imaging, Microdiffraction, and Microanalysis Techniques," pp. 196–200 in *Analytical Electron Microscopy 1984*, proceedings of workshop held at Bethlehem, Pa., July 16–20, 1984, ed. D. B. Williams and D. C. Joy, sponsored by the Microbeam Analysis Society, San Francisco Press, San Francisco, 1984.

G. C. Farlow, B. R. Appleton, L. A. Boatner, C. J. McHargue, and C. W. White, "Thermodynamic Constraints on Ion Beam Mixing of Metals on Insulators," *Materials Research Society Symposia Proceedings*, vol. 45, 1985.

G. C. Farlow, C. W. White, B. R. Appleton, P. S. Sklad, and C. J. McHargue, "The Use of Ion Channeling Axial Scans in the Study of Ion-Implanted Al_2O_3," pp. 295–99 in *Advanced Photon and Particle Techniques for the Characterization of Defects in Solids*, proceedings of symposium held in Boston Nov. 27–29, 1984, ed. J. B. Roberto, R. W. Carpenter, and M. C. Wittels, Materials Research Society, Pittsburgh, 1985 (*Materials Research Society Symposia Proceedings*, vol. 41).

G. C. Farlow, C. W. White, C. J. McHargue, P. S. Sklad, and B. R. Appleton, "Thermal Annealing of Fe Implanted Al_2O_3 in an Oxidizing and Reducing Environment," *Nucl. Instrum. Methods Phys. Res.* **B**(7/8), 541–46 (1985).

K. Farrell and E. H. Lee, "Ion Bombardment Damage in a Modified Fe–9 Cr–1 Mo Steel," pp, 383–93 in *Effects of Radiation on Materials*, ASTM STP 870, proceedings of the Twelfth International Symposium, Williamsburg, Va., June 18–20, 1984, ed. F. A. Garner and J. S. Perrin, American Society for Testing and Materials, Philadelphia, 1985.

J. S. Faulkner, "Non-Muffin-Tin Band Theories of the Multiple-Scattering Type," *Phys. Rev. B* **32**(2), 1339–42 (July 15, 1985).

C. B. Finch, M. K. Ferber, W. A. Simpson, Jr., and R. K. Williams, "Anisotropy of Thermal Expansion, Elasticity, and Electrical Resistivity in Single-Crystal Trinickel Boride, Ni_3B," *J. Mater. Sci. Lett.* **3**, 1074–76 (1984).

A. T. Fisher and P. Angelini, "Preparation of Backthinned Ceramic Specimens," pp. 182–83 in *Proceedings of the 43rd Annual Meeting of the Electron Microscopy Society of America, Louisville, Kentucky, August 5–9, 1985*, ed. G. W. Bailey, San Francisco Press, San Francisco, 1985.

B. L. Gyorffy, J. Kollar, A. J. Pindor, G. M. Stocks, J. Staunton, and H. Winter, "On the Theory of Ferro-Magnetism of Transition Metals at Finite Temperatures," pp. 593–656 in *The Electronic Structure of Complex Systems*, proceedings of a NATO Advanced Study Institute held at State University of Ghent, Belgium, on July 12–23, 1982, vol. 113, ed. P. Phariseau and W. M. Temmerman, Plenum Publishing Corporation, New York, 1984.

B. L. Gyorffy, A. J. Pindor, J. Staunton, G. M. Stocks, and H. Winter, "A First-Principles Theory of Ferromagnetic Phase Transitions in Metals," *J. Phys. F: Met. Phys.* **15**, 1337–86 (1985).

B. L. Gyorffy, J. B. Staunton, and G. M. Stocks, "Ferromagnetism in Metals at Finite Temperatures," pp. 231–47 in *High-Temperature Alloys: Theory and Design*, proceedings of conference sponsored by the Alloy Phases Committee of the Metallurgical Society of AIME and the Metals and Ceramics Division, Oak Ridge National Laboratory, held in Bethesda, Md., Apr. 9–11, 1984, ed. J. O. Stiegler, The Metallurgical Society of AIME, Warrendale, Pa., 1984.

C. P. Haltom, "Mechanical Prethinning and Thinning of Unique Materials for TEM," pp. 180–81 in *Proceedings of the 43rd Annual Meeting of the Electron Microscopy Society of America, Louisville, Kentucky, August 5–9, 1985*, ed. G. W. Bailey, San Francisco Press, San Francisco, 1985.

J. P. Hammond, S. A. David, and J. J. Woodhouse, "Indirect Brazing of Structural Ceramics for Uncooled Diesels," pp. 523–29 in *Proceedings of the Twenty-Second Automotive Technology Development Contractors' Coordination Meeting*, P-155, held in Dearborn, Mich., Oct. 29–Nov. 2, 1984 Society of Automotive Engineers, Warrendale, Pa., 1985.

E. H. Henninger and D. S. Easton, "Crystallization Kinetics of Mo–N," *J. Mater. Sci.* **20**, 4298–4308 (1985).

A. Hishinuma, N. H. Packan, E. H. Lee, and L. K. Mansur, "Effects of Pulsed and/or Dual Ion Irradiation on Microstructural Evolution in a Ti and Si Modified Austenitic Alloy," *J. Nucl. Mater.* **122&123**, 260–65 (1984).

J. A. Horton and C. T. Liu, "Anisotropic Antiphase Boundaries in Rapidly Solidified Ni_3Al," *Acta. Metall.* **33**(12), 2191–98 (1985).

L. L. Horton, "Experimental Determination of the Critical Cavity Radius in Fe–10% Cr for Ion Irradiation," *Proceedings 42d Annual Meeting of the Electron Microscopy Society of America, Detroit, Michigan, August 13–17, 1984*, ed. G. W. Bailey, San Francisco Press, San Francisco, 1984.

L. L. Horton and J. Bentley, "Swelling Behavior of a Simple Ferritic Alloy," pp. 569–78 in *Proceedings of Topical Conference on Ferritic Alloys for Use in Nuclear Energy Technologies, Snowbird, Utah, June 19-23, 1983*, ed. J. W. Davis and D. J. Michel, The Metallurgical Society of AIME, Warrendale, Pa., 1984.

L. L. Horton and K. Farrell, "The Temperature Dependence of the Damage Microstructures in Neutron-Irradiated Vanadium," *J. Nucl. Mater.* **122&123**, 687–92 (1984).

L. L. Horton and L. K. Mansur, "Experimental Determination of the Critical Cavity Radius in Fe-10Cr for Ion Irradiation," pp. 344–62 in *Effects of Radiation on Materials*, ASTM STP 870, proceedings of the Twelfth International Symposium, Williamsburg, Va., June 18–20, 1984, ed. F. A. Garner and J. S. Perrin, American Society for Testing and Materials, Philadelphia, 1985.

G. E. Ice and C. J. Sparks, Jr., "Focusing Optics for a Synchrotron X-Radiation Microprobe," *Nucl. Instrum. Methods* **222**, 21–27 (1984).

G. E. Ice, C. J. Sparks, Jr., and A. Habenschuss, "X14A - ORNL's X-Ray Scattering Beamline," pp. 229–32 in *National Synchrotron Light Source Annual Report 1985, for the period October 1, 1984, through September 30, 1985*, BNL-51947, ed. W. Thomlinson and S. White-DePace, Brookhaven National Laboratory, Upton, New York, 1985.

D. D. Johnson, F. J. Pinski, and G. M. Stocks, "Fast Method for Calculating the Self-Consistent Electronic Structure of Random Alloys," *Phys. Rev. B* **30**(10), 5508–15 (November 1984).

D. D. Johnson, F. J. Pinski, and G. M. Stocks, "Self-Consistent Electronic Structure of Disordered $Fe_{0.65}Ni_{0.35}$," *J. Appl. Phys.* **57**(1), 3018–20 (1985).

E. A. Kenik, "Segregation to Boundaries in an Antimony-Containing Stainless Steel," pp. 252–53 in *Proceedings of the 43rd Annual Meeting of the Electron Microscopy Society of America, Louisville, Kentucky, August 5–9, 1985*, ed. G. W. Bailey, San Francisco Press, San Francisco, 1985.

E. A. Kenik, "Shared Research Equipment (SHaRE) Program," *Electron Micros. Soc. Bull.* **14**(1), 33–4 (1984).

E. A. Kenik and P. J. Maziasz, "Application of Extraction Replicas and Analytical Electron Microscopy to Precipitate Phase Studies," pp. 231–34 in *Analytical Electron Microscopy 1984*, proceedings of workshop held at Bethlehem, Pa., July 16–20, 1984, sponsored by Microbeam Analysis Society, ed. D. B. Williams and D. C. Joy, San Francisco Press, San Francisco, 1984.

H. R. Kerchner, D. K. Christen, A. DasGupta, and S. T. Sekula, "Flux-Line Pinning by the Grain Boundary in Niobium Bicrystals," pp. 463–64 in *Proceedings of the 17th International Conference on Low Temperature Physics, LT-17, Part II – Contributed Papers, Universität Karlsruhe and Kernforschungszentrum Karlsruhe, Federal Republic of Germany, August 15–22, 1984*, Elsevier Science Publishers, The Netherlands, 1984.

C. C. Koch, C. L. White, R. A. Padgett, and C. T. Liu, "Boron Segregation at Grain Boundaries in Rapidly Solidified Ni_3Al," *Scr. Metall.* **19**, 963–66 (1985).

D. M. Kroeger, C. C. Koch, C. G. McKamey, J. O. Scarbrough, and R. A. Padgett, "A Study of the Mechanism for Annealing Embrittlement of an Iron-Based Metallic Glass," pp. 1369–72 in *Rapidly Quenched Metals*, vol. II, proceedings of Fifth International Conference on Rapidly Quenched Metals held in Würzburg, Germany, Sept. 3–7, 1984, ed. S. Steeb and H. Warlimont, North-Holland, Amsterdam, 1985.

E. H. Lee and L. K. Mansur, "Evidence for a Mechanism of Swelling Variation with Composition in Irradiated Fe-Cr-Ni Alloys," *Phil. Mag. A*, Vol. 52, No.4, (1985) p. 493.

E. H. Lee, L. K. Mansur, and A. F. Rowcliffe, "The Effect of Phosphorous on the Swelling and Precipitation Behavior of Austenitic Stainless Steels During Irradiation," *J. Nucl. Mater.*, **122&123** 299–304 (1984).

T. Leventouri, O. B. Cavin, and J. S. Faulkner, "Preliminary Study of the Thermal-Expansion Coefficients of Long-Range-Ordered Aluminides," *Phys. Rev. B* **31**(11), 7436–39 (June 1, 1985).

M. B. Lewis, "Deuterium-Defect Trapping in Ion-Irradiated Zirconium," *J. Nucl. Mater.* **125**, 152–59 (1984).

M. B. Lewis, "Improved Extraction of Zirconium and Molybdenum Beams from a Penning Discharge Ion Source," *Nucl. Instrum. Methods Phys. Res.* **219**, 247–49 (1984).

M. B. Lewis, "Long-Range Recoil Extension of High Energy Heavy Ion Damage in Ceramics," *Nucl. Instrum. Methods. Phys. Res. B* **7**(8), 530–34 (1985).

M. B. Lewis and C. J. McHargue, "High Energy Ion Beam Mixing in Al_2O_3," pp. 771–76 in *Ion Implantation and Ion Beam Processing*, proceedings of symposium held in Boston in November 1983, ed. G. K. Hubler, O. W. Holland, C. R. Clayton, and C. W. White, North-Holland, New York, 1984 (*Materials Research Society Symposia Proceedings*, vol. 27).

M. B. Lewis and G. K. Schulze, "Chopped Ion Beams for Radiation Effects Simulation," *Nucl. Instrum. Methods* **B9**, 100–102 (1985).

C. T. Liu, "Design of Ordered Intermetallic Alloys for High-Temperature Structural Use," pp. 289–308 in *High Temperature Alloys: Theory and Design*, proceedings of conference sponsored by the Alloy Phases Committee of the Metallurgical Society of AIME and the Metals and Ceramics Division, Oak Ridge National Laboratory, held in Bethesda, Md., Apr. 9–11, 1984, ed. J. O. Stiegler, The Metallurgical Society of AIME, Warrendale, Pa., 1984.

C. T. Liu and J. O. Stiegler, "Ductile Ordered Intermetallic Alloys," *Sci.* **226**, 636–42 (1984).

C. T. Liu and J. O. Stiegler, "Ordered Intermetallic Alloys; High Temperature Structural Materials of the Future?," *Mater. Eng.* **100**(5), 29–33 (1984).

C. T. Liu, C. L. White, and J. A. Horton, "Effect of Boron on Grain-Boundaries in Ni_3Al," *Acta Metall.* **33**(2), 213–29 (1985).

C. T. Liu, C. L. White, and E. H. Lee, "Effect of Test Environment on Ductility and Fracture Behavior of Boron-Doped Ni_3Al at 600°C," *Scr. Metall.* **19**, 1247–50 (1985).

A. P. Maclin and G. M. Stocks, "Band-Structure Calculations of Aluminides," pp. 249–55 in *High-Temperature Alloys: Theory and Design*, proceedings of conference sponsored by the Alloy Phases Committee of the Metallurgical Society of AIME and the Metals and Ceramics Division, Oak Ridge National Laboratory, held in Bethesda, Md., Apr. 9–11, 1984, ed. J. O. Stiegler, The Metallurgical Society of AIME, Warrendale, Pa., 1984.

L. K. Mansur, A. D. Brailsford, and W. A. Coghlan, "A Cascade Diffusion Theory of Sink Capture Fluctuations During Irradiation of a Solid," *Acta Metall.* **33**(8), 1407–23 (1985).

L. K. Mansur, A. D. Brailsford, and W. A. Coghlan, *A Cascade Diffusion Theory of Sink Capture Fluctuations During Irradiation of a Solid*, ORNL-6123, January 1985.

L. Martinez and J. H. Schneibel, "Comments on 'A New Method for the Determination of the Precipitate-Matrix Interfacial Energy'," *Scr. Metall.* **19**, 1015–18 (1985).

C. J. McHargue, B. R. Appleton, and C. W. White, "Structure Property Relationships in Ion Implanted Ceramics," pp. 228–42 in *Surface Engineering, Surface Modification of Materials*, proceedings of NATO Advanced Study Institute on Surface Engineering meeting held in Les Arcs, France, on July 13–15, 1983, Series E, Applied Sciences, No. 85, ed. R. Kossowsky and S. C. Singhal, Advanced Study Institute on Surface Engineering, Martinus Nijhoff Publishers, Dordrecht, The Netherlands, 1984.

C. J. McHargue, G. C. Farlow, C. W. White, B. R. Appleton, P. Angelini, and H. Naramoto, "The Structure and Properties of Ion-Implanted Al_2O_3," *Nucl. Instrum. Methods Phys. Res.* **B10/11**, 569–73 (1985).

C. J. McHargue, G. C. Farlow, C. W. White, B. R. Appleton, J. M. Williams, P. S. Sklad, P. Angelini, and C. S. Yust, "Surface Property Modification of Ceramics by Ion Beams," pp. 1–11 in *Metals/Materials Technology Series*, First National Conference on the Applications of Ion Plating and Implantation to Materials held in Atlanta June 3–5, 1985, American Society for Metals, Metals Park, Ohio, 1985.

C. J. McHargue, G. C. Farlow, C. W. White, J. M. Williams, B. R. Appleton, and H. Naramoto, "The Amorphization of Ceramics by Ion Beams," *Mater. Sci. Eng.* **69**, 123–27 (1985).

C. J. McHargue, M. B. Lewis, J. M. Williams, and B. R. Appleton, "The Reactivity of Ion-Implanted SiC," *Mater. Sci. Eng.* **69**, 391–95 (1985).

C. J. McHargue, H. Naramoto, C. W. White, J. M. Williams, B. R. Appleton, P. S. Sklad, and P. Angelini, "Structure of Ceramic Surfaces Modified by Ion Beam Techniques," pp. 519–31 in *Emergent Process Methods for High-Technology Ceramics*, proceedings of 19th University Conference on Ceramic Science held in Raleigh, N.C., on Nov. 8–10, 1982, ed. R. F. Davis, H. Palmour III, and R. L. Porter, Materials Science Research, vol. 17, Plenum Press, New York, 1984.

C. J. McHargue and Sigfred Peterson, *Metals and Ceramics Division Materials Science Program Annual Progress Report for Period Ending June 30, 1984*, ORNL/TM-9357, November 1984.

C. J. McHargue, C. W. White, B. R. Appleton, G. C. Farlow, and J. M. Williams, "Ion Beam Modification of Ceramics," pp. 385–93 in *Defect Properties and Processing of High-Technology Nonmetallic Materials*, proceedings of symposium held in Boston on Nov. 14–18, 1983, ed. J. H. Crawford, Jr., Y. Chen, and W. A. Sibley, Elsevier, New York, 1984 (*Materials Research Society Symposia Proceedings*, vol. 24).

M. K. Miller, "Imaging Atom Probe Computer Experiments," *J. Phys.* C9(12), 337–42 (December 1984).

M. K. Miller, J. Bentley, S. S. Brenner, and J. A. Spitznagel, "Long Term Thermal Aging of Type CF 8 Stainless Steel," *J. Phys.* C9(12), 385–90 (December 1984).

M. K. Miller, J. Bentley, S. S. Brenner, and J. A. Spitznagel, "Thermal Aging of Primary Coolant Pipe Steel," pp. 326–27 in *Proceedings of the 43rd Annual Meeting of the Electron Microscopy Society of America, Louisville, Kentucky, August 5–9, 1985*, ed. G. W. Bailey, San Francisco Press, San Francisco, 1985.

M. K. Miller, S. S. Brenner, M. G. Burke, and W. A. Soffa, "Atom Probe Field-Ion Microscopy Studies of Triaxially Modulated Microstructures in Fe-Be Alloys," *Scr. Metall.* **18**, 111–16 (1984).

M. K. Miller, S. S. Brenner, P. P. Camus, and W. A. Soffa, "The Atom Probe - A Direct Technique for Kinetic Measurements," pp. 63-66 in *Proceedings of International Topical Conference on Kinetics of Aggregation and Gelation, Athens, Georgia, Apr. 2-4, 1984*, ed. F. Family and D. P. Landau, North-Holland Publishers, New York, 1984.

M. K. Miller, M. G. Burke, and S. S. Brenner, "Measurement of Characteristic Wavelengths in Modulated Microstructures by Field-Ion Microscopy," *J. Micros.* **139**(Pt. 1), 41-47 (July 1985).

M. K. Miller, M. G. Burke, and S. S. Brenner, "Morphological Interpretation of Modulated Microstructures," *J. Phys.* C9(12), 239-44 (December 1984).

M. K. Miller, M. G. Burke, S. S. Brenner, and W. A. Soffa, "A TEM/FIM Study of Modulated Microstructures in the Fe-Be System," pp. 182-84 in *Analytical Electron Microscopy 1984*, proceedings of workshop held at Bethlehem, Pa., July 16-20, 1984, sponsored by the Microbeam Analysis Society, ed. D. B. Williams and D. C. Joy, San Francisco Press, San Francisco, 1984.

M. K. Miller, M. G. Burke, S. S. Brenner, W. A. Soffa, K. B. Alexander, and D. E. Laughlin, "Identification of B32 Metastable Precipitate in the Fe-Be System," *Scr. Metall.* **18**, 285-90 (1984).

K. Miyahara, N. H. Packan, and N. Igata, "The Effect of Pulsed Irradiation on Void Swelling of a Pure Austenitic Alloy," *J. Nucl. Mater.* **122&123**, 624-28 (1984).

J. P. Moore, "Analysis of Apparatus with Radial Symmetry for Steady-State Measurements of Thermal Conductivity," pp. 61-123 in *Compendium of Thermophysical Property Measurement Methods*, vol. 1, ed. K. D. Maglic, Plenum Press, New York, 1984.

J. P. Moore, F. J. Weaver, R. S. Graves, and D. L. McElroy, "The Thermal Conductivities of $SrCl_2$ and SrF_2 from 85 to 400 K," pp. 115-124 in *Thermal Conductivity 18*, proceedings of the 18th International Conference on Thermal Conductivity held in Rapid City, S.Dak., Oct. 3-5, 1983, ed. T. Ashworth and D. R. Smith, Plenum Press, New York, 1985.

J. P. Moore, F. J. Weaver, R. S. Graves, and D. L. McElroy, "The Thermal Conductivity and Expansion Enhancement Associated with Formation of the Superionic State in $SrCl_2$," pp. 105-114 in *Thermal Conductivity 18*, proceedings of the 18th International Conference on Thermal Conductivity held in Rapid City, S.Dak., Oct. 3-5, 1983, ed. T. Ashworth and D. R. Smith, Plenum Press, New York, 1985.

J. Narayan, D. Fathy, O. W. Holland, B. R. Appleton, R. F. Davis, and P. F. Becher, "Ion-Beam and Laser Mixing of Nickel Overlayers on Silicon Carbide," *J. Appl. Phys.* **56**(6), 1577-82 (September 1984).

D. Nicholson and A. Chowdhary, "Electronic Structure of Liquid Metal Alloys," pp. 257–64 in *High-Temperature Alloys: Theory and Design*, proceedings of conference sponsored by the Alloy Phases Committee of the Metallurgical Society of AIME and the Metals and Ceramics Division, Oak Ridge National Laboratory, held in Bethesda, Md., Apr. 9–11, 1984, ed. J. O. Stiegler, The Metallurgical Society of AIME, Warrendale, Pa., 1984.

N. H. Packan, "Temperature Aspects of Pulsed Ion Bombardment in an Austenitic Alloy," *J. Nucl. Mater.* **122&123**, 644–49 (1984).

F. Parente and G. E. Ice, "Predictions of Scattering from an Absorbing Gas Target," *Nucl. Instrum. Methods Phys. Res.* **B**(9) 89–96 (1985).

F. J. Pinski and G. M. Stocks, "Fast Method for Calculating the Self-Consistent Electronic Structure of Random Alloys. II. Optimal Use of the Complex Plane," *Phys. Rev. B.* **32**(6), 4204–07 (September 1985).

K. F. Russell and L. L. Horton, "Specimen Preparation of Near Surface Ion Irradiated Samples," pp. 170–71 in *Proceedings of the 43rd Annual Meeting of the Electron Microscopy Society of America, Louisville, Kentucky, August 5–9, 1985*, ed. G. W. Bailey, San Francisco Press, San Francisco, 1985.

J. H. Schneibel and G. F. Petersen, "Grain Boundary Sliding in Nickel Wires Having a Bamboo Structure," *Acta. Metall.* **33**(3), 437–42 (1985).

J. H. Schneibel, C. L. White, G. F. Petersen, and R. A. Padgett, "Creep Fracture in Austenitic Stainless Steels Containing Antimony or Titanium," pp. 1–9 in *Metals/Materials Technology Series*, proceedings of 1984 ASM International Conference on New Developments in Stainless Steel Technology (in conjunction with ASM Metals Congress) held in Detroit on Sept. 17–20, 1984, American Society for Metals, Metals Park, Ohio, 1984.

J. H. Schneibel, C. L. White, and M. H. Yoo, "On the Improvement of Creep Strength and Ductility of Ni–20% Cr by Small Zirconium Additions," *Metall. Trans. A* **16A**, 651–60 (April 1985).

E. M. Schulson, T. P. Weihs, I. Baker, H. J. Frost, and J. A. Horton, "Boron-Induced Grain Boundary Accommodation of Slip in Ni_3Al," *Scr. Metall.* **19**, 1497–98 (1985).

E. P. Simonen, N. M. Ghoniem, and N. H. Packan, "Pulsed Flux Effects on Radiation Damage," *J. Nucl. Mater.* **122&123**, 391–401 (1984).

P. S. Sklad, "Analytical Electron Microscopy of Surface-Modified Ceramics," pp. 276–79 in *Proceedings of the 43rd Annual Meeting of the Electron Microscopy Society of America, Louisville, Kentucky, August 5–9, 1985*, ed. G. W. Bailey, San Francisco Press, San Francisco, 1985.

P. S. Sklad, P. Angelini, M. B. Lewis, and C. J. McHargue, "Microstructural Development of TiB_2 Ion Implanted with 1 MEV Nickel," pp. 407-12 in *Defect Properties and Processing of High-Technology Nonmetallic Materials*, proceedings of symposium held in Boston on Nov. 14-18, 1983, ed. J. H. Crawford, Jr., Y. Chen, and W. A. Sibley, Elsevier, New York, 1984 (*Materials Research Society Symposia Proceedings*, vol. 24).

P. S. Sklad, J. Bentley, P. Angelini, and G. L. Lehman, "Reliability of the Quantification of EELS Measurements," pp. 285-88 in *Analytical Electron Microscopy 1984*, proceedings of workshop held in Bethlehem, Pa., July 16-20, 1984, sponsored by Microbeam Analysis Society, ed. D. B. Williams and D. C. Joy, San Francisco Press, San Francisco, 1984.

P. S. Sklad, P. Angelini, C. J. McHargue, and J. M. Williams, "Analytical Electron Microscopy of SiC Implanted with Cr Ions," pp. 416-17 in *Proceedings 42d Annual Meeting of the Electron Microscopy Society of America, Detroit, Michigan, August 13-17, 1984*, ed. G. W. Bailey, San Francisco Press, San Francisco, 1984.

P. S. Sklad and H. Schroeder, "The Effect of Implanted Helium on the Microstructure and Creep Properties of Ordered $(Fe_{0.49}Ni_{0.51})_3V$ Alloys," *J. Nucl. Mater.* **122&123**, 709-14 (1984).

C. J. Sparks, Jr., "X-Ray Microprobe Characterization of Materials: The Case for Undulators on Advanced Storage Rings," pp. 91-125 in *Major Facilities for Materials Research and Related Disciplines*, presentations to the Major Materials Facilities Committee, Commission on Physical Sciences, Mathematics, and Resources, National Research Council, on March 17, 1984, Washington, D.C., National Academy Press, Washington, D.C., 1984.

J. A. Spitznagel, B. O. Hall, N. J. Doyle, R. Jayram, R. W. Wallace, J. R. Townsend, and M. Miller, "Effects of Nitrogen and Helium Ion Implantation on Uniaxial Tensile Properties of 316 SS Foils," pp. 597-601 *Ion Implantation and Ion Beam Processing of Materials*, proceedings of symposium held in Boston Nov. 14-17, 1983, ed. G. K. Hubler, O. W. Holland, C. R. Clayton, and C. W. White, North Holland, New York, 1984 (*Materials Research Society Symposia Proceedings*, vol. 27).

J. Staunton, B. L. Gyorffy, A. J. Pindor, G. M. Stocks, and H. Winter, "Electronic Structure of Metallic Ferromagnets Above the Curie Temperature," *J. Phys. F: Met. Phys.* **15**, 1387-1404 (1985).

J. Staunton, B. L. Gyorffy, A. J. Pindor, G. M. Stocks, and H. Winter, "The 'Disordered Local Moment' Picture of Itinerant Magnetism at Finite Temperatures," *J. Magn. Magn. Mater.* **45**, 15-22 (1984).

G. M. Stocks, J. Wadsworth, and B. L. Gyorffy, "First Principles Theory of Fermi-Surface Driven Concentration Waves in Cu_cPd_{1-c} Alloys," pp. 15-17 in *Alloy Phase Diagrams*, proceedings of Symposium O, 1984 Fall Meeting of the Materials Research Society held in Boston on Nov. 29-30, 1984, Materials Research Society, Pittsburgh, 1984.

G. M. Stocks and H. Winter, "A First Principles Approach to the Band Theory of Random Metallic Alloys," pp. 463–579 in *The Electronic Structure of Complex Systems*, proceedings of a NATO Advanced Study Institute on Electronic Structure of Complex Systems held at the State Univeristy of Ghent, Belgium, on July 12–23, 1982, ed. P. Phariseau and W. M. Temmerman, Plenum Press, New York, 1984.

R. E. Stoller and G. R. Odette, "Analytical Solutions for Helium Bubble and Critical Radius Parameters Using a Hard Sphere Equation of State," *J. Nucl. Mater.* **131** 118–25 (1985).

M. Strauss, T. Ring, A. Bleier, and H. K. Bowen, "Coagulation in Processing of Ceramic Suspensions: Powder Size Distribution Effects," *J. Appl. Phys.* **58**(10), 3871–79 (November 1985).

Z. Szotek, B. L. Gyorffy, G. M. Stocks, and W. M. Temmerman, "Electron and Electron-Positron Momentum Distributions in Concentrated Random Alloys," *J. Phys. F* **14**, 2571–99 (1984).

H. Trinkaus and W. G. Wolfer, "Conditions for Dislocation Loop Punching by Helium Bubbles," *J. Nucl. Mater.* **122&123**, 552–57 (1984).

H. Trinkaus and M. H. Yoo, "On Cavity Nucleation Under Time-Dependent Stress Concentration and Solute Segregation," *Scr. Metall.* **18**, 1165–69 (1984).

C. H. Vasel, A. D. Krawitz, E. F. Drake, and E. A. Kenik, "Binder Deformation in WC–(Co,Ni) Cemented Carbide Composites," *Metall. Trans. A* **16A**, 2309–17 (December 1985).

J. M. Vitek, "Round Robin EDS Evaluation of Fully Austenitic Stainless Steel," pp. 409–10 in *Instrumentation Physics and Materials Science Applications I, Electron Microscopy 1984*, ed. A. Csanády, P. Röhlich and D. Szabó, vol. 1 of proceedings of the Eighth European Congress on Electron Microscopy held in Budapest, Hungary, August 13–18, 1984, Programme Committee of the Eighth European Congress on Electon Microscopy, Budapest, 1984.

J. M. Vitek, "An EDS Round-Robin Evaluation of Type 308 Austenitic Stainless Steel," pp. 374–76 in *Analytical Electron Microscopy 1984*, proceedings of workshop held at Bethlehem, Pa., July 16–20, 1984, sponsored by the Microbeam Analysis Society, ed. D. B. Williams and D. C. Joy, San Francisco Press, San Francisco, 1984.

J. M. Vitek and S. A. David, "The Concept of an Effective Quench Temperature and Its Use in Studying Elevated-Temperature Microstructures," *Metall. Trans. A* **16A**, 1521–24 (August 1985).

J. M. Vitek and S. A. David, "Metastable Equilibrium of Ferrite in Type 308 Stainless Steel," *Scr. Metall.* **19**(1), 23–26 (1985).

J. M. Vitek and S. A. David, "The Solidification and Aging Behavior of Types 308 and 308CRE Stainless Steel Welds," *Weld J. (Miami)* **63**(8), 246–53–s (August 1984).

J. M. Vitek, S. A. David, W. H. Smith, and R. W. Reed, *Solidification and Aging Behavior of Types 308 and 308CRE Stainless Steel Welds*, ORNL/TM-9086, August 1984.

J. Wadsworth, B. L. Gyorffy, and G. M. Stocks, "First Principles Calculations of Short-Range Order Diffuse Scattering: Fermi-Surface Driven Concentration Waves in Cu_cPd_{1-c} Alloys," pp. 183-98 in *High-Temperature Alloys: Theory and Design*, proceedings of conference sponsored by Alloy Phases Committee of the Metallurgical Society of AIME and the Metals and Ceramics Division, Oak Ridge National Laboratory, held in Bethesda, Md., Apr. 9-11, 1984, ed. J. O. Stiegler, The Metallurgical Society of AIME, Warrendale, Pa., 1984.

C. A. Walls and R. J. Lauf, "A Protection Tube for Spare SEM Column Liners," *Bull. Electron Microsc. Soc. Am.* **15**(1), 117-18 (1985).

C. L. White, "Study of Solute Segregation at Interfaces Using Auger Electron Spectroscopy," *Ceram. Bull.* **64**(12), 1571-80 (1985).

C. L. White, R. Dimas, and W. Losch, "High-Temperature Specimen Holder for Use with the PHI Model 2100 Specimen Introduction/Reaction Chamber," *Rev. Sci. Instrum.* **55**(7), 1171-72 (July 1984).

C. L. White and W. Losch, "Concerning the Mass Mechanisms for Sulfur and Antimony Segregation to External Free Surfaces in Ni-1 wt % Sb," *Scr. Metall.* **19**, 665-68 (1985).

C. L. White, R. A. Padgett, and C. T. Liu, "Surface and Grain Boundary Segregation in Relation to Intergranular Fracture: Boron and Sulfur in Ni_3Al," *Scr. Metall.* **18**, 1417-20 (1984).

C. W. White, G. C. Farlow, C. J. McHargue, P. S. Sklad, P. Angelini, and B. R. Appleton, "Formation of Amorphous Layers in Al_2O_3 by Ion Implantation," *Nucl. Instrum. Methods Phys. Res. B* **7**(8), 473-78 (1985).

C. W. White, G. C. Farlow, H. Naramoto, C. J. McHargue, and B. R. Appleton, "Modification of the Near-Surface Region of Al_2O_3 by Ion Implantation," pp. 163-72 in *Defect Properties and Processing of High-Technology Nonmetallic Materials*, proceedings of symposium held in Boston on Nov. 14-18, 1983, ed. J. H. Crawford, Jr., Y. Chen, and W. A. Sibley, Elsevier, New York, 1984 (*Materials Research Society Symposia Proceedings*, vol. 24).

R. K. Williams, P. F. Becher, and C. B. Finch, "Study of the Kondo Effect and Intrinsic Electrical Conduction in Titanium Diboride," *J. Appl. Phys.* **56**(8), 2295-2302 (October 1984).

R. K. Williams, R. S. Graves, and D. L. McElroy, "Thermal Conductivity of Cr_2O_3 in the Vicinity of the Neel Transition," *J. Am. Ceram. Soc.* **67**(7), C-151-52 (July 1984).

R. K. Williams, R. S. Graves, F. J. Weaver, and D. L. McElroy, "Physical Properties of Ni_3Al Containing 24 and 25 Atomic Percent Aluminum," pp. 505–12 in *High-Temperature Ordered Intermetallic Alloys*, proceedings of symposium held in Boston Nov. 26–28, 1984, ed. C. C. Koch, C. T. Liu, and N. S. Stoloff, Materials Research Society, Pittsburgh, 1985 (*Materials Research Society Symposia Proceedings*, vol. 39).

R. K. Williams, R. S. Graves, and F. J. Weaver, "Transport Properties of High Purity, Polycrystalline Titanium Diboride," *J. Appl. Phys.* **59**(5), 1552–56 (March 1986).

R. K. Williams, F. J. Weaver, and R. S. Graves, "Transport Properties of Polycrystalline Ni_3Al," pp. 165–74 in *Thermal Conductivity 18*, proceedings of the 18th International Conference on Thermal Conductivity held in Rapid City, S.Dak., Oct. 3–5, 1983, ed. T. Ashworth and D. R. Smith, Plenum Press, New York, 1985.

R. O. Williams, "Orthogonal Coordinates for Systems of Many Components," *Metall. Trans. A* **16A**, 929–33 (May 1985).

H. Winter, P. J. Durham, W. M. Temmerman, and G. M. Stocks, "Electronic Density of States and the X-Ray Photoelectron Spectra of the Valence Band of Cu-Pd Alloys," *Phys. Rev. B* **33**(4), 2370–79 (Feb. 15, 1986).

H. L. Yakel, "Optimizing Estimates of Long-Range-Order Parameters with Anomalous Bragg X-Ray Scattering Data," p. 49 in *11th Annual User's Group Meeting, Stanford Synchrotron Radiation Laboratory*, held in Stanford, California, on Oct. 25-26, 1984, SSRL Report No. 84/06, Stanford University, 1984.

H. L. Yakel, "Crystal Structures of Stable and Metastable Iron-Containing Carbides," *Int. Met. Rev.* **30**(1), 17–40 (1985).

M. H. Yoo, J. C. Ogle, J. H. Schneibel, and R. W. Swindeman, "SANS and TEM Studies of Carbide Precipitation and Creep Damage in Type 304 Stainless Steel," pp. 595–600 in *Microstructural Characterization of Materials by Non-Microscopical Techniques*, proceedings of 5th Riso International Symposium on Metallurgy and Materials Science held in Roskilde, Denmark, on Sept. 3–7, 1984, ed. N. Hessel Anderson, M. Eldrup, N. Hansen, D. Juul Jensen, T. Leffers, H. Lilholt, O. B. Pedersen, and B. N. Singh, Riso National Laboratory, Roskilde, Denmark, 1984.

M. H. Yoo, C. L. White, and H. Trinkaus, *Interfacial Segregation and Fracture*, ORNL/TM-9016, March 1985.

C. S. Yust, "Tribology and Wear," *Int. Met. Rev.* **30**(3), 141–54 (1985).

Appendix D

PENDING PUBLICATIONS

P. B. Allen, T. P. Beaulac, F. A. Khan, W. H. Butler, F. J. Pinski, and J. C. Swihart, "Calculations of Resistivity and Superconducting T_c in Metals," Materials Research Society Symposium, Dec. 2–7, 1985, to be published in proceedings.

A. Al-Lehaibi, J. C. Swihart, W. H. Butler, and F. J. Pinski, "Electron-Phonon Interaction Effects in Tantalum," to be submitted to *Phys. Rev.*

P. Angelini and J. Bentley, "Thermal Expansion Coefficient Determination by CBED," 4th Workshop on Analytical Electron Microscopy, Lehigh University, Bethlehem, Pa., July 16–20, 1984, to be published in proceedings.

P. Angelini and W. Mader, "Strain Contrast in SiC Whisker Reinforced Al_2O_3," 44th Annual Meeting of the Electron Microscopy Society of America, Albuquerque, N.Mex., Aug. 10–15, 1986, to be published in proceedings.

F. W. Averill and G. S. Painter, "Orbital Forces and Chemical Bonding in Density Functional Theory: Application to First Row Dimers," submitted to *Phys. Rev. B.*

S. Baik, "Segregation of Mg to the (0001) Surface of Single-Crystal Alumina; Quantification of AES Results," submitted to *J. Am. Ceram. Soc.*

S. Baik, A. Bleier, and P. F. Becher, "Preparation of Al_2O_3-ZrO_2 Composites by Adjustment of Surface Chemical Behavior," Materials Research Society 1986 Spring Meeting, Palo Alto, Calif., Apr. 14–18, 1986, to be published in proceedings.

I. Baker, J. A. Horton, and E. M. Schulson, "TEM of Rapidly Solidified Powders of Ni_3Al," submitted to *Metallography*.

I. Baker, E. M. Schulson, and J. A. Horton, "Observation of Slip Propagation Across Grain Boundaries in Ni_3Al," 44th Annual Meeting of the Electron Microscopy Society of America, Albuquerque, N.Mex., Aug. 10–15, 1986, to be published in proceedings.

P. F. Becher, "Toughening Behavior in Ceramics Associated with the Transformation of Tetragonal ZrO_2," submitted to *J. Mater. Sci.*

P. F. Becher, C. B. Finch, and M. K. Ferber, "Effect of Residual Nickel Content on the Grain Size Dependent Mechanical Properties of TiB_2," submitted to *Commun. Am. Ceram. Soc.*

P. F. Becher and M. V. Swain, "Relation of Transformation Temperature to the Fracture Toughness of Transformation Toughened Ceramics," submitted to *J. Mater. Sci.*

P. F. Becher and T. N. Tiegs, "Toughening Behavior Involving Multiple Mechanisms: Whisker Reinforcement and Transformation Toughening," submitted to *J. Mater. Sci.*

J. Bentley, "A Review of the Application of Analytical Electron Microscopy to Ion-Implanted Materials," submitted to *Nucl. Instrum. Methods B.*

J. Bentley, "Site Occupations in $L1_2$ Ordered Alloys by Axial Electron Channeling Microanalysis," 44th Annual Meeting of the Electron Microscopy Society of America, Albuquerque, N.Mex., Aug. 10–15, 1986, to be published in proceedings.

J. Bentley, "Axial Electron Channeling Microanalysis of $L1_2$ Ordered Alloys," 11th International Congress on Electron Microscopy, Kyoto, Japan, Aug. 31–Sept. 7, 1986, to be published in proceedings.

J. Bentley and P. Angelini, "Microanalysis by Electron Energy Loss Spectroscopy at 300kV," 11th International Congress on Electron Microscopy, Kyoto, Japan, Aug. 31– Sept. 7, 1986, to be published in proceedings.

A. D. Brailsford and L. K. Mansur, "Response Function Analysis of Time-Dependent Diffusional Defect Processes," submitted to *Acta Metall.*

B. C. Cai, Y. T. Chou, and A. DasGupta, "Flux Pinning by Symmetrical Grain Boundaries in Niobium Bicrystals," submitted to *Philos. Mag. B.*

B. C. Cai, Y. T. Chou, and A. DasGupta, "Flux Pinning by a Special Grain Boundary in a Niobium Bicrystal," submitted to *Philos. Mag. B.*

P. P. Camus, W. A. Soffa, S. S. Brenner, and M. K. Miller, "Quantification of Interconnected Microstructures by FIM," submitted to *J. Phys.*

A. Choudhury, C. R. Brooks, and C. L. White, "The Effect of Thermal History on the Level of Intergranular Boron Segregation and Fracture Morphology of Substoichiometric Ni_3Al," submitted to *Scr. Metall.*

A. Chowdhary, D. M. Nicholson, and L. M. Schwartz, "Electronic Structure Calculations in Liquid and Amorphous Metals," submitted to *J. Non-Cryst. Solids.*

A. DasGupta, L. C. Smedskjaer, D. G. Legnini, and R. W. Siegel, "Positron Annihilation Study of Boron-Doped Ni_3Al," submitted to *Mater. Lett.*

S. A. David, D. N. Braski, and C. T. Liu, "Structure and Properties of Welded Long-Range-Ordered Alloys," submitted to *Weld. J.*

S. A. David and V. P. Kujanapää, "Correlation Between Solidification Parameters and Weld Microstructure," Metallurgical Society of AIME Symposium on Metallurgy of Joining of Materials, New York, Feb. 24–28, 1985, to be published in proceedings.

S. A. David and J. M. Vitek, "Microstructural Modifications during Laser and Electron Beam Welding," International Conference on Power Beam Technology, Brighton, UK, Sept. 10–12, 1986, to be published in proceedings.

A. G. Dhere, R. J. De Angelis, P. J. Reucroft, and J. Bentley, "Twinned Colloidal Gold Particles," Seminar, High Resolution Electron Microscopy Meeting, Arizona State University, Tempe, Jan. 7–11, 1985, to be published in proceedings.

A. G. Dhere, R. J. De Angelis, P. J. Reucroft, J. Bentley, G. E. Ice, and A. Habenschuss, "Morphological Developments of Nickel Particles in Supported Metal Catalysts," Materials Research Society Annual Meeting, Boston, Dec. 2–7, 1985, to be published in proceedings.

N. D. Evans, R. J. Bayuzick, and E. A. Kenik, "Metastable Phases Formed in Rapidly Solidified Nb-Ge Alloys," 44th Annual Meeting of the Electron Microscopy Society of America, Albuquerque, N.Mex., Aug. 10–15, 1986, to be published in proceedings.

G. C. Farlow, C. W. White, C. J. McHargue, and B. R. Appleton, "Annealing of Implanted Al_2O_3 in a Reducing Environment," Seminar, 1984 Conference on Ion Beam Modification of Materials, Cornell University, Ithaca, N.Y., July 16–20, 1984, to be published in proceedings.

K. Farrell, N. Kishimoto, R. E. Clausing, L. Heatherly, and G. L. Lehman, "Complementary AES and AEM of Grain Boundary Regions in Irradiated q,-Strengthened Alloys," 2nd International Conference on Fusion Reactor Materials, Chicago, Apr. 13–17, 1986, to be published in proceedings.

K. Farrell and E. H. Lee, "Ion Damage Microstructures in a Fe-10Cr-6Mo-0.5Nb," 13th International Symposium on Effects of Radiation on Materials, Seattle, Wash., June 23–25, 1986, to be published in proceedings.

J. S. Faulkner, "Electronic States in Disordered Solids. III Applications to Materials Sciences," Part II of 1985 Sanibel Symposia on Quantum Chemistry and Solid-State Theory, St. Augustine, Fla., Mar. 18–23, 1985, to be published in proceedings.

A. T. Fisher and J. Bentley, "Localized Ion Milling of Metallic and Ceramic TEM Specimens," 44th Annual Meeting of the Electron Microscopy Society of America, Albuquerque, N.Mex., Aug. 10–15, 1986, to be published in proceedings.

L. A. Harris, E. A. Kenik, and C. S. Yust, "In Situ Heating of Coal in a Transmission Electron Microscope," submitted to *Fuel*.

W. C. Hasz and A. Bleier, "Surface Reactivity of Silica and Alumina Ceramic Powders," to be submitted to *Advances in Materials Characterization II (Plenum Press).*

M. R. Hayns and L. K. Mansur, "Cascade-induced Fluctuations and the Transition from the Stable to the Critical Cavity Radius for Swelling," Fall TMS-AIME Meeting, Toronto, Canada, Oct. 13–17, 1985, to be published in proceedings.

J. A. Horton and M. K. Miller, "Atom Probe Analysis of Grain Boundaries in Rapidly-Solidified Ni_3Al," submitted to Acta Metall.

J. A. Horton and M. K. Miller, "APFIM Study of Antiphase and Grain Boundaries in Ni_3Al," Microbeam Analysis Society Meeting, Albuquerque, N.Mex., Aug. 10–15, 1986, to be published in proceedings.

J. A. Horton and M. K. Miller, "A TEM–APFIM Investigation of Boron-Doped Ni_3Al," 32nd International Field Emission Symposium, Wheeling, W. Va., July 15–19, 1985, to be published in proceedings.

L. L. Horton and J. Bentley, "Dislocation Evolution in Fe–10% Cr," 13th Symposium on Effects of Radiation on Materials, Seattle, Wash., June 23–26, 1986, to be published in proceedings.

L. L. Horton, J. Bentley, and M. B. Lewis, "Radiation Damage in Ion-Irradiated MgO," Fall TMS-AIME Meeting, Toronto, Canada, Oct. 13–17, 1985, to be published in proceedings.

L. L. Horton, M. K. Miller, and S. Spooner, "Characterization of Spinodally-Decomposed Fe–30.1% Cr–9.9% Co: Part I," 44th Annual Electron Microscopy Society of America Meeting, Albuquerque, N.Mex., Aug. 10 –15, 1986, to be published in proceedings.

D. D. Johnson, D. M. Nicholson, F. J. Pinski, B. L. Gyorffy, and G. M. Stocks, "Density Functional Theory for Random Alloys: Total Energy Within the Coherent Potential Approximation," submitted to *Phys. Rev. Lett.*

E. A. Kenik, "High Voltage Electron Microscope in Situ Studies of Strain Localization in Al-Li Alloys," to be submitted to The Metallurgical Society of AIME.

E. A. Kenik, R. B. Bayuzick, M. S. Kim, and C. C. Koch, "Microstructural Evolution on Mechanically Alloyed Nb-25 at. % Ce," 44th Annual Meeting of the Electron Microscopy Society of America, Albuquerque, N.Mex., Aug. 10-15, 1986, to be published in proceedings.

W. Kesternich, N. H. Packan, and H. Schroeder, "Radiation-Induced Segregation to Grain Boundaries in a Ni-Si Alloy," ICEM 11th International Congress on Electron Microscopy, Kyoto, Japan, Aug. 31-Sept. 7, 1986, to be published in proceedings.

J. F. King, S. A. David, J. E. Sims, and A. Nasreldin, "Electron Beam Welding of Heavy-Section 3Cr-1.5Mo Alloy," 67th Annual American Welding Society Meeting, Atlanta, Apr. 13-18, 1986, to be published in proceedings.

C. C. Koch, J. A. Horton, C. T. Liu, O. B. Cavin, and J. O. Scarbrough, "Rapid Solidification Studies of Ni_3Al Alloys," 3rd International Conference on Rapid Solidification Processing at Gaithersburg, Md., Dec. 6-8, 1982, to be published in proceedings.

V. P. Kujanapää, S. A. David, and C. L. White, "Formation of Hot Cracks in Austenitic Stainless Steel Welds - Part I: Solidification Cracking," submitted to *Weld. J.*

P. Lamparter, A. Habenschuss, and A. H. Narten, "Neutron and X-Ray Diffraction Study of the $Ti_{84}Si_{16}$ Metallic Glass," submitted to *J. Non-Cryst. Solids.*

W. E. Lawrence, W. Chen, and J. C. Swihart, "Suggested Mechanism for Temperature of Orbitally Averaged Fermi Surface Scattering Rates in Cd," submitted to *J. Phys. F.*

E. H. Lee and L. K. Mansur, "Evidence for a Mechanism of Swelling Variation with Composition in Irradiated Fe-Cr-Ni Alloys," submitted to *Philos. Mag.*

E. H. Lee, N. H. Packan, M. B. Lewis, and L. K. Mansur, "Effects of Rapidly Pulsed Ion Bombardment on Microstructure and Phase Stability in Ti-Modified Stainless Steel," Fall TMS-AIME Meeting, Toronto, Canada, Oct. 13-17, 1985, to be published in proceedings.

M. B. Lewis and K. Farrell, "Migration Behavior of Helium Under Displacive Irradiation in Stainless Steel," submitted to *Nucl. Instrum. Methods.*

F. A. List and R. A. McKee, "Measurements of Mechanical Properties of Thin Films and Interfaces by the Dynamic Resonance Method," submitted to *Rev. Sci. Instrum.*

F. A. List and R. A. McKee, "Mechanical Properties of Metallic Films on Sapphire," to be published in Materials Research Society conference proceedings.

C. T. Liu and J. O. Stiegler, "Ordered Intermetallic Alloys," submittted to 1987 *Yearb. Sci. Technol.*

C. T. Liu and C. L. White, "Design of Ductile Polycrystalline Ni_3Al Alloys," Boston Materials Research Society Meeting, Boston, Nov. 26–30, 1984, to be published in proceedings.

C. T. Liu and C. L. White, "Dynamic Embrittlement of B-Doped Ni_3Al Alloys at 600°C," submitted to *Acta Metall.*

L. M. Mansur, "Mechanisms and Kinetics of Radiation Effects in Metals and Alloys," submitted to *Kinetics of Nonhomogeneous Processes.*

L. K. Mansur, A. F. Rowcliffe, M. L. Grossbeck, and R. E. Stoller, "On Isotopic Alloying to Tailor Transmutation Rates in Mixed Spectrum Reactors," submitted to *J. Nucl. Mater.* and *DAFS Quarterly Report.*

C. J. McHargue, "Ion Implantation in Metals and Ceramics," submitted to *Int. Met. Rev.*

C. J. McHargue, "The Mechanical and Tribological Properties of Ion Implanted Ceramics," submitted to *Ion Beam Modification in Insulators.*

C. J. McHargue, "Effect of Ion Implantation on Subsequent Erosion and Wear Behavior of Solids," NATO Advanced Study Institute on Erosion and Growth of Solids Stimulated by Atom and Ion Beams, Heraklion, Crete, Greece, Sept. 16–27, 1985, to be published in proceedings.

C. J. McHargue, C. S. Yust, P. Angelini, P. S. Sklad, and M. B. Lewis, "The Surface Mechanical Properties and Wear Behavior of Ion Implanted TiB_2," 2nd International Conference on Science of Hard Materials, Rhodes, Greece, Sept. 22– 28, 1984, to be published in proceedings.

C. J. McHargue, G. C. Farlow, G. M. Begun, J. M. Williams, C. W. White, B. R. Appleton, P. S. Sklad, and P. Angelini, "Damage Accumulation in Ceramics During Ion Implantation," Irradiation Effects Associated with Ion Implantation Session at TMS-AIME Meeting, Toronto, Canada, Oct. 12–17, 1985, to be published in proceedings.

C. G. McKamey, D. M. Kroeger, and D. S. Easton, "Evidence for the Formation of a Metastable Crystalline Phase During Crystallization of Zr-Ni Metallic Glasses of Approximately 57-63.2 at % Zr," Materials Research Society Fall Meeting, Boston, Dec. 2- 4, 1985, to be published in proceedings.

C. G. McKamey, D. M. Kroeger, D. S. Easton, and J. O. Scarbrough, "Crystallization of Zr-Ni Metallic Glasses," submitted to *J. Mater. Sci.*

C. G. McKamey, D. M. Kroeger, D. S. Easton, and J. O. Scarbrough, "Thermal Evidence of the Formation of a New Metastable Crystalline Phase from the Zr-Ni Metallic Glass System," submitted to *J. Non-Cryst. Solids.*

R. A. McKee, "Reply to Comment on: Analysis of the Stoichiometry and Temperature Dependence of Cation Diffusion in Wustite, $Fe_{1-\delta}O$," submitted to *Phys. Rev. B.*

G. M. Michal, B. Gabriel, and E. Kenik, "Application of Electron Microscopes in Metallurgy," submitted to *Metals Handbook.*

M. K. Miller, "The ORNL Atom Probe," submitted to *J. Phys.*

M. K. Miller, "The ORNL Atom Probe Software Package," submitted to *J. Phys.*

M. K. Miller, "APFIM Studies of Phase Transformations," Microbeam Analysis Society Meeting, Albuquerque, N.Mex., Aug. 10, 1986, to be published in proceedings.

M. K. Miller, "Atom Probe Field Ion Microscopy," Microbeam Analysis Society Meeting, Albuquerque, N.Mex., Aug. 10, 1986, to be published in proceedings.

M. K. Miller and J. A. Horton, "Site Occupation Determination by APFIM for Hf, Fe, and Co in Ni_3Al," submitted to *Scripta Metall.*

M. K. Miller and J. A. Horton, "An Atom Probe Field Ion Microscope Study of Boron Decorated Boundaries in Ni_3Al," submitted to *Scripta Metall.*

M. K. Miller, L. L. Horton, and S. Spooner, "A Comparison of Characteristic Distance Measurement by AP, TEM, and SANS," submitted to *J. Phys.*

M. K. Miller, J. A. Spitznagel, S. S. Brenner, and M. G. Burke, "Microanalytical Investigations of Light Water Reactor Materials Using the Atom Probe," submitted to *Trans. Am. Nuc. Soc.*

J. P. Moore, F. J. Weaver, and D. L. McElroy, "The Thermal Conductivities of $SrCl_2$ NS AeD_2 from 85 to 400K," submitted to *J. Am. Ceram. Soc.*

D. M. Nicholson, A. Chowdhary, and L. Schwartz, "Monte Carlo Optimization of Pair Distribution Functions: Applications to the Electronic Structure of Disordered Metals," submitted to *Phys. Rev. B.*

D. Nicholson, A. Chowdhary, and L. Schwartz, "Pair Distribution Functions and the Electronic Properties of Liquid and Amorphous Metals," submitted to *J. Non-Cryst. Solids.*

W. C. Oliver, R. Hutchings, and J. B. Pethica, "Measurement of Hardness at Indentation Depths as Low as 20 Nanometres," submitted to American Society for Testing and Materials.

W. C. Oliver, C. J. McHargue, G. C. Farlow, and C. W. White, "The Hardness of Ion Implanted Ceramics," Materials Research Society Meeting, Boston, Dec. 2-7, 1985, to be published in proceedings.

N. H. Packan, "The Effect of Pulsed Irradiation on Microstructural Evolution," Workshop on Relation Between Mechanical Properties and Microstructure Under Fusion Irradiation Conditions, Ebeltoft, Denmark, June 27-July 2, 1985, to be published in proceedings.

N. H. Packan, L. Heatherly, W. Kesternich, and H. Schroeder, "Radiation-Induced Segregation in Light-Ion-Bombarded Ni-8% Se," 13th Symposium on Effects of Testing and Materials, Seattle, Wash., June 23-26, 1986, to be published in proceedings.

N. H. Packan, H. Schroeder, and W. Kesternich, "The Influence of Radiation-Induced Segregation on Ductility of Nickel-Silicon Alloy," 2nd International Conference on Fusion Reactor Materials, Chicago, Apr. 13-17, 1986, to be published in proceedings.

G. S. Painter, "Density Functional Description of Molecular Bonding Within the Local Spin Density Approximation," submitted *J. Phys. Chem.*

R. W. Pawel and J. J. Campbell, "Cation Vacancy Concentrations in Ferrous Sulfide Containing Chromium and Manganese," submitted to *Oxid. Met.*

D. F. Pedraza, "A Method for Analyzing the Swelling Behavior of a Metal Using the Minimum Critical Radius as a Steady State Parameter," submitted to *J. Nucl. Mater.*

D. F. Pedraza, "Mechanisms of the Electron Irradiation Induced Amorphous Transition in Intermetallic Compounds," submitted to *J. Mater. Res.*

D. F. Pedraza and L. K. Mansur, "The Effect of Point Defects on the Amorphization of Metallic Alloys During Ion Implantation," Fall TMS-AIME Meeting, Toronto, Canada, Oct. 13- 17, 1985, to be published in proceedings.

D. F. Pedraza and P. J. Maziasz, "Void-Precipitate Association During Neutron Irradiation of Austenitic Stainless Steel," 13th International Symposium on Effects of Radiation of Materials, Seattle, Wash., June 23-25, 1986, to be published in proceedings.

A. J. Pedraza and D. Pedraza, "An Analysis of Carbide Precipitation in V and Nb During Aging and Ion Bombardment," Fall TMS-AIME Meeting, Toronto, Canada, Oct. 13-17, 1985, to be published in proceedings.

F. J. Pinski, B. L. Gyorffy, D. D. Johnson, J. Staunton, and G. M. Stocks, "Ferromagnetism Versus Antiferromagnetism in Face Centered Cubic Iron," submitted to *Phys. Rev. Lett.*

J. H. Schneibel and L. Martinez, "Determination of Cavity Growth Rates from Cavity Size Distributions," submitted to *Philos. Mag.*

J. H. Schneibel and G. F. Petersen, "Grain Boundary Sliding in Wires with Bamboo Structure," 4th Japan Institute of Metals International Symposium (JIMIA-4), Minakami Spa, Japan, Nov. 25- 29, 1985, to be published in proceedings.

J. H. Schneibel, G. F. Petersen, and C. T. Liu, "Creep Behavior of a Polycrystalline Nickel-Aluminide: Ni-23.5 at. % Al-0.5 at. % Hf-0.2 at. % B," submitted to *J. Mater. Res.*

E. M. Schulson, T. P. Weihs, I. Baker, H. J. Frost, and J. A. Horton, "Grain Boundary Accomodation of Slip in Ni_3Al Containing Boron," submitted to *Acta Metall.*

Y. K. Simpson, C. B. Carter, P. S. Sklad, and J. Bentley, "Grain Boundary, Glass-Phase Identification and Possible Artifacts," Materials Research Society Symposium, Boston, Dec. 2-7, 1985, to be published in proceedings.

P. S. Sklad, "Recrystallization Behavior of Ion Beam Modified α-Al_2O_3," 44th Annual Meeting of the Electron Microscopy Society of America, Albuquerque, N.Mex., Aug. 10- 15, 1986, to be published in proceedings.

P. S. Sklad, P. Angelini, and J. T. Houston, "Analytical Electron Microscopy of Ion Implanted Silicon Carbide," 17th Annual Meeting of International Metallographic Society, Philadelphia, July 15- 18, 1984, to be published in proceedings.

L. D. Stephenson, J. Bentley, R. B. Benson, Jr., and G. K. Hubler, "Some Characteristics of $Al_{12}Mo$ in Aluminum Annealed after Implantation with Molybdenum," to be published in Materials Research Society Symposia Proceedings.

G. M. Stocks, M. Boring, D. M. Nicholson, F. J. Pinski, D. D. Johnson, J. S. Faulkner, and B. L. Gyorffy, "Self-Consistent Electronic Structures of α-Phase Hume-Rothery Electron Alloys Cu_cZn_{1-c}, $Cu_cGa_{1-c}Ge_{1-c}$," Symposium on Noble Metal Alloys, Metallurgical Society of AIME, Feb. 25-27, 1985, to be published in proceedings.

G. M. Stocks, D. D. Johnson, B. L. Gyorffy, F. J. Pinski, and J. Staunton, "A First-Principles Calculation of the Magnetic Properties of Paramagnetic fcc Iron," 1985 International Conference on Magnetism, San Francisco, Aug. 26-30, 1985, to be published in proceedings.

R. E. Stoller and G. R. Odette, "A Comparison of the Relative Importance of Helium and Vacancy Accumulation in Void Nucleation," 13th International Symposium on Effects of Radiation on Materials, Seattle, Wash., June 23-25, 1986, to be published in proceedings.

R. E. Stoller and G. R. Odette, "A Composite Model of Microstructural Evolution in Austenitic Stainless Steel Under Fast Neutron Irradiation," 13th International Symposium on Effects of Radiation on Materials, Seattle, Wash., June 23-25, 1986, to be published in proceedings.

R. E. Stoller and G. R. Odette, "A Composite Model of Microstructural Evolution in Austenitic Stainless Steel Under Fast Neutron Irradiation," submitted to *Damage Analysis and Fundamental Studies Quarterly Progress Report*.

J. C. Swihart, W. H. Butler, and G. M. Stocks, "First Principles Calculation of Residual Electrical Resistivity of Random Alloys," submitted to *Phys. Rev. Lett*.

H. Trinkaus and M. H. Yoo, "Nucleation Under Time-Dependent Supersaturation," submitted to *Philos. Mag*.

J. M. Vitek, "G-Phase Formation in Aged Type 308 Stainless Steel," submitted to *Metall. Trans. A*.

J. M. Vitek and S. A. David, "Use of Analytical Electron Microscopy in Evaluating Ferrite Stability in Austenitic Stainless Steel Welds," 21st MAS Conference, Applications of Microanalysis to Welding, Albuquerque, N.Mex., Aug. 10-15, 1986, to be published in proceedings.

J. M. Vitek and S. A. David, "The Sigma Phase Transformation in Austenitic Stainless Steels," submitted to *Weld. J.*

J. M. Vitek and M. Ruhle, "Diffraction Effects from Internal Interfaces. Part II. Interphase Interfaces," submitted to *Acta Metall.*

J. M. Vitek and M. Ruhle, "Diffraction Effects from Internal Interfaces, Part I: General Considerations and Grain Boundary Effects," submitted to *Acta Metall.*

C. L. White, "Recent Development Concerning Segregation and Fracture at Grain Boundaries," Annual American Vacuum Society Meeting, Houston, Nov. 19–22, 1985, to be published in proceedings.

C. L. White, "On the Temperature and Composition Dependence of Interfacial Energies in Binary Substitutional Solid Solutions," submitted to *Metall. Trans.*

H. L. Yakel, "Atom Distribution in Tau Carbide Phases: Fe and Cr Distributions in $(Cr_{23-x}Fe_x)C_6$ With x = 0, 0.7_4, 1.7_0, 4.1_3, and 7.3_6," submitted to *Acta Crystall.*

ORNL/TM-10033
Distribution
Category UC-25

INTERNAL DISTRIBUTION

1–2. Central Research Library
3. Document Reference Section
4–5. Laboratory Records Department
6. Laboratory Records, ORNL RC
7. ORNL Patent Section
8. P. Angelini
9. B. R. Appleton
10. S. Baik
11. P. F. Becher
12. J. Bentley
13. A. Bleier
14. E. E. Bloom
15. L. A. Boatner
16. K. W. Boling
17. R. A. Bradley
18. V. R. Bullington
19. W. H. Butler
20. A. J. Caputo
21. O. B. Cavin
22. R. E. Clausing
23. R. S. Crouse
24. S. A. David
25. J. H. DeVan
26. C. K. H. DuBose
27. D. S. Easton
28. W. P. Eatherly
29. R. L. Heestand
30. L. L. Horton
31. J. A. Horton, Jr.
32. D. W. Jared
33. D. R. Johnson
34. J. E. Jones, Jr.
35. M. J. Kania
36. J. R. Keiser
37. E. A. Kenik
38. J. W. Koger
39. E. H. Lee
40. M. B. Lewis
41. C. T. Liu
42. E. L. Long, Jr.
43. T. S. Lundy
44. L. K. Mansur
45. R. W. McClung
46. C. J. McHargue
47. C. G. McKamey
48. M. K. Miller
49. W. H. Miller, Jr.
50. R. M. Moon
51. A. J. Moorhead
52. R. K. Nanstad
53. N. H. Packan
54. D. F. Pedraza
55. M. L. Poutsma
56. P. L. Rittenhouse
57. A. F. Rowcliffe
58. A. C. Schaffhauser
59. P. S. Sklad
60. G. M. Slaughter
61–65. J. O. Stiegler
66. R. E. Stoller
67–183. P. T. Thornton
184. P. F. Tortorelli
185. D. B. Trauger
186. J. M. Vitek
187. J. R. Weir
188. C. W. White
189. F. W. Wiffen
190. R. O. Williams
191. J. M. Williams
192. M. H. Yoo
193. F. W. Young, Jr.
194. A. Zucker
195. R. J. Charles (Consultant)
196. G. Y. Chin (Consultant)
197. H. E. Cook (Consultant)
198. Alan Lawley (Consultant)
199. W. D. Nix (Consultant)
200. J. C. Williams (Consultant)

EXTERNAL DISTRIBUTION

201–203. AERE, Harwell, Didcot, Oxon, OX11, ORB, England

J. P. Charlesworth, Chemistry Division
A. B. Lidiard, Theoretical Physics Division
S. F. Pugh, Metallurgy Division

204–205. Ames Laboratory, Iowa State University, Ames, IA 50011

D. Finnemore
R. S. Hanson

206–208. Argonne National Laboratory, 9700 South Cass Ave., Argonne, IL 60439

F. Y. Fradin
B. R. T. Frost
H. Wiedersich

209–211. Arizona State University, Tempe, AZ 85218

R. W. Carpenter
W. A. Coghlan
J. B. Wagner

212. Australian Atomic Energy Commission, Lucas Heights, NSW, Australia

Adam Jostsons

213–214. Brookhaven National Laboratory, Upton, NY 11973

A. N. Goland
M. Suenaga, Materials Science Division

215. Brown University, Division of Engineering, Providence, RI 02912

J. Gurland

216–217. Carnegie-Mellon University, Department of Metallurgy and Materials Science, Pittsburgh, PA 15213

H. I. Aaronson
R. F. Sekerka

218–221. Case-Western Reserve University, Metallurgy and Materials Science, Cleveland, OH 44106

R. F. Hehemann
A. H. Heuer
L. W. Hobbs
T. E. Mitchell

222. Central Electrical Generating Board, Berkeley Nuclear Laboratories, Berkeley, Gloucestershire, CL13 9PB, England

J. E. Harris

223. Centre d'Etúdes Nucléaires, Fontenay-aux-Roses, France

Y. Queré, Section d'Etúdes des Solides Irradies

224–225. Cornell University, Department of Materials Science and Engineering, Ithaca, NY 14850

C. Y. Li
J. W. Mayer

226. Dresser Industries, Security Division, P.O. Box 24647, Dallas, TX 75224

W. E. Littman, Vice-President, Research and Engineering

227. EG&G Idaho, Inc., P.O. Box 1625, Idaho Falls, ID 83415

J. Seydel, Branch Manager

228. Ford Motor Company, Dearborn, MI 48121

A. D. Brailsford

229. General Electric Research and Development Center, Schenectady, NY 12301

W. Johnson

230–231. Georgia Institute of Technology, Department of Chemical Engineering, Atlanta, GA 30332

B. R. Livesay
R. A. Young

232. GLCA Denison University, Main Street, Granville, OH 43023

R. R. Winters, Director, Oak Ridge Science Semester

233. Hanford Engineering Development Laboratory, P.O. Box 1970, Richland, WA 99352

D. G. Doran

234. Idaho National Engineering Laboratory, 550 2nd Street, Idaho Falls, ID 83415

D. D. Keiser

235. Illinois Institute of Technology, Department of Metallurgical and Materials Engineering, Chicago, IL 60612

N. N. Brever

236–239. Institute für Festkörperforschung der Kernforschungsanlage Jülich, D-5170, Postfach 1913, Federal Republic of Germany

H. G. Bohn
W. Schilling
H. Ullmaier
H. Wenzl

240. Institute für Metallphysik, University of Göttingen, Federal Republic of Germany

P. Haasen

241. Institute für Reaktorwerkostoffe, Kernforschungsanlage Jülich GmbH, 517 Jülich 1, Postfach 1913, Federal Republic of Germany

H. Nickel, Director

242–243. Institute für Theoretische und Angewandte Physik der Universität Stuttgart, 7000 Stuttgart 80-Pfaffenwaldring 57/V1, Federal Republic of Germany

H. P. Lamparter
A. Seeger

244–245. Lawrence Berkeley Laboratory, Materials and Molecular Research Division, Berkeley, CA 94720

J. W. Morris, Jr.
N. E. Phillips

246. Lawrence Livermore National Laboratory, University of California, P.O. Box 808, Livermore, CA 94550

Glen Mara

247. Los Alamos Scientific Laboratory, P.O. Box 1663, Los Alamos, NM 87545

S. S. Hecker

248. Loughborough University of Technology, 51 Tynedale Road, Loughbrough, Leicestershire, England LE113TA

R. G. Faulkner

249–250. Massachusetts Institute of Technology, Department of Materials Science and Engineering, Cambridge, MA 02139

R. L. Coble
W. S. Owen

251. Michigan Technological University, Department of Metallurgical Engineering, Houghton, MI 49931

L. A. Heldt

252. National Bureau of Standards, Gaithersburg, MD 20899

S. J. Dapkunas

253–254. National University of Athens, Institute of Mineralogy and Petrology, Panepistimiopolis, Ano Ilissia, Athens 621, Greece

C. N. Koumelis
D. L. Koumelis

255. Naval Research Laboratory, Washington, DC 20375

D. J. Michel, Metallurgy Division, Code 6397

256–258. North Carolina State University, Department of Materials Engineering, Raleigh, NC 27607

R. B. Bensen, Jr.
H. Conrad
C. C. Koch

259–260. Northwestern University, Department of Materials Science and Engineering, Evanston, IL 60201

M. Meshii
J. R. Weertman

261. Oak Ridge Associated Universities, P.O. Box 117, Oak Ridge, TN 37831

Beth Jinkerson

262. Office of Naval Research, Metals and Ceramics Program, Code 471, 800 N. Quincy, Arlington, VA 22217

R. C. Pohanka

263–264. Ohio State University, 116 W. 19th Street, Columbus, OH 43210

R. Mills, Department of Physics
P. G. Shewmon, Department of Metallurgical Engineering

265. Pacific Northwest Laboratories, P.O. Box 999, Richland, WA 99352

J. T. A. Roberts

266. Pennsylvania State University, Department of Materials Science, University Park, PA 16802

K. Spear

267–268. Rensselaer Polytechnic Institute, Department of Materials Engineering, Troy, NY 12181

M. E. Glicksman
N. P. Stoloff

269. Research Laboratory of Engineering Materials, 4259 Nagatsuta, Midori, Yokohama 227, Japan

Shigeyuki Sōmiya, Laboratory of Engineering Materials

270. Rice University, P.O. Box 192, Department of Materials Science, Houston, TX 77001

R. B. McLellan

271–273. Sandia Laboratories, Albuquerque, NM 87115

W. Brinkman, Vice-President
R. L. Schwoebel, Director, Material and Process Sciences
F. L. Vook, Director, Solid State Sciences

274. Sandia Laboratories, Livermore, CA 44550

W. Bauer, Physical Research

275. SCIENCE, 1515 Massachusetts Ave., NW, Washington, DC 20005

P. H. Abelson

276. SCK/CEN, B 2400 Mol, Belgium

S. Amelinckx

277–278. Stanford University, Department of Materials Science and Engineering, Stanford, CA 94305

R. H. Bube
R. Sinclair

279. Technische Hochschule Aachen, Aachen, Federal Republic of Germany

K. Lücke

280. Toyota Central Research and Development Laboratories, Inc., 41-1 Nagakute, Aichi-ken, Aichi, 480-11, Japan

T. Hioki

281. United Technologies Research Center, East Hartford, CT 06108

E. R. Thompson

282. University of Birmingham, Department of Physical Metallurgy and Science and Materials, Birmingham, B152TT England

R. E. Smallman

283. University of California, Department of Materials Science and Mineral Engineering, Berkeley, CA 94720

R. H. Bragg

284. University of Cincinnati, Department of Materials Science and Metallurgical Engineering, Cincinnati, OH 45221

J. Moteff

285. University of Connecticut, Department of Metallurgy, Storrs, CT 06268

P. C. Clapp

286. University of Crete, Physics Department, P.O. Box 470, Iraklion, Crete, Greece

G. Kiriakidis

287–288. University of Florida, Department of Materials Science and Engineering, Gainesville, FL 32611

J. J. Hren
E. D. Vernik, Jr.

289. University of Houston, Department of Physics, Houston, TX 77004

S. C. Moss

290–292. University of Illinois, Urbana, IL 61801

C. G. Bergeron, Department of Ceramic Engineers
C. P. Flynn, Director, Materials Research Laboratory
N. Peterson, Department of Metallurgy and Mining Engineers

293. University of Lancaster, Department of Physics, Lancaster LA1 4YB, England

H. M. Pollock

294. University of Mexico, Instituto de Fisica, A.P. 20-364, 01000 Mexico, D.F. Mexico

J. A. Soullard

295. University of Michigan, Department of Materials and Metallurgical Engineering, Ann Arbor, MI 48109

R. D. Pehlke

296. University of Minnesota, Department of Chemical Engineering and Materials Science, Minneapolis, MN 55455

W. W. Gerberich

297. University of Missouri-Rolla, Department of Metallurgical and Nuclear Engineering, Rolla, MO 65401

H. W. Weart

298. University of Oslo, Department of Chemistry, Blindern, Oslo, Norway

K. Kofstad

299-301. University of Tennessee, Department of Materials Science, Knoxville, TN 37996

B. F. Oliver
J. E. Spruiell
E. E. Stansbury

302-304. University of Virginia, Department of Material Science, Thornton Hall, Charlottesville, VA 22901

W. A. Jesser
K. R. Lawless
H. G. Wilsdorf

305. University of Washington, Department of Metallurgical Engineering, Seattle, WA 98195

D. H. Polonis

306-307. University of Wisconsin, Madison, WI 53706

R. A. Dodd, Department of Metallurgical and Mineral Engineering
W. Wolfer, Department of Nuclear Engineering

308. Virginia Polytechnic Institute and State University, Department of Materials Engineering, Blacksburg, VA 24060

C. W. Spencer

309. Vanderbilt University, Mechanical Engineering and Materials Science, Nashville, TN 37235

J. J. Wert

310. H. H. Willis Physics Laboratory, University of Bristol, Bristol, England

K. H. G. Ashbee

311. DOE, Division of Magnetic Fusion Energy, Washington, DC 20545

T. C. Reuther (ER-533, J224/GTN)

312-317. DOE, Division of Materials Sciences, Washington, DC 20545

R. J. Gottschall (ER-131, J321/GTN)
L. C. Ianniello (ER-13, J317/GTN)
R. H. Kropschot (ER-10, J304/GTN)
F. V. Nolfi (ER-131, J314/GTN)
D. K. Stevens (ER-11, J304/GTN)
M. C. Wittels (ER-132, J325/GTN)

318. DOE, Office of Fossil Energy, Washington, DC 20545

M. I. Singer (FE-14, B115/GTN)

319. DOE, Oak Ridge Operations Office, P.O. Box E, Oak Ridge, TN 37831

Office of Assistant Manager for Energy Research and Development

320-499. DOE, Technical Information Center, Office of Information Services, P.O. Box 62, Oak Ridge, TN 37831

For distribution as shown in DOE/TIC-4500, Distribution Category UC-25 (Materials).